PROTOPLANETARY DISK ANATOMY

EXAMINING THE STRUCTURE AND CHEMISTRY OF PLANETARY BIRTHPLACES WITH SIMPLE MOLECULES

PROEFSCHRIFT

ter verkrijging van
de graad van Doctor aan de Universiteit Leiden,
op gezag van de Rector Magnificus prof. mr. C. J. J. M. Stolker,
volgens besluit van het College voor Promoties
te verdedigen op donderdag 06 december 2018
klokke 10:00 uur

door
Mason Carney
geboren te Maine, USA
in 1988

Promotiecommissie

Promotores:	Prof. dr. M. R. Hogerheijde	
	Prof. dr. E. F. van Dishoeck	
Overige leden:	Prof. dr. C. Dominik	University of Amsterdam
	Prof. dr. A. Isella	Rice University
	Prof. dr. H. Nomura	Tokyo Institute of Technology
	Prof. dr. C. U. Keller	Leiden Observatory
	Prof. dr. H. J. A. Röttgering	Leiden Observatory

ISBN: 978-94-028-1258-9

Cover: A surgical hand unveils the anatomy of a protoplanetary disk.
Linoleum cut, digitally scanned.

Designed by Mart van de Wiel & Mason Carney

Created by Mart van de Wiel

To the curious

“If people sat outside and looked at the stars each night, I’ll bet they’d live a lot differently. When you look into infinity, you realize that there are more important things than what people do all day.”

– Bill Watterson, *Calvin and Hobbes*

TABLE OF CONTENTS

1 Introduction 1
1.1 The Origins of Planetary Systems 2
1.2 Star and Planet Formation 2
1.2.1 Molecular cloud cores and the embedded protostellar phase 4
1.2.2 The pre-main sequence and protoplanetary disk phase . . . 5
1.3 The Protoplanetary Disk 6
1.3.1 Disk structure and evolution 6
1.3.2 Disk chemistry 11
1.4 Disks in the Age of ALMA 14
1.4.1 Overview of ALMA 15
1.4.2 Revolutionary imaging with ALMA 16
1.4.3 Modeling line emission from ALMA observations 19
1.5 This Thesis 22
1.6 Outlook 25
1.6.1 ALMA and VLT/SPHERE 25
1.6.2 Future facilities 26
References 29

2 Increased H_2CO production in the outer disk around HD 163296 35
2.1 Introduction 36
2.2 Observations and reduction 38
2.3 Results 40
2.3.1 Detection and distribution of H_2CO 40
2.3.2 Modeling H_2CO and $C^{18}O$ emission 45
2.3.3 H_2CO excitation temperature 53
2.4 Discussion 54
2.4.1 H_2CO and the CO snow line 55
2.4.2 H_2CO inner hole 56
2.4.3 H_2CO and the millimeter continuum edge 57
2.5 Conclusions 57
Appendix 60
References 66

3 ALMA unveils rings and gaps in the protoplanetary system HD 169142: signatures of two giant protoplanets 69
3.1 Introduction 70
3.2 HD 169142 71
3.3 Observations and data reduction 72
3.4 Results 73
3.4.1 Dust continuum emission 73
3.4.2 CO isotopolog emission 74
3.4.3 Disk surface density 77
3.5 Analysis 78
3.5.1 Disk model description 78
3.5.2 Surface density 78
3.5.3 Model grid 80
3.5.4 Fiducial model and comparison with observations 81
3.6 Discussion 84
3.7 Conclusions 85
Appendix 87
References 91

4 Probing midplane CO abundance and gas temperature with DCO^+ in the protoplanetary disk around HD 169142 93
4.1 Introduction 94
4.2 Observations and reduction 96
4.3 Results 97
4.3.1 Radial distribution of DCO^+ 99
4.3.2 Column density and disk-averaged abundance in LTE . . . 101
4.4 Modeling DCO^+ emission 102
4.4.1 Fiducial physical structure 102
4.4.2 Vertically averaged radial abundance profile in LTE 103
4.4.3 Parameterized models 105
4.5 Discussion 112
4.5.1 Inner disk DCO^+ 112
4.5.2 Outer disk DCO^+ 112
4.6 Conclusions 113
Appendix 116
References 121

5 Upper limits on CH_3OH in the HD 163296 protoplanetary disk: evidence for a low gas-phase CH_3OH/H_2CO ratio 125
5.1 Introduction 126
5.2 Observations and reduction 128
5.3 Results 130
5.3.1 Line extraction 131
5.3.2 CH_3OH column density and abundance upper limits 133
5.3.3 H_2CO and CH_3OH in HD 163296 and TW Hya 136
5.3.4 Model CH_3OH spectra for HD 163296 136
5.4 Discussion 137
5.4.1 The CH_3OH/H_2CO ratio in HD 163296 and TW Hya . . . 137
5.4.2 Detectability of methanol 141
5.5 Conclusions 141

Appendix 144
References 145

Anatomy of a thesis **150**

English summary **153**

Nederlandse samenvatting **156**

Publications **163**

Curriculum Vitae **165**

Acknowledgements **167**

The White Rabbit put on his spectacles.
“Where shall I begin, please your Majesty?” he asked.
“Begin at the beginning,” the King said gravely,
“and go on till you come to the end: then stop.”

– Lewis Carroll, *Alice’s Adventures in Wonderland*

CHAPTER 1

INTRODUCTION

1.1 The Origins of Planetary Systems

The question of life beyond Earth has fascinated humankind for millennia. There is still no clear answer as to whether or not complex organisms and other forms of developed life exist elsewhere in the Universe, but it is a question that is pursued relentlessly, driven by an innate human curiosity and a desire to understand our own origins. The building blocks of life are present beyond the Solar System, but evidence for life itself remains elusive.

In the modern age, we have the technology to search for the signatures of life both within and outside of our own planetary system. The past several decades have seen the first detection of planets around stars other than our own Sun (Mayor & Queloz 1995), and significant advances in our understanding of the formation of planets. We are able to probe their birthplaces in disks of gas and dust around young, forming stars (Strom et al. 1989; Weintraub et al. 1989; Beckwith et al. 1990). We can detect fully formed planetary systems around distant stars and investigate the diversity of individual planets, their sizes, their compositions, their orbits, even their atmospheres, and the overall configuration of these systems (Lissauer 2002; Burrows 2014; Winn & Fabrycky 2015). To date, thousands of extrasolar planetary systems have been discovered and we see that they have a rich complexity and often look very different from our own Solar System[1,2]. Why are these systems so highly diverse, how did they come be this way, and what can we learn about their formation and the implications for planet habitability? To answer these questions, we must develop a thorough understanding from start to finish of the processes that create planetary systems: from giant clouds of gas and dust in space, to stellar formation within these clouds, to the protoplanetary disks that surround young stars, to the aggregation of planetary bodies within these disks.

The complexity of these processes cannot be understated. The scientific community at large must work together to build a framework for planet formation that is well-described by both theory and observation. A wealth of information awaits out in the vast reaches of space that will help us to develop our understanding of how life emerges in the Universe. Ultimately, we aim to fully comprehend the planet formation process in order to accurately describe the diversity of planetary systems that we see and to make predictions about where to look for life beyond the Solar System.

1.2 Star and Planet Formation

The formation of stars occurs in dense regions of gas and dust, most often found in Giant Molecular Clouds (GMCs). The formation of individual stars can be relatively isolated or tightly grouped, depending on their environment. This section presents a description of the simplest star formation case – an isolated low-mass star – in order to highlight the important steps of the formation process (Figure 1.1). In reality, star formation can result in a wide variety of outcomes including binaries, other multiple systems, and dense stellar clusters (Batten 1973; Archinal & Hynes 2003). Initial conditions in the natal molecular cloud are diverse and ultimately determine the final composition and configuration of stars

---

[1] `http://exoplanets.org/`

[2] `http://exoplanet.eu/`

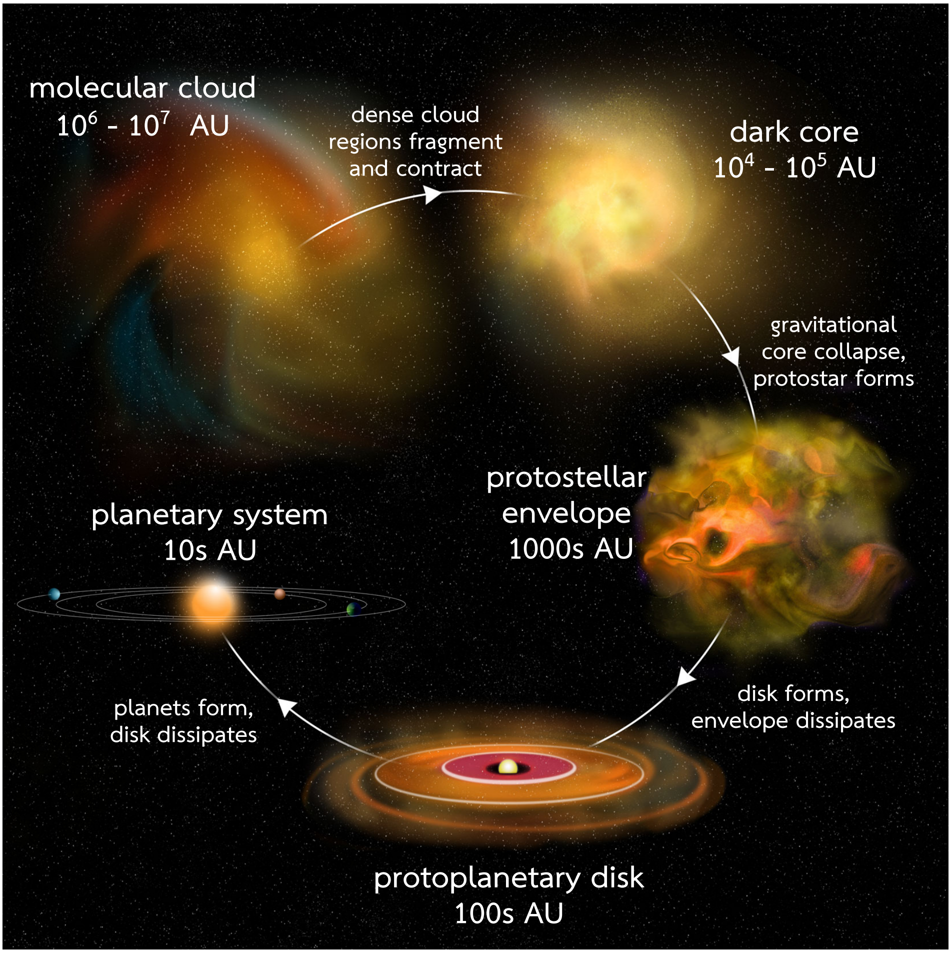
molecular cloud
10^6 - 10^7 AU
dense cloud
regions fragment
and contract
dark core
10^4 - 10^5 AU
gravitational
core collapse,
protostar forms
protostellar
envelope
1000s AU
planetary system
10s AU
disk forms,
envelope dissipates
planets form,
disk dissipates
protoplanetary disk
100s AU

Figure 1.1: The low-mass star formation process. Star formation begins in dense molecular clouds, which can fragment and contract into dark cores of gas and dust. Within dark cores, material undergoes gravitational collapse to form a protostar at the center with a disk and envelope surrounding it. The envelope and the disk dissipate as the central star evolves toward the main sequence, leaving behind a planetary system.
Credit: Adapted from Bill Saxton (NRAO/AUI/NSF).

that will be produced. The process can lead to a bimodal distribution (Herbig 1962) that results in both high-mass stars ($> 8\ M_\odot$) and low-mass stars ($< 8\ M_\odot$). High-mass stars are formed in the most massive cloud cores, quickly reach the hydrogen-burning main sequence stage, and rapidly evolve to become supergiants over timescales of tens to hundreds of millions of years before going supernova, leaving behind compact neutron stars or black holes. Low-mass stars are far more common, take longer to reach the main sequence, remain on the main sequence with lifetimes of several billion years, and eventually evolve into red giants that shed their outer layers to become nebulae containing a white dwarf remnant (for an overview of stellar evolution, see e.g., Prialnik 2009). The formation of low-mass stars is thought to be reasonably well-understood as described in the following text. The path leading to high-mass stars remains subject to debate because they form most often in massive cores that result in stellar clusters and therefore may have different formation pathways than a single, low-mass pre-stellar core. Theories such as competitive accretion and stellar mergers have been proposed to explain the existence of the most massive stars (Bonnell et al. 1997, 1998). The remainder of this section describes the formation of low-mass stars specifically, while the rest of the introduction and the scientific chapters of this thesis focus on the environment around young, low-mass stars.

1.2.1 Molecular cloud cores and the embedded protostellar phase

GMCs are composed of dense material ($> 10^2 - 10^3$ cm^{-3}) relative to the interstellar medium (ISM) and span several to hundreds of parsecs. The gas and dust contained in GMCs is not homogeneous. Rather, the cloud contains density variations. The regions of overdense gas and dust can become unstable due to the internal motions of cloud material, cloud-cloud interactions, or shocks created by an external event such as nearby supernovae (Elmegreen 1998). Such unstable regions begin to gradually contract into even denser, dark cores ($> 10^5 - 10^6$ cm^{-3}) on scales of a few hundred thousand astronomical units (10^5 AU) within the GMC. Recent observations have shown that the star-forming regions of molecular clouds have a filamentary structure which can efficiently funnel cloud material along the filament axis and set the rotational velocity pattern of dark pre-stellar cores (Hacar & Tafalla 2011; Hacar et al. 2013, 2018). The Orion GMC is the most famous example for high- and low-mass star formation. Examples of other nearby dark cloud complexes with active low-mass star formation include the Perseus, Taurus, Chameleon, Ophiuchus, Lupus, Corona Australis, Upper Scorpius, and Serpens molecular clouds.

As the dark cores found in GMCs continue to contract, the densest regions eventually overcome the magnetic and turbulent forces supporting against collapse at such scales. These dense, unstable pockets then undergo inside-out gravitational collapse on scales of tens of thousands of astronomical units (10^4 AU) (Shu 1977). As infalling material collects at the center of the collapse site, rapid contraction occurs under significant self-gravity, which stops only once a central hydrostatic core has been formed (Hayashi 1961, 1966). The surrounding envelope continues to collapse onto this central hydrostatic core as it grows in mass. Deuterium burning occurs at this stage, which generates energy that stops further contraction of the central hydrostatic core – now a protostellar object – and prevents hydrogen burning (Bally & Reipurth 2006). The formation of the central protostellar object is often considered the $t = 0$ mark during the stellar formation process. The protostar remains embedded in an envelope of gas and dust on scales of thousands of astronomical units (10^3 AU). The envelope continues to feed material onto the protostar over timescales of tens to hundreds of thousands of years ($10^4 - 10^5$ yr) as the system evolves. It is during this embedded phase that a disk of envelope material forms around the protostar on scales of hundreds of astronomical units (10^2 AU). The circumstellar disk is formed as a consequence of angular momentum conservation and acts as an intermediary between infalling material from the envelope and material that is accreted onto the protostar (Shu et al. 1987). Dissipation of angular momentum is required at this stage in order to prevent the protostar from rotating faster than its breakup velocity, thus the disk transports angular momentum outward away from the protostar through viscous spreading, causing the disk to grow larger as the system evolves (Terebey et al. 1984). During this embedded phase, high stellar accretion rates give rise to powerful outflows of supersonic material that emanate from the poles of the protostar. These powerful outflows serve as another mechanism to remove angular momentum from the system, and they penetrate the surrounding envelope creating high energy shocks that propel material away from the protostellar poles across vast distances relative to the size of the envelope, up to hundreds of thousands of astronomical units (Herbig 1951; Haro 1952; Bachiller 1996; Bally 2016). Outflows are a key observational signature of an embedded young stellar object (YSO).

1.2.2 The pre-main sequence and protoplanetary disk phase

The opening created in the envelope by the YSO outflows widens as the system continues to evolve. The envelope material is depleted as it is accreted onto the protostar-disk system and blown away by the powerful outflows at the poles. When the envelope dissipates and the system becomes optically visible, the central protostar has accumulated most of its mass and is classified as a pre-main sequence (PMS) star on the Hertzsprung-Russell diagram. PMS stars are broadly separated into two categories: T Tauri PMS stars with low stellar mass ($< 2\ M_\odot$) and spectral type M, K, G, or F; and Herbig Ae/Be PMS stars with intermediate stellar mass ($2 - 8\ M_\odot$) and spectral type A or B (Appenzeller & Mundt 1989; Waters & Waelkens 1998). High-mass stars ($> 8\ M_\odot$) do not have an observable PMS stage because they evolve so quickly that they are already main sequence stars by the time they have dispersed their envelope and become optically visible.

In this stage of star formation, only the circumstellar accretion disk is left behind, which continues to supply the PMS star with a steady flow of material as it evolves toward the main sequence. The circumstellar accretion disk contains the gaseous and solid – e.g., carbonaceous and silicate – ingredients that will eventually be incorporated into planets as the system evolves on timescales of a few million years (10^6 yr; Myr), thus it is called a protoplanetary disk (Williams & Cieza 2011). The gaseous protoplanetary disk is dissipated through a combination of photoevaporation by stellar winds from the central PMS star and incorporation of gas and dust into large solids at the disk midplane. The remaining circumstellar material is composed of dense, rocky bodies which will continue to undergo collisional aggregation and fragmentation on timescales of tens of millions of years (10^7 yr; 10s Myr) – potentially evolving as a debris disk containing a secondary dust particle population arising from these collisions. Eventually a mature, fully formed planetary system emerges.

Observational constraints on the evolutionary phases of star formation are essential to improve our understanding of the timescales involved in each phase leading to the development of planetary systems. Historically, determining the evolutionary phase of YSOs has been done using the spectral energy distribution (SED), which measures the flux of an object across a range of wavelengths. The SED will have a blackbody contribution from the central star and an excess of flux in the infrared (IR) indicative of surrounding material from the envelope and/or the disk that is heated by the central star (Lada & Wilking 1984). The amount of infrared flux excess is an indication of the evolutionary phase, with three distinct SED observational classes. The classes are based on the SED infrared slope over the 2 to 24 μm wavelength range – officially $\alpha_{\rm IR}$ (Lada & Wilking 1984; Greene et al. 1994; André et al. 2000). YSOs evolve from Class I to Class III as the contribution to the SED shifts towards optical wavelengths and gradually loses flux at far-IR/submillimeter wavelengths. The observational Class is expected to correspond to the physical stage of star formation, with Class I objects being deeply embedded in an envelope, Class II objects being optically visible and hosting gas-rich protoplanetary disks, and Class III objects hosting no detectable disk. The timescales previously noted for each stage of low-mass star formation are determined by Class statistics. The median lifetime of a specific Class is assumed – usually the Class II stage at ~2 – 3 Myr – and the total number of objects in each Class are counted in order to estimate their relative lifetimes (Kenyon & Hartmann 1995; Wilking et al. 2005; Evans et al. 2009). Recent work has shown that the link between Class and physical stage is not always clear, and that object geometry and foreground contamination can lead to misidentified YSOs using the $\alpha_{\rm IR}$ criteria (Evans et al. 2009; Heiderman & Evans 2015; Carney et al. 2016). Statistics and accurate categorization of YSOs are crucial for determining the lifetime of each phase of star formation. It is important to know the timescales necessary for planets to develop within the protoplanetary disk in order to test hypotheses about the physical processes involved in planet-disk interactions and planet formation.

1.3 The Protoplanetary Disk

The protoplanetary disk is the birthplace of planets, comets, and asteroids that remain in orbit around a fully formed main sequence star. The previous section outlines its formation and importance in the star formation process. In this section, more detail is provided on the physical and chemical structure and evolution throughout the lifetime of the gas-rich protoplanetary disk.

1.3.1 Disk structure and evolution

The bulk content of a protoplanetary disk is inherited from the natal envelope as material falls inward during the core collapse phase of star formation. The disk is composed of gas and dust (see Figure 1.2), predominantly in the form of (sub)micron-sized dust particles and molecular hydrogen. The gas makes up the vast majority (~99%) of the total disk mass, mostly in the form of H_2 and He gas (H_2:76% – He:22%; Ollivier et al. 2009). Although H_2 is the most abundant gas, it is difficult to observe due to its lack of an electric dipole moment as a symmetric molecule. Only magnetic quadrupole transitions ($\Delta J = \pm 2$) are allowed, with low-J transitions occurring in the mid-IR regime at high temperatures ($T > 100 - 200$ K) that are found close to the PMS star and in the upper disk layers, but not in the bulk outer disk (Henning & Semenov 2013). Measurements of disk mass are therefore traditionally done using observations of (sub)millimeter emission ($\lambda \approx 0.3 - 10$ mm; $\nu \approx 30 - 1000$ GHz) from thermally heated (sub)millimeter-sized dust particles, which are optically thin except for the inner-most radii of the disk (Beckwith et al. 1990; André & Montmerle 1994). A fixed ISM gas-to-dust ratio of 100 is assumed due to lack of accurate constraints on the gas-to-dust ratio in protoplanetary disks, and the disk mass M is directly related to the continuum flux at (sub)millimeter wavelengths

$$M(\text{dust} + \text{gas}) = \frac{F_\nu d^2}{\kappa_\nu B_\nu(T)}, \tag{1.1}$$

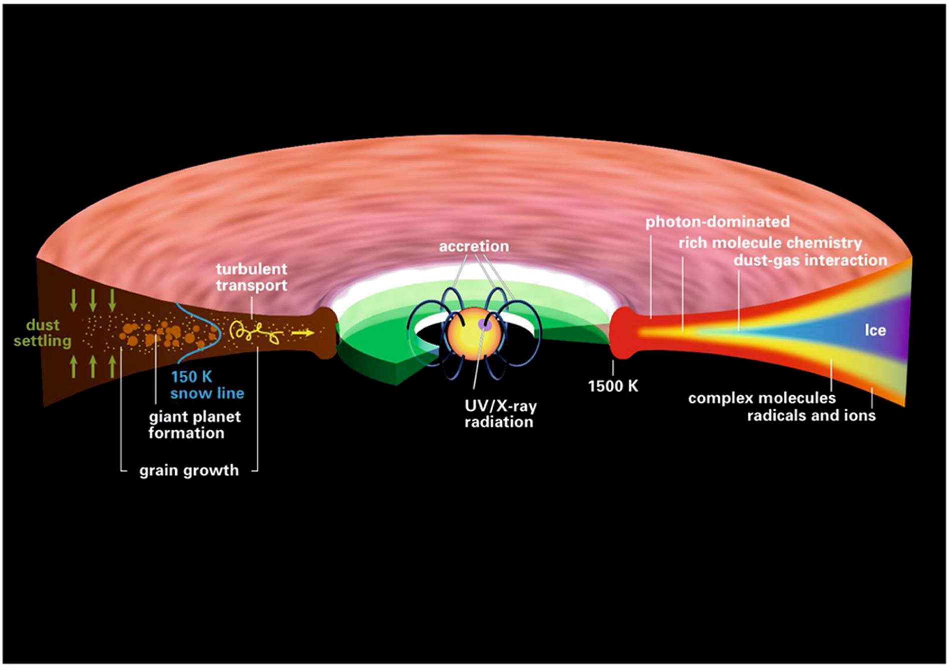
dust settling
turbulent transport
accretion
photon-dominated
rich molecule chemistry
dust-gas interaction
Ice
150 K snow line
giant planet formation
grain growth
UV/X-ray radiation
1500 K
complex molecules
radicals and ions

Figure 1.2: Structure of a protoplanetary disk. The left side shows the dust and highlights dynamical processes such as grain growth, vertical settling, and radial drift. The right side shows the stratified gas structure with a photon-dominated atomic upper layer, a warm intermediate layer with molecule-rich chemistry, and an icy disk midplane where temperatures are cold enough for molecular freeze-out.
Credit: Henning & Semenov (2013)

where F_ν is the measured flux at frequency ν, d is the distance to the source, κ_ν is the dust opacity, and $B_\nu(T)$ is the Planck function. The estimated mass of protoplanetary disks using this method has large uncertainties, as the gas-to-dust ratio in disks can differ significantly from the ISM value, and additional mass can be hidden in larger rocky bodies not probed at millimeter wavelengths. In general, protoplanetary disks around low-mass T Tauri and intermediate-mass Herbig Ae/Be PMS stars have masses of a few percent relative to the stellar mass ($M_{\rm disk}/M_* \approx 1\%$) under these assumptions (Andrews & Williams 2005, 2007).

Protoplanetary disks rotate due to the angular momentum of infalling material inherited from the parent dark core, which causes most of the disk material to be concentrated along the plane of rotation. A stable disk is supported by a combination of the gas pressure gradient and rotation. The disk rotational velocity profile is very close to Keplerian when the disk mass is a small fraction of the central PMS star (Guilloteau & Dutrey 1998; Qi et al. 2004)

$$v_{\rm K} = \sqrt{\frac{GM_*}{R}}, \tag{1.2}$$

where $v_{\rm K}$ is the Keplerian velocity, G is the gravitational constant, M_* is the mass of the central PMS star, and R is the radius away from the star. When observing gas toward YSOs, emission seen in Keplerian rotation is a significant piece of evidence that the gas resides in the circumstellar disk.

In physical descriptions of protoplanetary disks, the radially dependent surface density profile is a key structural property. Viscous transport of gas and dust in disks is thought to be the primary driver of disk evolution, which will alter the surface density profile throughout different evolutionary phases of the disk. However, purely molecular viscosity[3] cannot be the only source because the viscous evolution timescales are many orders of magnitude longer – e.g., on the order of $t > 10^{13}$ years for typical disk conditions at $R \approx 10$ AU – than the observed $10^6 - 10^7$ year lifetimes of protoplanetary disks (Pringle 1981; Gammie & Johnson 2005; Dullemond et al. 2007; Dominik 2015). The exact mechanism responsible for viscous transport of disk material is still not well-known, but may be associated with localized turbulence and/or magneto-rotational instability (MRI). MRI occurs when weak magnetic field lines exert a pull on rotating disk material, which results in angular momentum exchange and thus a radial velocity gradient leading to unstable turbulent motion (Balbus & Hawley 1998). However, in some regions of the disk MRI will be less effective due to variations in ionization resulting in a "dead zone" where disk particles no longer couple to the magnetic field (Armitage 2011). Without knowledge of the micro-processes powering disk viscosity, its description is traditionally parameterized and related to more general disk properties (Shakura & Sunyaev 1973)

$$\nu = \alpha \frac{c_{\rm s}}{\Omega_{\rm K}}, \tag{1.3}$$

where here ν is the disk viscosity, $c_{\rm s}$ is the local sound speed, $\Omega_{\rm K} = \sqrt{(GM_*/R^3)}$ is the Keplerian angular frequency, and α is a free parameter constant that describes the efficiency of angular momentum transport through the disk. The α parameter allows for tuning of the global disk viscosity to avoid the timescale issue with purely molecular viscosity. Historically, α-prescription viscous evolution models provide a simple, first-order approximation in good agreement with observed disk parameters such as mass, size, and the decrease in accretion rate with age of the system (Lynden-Bell & Pringle 1974; Hartmann et al. 1998).

Both viscous evolution models and fits to interferometric observations (e.g., Hughes et al. 2008; Andrews et al. 2009) show that the surface density profile $\Sigma(R)$ of protoplanetary disks follows a radial power-law with an exponentially tapered edge

$$\Sigma(R) = (2-\gamma)\frac{M_{\rm disk}}{2\pi R_{\rm c}^2}\left(\frac{R}{R_{\rm c}}\right)^{-\gamma} \exp\left[\left(-\frac{R}{R_{\rm c}}\right)^{2-\gamma}\right], \tag{1.4}$$

where $M_{\rm disk}$ is the disk mass, $R_{\rm c}$ is the characteristic radius, and γ is the power-law exponent that describes the radial dependence of the disk viscosity. The exponential tail in Equation 1.4 arises from the viscous spreading of material to larger radii as angular momentum is transported outward, and it has consequences for measurements of the outer radius of disks. It implies that the intensity of emission will drop off exponentially in the outer regions, thus making it difficult to detect low levels of optically thin disk material and calculate an unambiguous value for the size of the disk.

---

[3] $\nu_{\rm mol} \approx \lambda c_{\rm s}$ describes the molecular viscosity where $c_{\rm s}$ is the local sound speed and $\lambda = 1/n\sigma_{\rm m}$ is the mean-free path of molecules in the disk with n being the molecular number density and $\sigma_{\rm m}$ being the molecular collisional cross-section. The viscous timescale is given by $t = R^2/\nu_{\rm mol}$.

Disks have low vertical scale heights close to the central PMS star that increase with radius, which follows from the description for vertical hydrostatic equilibrium $H = c_s/\Omega_K$. The relationship between scale height and radius can be approximated as a power-law with vertical scale height $H \propto R^p$ and $p \approx 1.3 - 1.5$ (Chiang & Goldreich 1997; D'Alessio et al. 1998) The flared ($p > 1$) disk shape was first noted because of a large far-IR excess in observed disk flux that could not be explained by a flat disk geometry (Kenyon & Hartmann 1987). Disk flaring gives rise to a stratified density and temperature structure (Figure 1.2). The uppermost disk layers host low gas densities ($< 10^6$ cm^{-3}) and high temperatures (> 1000 K) due to direct exposure to radiation from the PMS star. The (sub)micron-sized dust particles in the disk are well-coupled to the gas and are therefore also present in the disk upper layers below the dust sublimation temperature of $\sim$1500 K (Gail 2010). The intermediate disk layers have higher gas densities ($10^6 - 10^8$ cm^{-3}) than the upper layers and are therefore partially shielded from stellar radiation, remaining warm ($> 30-40$ K). The heavily shielded disk midplane is cold (< 30 K) and hosts the highest gas densities ($> 10^8$ cm^{-3}) as well as the largest dust grain population in the disk due to the settling of $\gtrsim$ millimeter-sized particles.

The evolution of dust in the protoplanetary disk provides the seeds for planet formation. Dynamical motions within the rotating disk such as turbulence, viscous radial transport, vertical mixing, and Brownian motion all contribute to the aggregation of (sub)micron-sized dust particles into larger dust grains (Dullemond & Dominik 2005). Evidence for grain growth can be found in measurements of the SED slope at submillimeter wavelengths, α_{mm}, over approximately $0.5-1$ mm. The value for α_{mm} can be directly related to the millimeter dust opacity in the Rayleigh-Jeans limit (Williams & Cieza 2011). In the ISM, $\alpha_{\mathrm{mm}} \approx 4$ (Boulanger et al. 1996) is found to be significantly steeper than in disks, where $\alpha_{\mathrm{mm}} \approx 2-3$ (Beckwith & Sargent 1991; Mannings & Emerson 1994). The difference in α_{mm}, and thus dust opacity, is attributed to the growth of dust grains in the protoplanetary disk environment, with disks hosting substantially larger grains than the ISM. Grain growth into the millimeter regime causes dust to decouple from the gas and settle down toward the disk midplane (Figure 1.3). Vertical settling causes the more massive ($\sim$mm $-$ cm) dust grains to remain concentrated at the midplane, while vertical mixing causes smaller particles to be reprocessed up toward the disk surface layers. Evidence for vertical settling is found in the slope of mid-IR emission from Class II disks, which display less flux than expected for a disk in hydrostatic equilibrium, indicating that the micron-sized dust grains are not absorbing and re-emitting as much as stellar radiation as expected. Such an observation implies that the vertical scale heights for this grain population are not as flared as expected and therefore less than the gas vertical scale heights, which is a consequence of decoupling from the gas as larger grains settle to the disk midplane (Dullemond & Dominik 2004; D'Alessio et al. 2006).

Differences between T Tauri and Herbig Ae/Be PMS stars divide protoplanetary disks into two broad categories. Those around T Tauri PMS stars are generally less massive, cooler, and smaller while their Herbig Ae/Be counterparts are more massive, warmer, and larger. Herbig Ae/Be systems inherit a greater amount of material from the natal envelope, and they have a larger overall stellar luminosity (L_*) and stronger ultraviolet (UV) radiation (Waters & Waelkens 1998). The dominant source of ionization in these two classes of disks is an important con-

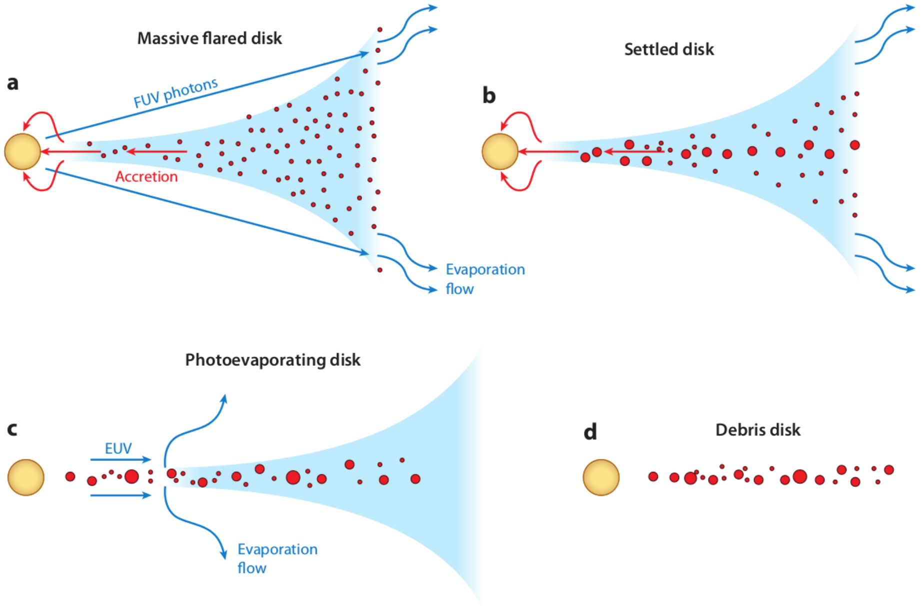

Figure 1.3: Evolution of a protoplanetary disk around a low-mass pre-main sequence star. a) A gas-rich, flared protoplanetary disk with predominantly small dust grains and active accretion. Radiation from the central PMS star evaporates the disk surface layers. b) The settled disk has undergone dust grain growth to millimeter, centimeter, and larger sizes that settle to the disk midplane and drift radially inward. c) The outer disk can no longer resupply the inner disk with material to accrete onto the PMS star. UV photoevaporation clears an inner hole in the disk. d) Photoevaporation continues until the gaseous disk is cleared, leaving behind a debris disk composed of dust.
Credit: Williams & Cieza (2011)

sideration for their structure and chemistry. Herbig Ae/Be disks are ionized in the surface layers primarily by the stronger UV spectrum of the PMS star, while T Tauri disks have a large contribution to their overall ionization from X-rays produced by magneto-accretion onto the central PMS star (Güdel & Nazé 2009). As X-ray emitters, T Tauri disks have strong, ionizing radiation penetrating deep into the intermediate disk layers. Atomic ionization of oxygen by X-rays can be a significant driver of disk chemistry. Additionally, X-ray ionization of H_2 produces excited electrons that can collisionally excite other H_2 molecules. These excited H_2 molecules then decay to emit photons in the Lyman and Werner bands that go on to ionize other species. In both types of disks, high energy cosmic ray particles have a low contribution to the overall disk ionization, but are the primary source of H_2 ionization deep in the disk midplane, playing a role similar to that of X-rays in the intermediate layers.

The dissipation of a protoplanetary disk is a result of viscous evolution and/or photoevaporation (Figure 1.3). As dust grains aggregate, decouple from the gas, and settle toward the midplane of the disk, the decoupled grains also drift radially inward toward the PMS star due to the drag forces felt as they travel through the dense gas. Through continued viscous transport and collisions, dust grows into rocks and eventually planetesimals and planets. Accretion onto the star diminishes over time and planetesimals sweep up gas until the material from the outer disk can no longer resupply the inner disk. The photoevaporation of inner disk material then dominates disk evolution and clears out an inner hole, halting accretion onto the central PMS star and speeding up the dissipation of the disk (Cieza et al. 2008). Protoplanetary disks with inner holes cleared out are classified as transition disks due to their transitional nature between a gas-rich and a gas-depleted disk. Disks can also be labeled as transitional by the opening of a gap due to the tidal forces of a secondary companion, possibly a planet (van der Marel et al. 2013; Casassus et al. 2013). These transition disks are traditionally identified based on their SED characteristics, which show a decrease in flux at IR wavelengths relative to classical T Tauri disks (Najita et al. 2007; Cieza et al. 2010). When the gaseous disk has been completely photoevaporated, the large solid material remains. Continued collisions between these solids may go on to form a long-lived dusty debris disk which evolves for tens of millions of years, but this may not be the case for all systems. Ultimately, evolution and dissipation of the disk leads to a mature, stable planetary system.

For extensive reviews of dynamical processes in protoplanetary disks and disk structure and evolution, see Armitage (2011) and Williams & Cieza (2011), respectively.

1.3.2 Disk chemistry

Carbon monoxide is the second most abundant molecular species after H_2, with a measured ratio of $CO/H_2 \approx 1 \times 10^{-4}$ in some molecular clouds (Lacy et al. 1994; Herbst & van Dishoeck 2009; France et al. 2014). CO is an important tracer of disk mass, temperature, and surface density. With a small permanent electric dipole moment, CO has low-J rotational transitions that are easily excited at low temperatures of $10-20$ K and observable at (sub)millimeter wavelengths, making it an excellent tracer of the cool regions in the outer disk where most of the gaseous disk mass resides. However, the main isotopolog ^{12}CO becomes quickly optically thick and therefore only traces gas content down to the intermediate surface layers of the disk and does not trace the deepest parts of the disk midplane where density is highest (van Zadelhoff et al. 2001; Bergin & Williams 2017). Less abundant isotopologs, such as ^{13}CO and C^{18}O, remain optically thin deeper into the disk and give better constraints on the disk mass and gas surface density (Miotello et al. 2014). An even more effective probe of disk mass is the deuterated form of molecular hydrogen (HD), which experiences an increase in abundance at low temperatures ($T \lesssim 30$ K) where deuterium chemistry is active in the disk, has emission lines in the (sub)millimeter and far-IR regime, and is likely optically thin throughout the cold outer disk. HD must be observed from space or with very high-altitude facilities like the Stratospheric Observatory for Infrared Astronomy[4] (SOFIA) and requires long on-source integration times. To date HD has been detected in only three protoplanetary disks around the young stars TW Hya, DM Tau, and GM Aur with the Herschel Space Observatory[5,6] (Bergin et al. 2013; McClure et al. 2016).

---

[4] `https://www.sofia.usra.edu/`

[5] `http://www.esa.int/Our_Activities/Space_Science/Herschel`

[6] `https://www.nasa.gov/mission_pages/herschel/index.html`

The density, temperature, and ionization structure of a protoplanetary disk all play vital roles in the ongoing chemistry. The stratified nature of disks gives rise to regions dominated by different drivers of atomic or molecular chemistry (Aikawa et al. 2002). Upper layers directly exposed to radiation from the central PMS star are subject to UV photodissociation and host atomic ionized species (Millar et al. 2003). Intermediate layers that are partially shielded from stellar radiation host a rich molecular gas-phase chemical environment (Walsh et al. 2014b). The cold disk midplane has temperatures low enough for many gas-phase species – H_2 excluded – to condense into ices around dust grains, where grain surface chemistry becomes important for the formation of complex molecular species (Herbst & van Dishoeck 2009; Öberg et al. 2009, 2010).

To better constrain the vertical temperature structure, and thus the available chemistry, atomic and molecular line observations are crucial diagnostics. Carbon monoxide again acts as a valuable tracer of bulk disk temperature due to its optically thick nature at different vertical locations in the disk, with low-J transitions at (sub)millimeter wavelengths probing the coldest parts of the disk and medium- to high-J transitions probing the upper disk layers. Combining observations of ^{12}CO and ^{13}CO $J = 1-0$, $J = 2-1$ and/or $J = 3-2$ (Dartois et al. 2003; Akiyama et al. 2011) or combining observations of low-J CO transitions with ^{12}CO $J = 6-5$ (van Zadelhoff et al. 2001; Qi et al. 2006, 2011; Schwarz et al. 2016) reveals distinct temperature regions at different vertical scale heights.

Surface layers of the disk that are dominated by far UV radiation have chemical reactions driven by photochemistry, which can be traced by molecules such as the CN radical. CN can be a recombination product of atomic C and N, or a photodissociation product of the more stable HCN and HNC molecules via Lyman α radiation (Bergin et al. 2003). One would expect the HCN molecule to be abundant in the lukewarm conditions of the partially shielded intermediate disk layers, while CN is sensitive to upper molecular layers and disk surface that are subject to strong stellar radiation (Aikawa & Herbst 1999). Simultaneous observations of CN and HCN can help to constrain their distribution throughout the disk and their sensitivity to UV flux (Chapillon et al. 2012; Cazzoletti et al. 2018). Even higher in the disk, molecules are destroyed completely and neutral and ionized atomic species dominate the most diffuse parts of the disk surface. Of particular interest for disk chemistry and structure is the elemental abundance of carbon, which can be constrained by observations of CO, neutral C, and ionized C (Kama et al. 2016).

Deeper in the disk and close to the midplane, the role of freeze-out has a great effect on the gas-phase and solid-phase chemistry, as well as the structure. Molecules will freeze out into ices around dust grains at different temperatures and densities, depending on their binding energy and also depending on the specific nature of the substrate. The substrate composition will change at different locations in the disk based on molecules that have already frozen out and been incorporated into the icy mantle. The midplane radius at which a particular molecule condenses is called the snow line or ice line. Because freeze-out is density- and temperature-dependent, there will be a vertical component to the location of molecular freeze-out, defining a snow surface. Characterizing the vertical component is difficult considering the uncertainties in the vertical structure of disks. Outside of its snow line, the molecule is removed from gas-phase chemistry and is incorporated into ices that can have active grain surface chemistry. Snow lines of abundant species, in particular H_2O, CO_2, CO, and N_2, have the most significant effect on the midplane structure and chemistry. For typical disk pressures, H_2O has a condensation temperature of ~100 – 150 K (Collings et al. 2004; Fayolle et al. 2011) while CO has a condensation temperature of ~20 K (Qi et al. 2004, 2011, 2013), meaning that H_2O freezes out much closer to the central PMS star than CO. The location of molecular snow lines is dependent on the stellar mass. Warmer disks around intermediate-mass Herbig Ae/Be PMS stars will push snow lines farther out in the disk compared to T Tauri low-mass objects. In most disks, the H_2O snow line is located at a radius of a few AU while the CO snow line can be a few tens of AU up to ~100 AU away from the central PMS star (Lecar et al. 2006; Qi et al. 2013, 2015).

The freeze-out of volatile species impacts the disk in two major ways. First, the accumulation of ices on grains increases their total surface area and sticking efficiency (Blum & Wurm 2008). The increased stickiness aids in the rapid aggregation of dust particles into larger bodies, which is one proposed mechanism for the rapid growth of planetesimals early in the disk lifetime (Stevenson & Lunine 1988; Zhang et al. 2016). Second, ices are active sites of solid-phase chemistry, which can lead to the production of large polyatomic species on the surfaces of grains. For example, beyond the CO snow line, CO ice can be hydrogenated to form organic molecules such as formaldehyde (H_2CO) and methanol (CH_3OH) (Tielens & Hagen 1982; Watanabe et al. 2003). Methanol can be the starting point for a rich complex molecular chemistry. Laboratory experiments have shown that continued hydrogenation reactions with CH_3OH can lead to the formation of organic compounds such as methyl formate ($HC(O)OCH_3$), glycolaldehyde ($HC(O)CH_2OH$) and ethylene glycol ($H_2C(OH)CH_2OH$) (Chuang et al. 2016), which can then evolve into amino acids and other prebiotic compounds that are the building blocks of life. Snow lines are therefore of great interest regarding the planet formation process in protoplanetary disks. At the same time they increase the efficiency of forming planetesimals and enrich the chemical environment in which planets will ultimately form. Much of the material in the cold outer disk will be incorporated into comets, which can also act as a delivery mechanism for complex organics and water to planets close to the star (Mumma 2008).

The effect of a molecular snow line on the available gas-phase chemistry can be used as a tool to detect these snow lines. Certain molecular species only become abundant when major volatiles such as H_2O, CO_2, and CO are heavily depleted. The molecular ion HCO^+ and its isotopologs are expected to trace regions of H_2O depletion. Gas-phase dipolar, neutral molecules – of which H_2O is the most abundant – will quickly react with and destroy HCO^+. Therefore, a lack of centrally peaked HCO^+ emission toward a disk would indicate a significant amount of water in the gas-phase, whereas H_2O will be frozen out throughout the rest of the disk beyond the water snow line. This phenomenon has already been observed in protostellar envelopes (Jørgensen et al. 2013; Bjerkeli et al. 2016; van 't Hoff et al. 2018), but detecting a central depression of HCO^+ in protoplanetary disks is much more difficult due to the small angular scales of the water snow line.

The molecular ions N_2H^+ and DCO^+ become abundant in regions of heavy and moderate CO depletion, respectively. The molecular ion H_3^+ associated with the formation of DCO^+ is destroyed by gas-phase CO, while N_2H^+ itself is destroyed by gas-phase CO. Thus, the conditions for efficient formation of N_2H^+ and DCO^+ are found deep within the cold disk midplane. Unlike N_2H^+, some remaining gas-phase CO is necessary to form DCO^+. These chemical characteristics make the ions effective tracers of the CO snow line (Mathews et al. 2013; Qi et al. 2013,

2015) and probes of the conditions in the comet- and planet-forming regions of the outer disk.

Protoplanetary disk midplanes have sufficiently low temperatures to maintain an active deuterium chemistry. Deuterium fractionation – or deuterium enrichment – is a process that refers to an increase in the abundance of the deuterated version of molecules compared to the initial deuterium-to-hydrogen ratio set right after the Big Bang (D/H $\approx 3 \times 10^{-5}$), half of which has now been burned in stellar interiors (Henning & Semenov 2013). The other half (D/H $\approx 1.5 \times 10^{-5}$) remains available for deuterium fractionation, which occurs predominantly at low temperatures ($T < 30$ K). Deuterium enrichment is driven primarily by cosmic ray particles that ionize H_2, leading to H_3^+ formation. The main reaction is then $H_3^+ + HD \longleftrightarrow H_2D^+ + H_2 + \Delta E$, where $\Delta E = 220$ K (Albertsson et al. 2013), which forms H_2D^+ efficiently in the cold disk midplane. H_2D^+ then acts as a reactant to produce larger deuterium-bearing molecules and ions. The low zero-point energies of deuterated molecular ions imply that they are preferentially formed at low temperatures due to the energy needed for the backward reaction (Brown & Rice 1986; Millar et al. 1989). At low temperatures, deuterium fractionation can serve as an important record of chemical history, as the ratio between deuterated molecules and their non-deuterated counterparts (e.g., HDO/H_2O) will only differ from the cosmic D/H ratio in environments where deuterium chemistry is active (Ceccarelli et al. 2014). Deuterated species such as DCO^+ and DCN have already been observed in protoplanetary disks (van Dishoeck et al. 2003; Qi et al. 2008; Öberg et al. 2012), revealing significantly higher ratios between these species and their non-deuterated versions (~0.02) than the cosmic D/H ratio. Differences in the D/H ratio between the ISM, protostellar envelopes, protoplanetary disks, comets, and fully formed planets can be a unique diagnostic tool of the chemical history of important species like water and can help constrain theories on the delivery of water and organics to terrestrial planets (Mumma & Charnley 2011).

For an extensive review of protoplanetary disk chemistry, see Henning & Semenov (2013).

1.4 Disks in the Age of ALMA

The small angular scales subtended on the sky by protoplanetary disks require a high degree of angular resolution to observe in detail. The resolving power of a telescope is inversely proportional to its diameter, $\theta_{\rm res} \approx \lambda/D$ for small angles, where λ is the observed wavelength and D is the diameter of the telescope mirror or dish. Thus, to achieve angular resolution on the order of one arcsecond at (sub)millimeter wavelengths, the diameter of a telescope must be hundreds of meters. In order to properly resolve disks in the (sub)millimeter wavelength regime, single-dish telescopes are clearly insufficient and interferometers must be used to achieve the necessary resolving power. An interferometer is an array of antennas which emulates a large-diameter telescope by taking measurements at discrete locations and combining the data, such that the resolving power is $\theta_{\rm res} \approx \lambda/B$, where B is the interferometer baseline – the distance between each pair of antennas.

Earlier (sub)millimeter interferometers include the Submillimeter Array (SMA) in Hawaii; the Plateau de Bure Interferometer (PdBI) – now NOrthern Extended Millimeter Array (NOEMA) – in France; and the Combined Array for Research in Millimeter-wave Astronomy (CARMA) – now decommissioned – in California, USA. These interferometers could observe with angular resolutions on the order of one arcsecond or less and provided new insights into the dust distribution and gas kinematics of many protoplanetary disks, but lacked the capability to fully resolve substructure in the dust or gas, which requires resolving power on the order of milliarcseconds.

The Atacama Large Millimeter/submillimeter Array[7] (ALMA) is a revolutionary new facility – the largest ground-based observatory ever built – that has been operating since 2011. In only a few years, it has produced astounding new images of protoplanetary disks that have given astronomers a new understanding of disk evolution and planet formation. In this section, some of the advancements in the field as a result of new data from ALMA are outlined.

1.4.1 Overview of ALMA

ALMA is a (sub)millimeter wavelength interferometric observing facility located on the Chajnantor plateau at an altitude of 5000 meters in the Atacama desert in Chile. The facility was designed with several scientific goals in mind, one of which is the ability to image the gas kinematics in protostars and in protoplanetary disks around young Sun-like stars in the nearest molecular clouds with unprecedented sensitivity and spatial resolution in order to probe the formation of planets around distant stars. In the (sub)millimeter wavelength regime, atmospheric water vapor is the greatest source of disturbance. The high altitude of the Chajnantor plateau puts the facility above much of the Earth's atmosphere, reducing the amount of water vapor and increasing atmospheric transmission of (sub)millimeter wavelengths of light.

The array is composed of 66 antennas, 54 with a 12-meter diameter and 12 with a 7-meter diameter, and has a total collecting area of 6600 square meters. The 7-meter antennas are kept in a tight configuration called the Atacama Compact Array (ACA), along with 4 Total Power (TP) 12-meter antennas, which can operate independently of the main array for the purpose of observing large angular scales. ALMA is designed to cover a wide range of frequencies from 31 GHz to 950 GHz, which are separated into 10 different receiver bands. Currently, operational bands range from band 3 at 84 GHz to band 10 at 950 GHz. There are 192 antenna sites, and ground-based antenna transport vehicles allow the 12-meter antennas to be moved to each of these sites, making the array entirely reconfigurable. The minimum baseline between two antennas is ~150 m and the maximum baseline can reach up to ~16 km. In the most compact configuration, ALMA achieves a spatial resolution of $0.5''$ at 950 GHz to $4.8''$ at 110 GHz. In the most extended configuration, which at this moment in time is only available for a subset of receiver bands, the spatial resolution ranges from 20 milliarcseconds (mas) at 230 GHz to 43 mas at 110 GHz. The spectral resolution that can be obtained with ALMA ranges from 3.8 kHz and 15.6 MHz per resolution element (channel) with a maximum total bandwidth of 8 GHz. Spectral resources can be divided within the 8 GHz bandwidth to target the continuum and several individual atomic and molecular lines simultaneously.

---

[7] ALMA is an international collaborative effort involving the European Southern Observatory (ESO), the U.S. National Science Foundation (NSF) and the National Institutes of Natural Sciences (NINS) of Japan, together with NRC (Canada), NSC and ASIAA (Taiwan), and KASI (Republic of Korea), in cooperation with the Republic of Chile as the host nation. See `www.almaobservatory.org` for more information.

As an interferometer, ALMA does not measure the sky brightness of a source directly. Rather, it measures the interference pattern of each pair of antennas, which provides information on the spatial coherence of the observed light. Raw data is recorded by ALMA with the spatial coherence function – or the visibility function – $V(u, v)$, which is the Fourier transform of the sky brightness distribution

$$V(u, v) = \int_0^\infty \int_0^\infty I(x, y) e^{-2\pi i(ux+vy)} dx dy, \tag{1.5}$$

where (x, y) corresponds to the sky brightness distribution coordinates as measured from the phase center (i.e., the direction to the source), and (u, v) corresponds to the telescope baseline coordinates as measured in units of the observed wavelength for each pair of antennas as seen from the source. The measured visibilities must be first calibrated using reference objects such as Solar System bodies or distant quasars to correct for atmospheric variations, correct for the non-uniform response across the receiver band, and correct the flux values measured by the antennas. After calibration, the visibilities are Fourier transformed to produce an image of the sky brightness distribution of the target. Calibration and imaging is performed with the Common Astronomy Software Applications (CASA; McMullin et al. 2007) package that was developed for radio interferometer data.

1.4.2 Revolutionary imaging with ALMA

Since first light, ALMA has been producing groundbreaking images of protoplanetary disks that challenge our current understanding of disk formation and evolution. Well before becoming fully operational, the ALMA Science Verification campaign was already providing interesting physical and chemical insights. For example, observations of the disk around the Herbig Ae PMS star HD 163296 showed a spatially resolved millimeter continuum and ^{12}CO distribution which revealed compact millimeter dust and highly extended gas (de Gregorio-Monsalvo et al. 2013), and also showed a ring-like DCO$^+$ structure that hinted at the CO snow line (Mathews et al. 2013). Data from Cycle 0 Early Science revealed an asymmetric dust trap in a young transition disk around Oph IRS 48 that had never before been spatially resolved (van der Marel et al. 2013), and a similar dust asymmetry was observed in the HD 142527 transition disk with a possible radial flow of gas toward the central PMS star (Casassus et al. 2013). These results prompted a flurry of follow-up observations toward other disks to determine if such dust substructure is common and, if so, what is the cause.

Perhaps the most widely circulated and most surprising image of a protoplanetary disk observed with ALMA came from the first year of the Long Baseline Campaign, when the maximum baseline was increased to 16 km for the first time. The disk around the very young (~1 Myr) PMS star HL Tau was found to host a large number of gaps and rings in the millimeter dust, an unexpected phenomenon for such a young disk (ALMA Partnership et al. 2015). Rings and gaps are predicted in evolved disks with active planet formation, where planets or planetesimals would sweep up dust and gas as they orbit around the central PMS star. The surprising result suggested that planets begin to form in disks much earlier than previously predicted. Since this first discovery, ALMA observations on longer baselines have revealed dust rings, gaps, spirals, and other asymmetries in numerous young disks (van der Marel et al. 2013, 2015; Casassus et al. 2013; Walsh et al. 2014a; Andrews et al. 2016; Walsh et al. 2016; Isella et al. 2016; Fedele et al. 2018) that may hint

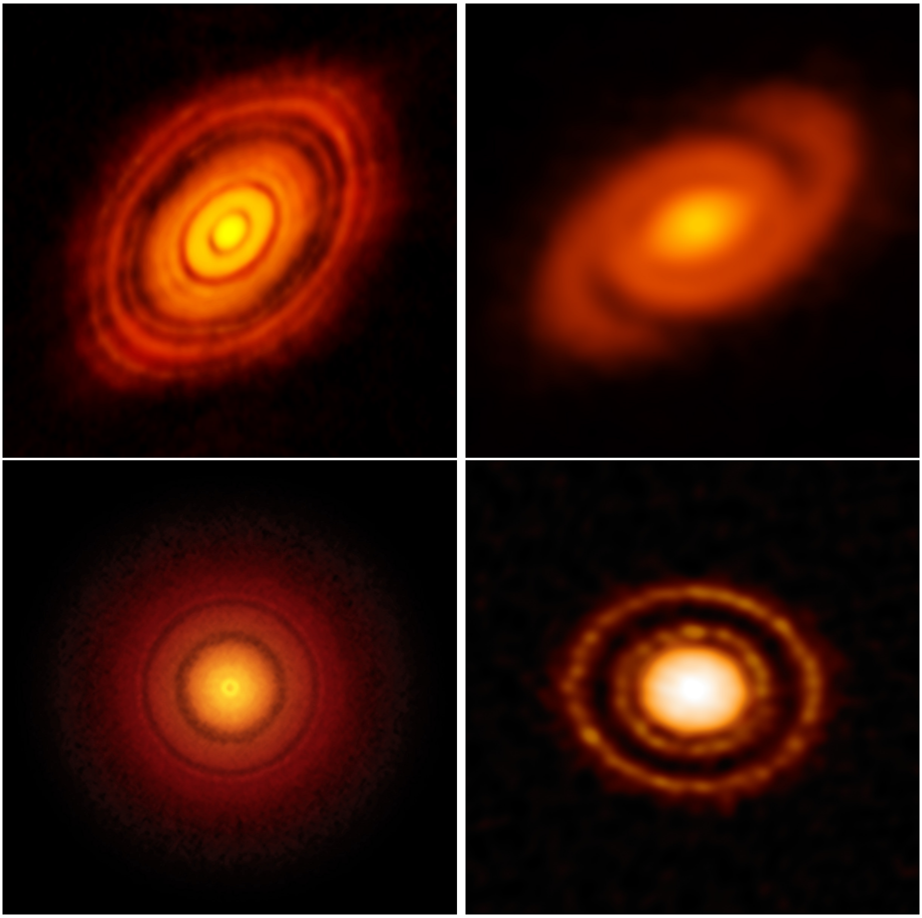

Figure 1.4: Examples of disks resolved by ALMA at (sub)millimeter wavelengths. The images show the presence of millimeter-sized dust in these young disks.
(Top left) HL Tauri. (Top right) Elias 2-27. (Bottom left) TW Hydrae. (Bottom right) AS 209.
Credit: (Top left) ALMA (ESO/NAOJ/NRAO), ALMA Partnership et al. (2015); (Top right) B. Saxton (NRAO/AUI/NSF), ALMA (ESO/NAOJ/NRAO) Pérez et al. (2016); (Bottom left) S. Andrews (Harvard-Smithsonian CfA), B. Saxton (NRAO/AUI/NSF), ALMA (ESO/NAOJ/NRAO), Andrews et al. (2016); (Bottom right) ALMA (ESO/NAOJ/NRAO), Fedele et al. (2018).

at the presence of low-mass companions. A subset of these highly resolved disks is shown in Figure 1.4. Much modeling work is being done to determine the exact cause of these dust morphologies. While planet-disk interactions are certainly one possible cause (Rice et al. 2006; Zhu et al. 2011; Pinilla et al. 2012; Rosotti et al. 2016; Dong et al. 2016; Bae et al. 2017), other explanations exist. Previous work has shown that radial gradients in disk viscosity (Flock et al. 2015; Pinilla et al. 2016), zonal flows (Johansen 2009; Simon & Armitage 2014), gravitational instabilities (Youdin 2011; Takahashi & Inutsuka 2014), particle growth across snow lines

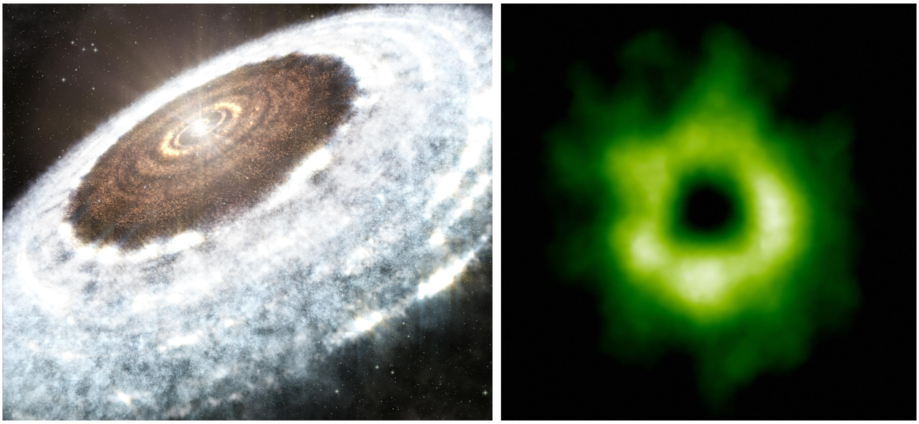

Figure 1.5: (Left) Artist's impression of the snow line in a protoplanetary disk. Molecules in the outer disk have frozen out into ices (white) due to the low temperatures farther away from the central star. (Right) ALMA image of the carbon monoxide snow line in the protoplanetary disk around the young star TW Hydrae. The N_2H^+ molecule (green) only appears in regions of the disk where carbon monoxide has frozen out. The star (not detectable at these wavelengths) is located at the center of the image.
Credit: (Left) A. Angelich (NRAO/AUI/NSF)/ALMA (ESO/NAOJ/NRAO); (Right) ALMA (ESO/NAOJ/NRAO), Qi et al. (2013).

(Ros & Johansen 2013; Zhang et al. 2016; Stammler et al. 2017), and sintering of dust particles (Okuzumi et al. 2016) can also result in similar dust morphologies. Simultaneous observations of highly resolved dust and gas observations will help to narrow down the possible mechanisms responsible.

The sensitivity and spatial resolution provided by ALMA enables precise observations of the gas in protoplanetary disks not available from any other instrument in the world. The ^{12}CO molecule has been observed in unprecedented detail, showing the emission layers above and below the midplane where the low-J rotational lines become excited (de Gregorio-Monsalvo et al. 2013). Asymmetries and "kinks" in the observed ^{12}CO emission pattern at specific disk velocities can even reveal the presence of planets that are disrupting the gas in the disk (Pinte et al. 2018; Teague et al. 2018). Several CO isotopologs – previously difficult to detect and resolve – are now regularly observed and easily detected with ALMA, allowing for better constraints on the vertical temperature and disk structure deeper toward the midplane (Rosenfeld et al. 2013; Isella et al. 2016). The rarest CO isotopologs (e.g., $^{13}C^{17}O$) can even probe the CO snow line directly in the nearest disks (Zhang et al. 2017). Disk geometry also plays a significant role at the spatial resolutions achieved by ALMA. When using CO and its isotopologs as tracers, the CO snow line becomes more apparent and is better characterized in edge-on disks (Dutrey et al. 2017).

Beyond CO, ALMA has the ability to probe rarer gas-phase molecular species that give important insights into disk structure and chemistry. Astronomers have already detected complex molecules in protoplanetary disks with ALMA, including CH_3CN (Öberg et al. 2015b; Bergner et al. 2018; Loomis et al. 2018) and CH_3OH (Walsh et al. 2016), promising a bright future for our understanding of the chemistry leading to prebiotic molecules in the planet-forming environment.

Molecular snow lines are now being resolved, mostly using rare chemical tracers that are present in regions of molecular freeze-out. During one of the ALMA Early Science cycles, the N_2H^+ molecule was observed in the disk around TW Hya with high spatial resolution. The results clearly showed a bright N_2H^+ ring where gas-phase CO becomes heavily depleted (Qi et al. 2013), showcasing the ability of ALMA to precisely characterize molecular snow lines in disks (see Figure 1.5). The N_2H^+ and DCO^+ molecules have both proven to be effective tracers of CO gas structure and the onset of CO freeze-out near the midplane of disks (Mathews et al. 2013; Qi et al. 2015; Salinas et al. 2017). In at least a one case, DCO^+ has been observed to have a double ring structure, hinting at the presence of a CO desorption front where CO returns to the gas phase in the outer disk (Öberg et al. 2015a). Formaldehyde, thought to be a precursor to methanol and another potential CO snow line tracer, has also been resolved in a few disks and shows that multiple formation pathways are likely to contribute to the overall H_2CO budget in the disks around DM Tau and TW Hya (Loomis et al. 2015; Öberg et al. 2017). Even the water snow line has been claimed to be detected in a very young disk surrounding the outbursting protostar V883 Ori as evidenced by changes in the dust distribution (Cieza et al. 2016). The object experienced a sudden increase in the accretion rate that raised the disk temperature and thus pushed the H_2O freeze-out radius farther away from the star, evaporating ices that act as a grain adhesive in the inner regions of the disk (Schoonenberg et al. 2017). Observations of multiple molecular snow lines in a protoplanetary disk is an exciting prospect, as it would allow for characterization of the radial temperature structure with high accuracy. ALMA is a powerful tool to help constrain the effect of molecular freeze-out on disk structure and the importance of grain surface chemistry in disk evolution and planetary composition.

The unrivaled capabilities of the ALMA facility have brought us into the age of statistical analysis of disk properties. Where astronomers were previously able to observe mainly the biggest, brightest, and nearest disks, ALMA now allows for an unbiased sampling of nearly all disks in nearby star-forming regions. Disk mass, size, and multiplicity are being estimated for recent ALMA disk surveys of several star-forming regions, such as those found in Orion, Lupus, IC 348, Taurus, ρ Ophiuchus, Chameleon I, and Upper Scorpius (Ansdell et al. 2016, 2017, 2018; Eisner et al. 2018; Ruíz-Rodríguez et al. 2018; Ward-Duong et al. 2018; Pascucci et al. 2016; Long et al. 2017; Carpenter et al. 2014). The ability to detect and characterize the entire population of nearby protoplanetary disks, rather than just the brightest subset, will help to connect the range of disk properties observed to the wide range of planetary systems observed, furthering our understanding of how planets form and which systems are most likely to host life.

1.4.3 Modeling line emission from ALMA observations

Images produced by ALMA come primarily in two forms: continuum emission and line emission. The images are three-dimensional, with two spatial dimensions and one spectral (frequency) dimension. Observing the continuum is simpler because the telescope collects light over a broad range of frequencies to produce an image of the thermal dust emission at (sub)millimeter wavelengths. The broad sampling of the frequency dimension means that observing the continuum does not provide resolved spectral information and is therefore spectrally integrated to produce a two-dimensional continuum image. Observing atomic and molecular line emission is more complicated: the emission is produced primarily by the excitation of specific rotational and vibrational energy levels in the (sub)millimeter regime, and is therefore produced at specific frequencies. The emission lines are intrinsically narrow, thus a high degree of spectral resolution is required in order to properly resolve them. At high spectral resolutions, line-of-sight velocity changes in the motions of the gas cause measurable Doppler shifts in the line emitting frequency. In turn, this allows us to infer the location within the disk of the emitting gaseous material.

To model line emission, one must have a description of the physical disk structure. That is, the density and temperature structure is modeled first. Disk density is traditionally described with an exponentially tapered radial power-law for the surface density (as in Equation 1.4) that is a natural consequence of the viscous accretion disk prescription with viscous spreading. Disk temperature is described with a simple radial power-law – $T(R) \propto R^p$, where R is the radius and p is the power-law index (Guilloteau & Dutrey 1998; Piétu et al. 2007) – that is a result of the flared disk surface layers being irradiated by the central PMS star. The physical disk model is then used in conjunction with a radiative transfer model, which uses radiative transfer equations to calculate how light will propagate through the disk physical model and creates a synthetic three-dimensional image of the line emission at a specific transition (e.g., CO $J = 2-1$). Line emission may be modeled in local thermodynamic equilibrium (LTE) or in non-LTE statistical equilibrium, depending on the conditions. The critical density $n_{\rm cr}$ of the line transition being modeled dictates the use of LTE or non-LTE, which is defined as the ratio between the Einstein coefficient A_{ul} for spontaneous emission and the collision rate coefficient C_{ul} between the upper and lower energy levels of the line transition, $n_{\rm cr} = A_{ul}/C_{ul}$. If the molecules reside in a region of the disk with densities higher than the critical density, then LTE conditions apply and the level populations of the line transition are described by the Boltzmann distribution

$$\frac{n_u}{n_l} = \frac{g_u}{g_l} e^{-\Delta E/kT}, \tag{1.6}$$

where n_u is the number of molecules in the excited upper energy state, n_l is the number of molecules in the lower energy state, and g_u and g_l are their statistical weights. The ΔE term is the difference in energy between the upper state and the lower state ($\Delta E = E_u - E_l$), k is the Boltzmann constant, and T is the kinetic temperature of the gas. If molecules reside in a region of the disk with densities less than the critical density, then non-LTE statistical equilibrium applies and the level populations must be calculated statistically with all the quantum mechanical transition probabilities taken into account: spontaneous emission, stimulated emission, and absorption – each which depend on their respective Einstein coefficients – as well as collisions up and down.

There are several software packages to facilitate the modeling of line emission. In this thesis, only two will be addressed. The first is the Line Modeling Engine (LIME: Brinch & Hogerheijde 2010), which is an excitation and radiative transfer code for protostars and protoplanetary disks. It requires a physical disk structure model, which can be described parametrically or imported from previous modeling with dust continuum radiative transfer codes (e.g., MCMAX, RADMC-3D: Min et al. 2009; Dullemond et al. 2012). The abundance structure of the molecule being modeled can then be adjusted parametrically by the user to reproduce observations. As a three-dimensional code, LIME is not limited to assumptions of cylindrical or spherical symmetry, which is commonplace in many other line radiative transfer codes. The LIME code enables modeling of line emission using non-LTE/statistical equilibrium. The second code addressed is Dust and Lines (DALI: Bruderer et al. 2012; Bruderer 2013), a two-dimensional Monte-Carlo method thermo-chemical code that models both the physical disk structure and the line emission. Thermo-chemical modeling combines radiative transfer, chemistry, and thermal-physics in order to obtain synthetic spectral image cubes of molecular or atomic lines. DALI takes as input a stellar spectrum, stellar mass, surface density profile, vertical scale height profile, dust settling parameters, cosmic ray ionization rate, and PAH abundance. The code creates a grid of the disk structure; it performs dust continuum radiative transfer; the chemical network calculates molecular and atomic abundances; the results of the chemical network are used to determine the disk thermal balance from the heating and cooling rates of the gas, which then acts as input for the next iteration of the chemistry; and it calculates the excitation (i.e., level populations) using the escape-probability for ray tracing in order to produce synthetic three-dimensional images of atomic or molecular lines. Both of these codes are used and referenced extensively throughout the work presented in the following chapters.

1.5 This Thesis

The work presented in this thesis explores various tracers of protoplanetary disk structure in the gas and dust, with particular focus on the disk midplane. Constraints on the composition and structure of the disk midplane are crucial to understanding the environment in which planets form and the ingredients that may be incorporated into planetary bodies. High resolution imaging with ALMA is used to investigate the relationship between observations of simple molecular tracers and the assumptions behind their chemical formation, as well as determine the substructure of spatially resolved millimeter dust and molecular line emission in order to characterize the disk midplane. Ultimately, the aim is to understand how simple molecules can be used to advance our knowledge of the ongoing physical and chemical processes that shape the conditions in the planet-forming regions of protoplanetary disks.

Chapter 2 – Increased H_2CO production in the outer disk around HD 163296

Formaldehyde is expected to form primarily via the hydrogenation of CO ices in the cold disk midplane and thus acts as a precursor to more complex molecular species such as methanol and other alcohols, but there is also a contribution from a gas-phase formation pathway (Loomis et al. 2015; Öberg et al. 2017). This thesis chapter explores the distribution of H_2CO and its relation to CO gas structure in the protoplanetary disk around the young Herbig Ae star HD 163296. Three H_2CO lines were observed with ALMA toward the HD 163296 disk. Radiative transfer models are used to reproduce the observed radial intensity profiles and disk-integrated spectral profiles of H_2CO and CO. To fit the observations, the H_2CO abundance must increase sharply by a factor of two and the CO abundance must decrease sharply by an order of magnitude at the edge of the millimeter grain distribution. The depletion of CO may be due to freeze-out and/or photodissociation, while the increase in H_2CO may be due to increased formation on icy grain surfaces or a more active gas-phase chemistry in the outer disk, making it difficult to draw robust conclusions about the exact formation pathway of the additional formaldehyde beyond the millimeter continuum.

Chapter 3 – ALMA unveils rings and gaps in the protoplanetary system HD 169142: signatures of two giant protoplanets[8]

Recent ALMA observations have shown rings and gaps in the dust and/or gas around protoplanetary disks even when they are not transitional disks (ALMA Partnership et al. 2015; Andrews et al. 2016; Isella et al. 2016). This chapter aims to characterize the nature of the millimeter dust distribution and gas as traced by CO isotopologs in the well-known protoplanetary disk around the Herbig Ae star HD 169142 using observations from ALMA. The millimeter continuum observations reveal two distinct dust rings that are resolved for the first time. Observations of ^{12}CO, ^{13}CO, and C^{18}O show that the dust has decoupled from the gas, which has substructure of its own. Self-consistent thermo-chemical models are used to reproduce these dust and gas observables. The gas outer radius (~180 AU) is much greater than the dust outer radius (~85 AU). The dust structure has an empty central cavity out to ~20 AU and consists of an inner ring from ~20 – 35 AU, a depleted dust gap from ~35 – 56 AU, and an outer ring from ~56 – 83 AU. The gas structure has an inner radius of ~13 AU and is depleted by a factor of 30 – 40 out to the edge of the dust gap (~13 – 56 AU) compared to regions of the disk beyond the dust gap (~56 – 180 AU). The structure seen in the dust and gas is consistent with multiple giant planets ($\gtrsim M_{\mathrm{Jupiter}}$) carving out gaps in the disk as they orbit the central star and sweep up disk material.

---

[8] This chapter is a second-author paper. Personal contribution to the work consisted of reduction of the full ALMA data set, generating simulated observations on the basis of thermo-chemical modeling, and model parameter optimization. There was contribution to the text and comments were given on the entire manuscript.

Chapter 4 – Probing midplane CO abundance and gas temperature with DCO^+ in the protoplanetary disk around HD 169142

The DCO^+ molecule is expected to be an excellent tracer of the disk midplane environment and an indicator of the CO snow line in disks because its formation requires a balance of gas-phase CO and CO depletion (Mathews et al. 2013; Öberg et al. 2015a; Salinas et al. 2017). This chapter investigates the ability of DCO^+ to trace physical structure in the dust and gas near the midplane of the protoplanetary disk around HD 169142 using observations from ALMA. The physical disk structure obtained from Chapter 3 is used with a simple deuterium network chemical model to reproduce the observed DCO^+ radial intensity profile. The models indicate that in order to recreate the 100 AU peak seen in the DCO^+ profile, the HD 169142 disk structure must be adapted to include a region that is colder and more CO-depleted than in the original model just beyond the edge of the millimeter grain distribution. The results indicate that DCO^+ is an effective CO snow line tracer in the HD 169142 disk, and that the molecule can reveal disk midplane structure that is not apparent even in rarer CO isotopologs – often thought to be optically thin, but which are shown to be optically thick in this disk at large radii.

Chapter 5 – Upper-limits on CH_3OH in the HD 163296 protoplanetary disk: evidence for a low CH_3OH/H_2CO gas-phase ratio

Methanol (CH_3OH) acts as a starting point for complex prebiotic chemistry and is therefore a desirable molecule to detect and characterize in protoplanetary disks (Öberg et al. 2009; Chuang et al. 2016). Currently, the only Class II protoplanetary disk with a detection of gas-phase methanol is TW Hya (Walsh et al. 2016). Four lines of the CH_3OH molecule are targeted with ALMA toward the disk around the young Herbig Ae star HD 163296. No methanol is detected in the disk, but upper limits place strong constraints on the disk-averaged methanol column density and abundance, with $N_{\mathrm{avg}} < 5 \times 10^{11}$ cm^{-2} and $CH_3OH/H_2 \lesssim 1.6 \times 10^{-12}$. The ratio of methanol to formaldehyde (H_2CO) is compared between the HD 163296 and TW Hya disks, as these molecules are both expected to form via the hydrogenation of CO ices. The analysis suggests that the methanol is less abundant with respect to formaldehyde in the HD 163296 disk ($CH_3OH/H_2CO < 0.24$) when compared to the TW Hya disk ($CH_3OH/H_2CO \approx 1.27$). Such a discrepancy may be due to differences in the desorption processes of CH_3OH and H_2CO between the disks, more efficient gas-phase formation of H_2CO in HD 163296, or differences in the efficiency of formaldehyde and methanol formation on grain surfaces.

Conclusions

The conclusions of this thesis based on the results of the chapters described above are the following:

The role of micron- and millimeter-sized dust populations in shaping the outer disk structure and chemistry is probed by molecules like H_2CO and DCO^+. The ability of these molecules to trace such processes is evidenced by the relationship between the strength of their emission and the location outer edge of the millimeter dust continuum. H_2CO and DCO^+ provide additional constraints on structure in the CO gas, midplane photodesorption, and the presence of cold midplane regions that are not apparent in the millimeter continuum or CO isotopologs.

The disk around HD 169142 provides yet another example of a ringed and gapped system as revealed by ALMA, which is now commonplace for large and bright disks around T Tauri and Herbig Ae/Be young stellar objects. Its substructure in the millimeter dust and CO gas may be evidence of planet-disk interaction as young gas giants begin to form within the protoplanetary disk.

TW Hya remains the only Class II disk with a detection of gas-phase methanol, which is not detected in the disk around HD 163296 despite achieving similar sensitivity and spatial/spectral resolution. Methanol abundance in the HD 163296 disk is low with respect to formaldehyde, which may be due to differences in the formation pathways of formaldehyde and methanol in Herbig Ae/Be versus T Tauri disks, diversity in disk structure, or variations in the molecular desorption processes.

In summary, this thesis shows that the observations of simple molecules such as CO isotopologs, DCO^+, and H_2CO at high spatial and spectral resolution examine the anatomy of protoplanetary disk regions connected to the underlying disk structure. Any substructure in the disk is reflected in the abundance structure of these molecules, which can be used as powerful diagnostics of the physical disk environment. Other simple organic species remain elusive and difficult to detect in disks, as is the case for CH_3OH despite the expected correlation with its related species H_2CO, which is readily detected in disks and shows radial variation. The degree to which H_2CO and CH_3OH production is connected in protoplanetary disks remains to be seen. Future observations with ALMA and other facilities will continue to provide insights into the complicated physical and chemical processes that determine the structure, molecular ingredients, and conditions of the planet-forming environment in protoplanetary disks.

1.6 Outlook

The future of protoplanetary disk observation is quite literally faint, but metaphorically bright. Many disk tracers that astronomers observe today emit weakly, are difficult to resolve, or are obscured by the disk itself and thus require world class telescopes to turn the faintest probes of disk structure and chemistry into bright new insights into the planet formation process. In this section the opportunities presented by a select group of current and future observing facilities are discussed. The focus remains on the characterization of the protoplanetary disk for the purpose of constraining the properties of planets and planetary systems that will form as the disk evolves.

1.6.1 ALMA and VLT/SPHERE

ALMA now accepts proposals for Large Programs (> 50 hours) which will allow unbiased surveys of disks with the same spatial resolution, integration time, and spectral setup (i.e., continuum bandwidth, targeted atomic and molecular lines, and spectral resolution). Thus far, disk surveys have been limited to a few minutes of on-source integration time per target and moderate spatial resolution (e.g., Ansdell et al. 2017, 2018). The mapping of gas kinematics in disks at high spatial and spectral resolution with long integration times should be a priority for future ALMA Large Programs.

Molecular tracers offer a promising direction for investigating chemical complexity and the planet-forming regions of disks in the years to come. Resolved coincident gas and dust gaps (van der Marel et al. 2016; Yen et al. 2016) and asymmetries in ^{12}CO gas (Pinte et al. 2018; Teague et al. 2018) probe planet-disk interactions. Resolved volatile snow lines provide insight into disk midplane chemistry, temperature, and structure. As an example, the N_2H^+ inner radius traces the CO snow line (Qi et al. 2013, 2015) while the outer radius, detectable with high sensitivity ALMA observations, traces the N_2 snow line – important for complex N-bearing molecules and prebiotic chemistry. Long-integration, wide-bandwidth ALMA observations can explore the complex chemical content of disks. Observations of the embedded protostar IRAS 16293-2422 revealed a forest of $> 10,000$ molecular emission lines, providing the first detections of many complex organics in such an object – e.g., glycolaldehyde, methyl formate, acetic acid (The ALMA-PILS survey: Jørgensen et al. 2016; Coutens et al. 2016; Lykke et al. 2017; Coutens et al. 2018). Pointing ALMA toward chemically active, young protoplanetary disks with a wide-bandwidth spectral setup may result in the detection of rare complex molecules expected to reside in disks.

On the Very Large Telescope[9] (VLT), the recently operational Spectro-Polarimetric High-contrast Exoplanet REsearch[10] extreme adaptive-optics instrument (VLT/SPHERE) now observes protoplanetary disks at milliarcsecond angular resolution in $0.5 - 2.32$ μm scattered light that probes the optically thick micron-sized dust in the disk surface layers. Disks exhibit rings and spirals in micron-sized dust as well, though their morphologies can be different from those observed in the millimeter continuum due to the vertical scale heights that each wavelength separately probes (Figure 1.6; Benisty et al. 2015; Ginski et al. 2016; de Boer et al.

---

[9] `https://www.eso.org/public/teles-instr/paranal-observatory/vlt/`

[10] `https://www.eso.org/public/teles-instr/paranal-observatory/vlt/vlt-instr/sphere/`

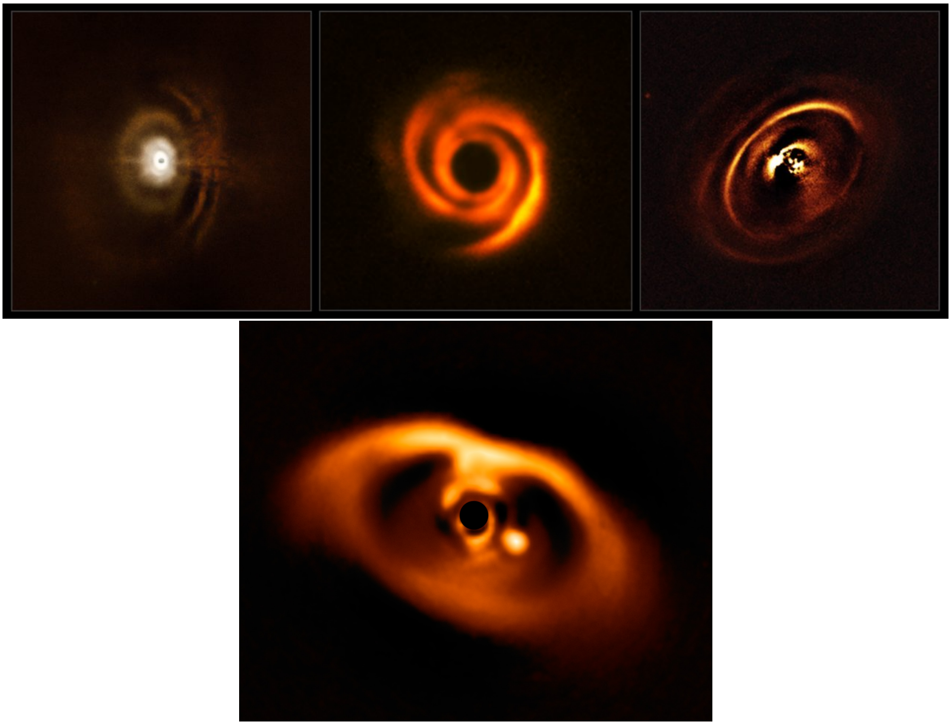

Figure 1.6: Images showcasing the power of VLT/SPHERE to resolve structure in scattered light coming from the surface layers of protoplanetary disks. The top image shows a variety of disk morphologies observed with VLT/SPHERE while the bottom image shows the first direct detection of an embedded planet.
(Top left) HD 97048. (Top middle) HD 135344B. (Top right) RX J1615.3-3255. (Bottom) PDS 70.
Credit: (Top) ESO, Ginski et al. (2016); Benisty et al. (2015); de Boer et al. (2016); (Bottom) ESO/A. Müller et al., Keppler et al. (2018); Müller et al. (2018).

2016; Stolker et al. 2016; Benisty et al. 2017; van Boekel et al. 2017). The discovery of the first directly imaged embedded planet was recently announced in the transition disk around PDS 70 using VLT/SPHERE (Figure 1.6; Keppler et al. 2018). Spectrophotometry was also done over most of the near-IR range (0.96 – 3.8 μm), and atmospheric models show the planet likely has a cloudy atmosphere between 1000 – 1600 K (Müller et al. 2018). Future observations and simultaneous modeling of ALMA and VLT/SPHERE data will provide a framework for investigating the relationship between dust grain morphologies, planet-disk interactions, and planetary atmospheres (de Juan Ovelar et al. 2016; Pohl et al. 2017; Muro-Arena et al. 2018; Casassus et al. 2018; Müller et al. 2018).

1.6.2 Future facilities

ALMA will remain the most powerful facility for the characterization of the bulk outer disk content and chemistry for decades to come. Future facilities that are currently near launch or under construction will be better suited to probe the inner

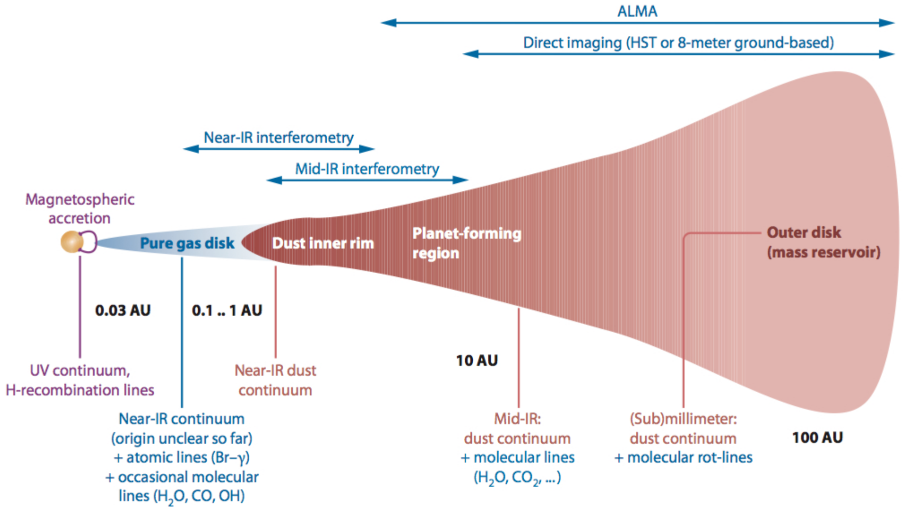
ALMA
Direct imaging (HST or 8-meter ground-based)
Near-IR interferometry
Mid-IR interferometry
Magnetospheric accretion
Pure gas disk
Dust inner rim
Planet-forming region
Outer disk (mass reservoir)
0.03 AU
0.1 .. 1 AU
10 AU
100 AU
UV continuum, H-recombination lines
Near-IR dust continuum
Near-IR continuum (origin unclear so far) + atomic lines (Br–γ) + occasional molecular lines (H$_2$O, CO, OH)
Mid-IR: dust continuum + molecular lines (H$_2$O, CO$_2$, ...)
(Sub)millimeter: dust continuum + molecular rot-lines

Figure 1.7: Diagram of a protoplanetary disk noting observable wavelengths and the disk regions probed by each wavelength regime.
Credit: Dullemond & Monnier (2010)

regions of the protoplanetary disk at mid- and near-IR wavelengths, which is significant for both terrestrial planet formation and giant planet formation between the water and carbon monoxide snow lines. These disk regions are important to characterize as the activity of the inner disk will affect structure that may be observable in the outer disk, for example through inner disk planets exciting spiral waves that propagate through the gas.

Facilities designed to probe the near-IR and mid-IR wavelengths include: the James Webb Space Telescope[11] (JWST), equipped with instruments to observe at both the near-IR (NIRCam/NIRSpec; $0.6 - 5$ μm) and the mid-IR (MIRI; $5 - 28$ μm); the Extremely Large Telescope[12] (ELT) and in particular the Mid-Infrared ELT Imager and Spectrograph[13] (METIS) instrument, which covers the $3 - 20$ μm wavelength range; and on the Very Large Telescope Interferometer (VLTI), the Multi AperTure mid-Infrared SpectroScopic Experiment[14] (VLTI/MATISSE), an imager and spectrograph operating in the $3{-}5$ μm window (L and M bands) and the $8 - 13$ μm window (N band). These facilities and instruments will be able to resolve the inner few to several AU of protoplanetary disks at these wavelengths to provide new insights into asymmetric disk structure indicative of planets, the spectral features of amorphous and crystalline dust, the distribution and kinematics of hot gas, and inner disk clearing. The spectrographs also enable the observation of absorption features from ices, simple molecules – e.g., N_2, CO_2 and H_2O –

---

[11] `https://www.jwst.nasa.gov/`

[12] `https://www.eso.org/public/teles-instr/elt/`

[13] `https://www.eso.org/public/teles-instr/elt/elt-instr/metis/`

[14] `https://www.eso.org/public/teles-instr/paranal-observatory/vlt/vlt-instr/matisse/`

in planetary atmospheres, and highly excited lines of water and other important species in the inner disk.

These future observatories will provide new and unique insights into the composition and evolution of protoplanetary disks and exoplanets, with an emphasis on the inner regions of disks and planetary atmospheres. Improvements in the spatial resolution and sensitivity of the near- and mid-IR wavelength regimes in particular will advance our understanding of the processes leading to the formation of extrasolar planets and the potential for life to arise in parts of the Universe beyond our own Solar System.

References

Aikawa, Y. & Herbst, E. 1999, A&A, 351, 233

Aikawa, Y., van Zadelhoff, G. J., van Dishoeck, E. F., & Herbst, E. 2002, A&A, 386, 622

Akiyama, E., Momose, M., Hayashi, H., & Kitamura, Y. 2011, PASJ, 63, 1059

Albertsson, T., Semenov, D. A., Vasyunin, A. I., Henning, T., & Herbst, E. 2013, ApJS, 207, 27

ALMA Partnership, Brogan, C. L., Pérez, L. M., et al. 2015, ApJ, 808, L3

André, P. & Montmerle, T. 1994, ApJ, 420, 837

André, P., Ward-Thompson, D., & Barsony, M. 2000, Protostars and Planets IV, 59

Andrews, S. M. & Williams, J. P. 2005, ApJ, 631, 1134

Andrews, S. M. & Williams, J. P. 2007, ApJ, 671, 1800

Andrews, S. M., Wilner, D. J., Hughes, A. M., Qi, C., & Dullemond, C. P. 2009, ApJ, 700, 1502

Andrews, S. M., Wilner, D. J., Zhu, Z., et al. 2016, ApJ, 820, L40

Ansdell, M., Williams, J. P., Manara, C. F., et al. 2017, AJ, 153, 240

Ansdell, M., Williams, J. P., Trapman, L., et al. 2018, ApJ, 859, 21

Ansdell, M., Williams, J. P., van der Marel, N., et al. 2016, ApJ, 828, 46

Appenzeller, I. & Mundt, R. 1989, A&A Rev., 1, 291

Archinal, B. A. & Hynes, S. J. 2003, Star Clusters

Armitage, P. J. 2011, ARA&A, 49, 195

Bachiller, R. 1996, ARA&A, 34, 111

Bae, J., Zhu, Z., & Hartmann, L. 2017, ApJ, 850, 201

Balbus, S. A. & Hawley, J. F. 1998, Reviews of Modern Physics, 70, 1

Bally, J. 2016, ARA&A, 54, 491

Bally, J. & Reipurth, B. 2006, The Birth of Stars and Planets

Batten, A. H. 1973, Binary and multiple systems of stars

Beckwith, S. V. W. & Sargent, A. I. 1991, ApJ, 381, 250

Beckwith, S. V. W., Sargent, A. I., Chini, R. S., & Guesten, R. 1990, AJ, 99, 924

Benisty, M., Juhasz, A., Boccaletti, A., et al. 2015, A&A, 578, L6

Benisty, M., Stolker, T., Pohl, A., et al. 2017, A&A, 597, A42

Bergin, E., Calvet, N., D'Alessio, P., & Herczeg, G. J. 2003, ApJ, 591, L159

Bergin, E. A., Cleeves, L. I., Gorti, U., et al. 2013, Nature, 493, 644

Bergin, E. A. & Williams, J. P. 2017, in Astrophysics and Space Science Library, Vol. 445, Astrophysics and Space Science Library, ed. M. Pessah & O. Gressel, 1

Bergner, J. B., Guzmán, V. G., Öberg, K. I., Loomis, R. A., & Pegues, J. 2018, ApJ, 857, 69

Bjerkeli, P., Jørgensen, J. K., Bergin, E. A., et al. 2016, A&A, 595, A39

Blum, J. & Wurm, G. 2008, ARA&A, 46, 21

Bonnell, I. A., Bate, M. R., Clarke, C. J., & Pringle, J. E. 1997, MNRAS, 285, 201

Bonnell, I. A., Bate, M. R., & Zinnecker, H. 1998, MNRAS, 298, 93

Boulanger, F., Abergel, A., Bernard, J.-P., et al. 1996, A&A, 312, 256

Brinch, C. & Hogerheijde, M. R. 2010, A&A, 523, A25

Brown, R. D. & Rice, E. H. N. 1986, MNRAS, 223, 429

Bruderer, S. 2013, A&A, 559, A46

Bruderer, S., van Dishoeck, E. F., Doty, S. D., & Herczeg, G. J. 2012, A&A, 541, A91

Burrows, A. S. 2014, Nature, 513, 345
Carney, M. T., Yıldız, U. A., Mottram, J. C., et al. 2016, A&A, 586, A44
Carpenter, J. M., Ricci, L., & Isella, A. 2014, ApJ, 787, 42
Casassus, S., Avenhaus, H., Pérez, S., et al. 2018, MNRAS, 477, 5104
Casassus, S., van der Plas, G., M, S. P., et al. 2013, Nature, 493, 191
Cazzoletti, P., van Dishoeck, E. F., Visser, R., Facchini, S., & Bruderer, S. 2018, A&A, 609, A93
Ceccarelli, C., Caselli, P., Bockelée-Morvan, D., et al. 2014, Protostars and Planets VI, 859
Chapillon, E., Guilloteau, S., Dutrey, A., Piétu, V., & Guélin, M. 2012, A&A, 537, A60
Chiang, E. I. & Goldreich, P. 1997, ApJ, 490, 368
Chuang, K.-J., Fedoseev, G., Ioppolo, S., van Dishoeck, E. F., & Linnartz, H. 2016, MNRAS, 455, 1702
Cieza, L. A., Casassus, S., Tobin, J., et al. 2016, Nature, 535, 258
Cieza, L. A., Schreiber, M. R., Romero, G. A., et al. 2010, ApJ, 712, 925
Cieza, L. A., Swift, J. J., Mathews, G. S., & Williams, J. P. 2008, ApJ, 686, L115
Collings, M. P., Anderson, M. A., Chen, R., et al. 2004, MNRAS, 354, 1133
Coutens, A., Jørgensen, J. K., van der Wiel, M. H. D., et al. 2016, A&A, 590, L6
Coutens, A., Willis, E. R., Garrod, R. T., et al. 2018, A&A, 612, A107
D'Alessio, P., Calvet, N., Hartmann, L., Franco-Hernández, R., & Servín, H. 2006, ApJ, 638, 314
D'Alessio, P., Cantö, J., Calvet, N., & Lizano, S. 1998, ApJ, 500, 411
Dartois, E., Dutrey, A., & Guilloteau, S. 2003, A&A, 399, 773
de Boer, J., Salter, G., Benisty, M., et al. 2016, A&A, 595, A114
de Gregorio-Monsalvo, I., Ménard, F., Dent, W., et al. 2013, A&A, 557, A133
de Juan Ovelar, M., Pinilla, P., Min, M., Dominik, C., & Birnstiel, T. 2016, MNRAS, 459, L85
Dominik, C. 2015, in European Physical Journal Web of Conferences, Vol. 102, European Physical Journal Web of Conferences, 00002
Dong, R., Fung, J., & Chiang, E. 2016, ApJ, 826, 75
Dullemond, C. P. & Dominik, C. 2004, A&A, 421, 1075
Dullemond, C. P. & Dominik, C. 2005, A&A, 434, 971
Dullemond, C. P., Hollenbach, D., Kamp, I., & D'Alessio, P. 2007, Protostars and Planets V, 555
Dullemond, C. P., Juhasz, A., Pohl, A., et al. 2012, RADMC-3D: A multi-purpose radiative transfer tool, Astrophysics Source Code Library
Dullemond, C. P. & Monnier, J. D. 2010, ARA&A, 48, 205
Dutrey, A., Guilloteau, S., Piétu, V., et al. 2017, A&A, 607, A130
Eisner, J. A., Arce, H. G., Ballering, N. P., et al. 2018, ApJ, 860, 77
Elmegreen, B. G. 1998, in Astronomical Society of the Pacific Conference Series, Vol. 148, Origins, ed. C. E. Woodward, J. M. Shull, & H. A. Thronson, Jr., 150
Evans, II, N. J., Dunham, M. M., Jørgensen, J. K., et al. 2009, ApJS, 181, 321
Fayolle, E. C., Öberg, K. I., Cuppen, H. M., Visser, R., & Linnartz, H. 2011, A&A, 529, A74
Fedele, D., Tazzari, M., Booth, R., et al. 2018, A&A, 610, A24
Flock, M., Ruge, J. P., Dzyurkevich, N., et al. 2015, A&A, 574, A68
France, K., Herczeg, G. J., McJunkin, M., & Penton, S. V. 2014, ApJ, 794, 160
Gail, H.-P. 2010, in Lecture Notes in Physics, Berlin Springer Verlag, Vol. 815, Lecture Notes in Physics, Berlin Springer Verlag, ed. T. Henning, 61–141

Gammie, C. F. & Johnson, B. M. 2005, in Astronomical Society of the Pacific Conference Series, Vol. 341, Chondrites and the Protoplanetary Disk, ed. A. N. Krot, E. R. D. Scott, & B. Reipurth, 145
Ginski, C., Stolker, T., Pinilla, P., et al. 2016, A&A, 595, A112
Greene, T. P., Wilking, B. A., Andre, P., Young, E. T., & Lada, C. J. 1994, ApJ, 434, 614
Güdel, M. & Nazé, Y. 2009, A&A Rev., 17, 309
Guilloteau, S. & Dutrey, A. 1998, A&A, 339, 467
Hacar, A. & Tafalla, M. 2011, A&A, 533, A34
Hacar, A., Tafalla, M., Forbrich, J., et al. 2018, A&A, 610, A77
Hacar, A., Tafalla, M., Kauffmann, J., & Kovács, A. 2013, A&A, 554, A55
Haro, G. 1952, ApJ, 115, 572
Hartmann, L., Calvet, N., Gullbring, E., & D'Alessio, P. 1998, ApJ, 495, 385
Hayashi, C. 1961, PASJ, 13
Hayashi, C. 1966, ARA&A, 4, 171
Heiderman, A. & Evans, II, N. J. 2015, ApJ, 806, 231
Henning, T. & Semenov, D. 2013, Chemical Reviews, 113, 9016
Herbig, G. H. 1951, ApJ, 113, 697
Herbig, G. H. 1962, Advances in Astronomy and Astrophysics, 1, 47
Herbst, E. & van Dishoeck, E. F. 2009, ARA&A, 47, 427
Hughes, A. M., Wilner, D. J., Qi, C., & Hogerheijde, M. R. 2008, ApJ, 678, 1119
Isella, A., Guidi, G., Testi, L., et al. 2016, Phys. Rev. Lett., 117, 251101
Johansen, A. 2009, in IAU Symposium, Vol. 259, Cosmic Magnetic Fields: From Planets, to Stars and Galaxies, ed. K. G. Strassmeier, A. G. Kosovichev, & J. E. Beckman, 249–258
Jørgensen, J. K., van der Wiel, M. H. D., Coutens, A., et al. 2016, A&A, 595, A117
Jørgensen, J. K., Visser, R., Sakai, N., et al. 2013, ApJ, 779, L22
Kama, M., Bruderer, S., Carney, M., et al. 2016, A&A, 588, A108
Kenyon, S. J. & Hartmann, L. 1987, ApJ, 323, 714
Kenyon, S. J. & Hartmann, L. 1995, ApJS, 101, 117
Keppler, M., Benisty, M., Müller, A., et al. 2018, ArXiv e-prints
Lacy, J. H., Knacke, R., Geballe, T. R., & Tokunaga, A. T. 1994, ApJ, 428, L69
Lada, C. J. & Wilking, B. A. 1984, ApJ, 287, 610
Lecar, M., Podolak, M., Sasselov, D., & Chiang, E. 2006, ApJ, 640, 1115
Lissauer, J. J. 2002, Nature, 419, 355
Long, F., Herczeg, G. J., Pascucci, I., et al. 2017, ApJ, 844, 99
Loomis, R. A., Cleeves, L. I., Öberg, K. I., et al. 2018, ApJ, 859, 131
Loomis, R. A., Cleeves, L. I., Öberg, K. I., Guzman, V. V., & Andrews, S. M. 2015, ApJ, 809, L25
Lykke, J. M., Coutens, A., Jørgensen, J. K., et al. 2017, A&A, 597, A53
Lynden-Bell, D. & Pringle, J. E. 1974, MNRAS, 168, 603
Mannings, V. & Emerson, J. P. 1994, MNRAS, 267, 361
Mathews, G. S., Klaassen, P. D., Juhász, A., et al. 2013, A&A, 557, A132
Mayor, M. & Queloz, D. 1995, Nature, 378, 355
McClure, M. K., Bergin, E. A., Cleeves, L. I., et al. 2016, ApJ, 831, 167
McMullin, J. P., Waters, B., Schiebel, D., Young, W., & Golap, K. 2007, in Astronomical Society of the Pacific Conference Series, Vol. 376, Astronomical Data Analysis Software and Systems XVI, ed. R. A. Shaw, F. Hill, & D. J. Bell, 127

Millar, T. J., Bennett, A., & Herbst, E. 1989, ApJ, 340, 906

Millar, T. J., Nomura, H., & Markwick, A. J. 2003, Ap&SS, 285, 761

Min, M., Dullemond, C. P., Dominik, C., de Koter, A., & Hovenier, J. W. 2009, A&A, 497, 155

Miotello, A., Bruderer, S., & van Dishoeck, E. F. 2014, A&A, 572, A96

Müller, A., Keppler, M., Henning, T., et al. 2018, ArXiv e-prints

Mumma, M. 2008, Astrobiology, 8, 339

Mumma, M. J. & Charnley, S. B. 2011, ARA&A, 49, 471

Muro-Arena, G. A., Dominik, C., Waters, L. B. F. M., et al. 2018, A&A, 614, A24

Najita, J. R., Strom, S. E., & Muzerolle, J. 2007, MNRAS, 378, 369

Öberg, K. I., Bottinelli, S., Jørgensen, J. K., & van Dishoeck, E. F. 2010, ApJ, 716, 825

Öberg, K. I., Furuya, K., Loomis, R., et al. 2015a, ApJ, 810, 112

Öberg, K. I., Garrod, R. T., van Dishoeck, E. F., & Linnartz, H. 2009, A&A, 504, 891

Öberg, K. I., Guzmán, V. V., Furuya, K., et al. 2015b, Nature, 520, 198

Öberg, K. I., Guzmán, V. V., Merchantz, C. J., et al. 2017, ApJ, 839, 43

Öberg, K. I., Qi, C., Wilner, D. J., & Hogerheijde, M. R. 2012, ApJ, 749, 162

Okuzumi, S., Momose, M., Sirono, S.-i., Kobayashi, H., & Tanaka, H. 2016, ApJ, 821, 82

Ollivier, M., Roques, F., Casoli, F., Encrenaz, T., & Selsis, F. 2009, Stellar Formation and Protoplanetary Disks (Berlin, Heidelberg: Springer Berlin Heidelberg), 135–169

Pascucci, I., Testi, L., Herczeg, G. J., et al. 2016, ApJ, 831, 125

Pérez, L. M., Carpenter, J. M., Andrews, S. M., et al. 2016, Science, 353, 1519

Piétu, V., Dutrey, A., & Guilloteau, S. 2007, A&A, 467, 163

Pinilla, P., Benisty, M., & Birnstiel, T. 2012, A&A, 545, A81

Pinilla, P., Flock, M., Ovelar, M. d. J., & Birnstiel, T. 2016, A&A, 596, A81

Pinte, C., Price, D. J., Ménard, F., et al. 2018, ApJ, 860, L13

Pohl, A., Benisty, M., Pinilla, P., et al. 2017, ApJ, 850, 52

Prialnik, D. 2009, An Introduction to the Theory of Stellar Structure and Evolution

Pringle, J. E. 1981, ARA&A, 19, 137

Qi, C., D'Alessio, P., Öberg, K. I., et al. 2011, ApJ, 740, 84

Qi, C., Ho, P. T. P., Wilner, D. J., et al. 2004, ApJ, 616, L11

Qi, C., Öberg, K. I., Andrews, S. M., et al. 2015, ApJ, 813, 128

Qi, C., Öberg, K. I., Wilner, D. J., et al. 2013, Science, 341, 630

Qi, C., Wilner, D. J., Aikawa, Y., Blake, G. A., & Hogerheijde, M. R. 2008, ApJ, 681, 1396

Qi, C., Wilner, D. J., Calvet, N., et al. 2006, ApJ, 636, L157

Rice, W. K. M., Armitage, P. J., Wood, K., & Lodato, G. 2006, MNRAS, 373, 1619

Ros, K. & Johansen, A. 2013, A&A, 552, A137

Rosenfeld, K. A., Andrews, S. M., Hughes, A. M., Wilner, D. J., & Qi, C. 2013, ApJ, 774, 16

Rosotti, G. P., Juhasz, A., Booth, R. A., & Clarke, C. J. 2016, MNRAS, 459, 2790

Ruíz-Rodríguez, D., Cieza, L. A., Williams, J. P., et al. 2018, MNRAS, 478, 3674

Salinas, V. N., Hogerheijde, M. R., Mathews, G. S., et al. 2017, A&A, 606, A125

Schoonenberg, D., Okuzumi, S., & Ormel, C. W. 2017, A&A, 605, L2
Schwarz, K. R., Bergin, E. A., Cleeves, L. I., et al. 2016, ApJ, 823, 91
Shakura, N. I. & Sunyaev, R. A. 1973, A&A, 24, 337
Shu, F. H. 1977, ApJ, 214, 488
Shu, F. H., Adams, F. C., & Lizano, S. 1987, ARA&A, 25, 23
Simon, J. B. & Armitage, P. J. 2014, ApJ, 784, 15
Stammler, S. M., Birnstiel, T., Panić, O., Dullemond, C. P., & Dominik, C. 2017, A&A, 600, A140
Stevenson, D. J. & Lunine, J. I. 1988, Icarus, 75, 146
Stolker, T., Dominik, C., Avenhaus, H., et al. 2016, A&A, 595, A113
Strom, K. M., Strom, S. E., Edwards, S., Cabrit, S., & Skrutskie, M. F. 1989, AJ, 97, 1451
Takahashi, S. Z. & Inutsuka, S.-i. 2014, ApJ, 794, 55
Teague, R., Bae, J., Bergin, E. A., Birnstiel, T., & Foreman-Mackey, D. 2018, ApJ, 860, L12
Terebey, S., Shu, F. H., & Cassen, P. 1984, ApJ, 286, 529
Tielens, A. G. G. M. & Hagen, W. 1982, A&A, 114, 245
van Boekel, R., Henning, T., Menu, J., et al. 2017, ApJ, 837, 132
van der Marel, N., van Dishoeck, E. F., Bruderer, S., et al. 2016, A&A, 585, A58
van der Marel, N., van Dishoeck, E. F., Bruderer, S., et al. 2013, Science, 340, 1199
van der Marel, N., van Dishoeck, E. F., Bruderer, S., Pérez, L., & Isella, A. 2015, A&A, 579, A106
van Dishoeck, E. F., Thi, W.-F., & van Zadelhoff, G.-J. 2003, A&A, 400, L1
van 't Hoff, M. L. R., Persson, M. V., Harsono, D., et al. 2018, A&A, 613, A29
van Zadelhoff, G.-J., van Dishoeck, E. F., Thi, W.-F., & Blake, G. A. 2001, A&A, 377, 566
Walsh, C., Juhász, A., Meeus, G., et al. 2016, ApJ, 831, 200
Walsh, C., Juhász, A., Pinilla, P., et al. 2014a, ApJ, 791, L6
Walsh, C., Millar, T. J., Nomura, H., et al. 2014b, A&A, 563, A33
Ward-Duong, K., Patience, J., Bulger, J., et al. 2018, AJ, 155, 54
Watanabe, N., Shiraki, T., & Kouchi, A. 2003, ApJ, 588, L121
Waters, L. B. F. M. & Waelkens, C. 1998, ARA&A, 36, 233
Weintraub, D. A., Sandell, G., & Duncan, W. D. 1989, ApJ, 340, L69
Wilking, B. A., Meyer, M. R., Robinson, J. G., & Greene, T. P. 2005, AJ, 130, 1733
Williams, J. P. & Cieza, L. A. 2011, ARA&A, 49, 67
Winn, J. N. & Fabrycky, D. C. 2015, ARA&A, 53, 409
Yen, H.-W., Liu, H. B., Gu, P.-G., et al. 2016, ApJ, 820, L25
Youdin, A. N. 2011, ApJ, 731, 99
Zhang, K., Bergin, E. A., Blake, G. A., et al. 2016, ApJ, 818, L16
Zhang, K., Bergin, E. A., Blake, G. A., Cleeves, L. I., & Schwarz, K. R. 2017, Nature Astronomy, 1, 0130
Zhu, Z., Nelson, R. P., Hartmann, L., Espaillat, C., & Calvet, N. 2011, ApJ, 729, 47

CHAPTER 2

INCREASED H_2CO PRODUCTION IN THE OUTER DISK AROUND HD 163296

M. T. CARNEY, M. R. HOGERHEIJDE, R. A. LOOMIS, V. N. SALINAS,
K. I. ÖBERG, C. QI, AND D. J. WILNER.

ASTRONOMY & ASTROPHYSICS
VOLUME 605, ARTICLE A21, 16 PP. (2017)

Abstract

Context. The gas and dust in circumstellar disks provide the raw materials to form planets. The study of organic molecules and their building blocks in such disks offers insight into the origin of the prebiotic environment of terrestrial planets.
Aims. We aim to determine the distribution of formaldehyde, H_2CO, in the disk around HD 163296 to assess the contribution of gas- and solid-phase formation routes of this simple organic.
Methods. Three formaldehyde lines were observed (H_2CO $3_{03}-2_{02}$, H_2CO $3_{22}-2_{21}$, and H_2CO $3_{21}-2_{20}$) in the protoplanetary disk around the Herbig Ae star HD 163296 with ALMA at ~0.5″ (60 AU) spatial resolution. Different parameterizations of the H_2CO abundance were compared to the observed visibilities, using either a characteristic temperature, a characteristic radius or a radial power law index to describe the H_2CO chemistry. Similar models were applied to ALMA Science Verification data of $C^{18}O$. In each scenario, χ^2 minimization on the visibilities was used to determine the best-fit model.
Results. H_2CO $3_{03}-2_{02}$ was readily detected via imaging, while the weaker H_2CO $3_{22}-2_{21}$ and H_2CO $3_{21}-2_{20}$ lines required matched filter analysis to detect. H_2CO is present throughout most of the gaseous disk, extending out to ~550 AU. An apparent 50 AU inner radius of the H_2CO emission is likely caused by an optically thick dust continuum. The H_2CO radial intensity profile shows a peak at ~100 AU and a secondary bump at ~300 AU, suggesting increased production in the outer disk. In all modeling scenarios, fits to the H_2CO data show an increased abundance in the outer disk. The overall best-fit H_2CO model shows a factor of two enhancement beyond a radius of 270 ± 20 AU, with an inner abundance (relative to H_2) of $2-5\times10^{-12}$. The H_2CO emitting region has a lower limit on the kinetic temperature of $T > 20$ K. The $C^{18}O$ modeling suggests an order of magnitude depletion of $C^{18}O$ in the outer disk and an abundance of $4-12\times10^{-8}$ in the inner disk.
Conclusions. There is a desorption front seen in the H_2CO emission that roughly coincides with the outer edge of the 1.3 millimeter continuum. The increase in H_2CO outer disk emission could be a result of hydrogenation of CO ices on dust grains that are then sublimated via thermal desorption or UV photodesorption. Alternatively, there could be more efficient gas-phase production of H_2CO beyond ~300 AU if CO is photodissociated in this region.

2.1 Introduction

Protoplanetary disks have a layered temperature and density structure that results in a cold, dense midplane where gaseous molecules freeze out onto icy mantles around small dust grains. Chemical reactions and radiative processing of atoms and molecules locked up in ices can create organic molecules of increasing complexity (Watanabe et al. 2003; Öberg et al. 2009, 2010a; Herbst & van Dishoeck 2009). The high densities and vertical settling of larger grains make the disk midplane an ideal site for grain growth and the formation of comets and planetesimals (Dullemond & Dominik 2005; Andrews & Williams 2005; D'Alessio et al. 2006). The cold, complex molecular reservoir may be incorporated into small icy bodies in the midplane and remain relatively unprocessed, thus comets may preserve the chemical composition of the disk at the time of their formation (van Dishoeck & Blake 1998; Mumma & Charnley 2011). Comets and other planetesimals are possible delivery mechanisms of organics to terrestrial bodies during the early stages of the Solar System, thus it is important to understand the chemistry and composition of their natal environments. Observations of molecular emission lines can determine the distribution and abundance of a molecular species and constrain its location in a protoplanetary disk. Characterizing simple organic molecules that may be produced in the disk midplane, such as H_2CO, can constrain available formation scenarios for complex organic molecules (COMs). H_2CO acts as a precursor to CH_3OH, which is an important building block for other COMs (Öberg et al. 2009; Walsh et al. 2014). Thus, determining the dominant formation mechanism for H_2CO and its distribution in disks can help to constrain abundances for CH_3OH and the complex organic reservoir.

A major formation pathway of H_2CO is expected to be the hydrogenation of CO ices in the cold midplane of the disk (Watanabe et al. 2003; Cuppen et al. 2009). H_2CO also has a gas-phase formation route via neutral-neutral reactions of CH_3 and O at higher ($\gtrsim$ 200 K) temperatures (Fockenberg & Preses 2002; Atkinson et al. 2006). Formaldehyde has already been detected toward several protoplanetary disks (Aikawa et al. 2003; Öberg et al. 2010b; Qi et al. 2013; van der Marel et al. 2014; Loomis et al. 2015; Öberg et al. 2017), but it is difficult to determine the contribution of H_2CO formed in the gas phase versus that formed via surface reactions. It is important to consider the distribution of H_2CO in relation to the freeze-out of CO, i.e., the CO snow line. H_2CO that exists well beyond the CO snow line is likely formed on the icy mantles of dust grains while H_2CO located within the CO snow line forms via gas-phase pathways at higher temperatures.

Qi et al. (2013) attempted to reproduce Submillimeter Array (SMA) observations of H_2CO around TW Hya and HD 163296 with two simple parameterized models: a power-law H_2CO column density with an inner radius, and a ring-like H_2CO distribution with an upper boundary set by the CO freeze-out temperature. They found that both models indicated H_2CO is produced mostly at larger radii beyond the CO snow line in the disk around HD 163296, which is consistent with a scenario in which formaldehyde forms in CO ice and is subsequently released back into the gas phase. Loomis et al. (2015) modeled H_2CO in DM Tau observed with the Atacama Large Millimeter/submillimeter Array (ALMA) using a small chemical network with and without grain-surface formation. They found that both gas- and solid-phase production of H_2CO were needed to reproduce the centrally peaked emission and the emission exterior to the CO snow line in DM Tau.

HD 163296 (MWC 275) is an ideal testbed for chemical processing in protoplanetary disks, in particular for organics. It is an isolated Herbig Ae pre-main sequence (PMS) star with spectral type A2Ve, an age of approximately 5 Myr, and is located at 122 pc (de Gregorio-Monsalvo et al. 2013). The PMS star is surrounded by a large gas-rich protoplanetary disk that extends to ~550 AU (Isella et al. 2007) with stellar mass $M_* = 2.3\ M_\odot$, disk mass $M_{\rm disk} = 0.089\ M_\odot$, and an inclination of 44° based on the Qi et al. (2011) physical model. At such an inclination, vertical structure as well as radial structure can be inferred from molecular line emission. The proximity and size of the disk combined with the strong UV field of the Herbig Ae PMS star provides a unique opportunity to fully resolve the location of the CO snow line around HD 163296. Several attempts have already been made to constrain the location of the CO snow line in this disk (Qi et al.

2011; Mathews et al. 2013; Qi et al. 2015). Current estimates by Qi et al. (2015) place CO freeze-out at 90 AU, corresponding to ~24 K in this disk. HD 163296 is one of the best candidates to probe the formation of organics with respect to the freeze-out of abundant volatiles such as CO. Observations of H_2CO in combination with tracers of the CO snow line, such as the optically thin $C^{18}O$ isotopolog, DCO^+, or N_2H^+, provide insight into the formation of organic molecules in Herbig Ae/Be disks.

This paper presents ALMA observations of H_2CO toward HD 163296 and characterizes its distribution throughout the disk. Our analysis also makes use of $C^{18}O$ ALMA Science Verification data, which has been previously reported (Rosenfeld et al. 2013; Qi et al. 2015). Section 2.2 describes the observations and data reduction. The detection of H_2CO, the modeling of H_2CO and $C^{18}O$ distributions and abundances, and the calculation of excitation temperatures for H_2CO are discussed in Section 2.3. In Section 2.4 we discuss the relationship between H_2CO, $C^{18}O$, and the millimeter continuum, and the implications for H_2CO formation. Section 2.5 presents the conclusions.

2.2 Observations and reduction

HD 163296 (J2000: R.A. = $17^h56^m21.280^s$, DEC = $-21°57'22.441''$) was observed on 2014 July 27, 28, and 29 with ALMA in band 6 as part of Cycle 2. In total 33 antennas were used in the C34 configuration to achieve a resolution of ~0.4″. Band 6 operates in the 211 − 275 GHz range as a 2SB receiver. The upper sideband contained continuum observations in the time domain mode (TDM) correlator setting with 128 channels over a 2 GHz bandwidth centered at 233 GHz, presented in Zhang et al. (2016). Three transitions of H_2CO were observed in the lower sideband with the frequency domain mode (FDM) correlator setting: H_2CO $3_{03} - 2_{02}$ at 218.22219 GHz, H_2CO $3_{22} - 2_{21}$ at 218.475632 GHz, and H_2CO $3_{21} - 2_{20}$ at 218.760066 GHz. Each line had a bandwidth of 56.6 MHz with 960 channels, providing a frequency (velocity) resolution of 0.061 MHz (0.084 km s^{-1}). Table 2.1 summarizes the observational parameters of each line. Three additional lines, DCO^+ 3 − 2 at 216.11258 GHz, DCN 3 − 2 at 217.23853 GHz, and N_2D^+ 3 − 2 231.321828 GHz were also observed with the same spectral parameters and have been presented in Salinas et al. (2017).

Visibility data were obtained over four execution blocks of ~30 minutes (×1) and ~90 minutes (×3) at 6.05 seconds per integration for 155 minutes total time on source. System temperatures varied from 50 − 150 K. The average precipitable water vapor across all observations was 1.0 mm. The Common Astronomy Software Applications (CASA) package was used to calibrate the data with an automated script provided by the ALMA staff. Calibration of each execution block was carried out with J1700-2610 as the delay calibrator, J1733-1304 as the bandpass and gain calibrator, J1733-1304 as the flux calibrator for three out of four blocks, and Titan as the flux calibrator for the final block. After initial calibration of individual execution blocks, gain calibration solutions obtained from models of Titan were used to derive fluxes for J1733-1304, which was then used as the flux calibrator in all spectral windows and all execution blocks for consistency. Amplitudes for HD 163296 were rescaled across all blocks using J1733-1304 as the flux calibrator. The average flux values for J1733-1304 were 1.329 Jy in the lower sideband and 1.255 Jy in the upper sideband. The total flux for HD 163296 was found to be

Table 2.1: HD 163296 observational parameters

	Project 2013.1.01268.S		
Dates observed	2014 July 27, 28, 29		
Baselines	21 – 795 m | 16 – 598 kλ		
	H_2CO $3_{03} - 2_{02}$	H_2CO $3_{22} - 2_{21}$	H_2CO $3_{21} - 2_{20}$
Rest frequency [GHz]	218.222	218.476	218.760
Synthesized beam [FWHM]	$0.54'' \times 0.42''$	$0.54'' \times 0.42''$	$0.53'' \times 0.42''$
Position angle	89.3°	86.6°	87.9°
rms noise[a] [mJy beam^{-1}]	1.8	2.6	2.6
Channel width [km s^{-1}]	0.084	0.084	0.084
Integrated flux [Jy km s^{-1}]	0.64 ± 0.06[b]	> 0.036, < 0.27[c]	> 0.032, < 0.31[c]
Weighting	natural	natural	natural
Continuum frequency [GHz]	225.0		
Synthesized beam [FWHM]	$0.42'' \times 0.33''$		
Position angle	77.5°		
rms noise [mJy beam^{-1}]	0.05		
Integrated flux [mJy]	652 ± 65		
Weighting	Briggs, robust = 0.5		
	Project 2011.1.00010.SV		
Dates observed	2012 June 09, 23, July 07		
Baselines	21 – 536 m | 16 – 402 kλ		
	$C^{18}O$ 2 – 1		
Rest frequency [GHz]	219.560		
Synthesized beam [FWHM]	$0.87'' \times 0.71''$		
Position angle	64.0°		
Channel width [km s^{-1}]	0.334		
rms noise[a] [mJy beam^{-1}]	4.2		
Integrated flux[d] [Jy km s^{-1}]	7.4 ± 0.7		
Weighting	natural		

Notes. Flux errors are dominated by systematic uncertainties, taken to be ∼10%. (a) Noise values are per image channel. (b) Line flux derived from spatial and spectral integration after masking pixels with $< 3\sigma$ emission. (c) Line flux lower limit derived from the peak σ-ratio based on matched-filter detections. Upper limits are $3\sigma_I$ where σ_I is defined in Section 2.3.1. (d) Line flux derived from spatial and spectral integration over a 5.6″ radius circular aperture and velocity channels 0.87 – 12.1 km s^{-1}.

within 5% across all execution blocks. All measurement sets were subsequently concatenated and time binned to 30 sec integration time per visibility for imaging and analysis.

Self-calibration for HD 163296 was performed with the continuum TDM spectral window and all line-free channels of the FDM spectral windows. DV11 was chosen as the reference antenna. A minimum of four baselines per antenna and a minimum signal-to-noise ratio (S/N) of two were required. Calibration solutions were calculated twice for phase and once for amplitude. The first phase solution interval (solint) was 500 sec, the second phase and amplitude solutions had solint equal to the binned integration time (30 sec). Continuum subtraction of the line data was carried out in the *uv* plane using a single-order polynomial fit to the line-free channels. The CLEAN imaging was performed with natural weighting for each continuum-subtracted H_2CO line down to a threshold of 4 mJy.

This work also uses $C^{18}O$ 2 – 1 calibrated data of HD 163296 from the ALMA project 2011.0.00010.SV obtained from the publicly available ALMA Science Verification Data website.[1] See Rosenfeld et al. (2013) for details on the calibration of the data set. The flux for the $C^{18}O$ 2 – 1 line (Table 2.1) is consistent with previously reported values (Rosenfeld et al. 2013; Qi et al. 2015).

The following software and coding languages were used for data analysis in this paper: the CASA package (McMullin et al. 2007), the MIRIAD package (Sault et al. 1995), and PYTHON.

2.3 Results

The following sections present results of H_2CO observations in the disk around HD 163296. Physical parameters of the lines and their distribution throughout the disk are discussed in Section 2.3.1. Models of H_2CO and $C^{18}O$ emission and their abundances are presented in Section 2.3.2. Constraints on the excitation temperature of H_2CO are discussed in Section 2.3.3.

2.3.1 Detection and distribution of H_2CO

The spatially integrated spectrum for each H_2CO line can be found in Figure 2.1. The H_2CO $3_{03} - 2_{02}$ transition is readily detected in the spectrum extracted from CLEAN imaging. The two weaker lines are not detected in the extracted spectra, but after applying a matched-filter technique the lines are clearly detected and can be used to provide constraints on the H_2CO excitation temperature. Physical parameters of the three lines and the continuum can be found in Table 2.1.

HD 163296 has a v_{LSR} systemic velocity of +5.8 km s^{-1} (Qi et al. 2011), which corresponds well to the central velocity of the H_2CO $3_{03} - 2_{02}$ line. The H_2CO $3_{03} - 2_{02}$ line flux was derived after masking pixels with $< 3\sigma$ emission in the image cube. The cube was then integrated spatially over a $7''$ radius and over velocity channels 0.76 – 10.84 km s^{-1}. Lower limits on H_2CO $3_{22} - 2_{21}$ and H_2CO $3_{21} - 2_{20}$ line fluxes are from estimates via the matched-filter method. Upper limits on the lines are based on spectra from the CLEAN images of H_2CO $3_{22} - 2_{21}$ and H_2CO $3_{21} - 2_{20}$ and are given at the $3\sigma_{\mathrm{I}}$ level, where $\sigma_{\mathrm{I}} = 0.5\sqrt{\pi/\log(2)}\Delta v \sigma_{\mathrm{rms}}$ estimates the area of a Gaussian curve, Δv is the FWHM of the detected H_2CO $3_{03} - 2_{02}$, and σ_{rms} is the rms noise in Jy from the disk-integrated spectra.

The H_2CO $3_{03} - 2_{02}$ image has a $0.54'' \times 0.42''$ (66×51 AU) synthesized beam (P.A. = 86.5°). Figure 2.2 shows a velocity-weighted (first-order moment) map of H_2CO $3_{03} - 2_{02}$ from 0.76 – 10.84 km s^{-1} that is clipped at the 3σ level, which reveals the full extent of the H_2CO emission in Keplerian rotation, while Figure 2.3 shows the channel maps of H_2CO $3_{03} - 2_{02}$ around HD 163296 Hanning smoothed to a resolution of 0.336 km s^{-1} over velocities where molecular emission is present. The inner and outer projected radii ($i = 44°$, P.A. = 133° east of north) of H_2CO $3_{03} - 2_{02}$ emission at the 3σ level along the major axis are $0.4''$ and $4.5''$, respectively, corresponding to projected physical distances $R_{\mathrm{in}} \approx 50$ AU and $R_{\mathrm{out}} \approx 550$ AU at a distance of 122 pc (van den Ancker et al. 1998).

The extent of H_2CO $3_{03} - 2_{02}$ was found to be greater than that of the 1.3 mm continuum (shown in black contours in Figure 2.2), suggesting that millimeter-sized grains have decoupled from the gas and drifted radially inward. de Gregorio-Monsalvo et al. (2013) observed the same phenomenon in ^{12}CO and the 850 μm continuum. The 1.3 mm continuum has a projected outer radius at 3σ of $2.2''$ or

---

[1] `https://almascience.nrao.edu/alma-data/science-verification`

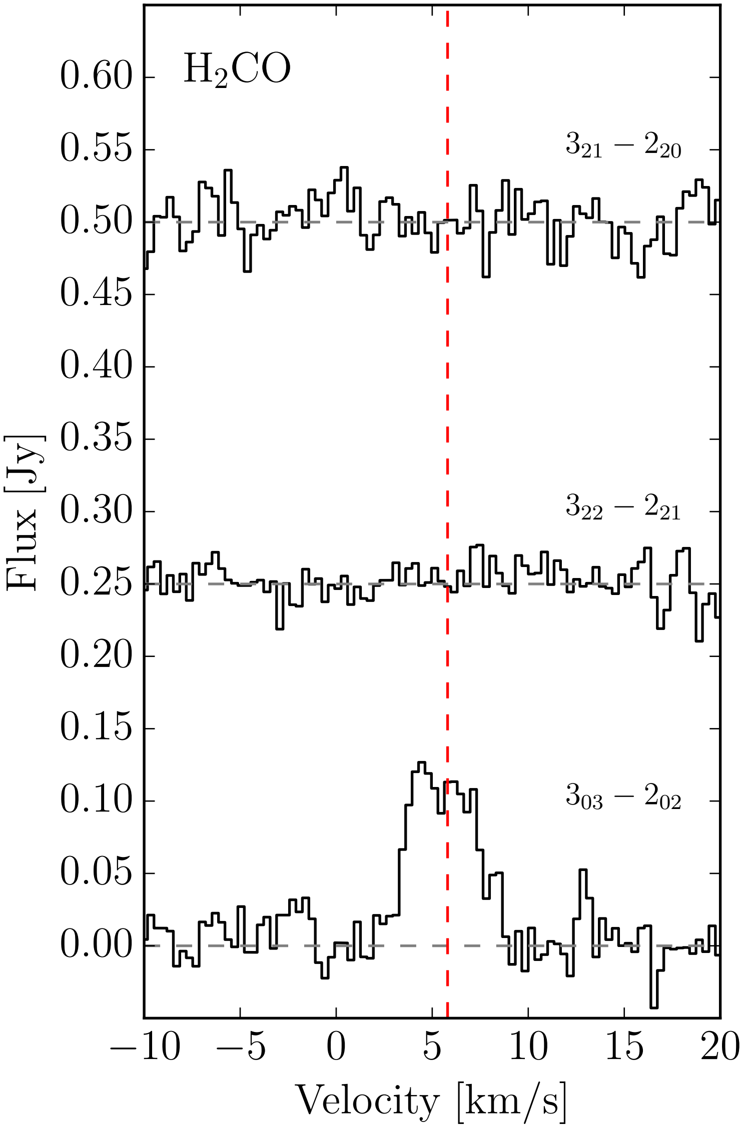

Figure 2.1: Disk-integrated H_2CO spectra using a 5.6″ radius circular aperture. H_2CO $3_{03} - 2_{02}$, H_2CO $3_{22} - 2_{21}$, and H_2CO $3_{21} - 2_{20}$ are at y-offsets of 0, 0.25, and 0.5 Jy, respectively, shown in dashed gray lines. The vertical dashed red line shows the systemic velocity. The spectra are Hanning smoothed to 0.336 km s^{-1} channels.

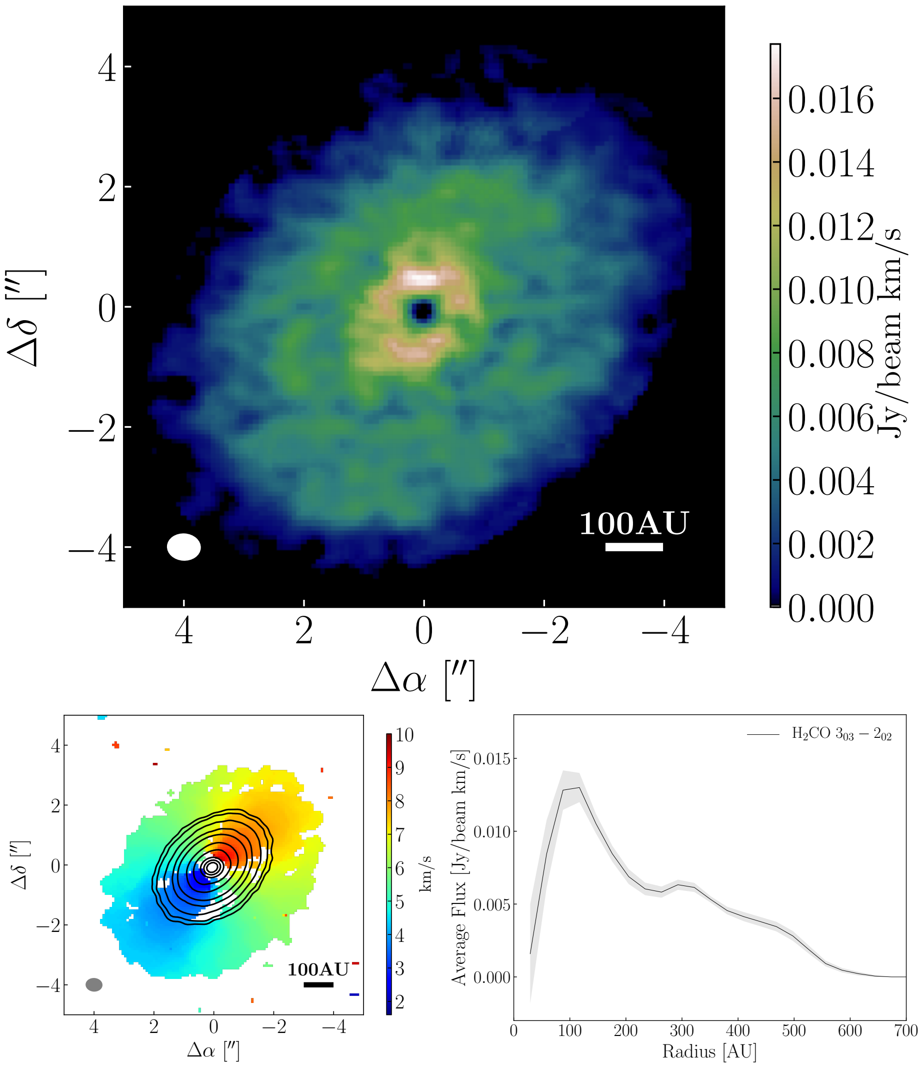

Figure 2.2: Moment maps and radial profile of H_2CO $3_{03} - 2_{02}$. (Top) Moment 0 map integrated over 0.76−10.84 km s^{-1} after applying a Keplerian mask. Synthesized beam and AU scale are shown in the lower corners. (Bottom left) Moment 1 map from 0.76 – 10.84 km s^{-1}, clipped at 3σ. Solid black contours show the 225 GHz/1.3 mm emission at 5.0×10^{-5} (1σ) × [5, 10, 25, 50, 100, 300, 500, 1000, 1500, 2000] Jy beam^{-1}. Synthesized beam and AU scale are shown in the lower corners. (Bottom right) Radial intensity curve from azimuthally-averaged elliptical annuli projected to $i = 44°$, P.A. = 133°. Shaded gray area represents 1σ errors.

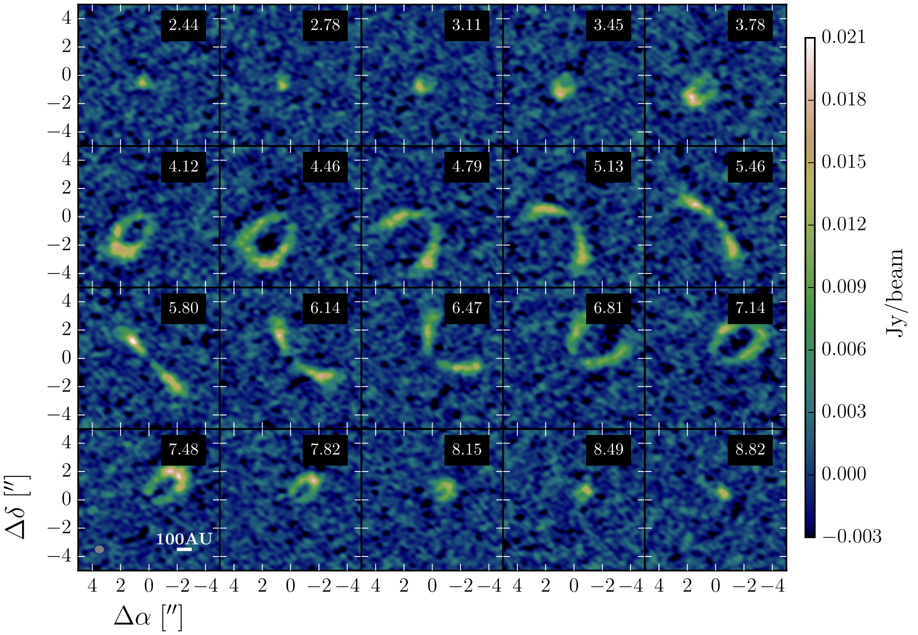

Figure 2.3: Channel maps of H_2CO $3_{03}-2_{02}$ from 2.44 − 8.82 km s^{-1}, Hanning smoothed to 0.336 km s^{-1} channels. Channel velocity is shown in the upper right corner. Synthesized beam and AU scale are shown in the lower left panel.

$R_{\rm out}^{\rm 1.3mm} \approx 270$ AU. The 1.3 mm emission extends beyond the 850 μm continuum reported by de Gregorio-Monsalvo et al. (2013) due to the increased sensitivity of our observations. Zhang et al. (2016) reported that analysis of the 1.3 millimeter continuum visibilities in this data set suggests a ring-like structure not seen in imaging at this resolution. The ring-like nature of the millimeter dust was confirmed by high-resolution observations after the original submission of our paper (Isella et al. 2016). They explained the dust morphology as three distinct dust gaps centered at 60, 100, and 160 AU.

To calculate the H_2CO $3_{03}-2_{02}$ radial intensity profile, an integrated intensity (zero-order moment) map was first created by applying a mask in right ascension, declination, and velocity to the image cube to enhance the S/N. The mask is based on the disk rotational velocity profile, which is assumed to be Keplerian with a mass of $M = 2.3\ M_\odot$, corresponding to the mass of the central star. In each velocity channel of the image cube, a subset of pixels were chosen where the calculated Keplerian velocity of the pixels matches the Doppler-shifted velocity of the line. All pixels that did not match these criteria were masked. Yen et al. (2016) use a similar method to extract their integrated intensity maps. The radial intensity profile and integrated intensity map for H_2CO $3_{03}-2_{02}$ emission are shown in Figure 2.2. Azimuthally-averaged elliptical annuli projected to an inclination of 44° and position angle of 133° were used to calculate the average flux in each radial step. This method provides more S/N per annulus, but results in a decrease in resolution by a factor of two due to the foreshortening along the inclined disk's minor axis in our radial intensity profiles. Radial step sizes of 0.24″ for H_2CO $3_{03}-2_{02}$ and 0.4″ for $C^{18}O$ $2-1$ were used for each annulus to provide a sampling of approximately two data points per original beam width.

The radial profile reveals an absence of emission at the center of the disk, a peak in intensity at ~100 AU with emission then decreasing until a turnover in the profile at ~200 AU and a bump at ~300 AU, signifying an enhancement in emission in the outer regions of the disk. The same curve for $C^{18}O$ has centrally peaked emission and intensity decreasing with radius. Already the shape of the radial profiles of the two molecules indicates a difference in abundance gradients throughout the disk. The $C^{18}O$ profile suggests that it follows more or less the smoothly decreasing H_2 gas density. On the other hand, H_2CO shows a peak at the approximate location of the CO snow line at 90 AU (Qi et al. 2015), and another enhancement is located roughly at the edge of the dust continuum. Such a radial profile highlights the need for two H_2CO formation mechanisms to account for the observed emission: one warm route that produces emission at temperatures above that of CO freeze-out in the inner disk within 100 AU and one cold route that produces emission outside of the CO snow line. Further explanations for these features are given in Section 2.3.2 and Section 2.4.

Matched filter detections

After subtracting the continuum from the line data, we employed a matched filter technique to the visibilities to detect the weaker H_2CO $3_{22}-2_{21}$ and H_2CO $3_{21}-2_{20}$ lines. In this technique, an image cube containing a template emission profile is sampled in *uv* space to obtain a set of template visibilities that act as the filter. The template is then cross-correlated with a set of visibilities with a low S/N in an attempt to detect the presence of the template emission within the low S/N data set. The cross-correlation is done by sliding the template visibilities channel-by-channel across the velocity axis of the low S/N visibilities. When the template reaches the source velocity in the low S/N data, there will be a sharp peak in the filter response spectrum of the correlation if the template signal is detected within the low S/N visibilities. This is analogous to image-based stacking approaches (e.g. Yen et al. 2016), but retains the advantages of working in the *uv* plane. In this work, to obtain a data-based template for the matched filter method, the H_2CO $3_{03}-2_{02}$ line was re-imaged with CLEAN in 0.084 km s^{-1} velocity channels using a *uv* taper to achieve a 1″ synthesized beam. Image channels showing H_2CO emission (1.6 – 10 km s^{-1}) were sampled in the *uv* plane using the PYTHON `vis_sample`[2] routine, and the resulting visibilities were then used as the template signal.

Figure 2.4 shows the filter impulse responses of the three H_2CO visibility data sets to the H_2CO $3_{03}-2_{02}$ template. The black curve is the response of the H_2CO $3_{03}-2_{02}$ visibility data to the template, highlighting the effectiveness of the filter to recover the line detection. The inset reveals the 4.5σ and 5σ detections of H_2CO $3_{22}-2_{21}$ and H_2CO $3_{21}-2_{20}$, respectively, where σ is calculated as the standard deviation of the response of emission-free visibility channels to the template. To constrain the total flux of the weaker lines, we compare the ratio of their peak filter responses and the peak response of the H_2CO $3_{03}-2_{02}$ visibilities (90σ, Figure 2.4). Under the assumption that all three observed H_2CO lines are co-spatial, the σ-ratio can be used to estimate the weaker line fluxes reported in Table 2.1. The

---

[2] `vis_sample` is publicly available at `https://github.com/AstroChem/vis_sample` or in the Anaconda Cloud at `https://anaconda.org/rloomis/vis_sample`

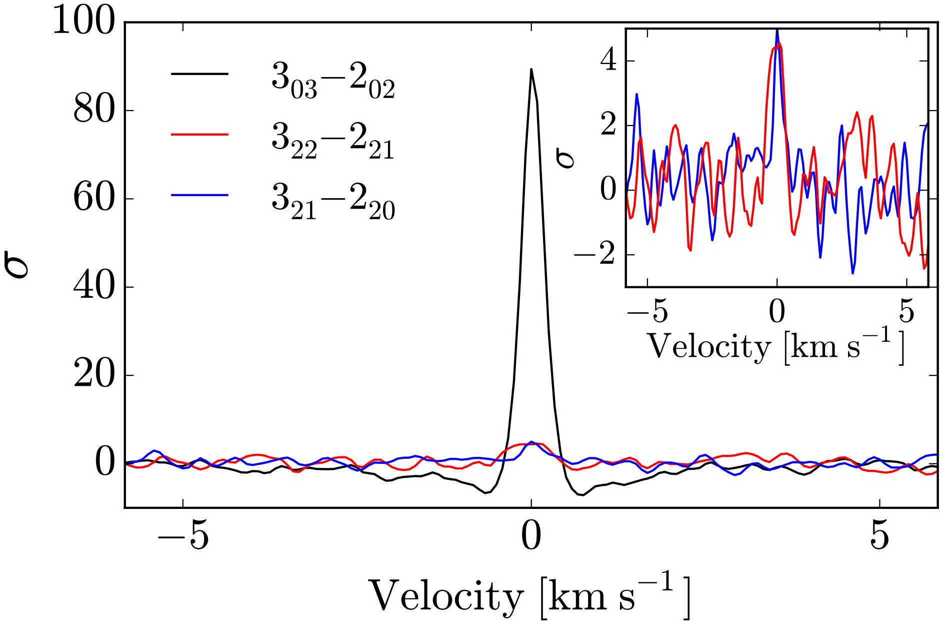

Figure 2.4: Matched filter responses of the observed H_2CO lines to the H_2CO $3_{03}-2_{02}$ data-based template. Self-response (black) shows template recovery of the $3_{03}-2_{02}$ detection. *Inset:* H_2CO $3_{22}-2_{21}$ (red) and H_2CO $3_{21}-2_{20}$ (blue) are detected at the 4.5σ and 5σ level, respectively.

response of the template is limited by how well it spatially matches the emission, thus making the derived line fluxes lower limits.

2.3.2 Modeling H_2CO and $C^{18}O$ emission

Previous studies (Qi et al. 2011; Rosenfeld et al. 2013; Qi et al. 2015) have attempted to use CO isotopologs to determine the radial location of CO freeze-out in HD 163296. Qi et al. (2011) modeled the ^{13}CO isotopolog and found a distinct drop in abundance at ~155 AU, which they attributed to CO freeze-out. However, in Qi et al. (2015) they claim ^{13}CO is a less robust tracer as it is difficult to separate CO freeze-out from opacity effects. ^{13}CO may remain optically thick out to radii beyond 100 AU. Thus, the apparent depletion may be due to a decrease in optical depth rather than an actual drop in abundance. These authors use $C^{18}O$ as a more robust, optically thin tracer of the column density of CO throughout the disk. Following this reasoning, we model only the $C^{18}O$ isotopolog to reveal structure in the CO gas. Although the $C^{18}O$ ALMA Science Verification data has been previously reported (Rosenfeld et al. 2013; Qi et al. 2015), we reanalyze the data in an effort to provide a ground truth for the CO surface density – particularly for the outer disk – within the same modeling approach as used for H_2CO and within the limits of the data resolution and our disk model.

The aims of modeling H_2CO and $C^{18}O$ are to determine likely formation scenarios for H_2CO and any relation to the CO snow line. If H_2CO is abundant in regions close to or below the CO freeze-out temperature, grain-surface formation of H_2CO on CO ices will contribute significantly to the overall H_2CO abundance. If H_2CO is abundant only in high temperatures zones of the disk, then gas-phase production of H_2CO dominates. By varying the relative molecular abundances in different regions of the models and comparing the model distribution to the data, we can determine which parts of the disk are harboring reservoirs of H_2CO.

This section describes the models used to reproduce the observed H_2CO $3_{03}-2_{02}$ and $C^{18}O$ $2-1$ emission based on the HD 163296 disk model created by Qi et al. (2011). In their paper they constrain the radial and vertical density and temperature structure of a steady viscous accretion disk with an exponentially tapered edge. Fitting the model continuum at multiple wavelengths to the observed spectral energy distribution (SED) constrained the radial structure. Observations of multiple optically thick ^{12}CO transitions were used to constrain the vertical structure. A modified version of this physical model was used by Mathews et al. (2013) to determine the distribution of DCO^+ in HD 163296. To constrain the vertical structure of the dust in the physical model, Mathews et al. (2013) refit the SED by varying independently the dust scale heights of Gaussian distributions of small ($a_{\rm max}$ = 25 μm) and large ($a_{\rm max}$ = 1 mm) populations of dust grains. Similarly, the vertical gas density distribution is treated as a two-component model with independent scale heights to simulate a Gaussian distribution at low heights with an extended tail higher in the disk. The gas scale heights are varied to recover the CO fluxes reported in Qi et al. (2011). Given these dust and gas distributions and assuming the dust continuum to be optically thin, the gas surface density of both H_2CO and $C^{18}O$ should be robustly measured in our models.

In this work, the Mathews et al. (2013) model was used as the physical disk structure for simulating molecular emission using the Line Modeling Engine (LIME: Brinch & Hogerheijde 2010) 3D radiative transfer code. Synthesized data cubes were created with LIME for H_2CO $3_{03}-2_{02}$ and $C^{18}O$ $2-1$ in non-LTE with H_2 as the primary collision partner. Both ortho- and para-H_2 species were included in collisional excitation, with a temperature-dependent ortho-to-para ratio (OPR) such that OPR = 3 at temperatures ≥ 200 K and decreases exponentially at lower temperatures. Molecular collision rates were taken from the Leiden Atomic and Molecular Database (LAMDA, Schoeier et al. 2005). The disk inclination, position angle, and distance are set to $i = 44°$, P.A. = 133°, and d = 122 pc.

Four types of models are used to test the distribution of observed H_2CO $3_{03}-2_{02}$ with different fractional abundance profiles relative to H_2. Figure 2.5 depicts examples of each of these scenarios with the relevant disk regions. Three of these models are used for $C^{18}O$ $2-1$. The first model assumes a constant abundance constrained to low temperatures at which H_2CO formation on the surface of icy grains is favorable. The low-temperature model is not used for $C^{18}O$ $2-1$. In the second model, H_2CO $3_{03}-2_{02}$ and $C^{18}O$ $2-1$ have a power-law abundance profile. The third model has a temperature-based step-abundance profile with a constant inner (high-temp) and outer (low-temp) abundance and a change-over temperature $T_{\rm c}$ as the boundary. The final model has a radial step-abundance profile with a constant inner abundance, constant outer abundance, and change-over radius $R_{\rm c}$. Analyses of the models make use of the `vis_sample` routine to read the *uv* coordinates directly from an observed ALMA measurement set and create synthetic visibilities based on an input sky model.

A central hole is observed in the H_2CO data, as seen in Figure 2.2, with a size approximately equal to the width of the beam. This hole is likely a result of strong

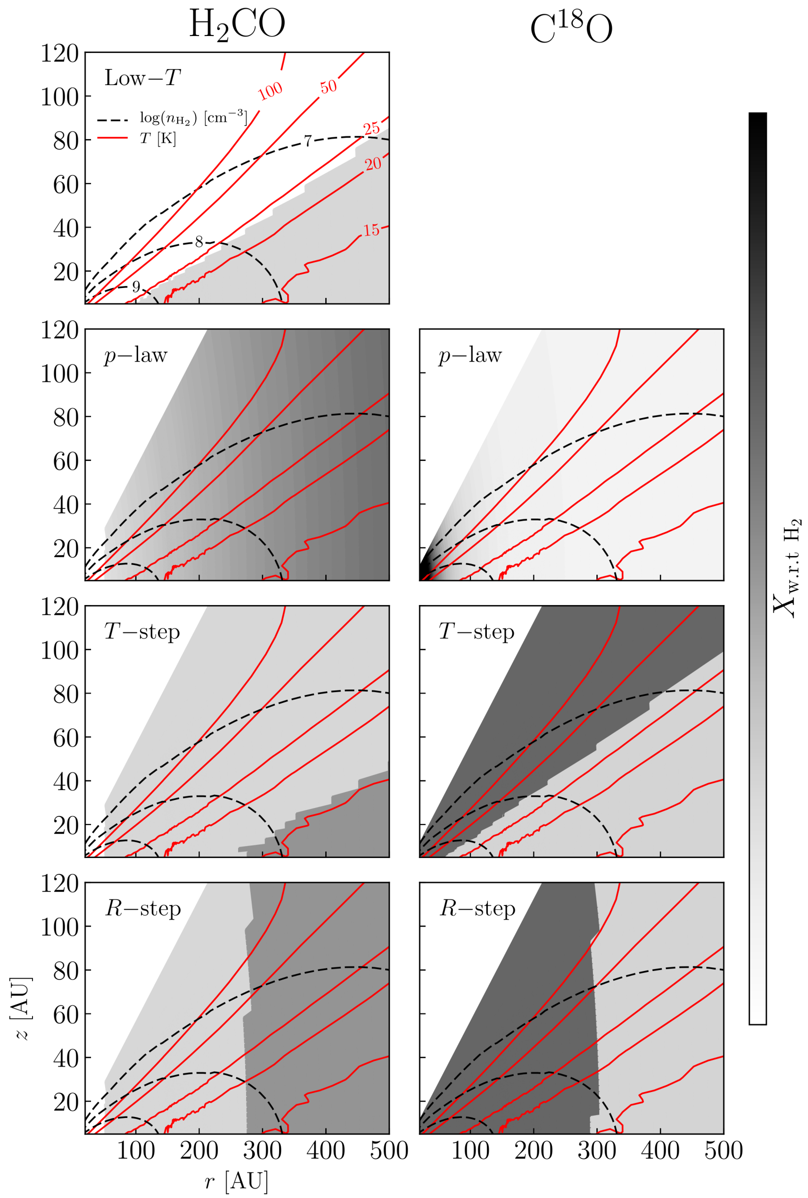

Figure 2.5: Toy model abundance scenarios for H_2CO (left) and $C^{18}O$ (right). X is the molecular abundance with respect to molecular hydrogen (grayscale). Red solid contours show the temperature structure of the gas in the disk. Black dashed contours show the density structure of the gas in the disk as the log of the molecular hydrogen number density n_{H_2}. The X distribution in each panel follows the best-fit normalized model (Table 2.2).

absorption by an optically thick dust continuum (see also Section 2.4.2). Beyond 50 AU, the optical depth radial profile for the LIME model continuum is found to be optically thin with $\tau < 0.6$, which ensures that features in the gas radial profile outside of 50 AU are not caused by dust opacity effects. The inner region (< 50 AU) cannot be properly modeled here due to the low resolution of the observations, which do not allow for proper description of any dust substructure. The modeling of Zhang et al. (2016) and new high-resolution observations by Isella et al. (2016) show significant substructure in the dust and a large increase in optical depth in the inner 50 AU. Such substructure is unlikely to be accurately described in our models, thus we ignore radii < 50 AU. The central hole is therefore treated as an H_2CO abundance inner radius in the modeling.

All H_2CO $3_{03}-2_{02}$ models have an inner radius set to $R_{\rm in} = 50$ AU. The value $R_{\rm in}$ was constrained for H_2CO by varying the inner radius of a constant abundance model to determine the best fit to the inner 150 AU of the radial intensity curve. Thereafter, $R_{\rm in}$ remains a fixed parameter in the models. $C^{18}O$ $2-1$ models have no such inner radius as the emission is centrally peaked.

Each LIME model was continuum-subtracted before running `vis_sample`. We first tested H_2CO $3_{03}-2_{02}$ and $C^{18}O$ $2-1$ models normalized to the total flux of the data in order to find the best-fit to the spatial distribution of each line, then we varied the abundance of the best-fit normalized model to match the absolute flux of the data. To determine the total flux, we took a vector average of visibilities with baselines < 30 m and integrated over all channels containing emission. The model was then scaled to match the total flux of the data. Goodness of fit for each model was determined by χ^2 minimization between the normalized visibilities of the model and the visibilities of the data. Initial reference abundances were chosen for the normalized models to ensure optically thin line emission. The H_2CO reference abundance was set to $X = 1.0 \times 10^{-12}$. $C^{18}O$ models used a reference abundance of $X = 1.0\times10^{-7}$. All normalized models remained optically thin with $\tau < 1$; there was no significant increase in the optical depth profile of the models for the parameter space explored here. The best-fit normalized model for each line was then used to vary the molecular abundances to find the best agreement between the absolute flux of the model and of the data using χ^2 minimization on the visibilities.

Low-temperature abundance model

The low-temperature model simulated H_2CO emission that is present due to grain-surface chemistry in regions below the expected CO freeze-out temperature and subsequent non-thermal desorption from icy grains. The models used a constant fractional abundance relative to H_2, constrained by a threshold temperature. Above the threshold temperature the H_2CO abundance was set to zero everywhere. Based on estimates of CO freeze-out temperatures from Qi et al. (2015), model threshold temperatures range from 14 – 50 K in steps of 2 K. Below the threshold temperature, gas-phase H_2CO is present. It is assumed that there is a mechanism to stimulate sufficient desorption of H_2CO from the icy grains, such as UV or X-ray photodesorption, or cosmic rays penetrating the disk midplane.

The best fit for the normalized low-temperature model for H_2CO has a threshold temperature of 24 ± 2 K, corresponding to a midplane radius of 65 ± 15 AU. Seen in Figure 2.6, the model radial intensity curve fails to recover the sharp decrease in emission between 100 – 200 AU and the turnover and secondary bump beyond ~200 AU. It is clear that a scenario in which H_2CO originates entirely beyond the

CO freeze-out temperature is not a good representation of the distribution seen in the observations. H_2CO must be present in other parts of the disk.

Power-law abundance model

In these models a varying abundance profile was considered for both H_2CO and $C^{18}O$, following a power-law distribution

$$X = X_{100\mathrm{AU}} \left(\frac{R}{100\ \mathrm{AU}} \right)^{p}, \tag{2.1}$$

where $X_{100\mathrm{AU}}$ is the abundance at 100 AU, R is the disk radius, and p is the power-law index. $C^{18}O$ is present throughout the disk. H_2CO has an inner radius $R_{\mathrm{in}} = 50$ AU, which was used in all subsequent H_2CO modeling.

The best-fit power-law H_2CO model has $p = 0.5$, with the abundance increasing with radius. The best-fit value found here is more gradual than the $p = 2$ positive power-law slope found by Qi et al. (2013), but both suggest that there is increased H_2CO production occurring in the outer disk. However, the $p = 0.5$ model does not provide the overall normalized best fit to the H_2CO $3_{03} - 2_{02}$ data presented here, as seen in Figure 2.6. The best-fit $C^{18}O$ model had $p = -2$, suggesting $C^{18}O$ is centrally peaked, but with a decreasing abundance in the outer regions of the disk. The model radial intensity curve underproduces emission beyond 200 AU and overproduces emission inside of 200 AU.

The simple power-law model does not capture the distribution seen in either H_2CO or $C^{18}O$. The failure of the H_2CO model to recover the shape of the radial intensity profile suggests that there are changes in the distribution of emission not captured in this model; we underestimate the contribution from grain surface formation. The failure of the $C^{18}O$ power-law model indicates that the effect of CO depletion is not properly taken into account. To reproduce the data at our resolution, the $C^{18}O$ abundance profile needs an abrupt change rather than the gradual change provided by the power-law model.

Temperature step-abundance model

Two-phase abundance models with a change-over temperature that distinguishes between the warm and cold regions of the disk were created to test H_2CO formed in the gas phase and H_2CO originating from icy grains, respectively. We assume that the change-over temperature represents the boundary below which H_2CO should form via hydrogenation of CO ice. The temperature step-abundance model for $C^{18}O$ reflects the freeze-out of CO, both radially and vertically, since there also is a vertical temperature gradient. While in these models we parameterize the $C^{18}O$ abundance with a change-over temperature, it is important to remember that this results in a radial column density profile that decreases gradually and extends well beyond the midplane CO snow line. Given our limited angular resolution, our data primarily samples the radial extent of the disk surface layer where $C^{18}O$ is present in the gas phase. Although we parameterize this with a temperature, we caution against the simplistic interpretation as an evaporation temperature, since its value depends on how well we know the vertical temperature structure and because our data do not resolve the location of the midplane CO snow line.

The change-over temperature T_{c} was tested in the range 12 – 36 K in steps of 2 K. The abundance ratio between the inner and outer regions varies to cover

Table 2.2: Best-fit normalized models

			H_2CO $3_{03}-2_{02}$		
Abundance Model	p	T_c [K]	$R_{in}{}^a$ [AU]	R_c [AU]	X_1/X_2
Low-temperature	–	24 ± 2	–	$65 \pm 15^{\dagger}$	–
Power-law	+0.5	–	50	–	–
Temperature step	–	16 ± 2	50	$230 \pm 60^{\dagger}$	0.5
Radial step	–	$15 \pm 1^{\dagger}$	50	270 ± 20	0.5

			$C^{18}O$ $2-1$		
Abundance Model	p	T_c [K]	$R_{in}{}^a$ [AU]	R_c [AU]	X_1/X_2
Power-law	−2	–	0.1	–	–
Temperature step	–	32 ± 2	0.1	$32 \pm 5^{\dagger}$	10
Radial step	–	$15 \pm 1^{\dagger}$	0.1	290 ± 20	10

Notes. χ^2 values are reduced by the number of points and free parameters in each model. [(a)] Fixed parameter. [(†)] Indicates the corresponding midplane value to the best-fit model parameter based on the density and temperature structure of the Mathews et al. (2013) physical model.

the range X_1/X_2 from 0.001 – 10 for H_2CO and 0.1 – 1000 for $C^{18}O$. The best-fit H_2CO model has a change-over temperature $T_c = 16 \pm 2$ K and an abundance ratio $X_1/X_2 = 0.5$, indicating a factor of 2 enhancement of H_2CO in the outer regions, but the model does not reproduce emission beyond 200 AU well (Figure 2.6). $C^{18}O$ is best fit by a change-over temperature $T_c = 32 \pm 2$ K with an order of magnitude reduction ($X_1/X_2 = 10$) in the outer regions. The temperature step-abundance model provides an improved normalized fit to the $C^{18}O$ observational data over models 1 & 2 and is consistent with CO depletion in the cold, outer disk.

As explained above, we do not claim that T_c is the evaporation temperature of CO, but rather that the value of T_c results in a reasonable match of the radial column density distribution of $C^{18}O$ given our adopted temperature structure and the limited angular resolution of the data. Even then, the radial profile of this model underproduces $C^{18}O$ within ~400 AU and overproduces $C^{18}O$ outside of ~400 AU.

While this model provides a better fit to the H_2CO emission than models 1 & 2, it fails to recover the shape of the turnover in the radial profile seen at ~200 AU. Instead, the temperature-based boundary causes a gradual change in the radial intensity due to the vertical temperature structure in the disk. To better fit the turnover seen in the radial profile, the H_2CO abundance profile must have an even more abrupt radial change. The improvement of the $C^{18}O$ normalized model fit over models 1 & 2 suggests CO freeze-out in the cold, outer parts of the disk.

Radial step-abundance model

In these models, molecular gas abundance is constant throughout the vertical extent of the disk with different abundance values in the inner and outer regions across the change-over radius. The outer abundance was varied such that X_1/X_2 spanned 0.1 – 10 for H_2CO and 0.1 – 1000 for $C^{18}O$. The change-over radius R_c ranged from 210 – 410 AU for H_2CO and 70 – 350 AU for $C^{18}O$ in steps of 20 AU.

The radial step-abundance model reproduces the turnover seen in the radial intensity of the H_2CO emission better than the first three models. Best-fit parame-

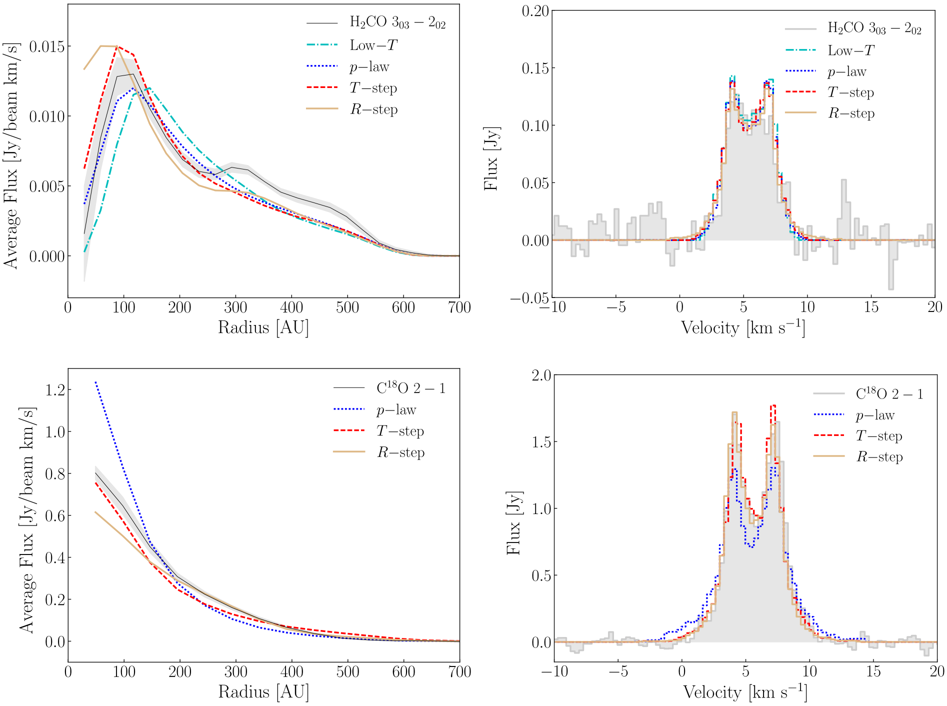

Figure 2.6: H_2CO $3_{03} - 2_{02}$ and $C^{18}O$ $2 - 1$ data are compared with best-fit normalized models for each scenario mentioned in Section 2.3.2. The low-temperature model (dot-dashed cyan), power-law model (dotted blue), temperature step-abundance model (dashed red), and radial step abundance model (solid gold) show the radial distribution and spectra. (Left) Radial intensity curves of the best-fit normalized models obtained from azimuthally-averaged elliptical annuli projected to $i = 44°$, P.A. $= 133°$. The shaded gray region represents 1σ error bars. H_2CO profiles are taken from integrated intensity maps after applying a Keplerian mask. (Right) Disk-integrated spectra of the best-fit normalized models obtained from a $5.6''$ radius circular aperture. H_2CO spectra are Hanning smoothed to 0.336 km $^{-1}$ channels. Parameters for each model can be found in Table 2.2.

ters are a change-over radius $R_c = 270 \pm 20$ AU and an abundance ratio $X_1/X_2 = 0.5$. The radial step-abundance model gives a radial intensity profile that has a steep drop between ~$100 - 200$ AU and a sharp turnover and plateau beyond ~200 AU. The best-fit $C^{18}O$ model has $R_c = 290 \pm 20$ AU and $X_1/X_2 = 10$, indicating a factor of 10 depletion of CO in the outer disk beyond the edge of the millimeter grains. This abundance scenario also provides a better normalized fit than models 1 & 2, and reproduces the distribution of $C^{18}O$ as well as model 3.

In this model the H_2CO bump in the radial intensity curve is well-captured due to the sharp change in abundance across the change-over radius. The radial step-abundance model provides the right amount of H_2CO production in the inner and outer regions that is likely a combination of gas-phase and grain-surface formation. Penetrating UV photons could photodesorb H_2CO that has formed via hydrogenation of CO ices beyond ~300 AU. There may also be more gas-phase

H_2CO formation beyond the edge of the millimeter continuum at ~270 ± 20 AU if UV photons can photodissociate CO in the upper layers and activate hydrocarbon chemistry for a more efficient CH_3 + O pathway.

The $C^{18}O$ radial step-abundance model provides an alternative scenario for outer disk CO depletion compared to model 3. If the micron-sized grains are depleted in the outer disk similar to the millimeter-sized grains, UV photons could photodissociate CO beyond ~300 AU. The fact that both a radial step at 290 ± 20 AU and a temperature step at 32 ± 2 K (32 ± 5 AU near the midplane) equally well fit the $C^{18}O$ data underlines our caution against interpreting the value of T_c as the evaporation temperature.

The consequences of each model scenario are further discussed in Section 2.4. The radial step-abundance case is chosen as the normalized model for estimating abundances in the following section.

H_2CO and $C^{18}O$ abundance

To estimate the absolute fractional abundances relative to H_2 in the inner and outer regions for H_2CO and $C^{18}O$, LIME was used to vary the abundances for the best-fit normalized scenario. Abundance ratios across the change-over boundaries, R_c, were kept the same as the normalized models: $X_1/X_2 = 0.5$ for the H_2CO radial step-abundance model and $X_1/X_2 = 10$ for the $C^{18}O$ radial step-abundance model.

H_2CO models had $R_c = 270$ AU and $X_1 = [1.0, 2.0, 3.0, 4.0, 5.0] \times 10^{-12}$. The best-fit fractional abundances were $X_1 = 4.0 \times 10^{-12}$ and $X_2 = 8.0 \times 10^{-12}$. $C^{18}O$ was found to have best-fit fractional abundances of $X_1 = 5.0 \times 10^{-8}$ and $X_2 = 5.0 \times 10^{-9}$ with $R_c = 290$ AU. Radial intensity profiles for these best-fit models are shown in Figure 2.7. Error estimates based on 3σ error bars of the radial intensity profiles put these abundances in the range $X_1 = 2 - 5 \times 10^{-12}$, $X_2 = 5 - 10 \times 10^{-12}$ for H_2CO and $X_1 = 4 - 12 \times 10^{-8}$ and $X_2 = 4 - 12 \times 10^{-9}$ for $C^{18}O$.

Integrated intensity maps of the best-fit models were compared to integrated intensity maps of observed H_2CO $3_{03} - 2_{02}$ and $C^{18}O$ 2 − 1 data. Figure 2.8 shows the images and the residuals. The model and the data are in good agreement for both lines, though the best-fit $C^{18}O$ has residual emission above the 3σ in the central part of the disk. The inner 50 AU are likely not well-described by our models, as noted in previous sections.

The modeling efforts presented here show that the H_2CO abundance is not uniform throughout the disk. Beyond ~300 AU there is an increase in the H_2CO abundance by a factor of two, as seen in the radial step-abundance scenario. The H_2CO abundance of $X_1 = 2 - 5 \times 10^{-12}$, $X_2 = 4 - 10 \times 10^{-12}$ is consistent to within a factor of a few with the global abundance value of 1×10^{-11} found in Qi et al. (2013). The increased sensitivity and resolution of our data allow us to better constrain the H_2CO abundance in HD 163296 than previous studies. $C^{18}O$ is well described by a model with a depletion of CO at 290 ± 20 AU and a depletion factor of 10. The $C^{18}O$ inner abundance of $4 - 12 \times 10^{-8}$ corresponds to a ^{12}CO abundance of $2.2 - 6.6 \times 10^{-5}$, assuming $^{12}CO/C^{18}O = 550$. Qi et al. (2015) report similar numbers for the CO abundance, but their depletion factor is lower by half and occurs at a radius of 90 AU. We found that a radius of 90 AU and depletion factor of 5 for our radial step-abundance models significantly overproduces the amount of $C^{18}O$ beyond 300 AU due to our different treatment of the vertical structure.

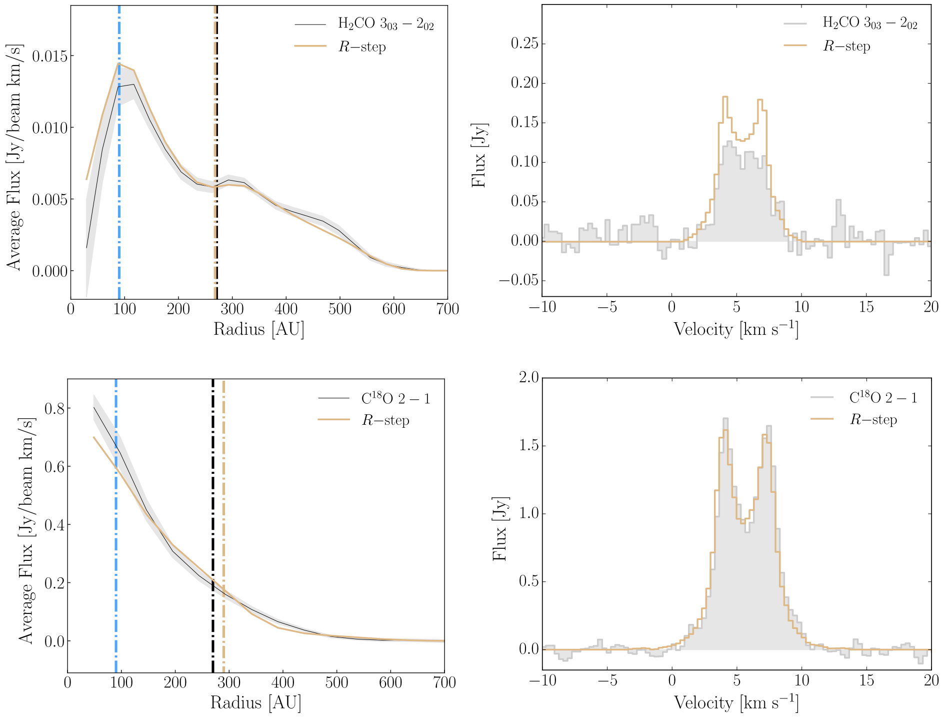

Figure 2.7: Radial intensity and spectra of observed H_2CO $3_{03}-2_{02}$ and $C^{18}O$ $2-1$ versus the best-fit models. (Left) Radial intensity curves from azimuthally-averaged elliptical annuli projected to i = 44°, P.A. = 133°. HD 163296 data is shown in black, best fits for H_2CO and $C^{18}O$ are in gold. The vertical dashed lines indicate the CO snow line (blue dash) from Qi et al. (2015), the 5σ outer radius of the 1.3 mm grains (black dash), and the change-over radii, R_c, for the best-fit radial step-abundance models (gold dash). H_2CO profiles are taken from integrated intensity maps after applying a Keplerian mask. (Right) Disk-integrated spectra. HD 163296 data is shown in filled gray. H_2CO spectra are Hanning smoothed to 0.336 km $^{-1}$ channels.

2.3.3 H_2CO excitation temperature

Line flux ratios H_2CO $3_{03}-2_{02}$/H_2CO $3_{22}-2_{21}$ and H_2CO $3_{03}-2_{02}$/H_2CO $3_{21}-2_{20}$ were used to constrain H_2CO excitation temperatures. Table 2.1 provides the line fluxes. We calculated the rotational temperature of the lines, assuming a single rotational temperature, following Qi et al. (2013)

$$T_{\mathrm{rot}} = \frac{E_1 - E_0}{\ln((\nu_1 S\mu_1^2 \int T_0 d\nu)/(\nu_0 S\mu_0^2 \int T_1 d\nu))}, \tag{2.2}$$

with the following definitions: E_0 and E_1 are the upper energy levels for the low and high H_2CO transitions, respectively; ν is the line frequency; $S\mu^2$ is the temperature-independent transition strength and dipole moment; and $\int T d\nu$ is the integrated line intensity. Line intensity in the Rayleigh-Jeans limit was calculated from the line flux with the following expression

$$T_{\mathrm{B}} = \frac{c^2}{2k\nu^2}\frac{F_\nu}{(a \times b)}\left(3600\frac{\mathrm{arcsec}}{\mathrm{deg}}\right)^2\left(\frac{180}{\pi}\frac{\mathrm{deg}}{\mathrm{sr}}\right)^2\left(\frac{1}{10^{26}\ \mathrm{Jy}}\right), \tag{2.3}$$

where F_ν is the line flux in Jy, T_{B} is the line intensity in Kelvins, ν is the line frequency in Hz, k is the Boltzmann constant, c is the speed of light, and a and b are the semi-major and semi-minor axes of the beam in arcsec.

The emitting regions of all three lines are expected to be similar, especially if the H_2CO reservoir is primarily locked up in icy grains. Local thermodynamic equilibrium (LTE) is a fair assumption for calculating rotational temperatures, as the gas density near the midplane is high in disks ($\sim10^9$ cm^{-3}; Walsh et al. 2014) and the critical densities of the observed transitions at 20 K are $1-3\times10^6$ (Wiesenfeld & Faure 2013). In the case of LTE, the derived rotational temperature is equal to the kinetic temperature of the gas. The values E and $S\mu^2$ are taken from the Cologne Database for Molecular Spectroscopy (CDMS; Müller et al. 2005), as reported on the Splatalogue[3] database.

The rotational temperatures of the H_2CO transitions are calculated based on the line flux ratios of H_2CO $3_{22}-2_{21}/3_{03}-2_{02}$ and H_2CO $3_{21}-2_{20}/3_{03}-2_{02}$. The matched filter technique only gives lower limits to the H_2CO $3_{22}-2_{21}$ and H_2CO $3_{21}-2_{20}$ line flux, thus lower limits on the rotational temperature are > 20.5 K and > 19.5 K, respectively, while upper limits for the weak lines are < 169 K and < 326 K based on the integrated flux upper limits listed in Table 2.1. These lower limits indicate that these transitions can be excited in regions of the disk near the CO freeze-out temperature, supporting the hypothesis that some of the H_2CO emission may originate from the cold molecular reservoir. There could also be H_2CO emitting at a higher temperature that is not well described by our template filter.

2.4 Discussion

In this work, the radial step-abundance model suggests an enhancement in H_2CO abundance by a factor of a few beyond 270 AU. It is difficult to distinguish which formation route is responsible for this modest increase in abundance.

Aikawa & Herbst (1999) estimated the radial column density and abundance profile of H_2CO formed in the gas phase in a T Tauri minimum mass solar nebula (MMSN) disk model extrapolated out to $R_{\mathrm{out}} = 700$ AU, with an order of magnitude lower mass. They did not consider other mechanisms for producing gas-phase H_2CO, such as desorption from icy grains. They excluded an activation energy barrier for the CH_3 + O reaction. The initial abundance of atomic oxygen may affect the inferred H_2CO abundances. Their model has a mostly flat radial distribution, but is consistent with an enhancement of H_2CO abundance by a factor of a few up to one order of magnitude in the outer regions beyond ~300 AU.

Walsh et al. (2014) created a series of increasingly complex T Tauri disk chemical evolution models that include grain-surface formation to estimate abundances of complex organic molecules (COMs) throughout the disk. Beginning with freeze-out and thermal desorption only, they also include non-thermal desorption, grain-surface chemistry, radiative reprocessing of ices, and reactive desorption in their full disk model. The vertical distribution of H_2CO included a large gas-phase

---

[3] `http://www.cv.nrao.edu/php/splat/`

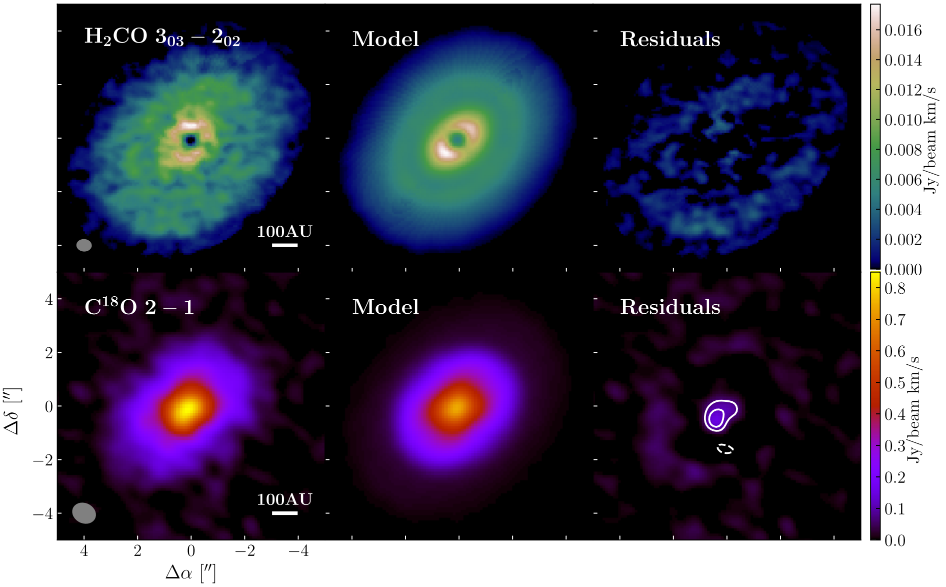

Figure 2.8: Data, model, and residual integrated intensity maps. H_2CO $3_{03} - 2_{02}$ data and model maps are created after applying a Keplerian mask to the image cube (see Section 2.3.1). (Left) H_2CO $3_{03} - 2_{02}$ data integrated intensity map from 0.76 – 10.84 km s^{-1} and $C^{18}O$ 2 – 1 data integrated intensity map from −0.88 – 12.48 km s^{-1}. Synthesized beam and AU scale are shown in the lower corners. (Center) Integrated intensity map of best-fit model taken over the same velocity channels as the left figure. (Right) Residual image with contours at 3σ intervals. Dashed contours are negative, solid contours are positive.

reservoir above the midplane reaching peak fractional abundances relative to H_2 of $\sim10^{-8}$ and an ice reservoir beyond 10 AU with peak fractional abundances of $\sim10^{-4}$. Beyond 50 AU, the radial column density of H_2CO in the Walsh et al. (2014) comprehensive disk model shows an increase by a factor of a few.

From these two examples it is clear that a modest outer disk enhancement of H_2CO cannot immediately reveal whether gas-phase or grain-surface production is the dominant formation route. Full chemical modeling of H_2CO production is required. In this section we discuss possible explanations for the H_2CO enhancement in the outer disk around HD 163296, its relation to the CO snow line and the millimeter continuum, and the implications for H_2CO formation.

2.4.1 H_2CO and the CO snow line

Previous SMA observations of H_2CO in the disk around HD 163296 showed ring-like formaldehyde emission outside the expected CO snow line (Qi et al. 2013). These authors suggested that a scenario with only grain-surface formation could be responsible for the observed distribution and the apparent lack of centrally peaked emission. The lower spatial resolution and S/N per channel of the SMA observations would preferentially place the H_2CO emitting region farther away from the central star since the emission at smaller radii is spread out over more velocity channels due to the shear in the Keplerian disk, thus resulting in a false ring-like structure. The ALMA results presented here show that H_2CO is not present in a ring, but rather emission is seen throughout most of the gaseous extent of the disk with a central depression in the inner ~50 AU.

Qi et al. (2015) presented new constraints on the CO snow line in HD 163296 based on observations of $C^{18}O$ and N_2H^+. N_2H^+ is readily destroyed by gas-phase CO, thus it is expected to be a reliable tracer of CO depletion. By refitting the location and degree of CO depletion, they found that a factor of 5 depletion in column density at 85 – 90 AU improved their best-fit models to the visibility data. They interpret this radius as the location of the CO snow line, corresponding to a CO freeze-out temperature of 25 K. The coincident CO depletion and N_2H^+ emission inner radius supports the claim that N_2H^+ traces regions of CO freeze-out. Recent results by van't Hoff et al. (2017) show that the N_2H^+ emission can peak from ~5 – 50 AU beyond the location of the CO snow line and that careful chemical modeling is necessary to properly interpret the location of CO freeze-out from N_2H^+ observations.

The data presented here show that H_2CO extends beyond the Qi et al. (2015) CO freeze-out radius, but with a peak at ~90 AU that coincides with the CO snow line. Öberg et al. (2017) presented H_2CO observations in the disk around TW Hya and find that grain-surface formation of H_2CO begins at temperatures where CO starts to spend even a short time on the grains, meaning that H_2CO can be produced – and the emission can peak – just inside of the CO snow line. Considering our ~50 AU resolution, the peak seen at ~90 AU may be the beginning of grain-surface formation of H_2CO, likely with some contribution from the warmer, gas-phase formation pathway at the innermost radii.

Recent analysis of ALMA Cycle 0 data for H_2CO in DM Tau explored the relative contributions of gas-phase and grain-surface formation pathways (Loomis et al. 2015). Their chemical models required both formation via gas-phase reactions and hydrogenation of CO ice in the outer regions of the disk to reproduce the centrally peaked and outer disk emission. Our simple parameterized models do not include chemical processing, but the presence of H_2CO at radii beyond the expected CO snow line at 90 AU and where millimeter grains are present indicates that grain-surface formation is a partial contributor to the H_2CO reservoir in the disk around HD 163296. Unlike the DM Tau results, our data also suggests that there is an intrinsic link between the edge of the millimeter continuum and the production of H_2CO in HD 163296.

2.4.2 H_2CO inner hole

A sharp drop in H_2CO emission within 50 AU is evident in the integrated intensity map (see Figure 2.8) and by the best-fit $R_{\rm in}$ of the H_2CO models. Optically thick dust may be responsible for the observed depletion, rather than a drop in H_2CO abundance. Photons emitted by H_2CO in the midplane of the disk can be absorbed by optically thick dust in the upper layers, causing the inner hole – after continuum subtraction – that is seen in the H_2CO integrated intensity map.

Zhang et al. (2016) model the HD 163296 continuum visibilities with a parameterized radial intensity distribution modulated by multiple sine waves. Their best-fit model shows that there is an increase in millimeter-wavelength intensity of ~60% in the innermost 50 AU of the disk, causing the millimeter continuum to become optically thick in this region. Zhang et al. (2016) produced simulated model images with a 0.035″ beam, which clearly shows the strong central continuum emission. At the spatial resolution presented in this work, ~0.4″ – 0.5″, the millimeter continuum appears smooth. Isella et al. (2016) presented 0.2″ observations of the 1.3 millimeter continuum and three CO isotopologs. They show central depressions in the ^{13}CO and C^{18}O maps, and concluded that both the CO and the dust become optically thick within 50 AU, leading to large uncertainties in their surface densities.

Öberg et al. (2017) observe a similar central H_2CO depression well within the CO snow line in the disk around TW Hya. While they do not rule out dust opacity effects completely, they prefer to explain it as a real drop in abundance, as the central depression is not seen in higher frequency lines of H_2CO or CO isotopologs. Observations of additional, high frequency H_2CO lines in the HD 163296 disk would be needed to test this scenario. The ^{13}CO and C^{18}O central holes seen by Isella et al. (2016) at high resolution already suggest dust opacity as an explanation for the central H_2CO depression in this disk.

2.4.3 H_2CO and the millimeter continuum edge

The millimeter grains in HD 163296 have decoupled from the gas and drifted radially inward. Millimeter emission in the outer disk is truncated at ~270 AU while the bulk of the gas, based on ^{12}CO observations, extends to ~550 AU (de Gregorio-Monsalvo et al. 2013). The outer edge of millimeter emission corresponds to the 270 ± 20 AU change-over radius for H_2CO enhancement found by the best-fit radial step-abundance model. Grain growth and radial drift in the outer regions of the disk can result in a decrease of small, micron-sized grains beyond ~270 AU. With less shielding from external and protostellar radiation, penetrating UV photons in the outer regions may cause an increase in the H_2CO photodesorption directly off icy grain surfaces (Öberg et al. 2009; Huang et al. 2016). Increased UV radiation in a dust-depleted outer disk could also lead to CO photodissociation in the upper layers, opening a more efficient gas-phase route for H_2CO where hydrocarbon radicals and atomic oxygen are readily available.

Dust evolution models for HD 163296 by Facchini et al. (2017) show that for a low-turbulence environment, a temperature inversion can occur around 300 AU, causing a second CO desorption front in the outer disk (also suggested qualitatively by Cleeves 2016). In that case, an increase of both C^{18}O and H_2CO abundance in the outer disk would be expected, but our models found a CO depletion. It may be that there are competing effects occurring in the outer disk for CO. A temperature inversion and/or UV photodesorption beyond 300 AU can cause the release of grain-surface H_2CO and a fraction of CO ice back into the gas phase near the midplane, but CO photodissociation in the upper layers may dominate the C^{18}O surface density profile so that we ultimately see an outer disk depletion in C^{18}O, and an increase in H_2CO production.

2.5 Conclusions

In this work, multiple detections with ALMA of H_2CO in the protoplanetary disk around HD 163296 are presented: one robust detection via imaging, H_2CO $3_{03} - 2_{02}$, and two weaker detections via matched filter analysis, H_2CO $3_{22} - 2_{21}$ and H_2CO $3_{21} - 2_{20}$. The distribution of H_2CO relative to C^{18}O and the millimeter continuum was analyzed using various model abundance profiles to test possible H_2CO formation scenarios. The conclusions of this work are as follows:

- H_2CO in HD 163296 is observed out to ~550 AU, equal to the full radial extent of the gas disk as observed with CO. It does not have a ring-like morphology.
- The kinetic temperature of the observed H_2CO gas has a lower limit of > 20 K, thus emission from these lines can originate from the cold molecular reservoir near the disk midplane.
- The best-fit radial step-abundance model to the H_2CO $3_{03} - 2_{02}$ data suggests that H_2CO has an inner radius $R_{\rm in} = 50$ AU, an outer disk abundance a factor of two higher than the inner disk ($X_1/X_2 = 0.5$), and a change-over radius of $R_{\rm c} = 270 \pm 20$ AU. There is a mechanism causing increased H_2CO production in the outer disk beyond the millimeter grains. One explanation is desorption of H_2CO from icy grains by thermal desorption due to a temperature inversion or by UV photodesorption where CO is frozen out. Alternatively, photodissociation of CO in the outer disk may increase the efficiency of the CH_3 + O gas-phase route to form H_2CO.
- Based on the $C^{18}O$ $2-1$ models presented in this work, two scenarios reproduce the the data well: step-abundance models with abundance boundaries based on temperature and radius, respectively. The best-fit models both indicate depleted CO in the outer disk based on the recovery of the $C^{18}O$ $2-1$ surface density profile. Both models have a CO depletion factor of 10 in the outer disk. The depletion is likely a combination of CO freeze-out in the disk midplane and photodissociation of CO in the disk upper layers due to penetrating UV radiation.
- The best-fit abundance for the $C^{18}O$ radial step-abundance model was $X_1 = 4 - 12 \times 10^{-8}$, $X_2 = 4 - 12 \times 10^{-9}$. The best-fit abundance for the H_2CO radial step-abundance model was $X_1 = 2 - 5 \times 10^{-12}$, $X_2 = 4 - 10 \times 10^{-12}$.

Further observations of HD 163296 can unambiguously determine the dominant formation pathway of H_2CO in the disk. Constraining the ortho-to-para ratio of the two H_2CO isomers can distinguish between grain-surface formation and gas-phase formation (Guzmán et al. 2011). The H_2CO OPR is expected to be less than three for grain-surface formation (Dulieu 2011; Fillion et al. 2012). Observations of co-spatial H_2CO and CH_3OH would also constrain the contributions of gas- and solid-phase H_2CO, as CH_3OH forms similarly via hydrogenation of CO ices and has no known gas-phase formation route.

Acknowledgements

The authors thank the referee for insightful comments and constructive suggestions. M.T.C. thanks S. Facchini and G.S. Mathews for useful discussion on dust evolution and CO chemistry in HD 163296. The authors acknowledge support by Allegro, the European ALMA Regional Center node in The Netherlands, and expert advice from Luke Maud in particular. This paper makes use of the following ALMA data: ADS/JAO.ALMA# 2013.1.01268.S and 2011.1.00010.SV. ALMA is a partnership of ESO (representing its member states), NSF (USA) and NINS

(Japan), together with NRC (Canada), NSC and ASIAA (Taiwan), and KASI (Republic of Korea), in cooperation with the Republic of Chile. The Joint ALMA Observatory is operated by ESO, AUI/NRAO and NAOJ.

Appendix A: Channel Maps

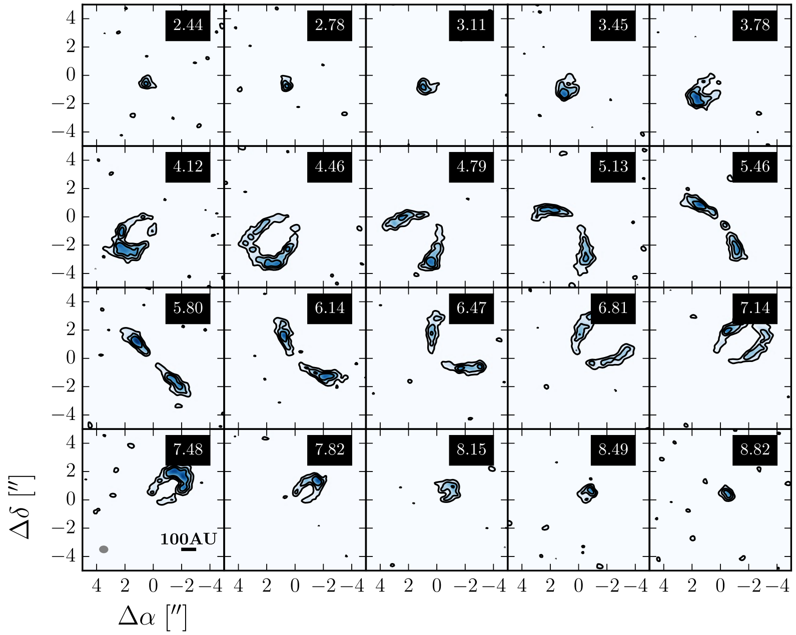

Figure 2.9: H_2CO $3_{03}-2_{02}$ data channel maps, Hanning smoothed to 0.336 km s^{-1} channels. Black contours mark 1.5×10^{-3} (1σ) $\times$ [3, 6, 9] Jy beam^{-1}. Synthesized beam and AU scale are shown in the lower left panel.

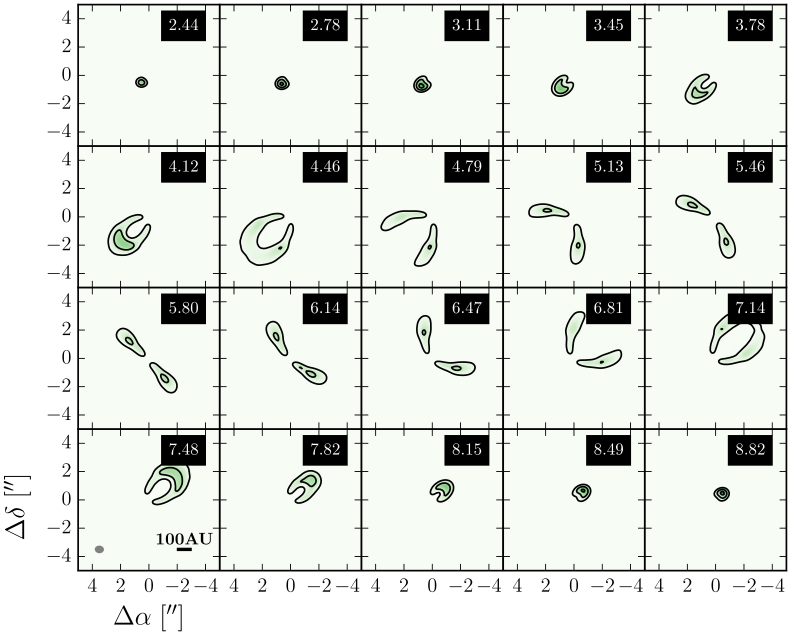

Figure 2.10: H_2CO $3_{03}-2_{02}$ best-fit model channel maps, Hanning smoothed to 0.336 km s^{-1} channels. Black contours mark 1.5×10^{-3} (1σ) × [3, 6, 9] Jy $beam^{-1}$. Synthesized beam and AU scale are shown in the lower left panel.

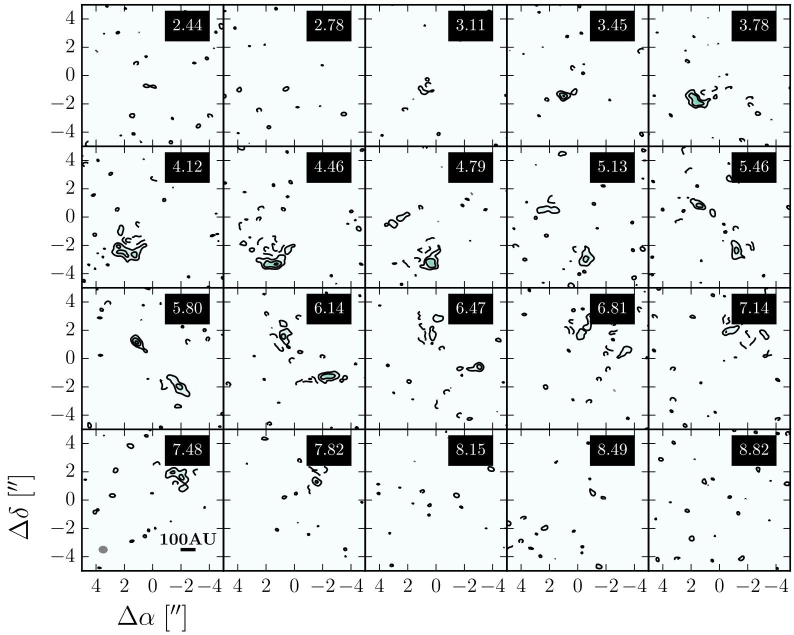

Figure 2.11: H_2CO $3_{03} - 2_{02}$ residual (data – model) channel maps, Hanning smoothed to 0.336 km s^{-1} channels. Black contours mark 1.5×10^{-3} (1σ) × [3, 6, 9] Jy beam^{-1}. Dashed contours are negative at the same intervals. Synthesized beam and AU scale are shown in the lower left panel.

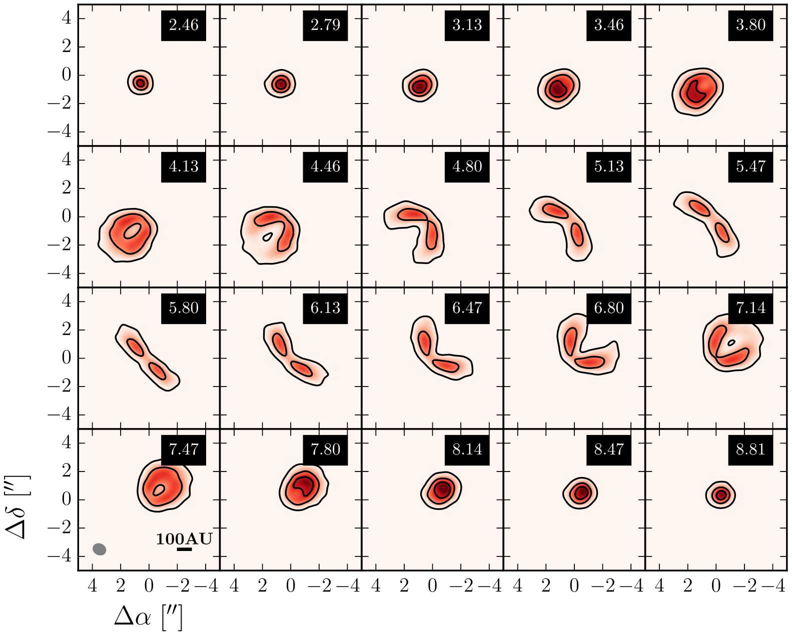

Figure 2.12: $C^{18}O$ $2-1$ data channel maps. Black contours mark 4.2×10^{-3} (1σ) × [5, 25, 45] Jy beam^{-1}. Synthesized beam and AU scale are shown in the lower left panel.

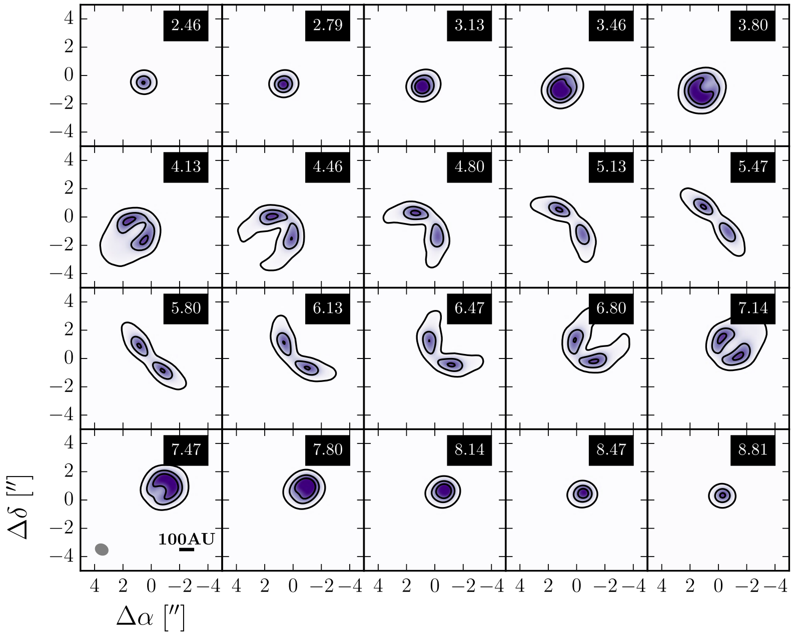

Figure 2.13: C^{18}O 2 − 1 best-fit model channel maps. Black contours mark 4.2×10^{-3} (1σ) × [5, 25, 45] Jy beam^{-1}. Synthesized beam and AU scale are shown in the lower left panel.

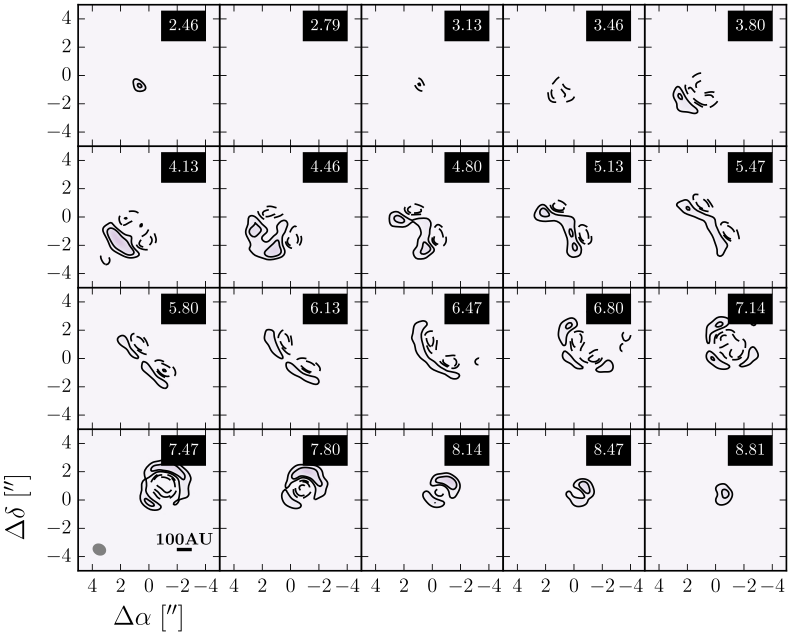

Figure 2.14: $C^{18}O$ 2 – 1 residual (data – model) channel maps. Black contours mark 4.2×10^{-3} (1σ) × [5, 10, 20] Jy beam^{-1}. Dashed contours are negative at the same intervals. Synthesized beam and AU scale are shown in the lower left panel.

References

Aikawa, Y. & Herbst, E. 1999, A&A, 351, 233

Aikawa, Y., Momose, M., Thi, W.-F., et al. 2003, PASJ, 55, 11

Andrews, S. M. & Williams, J. P. 2005, ApJ, 631, 1134

Atkinson, R., Baulch, D. L., Cox, R. A., et al. 2006, Atmospheric Chemistry & Physics, 6, 3625

Brinch, C. & Hogerheijde, M. R. 2010, A&A, 523, A25

Cleeves, L. I. 2016, ApJ, 816, L21

Cuppen, H. M., van Dishoeck, E. F., Herbst, E., & Tielens, A. G. G. M. 2009, A&A, 508, 275

D'Alessio, P., Calvet, N., Hartmann, L., Franco-Hernández, R., & Servín, H. 2006, ApJ, 638, 314

de Gregorio-Monsalvo, I., Ménard, F., Dent, W., et al. 2013, A&A, 557, A133

Dulieu, F. 2011, in IAU Symposium, Vol. 280, The Molecular Universe, ed. J. Cernicharo & R. Bachiller, 405–415

Dullemond, C. P. & Dominik, C. 2005, A&A, 434, 971

Facchini, S., Birnstiel, T., Bruderer, S., & van Dishoeck, E. F. 2017, A&A, 605, A16

Fillion, J.-H., Bertin, M., Lekic, A., et al. 2012, in EAS Publications Series, Vol. 58, EAS Publications Series, ed. C. Stehlé, C. Joblin, & L. d'Hendecourt, 307–314

Fockenberg, C. & Preses, J. M. 2002, Journal of Physical Chemistry A, 106, 2924

Guzmán, V., Pety, J., Goicoechea, J. R., Gerin, M., & Roueff, E. 2011, A&A, 534, A49

Herbst, E. & van Dishoeck, E. F. 2009, ARA&A, 47, 427

Huang, J., Öberg, K. I., & Andrews, S. M. 2016, ApJ, 823, L18

Isella, A., Guidi, G., Testi, L., et al. 2016, Phys. Rev. Lett., 117, 251101

Isella, A., Testi, L., Natta, A., et al. 2007, A&A, 469, 213

Loomis, R. A., Cleeves, L. I., Öberg, K. I., Guzman, V. V., & Andrews, S. M. 2015, ApJ, 809, L25

Mathews, G. S., Klaassen, P. D., Juhász, A., et al. 2013, A&A, 557, A132

McMullin, J. P., Waters, B., Schiebel, D., Young, W., & Golap, K. 2007, in Astronomical Society of the Pacific Conference Series, Vol. 376, Astronomical Data Analysis Software and Systems XVI, ed. R. A. Shaw, F. Hill, & D. J. Bell, 127

Müller, H. S. P., Schlöder, F., Stutzki, J., & Winnewisser, G. 2005, Journal of Molecular Structure, 742, 215

Mumma, M. J. & Charnley, S. B. 2011, ARA&A, 49, 471

Öberg, K. I., Bottinelli, S., Jørgensen, J. K., & van Dishoeck, E. F. 2010a, ApJ, 716, 825

Öberg, K. I., Garrod, R. T., van Dishoeck, E. F., & Linnartz, H. 2009, A&A, 504, 891

Öberg, K. I., Guzmán, V. V., Merchantz, C. J., et al. 2017, ApJ, 839, 43

Öberg, K. I., Qi, C., Fogel, J. K. J., et al. 2010b, ApJ, 720, 480

Qi, C., D'Alessio, P., Öberg, K. I., et al. 2011, ApJ, 740, 84

Qi, C., Öberg, K. I., Andrews, S. M., et al. 2015, ApJ, 813, 128

Qi, C., Öberg, K. I., & Wilner, D. J. 2013, ApJ, 765, 34

Rosenfeld, K. A., Andrews, S. M., Hughes, A. M., Wilner, D. J., & Qi, C. 2013, ApJ, 774, 16

Salinas, V. N., Hogerheijde, M. R., Mathews, G. S., et al. 2017, A&A, 606, A125
Sault, R. J., Teuben, P. J., & Wright, M. C. H. 1995, in Astronomical Society of the Pacific Conference Series, Vol. 77, Astronomical Data Analysis Software and Systems IV, ed. R. A. Shaw, H. E. Payne, & J. J. E. Hayes, 433
Schoeier, F. L., van der Tak, F. F. S., van Dishoeck, E. F., & Black, J. H. 2005, VizieR Online Data Catalog, 343
van den Ancker, M. E., de Winter, D., & Tjin A Djie, H. R. E. 1998, A&A, 330, 145
van der Marel, N., van Dishoeck, E. F., Bruderer, S., & van Kempen, T. A. 2014, A&A, 563, A113
van Dishoeck, E. F. & Blake, G. A. 1998, ARA&A, 36, 317
van't Hoff, M. L. R., Walsh, C., Kama, M., Facchini, S., & van Dishoeck, E. F. 2017, A&A, 599, A101
Walsh, C., Millar, T. J., Nomura, H., et al. 2014, A&A, 563, A33
Watanabe, N., Shiraki, T., & Kouchi, A. 2003, ApJ, 588, L121
Wiesenfeld, L. & Faure, A. 2013, MNRAS, 432, 2573
Yen, H.-W., Koch, P. M., Liu, H. B., et al. 2016, ArXiv e-prints
Zhang, K., Bergin, E. A., Blake, G. A., et al. 2016, ApJ, 818, L16

CHAPTER 3

ALMA UNVEILS RINGS AND GAPS IN THE PROTOPLANETARY SYSTEM HD 169142: SIGNATURES OF TWO GIANT PROTOPLANETS

D. FEDELE, M. CARNEY, M. R. HOGERHEIJDE, C. WALSH, A. MIOTELLO,
P. KLAASSEN, S. BRUDERER, T. HENNING, AND E. F. VAN DISHOECK.

ASTRONOMY & ASTROPHYSICS
VOLUME 600, ARTICLE A72, 14 PP. (2017)

Abstract

The protoplanetary system HD 169142 is one of the few cases where a potential candidate protoplanet has recently been detected by direct imaging in the near-infrared. To study the interaction between the protoplanet and the disk itself, observations of the gas and dust surface density structure are needed. This paper reports new ALMA observations of the dust continuum at 1.3 mm, ^{12}CO, ^{13}CO, and C^{18}O $J = 2-1$ emission from the system HD 169142 (which is observed almost face-on) at an angular resolution of ~$0\farcs3 \times 0\farcs2$ (~35×20 au). The dust continuum emission reveals a double-ring structure with an inner ring between $0\farcs17 - 0\farcs28$ (~$20 - 35$ au) and an outer ring between $0\farcs48 - 0\farcs64$ (~$56 - 83$ au). The size and position of the inner ring is in good agreement with previous polarimetric observations in the near-infrared and is consistent with dust trapping by a massive planet. No dust emission is detected inside the inner dust cavity ($R \lesssim 20$ au) or within the dust gap (~$35 - 56$ au) down to the noise level. In contrast, the channel maps of the $J = 2 - 1$ line of the three CO isotopologs reveal gas inside the dust cavity and dust gap. The gaseous disk is also much larger than the compact dust emission; it extends to ~$1\farcs5$ (~180 au) in radius. This difference and the sharp drop of the continuum emission at large radii point to radial drift of large dust grains ($> \mu$m size). Using the thermo-chemical disk code DALI, we modeled the continuum and the CO isotopolog emission to quantitatively measure the gas and dust surface densities. The resulting gas surface density is reduced by a factor of ~$30 - 40$ inward of the dust gap. The gas and dust distribution indicate that two giant planets shape the disk structure through dynamical clearing (dust cavity and gap) and dust trapping (double-ring dust distribution).

3.1 Introduction

Observations of the cold gas and dust reservoirs of protoplanetary disks are powerful tools for investigating the early phase of planet formation. In particular, addressing the radial distribution of gas and dust in the disk interior has the potential to unveil the initial conditions for the formation of gas giant planets. In contrast with optical and near-infrared scattered light data or infrared spectroscopy, submillimeter observations probe the bulk of the gas and dust mass in the disk. Recent observations in the submillimeter regime with the Atacama Large Millimeter/submillimeter Array (ALMA) brought to light evidence of discontinuous radial (gaps and cavities) and azimuthal (traps and vortices) dust distributions (e.g., Casassus et al. 2012; van der Marel et al. 2013; ALMA Partnership et al. 2015; Walsh et al. 2014; Andrews et al. 2016; Isella et al. 2016) and cold gas cavities that are smaller than the dust cavities (van der Marel et al. 2016).

Different theories have been proposed to explain the formation of dust gaps and rings, including dynamical interaction with one or more giant planets that carve out the dust (e.g., Papaloizou & Lin 1984), magneto-rotational instability that creates dead-zones (Flock et al. 2015), dust grain growth corresponding to condensation fronts (Zhang et al. 2015), fusing of dust grains at temperatures below the sublimation point (dust sintering, Okuzumi et al. 2016), and photoevaporation (Ercolano et al. 2017).

Submillimeter interferometric observations of both gas and dust may help to unveil the evolutionary status of protoplanetary systems and to distinguish the physical origin of dust cavities and dust gaps in disks. A particularly powerful test is to perform ALMA observations of disks for which optical and near-infrared data have previously suggested embedded planets.

3.2 HD 169142

HD 169142 is a young 6^{+6}_{-3} Myr and isolated (Grady et al. 2007) Herbig Ae/Be star (The et al. 1994) with $M_\star = 1.65\ M_\odot$ (Blondel & Djie 2006), spectral type A5, and $T_{\rm eff} = 8400$ K (Dunkin et al. 1997). The most recent measurement of the parallax is $\varpi = 8.53 \pm 0.29$ mas (Gaia Collaboration et al. 2016), which translates into a distance $d = 117 \pm 4$ pc. Previous estimates by de Zeeuw et al. (1999) instead were $d = 145$ pc. In the remaining paper we use the newest distance estimate and adjust all the relevant parameters. The stellar luminosity adopted in this paper is $L_\star = 10\ L_\odot$ based on the new distance estimate and on the optical V-magnitude and extinction (V = 8.15 mag, $A_{\rm V} = 0.43$ mag, e.g., Malfait et al. 1998). Submillimeter observations of the 1.3 mm dust continuum and CO $J = 2-1$ with the Submillimeter Array (SMA) measured a disk inclination of 13° and a position angle of 5° (Raman et al. 2006; Panić et al. 2008). Based on observations of multiple CO isotopologs with the SMA, Panić et al. (2008) derived a total gas mass of $0.6 - 3.0 \times 10^{-2}\ M_\odot$ in good agreement with the estimate by Pinte et al. (2010) of $\sim 10^{-2}\ M_\odot$ based on the *Herschel*/PACS detection of [OI] 63 μm (Meeus et al. 2010; Fedele et al. 2013). The spectral energy distribution (SED) suggests a discontinuous radial distribution of the dust (Malfait et al. 1998). This is confirmed by direct imaging observations of the thermal emission at mid-infrared wavelengths (Honda et al. 2012) as well as by $H-$band scattered light emission (Fukagawa et al. 2010; Quanz et al. 2013; Momose et al. 2015; Wagner et al. 2015). In particular, the $H-$band polarimetric image shows a ring-like dust distribution at a radius of $\sim 0\farcs17$ (20 au) from the star. The dust ring seen in scattered light is also detected in the 7 mm continuum (Osorio et al. 2014).

Biller et al. (2014) and Reggiani et al. (2014) detected a point-like emission at $\sim 0\farcs11 - 0\farcs16$ (13 – 18 au) in $L'-$band coronographic and polarimetric differential imaging, respectively. According to Reggiani et al. (2014), this emission is produced by a massive planet of $\sim 30\ M_{\rm Jupiter}$. Biller et al. (2014) instead warned that because of the non-detection in the H and $K_{\rm s}$ bands, this might be a disk feature. Nevertheless, the potential discovery of a protoplanet makes HD 169142 an ideal case to study the planet-disk interaction during the early phases of planetary formation and evolution.

This paper presents new ALMA high angular resolution observations of HD 169142 of the $J = 2 - 1$ transition of ^{12}CO, ^{13}CO, and C^{18}O and 1.3 mm dust continuum. From these observations we place more stringent constraints on the dust and gas density structures. In Section 3.3 we summarize the observing strategy and the data reduction. Results are presented in Section 3.4. In Section 3.5 we compare the observations with simulations of thermo-chemical disk models to constrain the gas and dust distributions. Discussion and conclusions are given in Section 3.6 and 3.7, respectively.

Table 3.1: HD 169142 observational parameters

Dates observed		2015 August 30	
Baselines		13 – 1445 m | 10 – 1120 kλ	
	$C^{18}O$ 2 – 1	^{13}CO 2 – 1	^{12}CO 2 – 1
Rest frequency [GHz]	219.56035	220.39868	230.53800
Synthesized beam [FWHM]	0.″36 × 0.″23	0.″37 × 0.″22	0.″37 × 0.″20
Position angle	−74.°5	−75.°2	−72.°8
Channel width [km s^{-1}]	0.084	0.084	0.040
r.m.s. noise (per channel) [mJy beam^{-1}]	6	8	13
Peak emission [mJy beam^{-1}]	100	200	540
Integrated flux^{a} [Jy km s^{-1}]	3.9 ± 0.5	7.6 ± 0.6	14.0 ± 2.0
Weighting		natural	
Continuum frequency [GHz]		233.0	
Synthesized beam [FWHM]	0.″28 × 0.″18	0.″24 × 0.″16	0.″22 × 0.″14
Position angle	−77.°9	−78.°3	−80.°0
r.m.s. noise [mJy beam^{-1}]	0.07	0.26	0.11
Peak emission [mJy beam^{-1}]	17	15	13
Integrated flux [mJy]	232 ± 23	226 ± 23	226 ± 23
Weighting	Briggs, robust = 0.5	Uniform	Superuniform

Notes. Flux calibration accuracy is taken to be 10%. $^{(a)}$ Integrated over a circular aperture of 3″ diameter.

3.3 Observations and data reduction

HD 169142 (J2000: R.A. = $18^{h}24^{m}29.776^{s}$, DEC = −29°46′49.900″) was observed on 2015 August 30 with the Atacama Large Millimeter/submillimeter Array (ALMA) in band 6 (211 – 275 GHz) as part of project 2013.1.00592.S. In total, 35 antennas were used to achieve a spatial resolution of ~0.″2 – 0.″3. The upper sideband (USB) contained two spectral windows. One window had continuum observations in the time domain mode (TDM) correlator setting with 2 GHz bandwidth centered at 233 GHz. The ^{12}CO $J = 2-1$ line at 230.538 GHz was observed in the second USB spectral window with the frequency domain mode (FDM) correlator setting at 30.5 kHz (0.040 km s^{-1}) frequency (velocity) resolution. ^{13}CO $J = 2 - 1$ at 220.39868 GHz and C^{18}O $J = 2-1$ at 219.56035 GHz were both observed in separate spectral windows in the lower sideband (LSB) in FDM mode. Each observed LSB line had a frequency (velocity) resolution of 61.0 kHz (0.084 km s^{-1}). Table 3.1 summarizes the observational parameters.

Visibility data were obtained in a single execution block with a 6.05 sec integration time per visibility for 50 minutes total on-source. System temperatures were between 50 – 200 K. Weather conditions on the date of observation gave an average precipitable water vapor of 1.8 mm. Calibration was made with J1924-2914 as the delay and bandpass calibrator, J1812-2836 as the gain calibrator, and Ceres as the flux calibrator. The flux values for Ceres on the date of observation were 1.941 Jy in the LSB and 2.165 Jy in the USB. The visibility data were subsequently time binned to 30 sec integration times per visibility for self-calibration, imaging, and analysis. Extended emission is present in ^{12}CO and ^{13}CO data and is poorly sampled on short baselines in the *uv*–space, which resulted in a reduced image quality. For this reason, the total flux listed in Table 3.1 is integrated in a circular aperture of 3″ diameter centered on the source position.

Self-calibration for HD 169142 was performed using the 233 GHz continuum TDM spectral window with DA59 as the reference antenna. Calibration solutions were calculated twice for phase and once for amplitude. The first phase solution

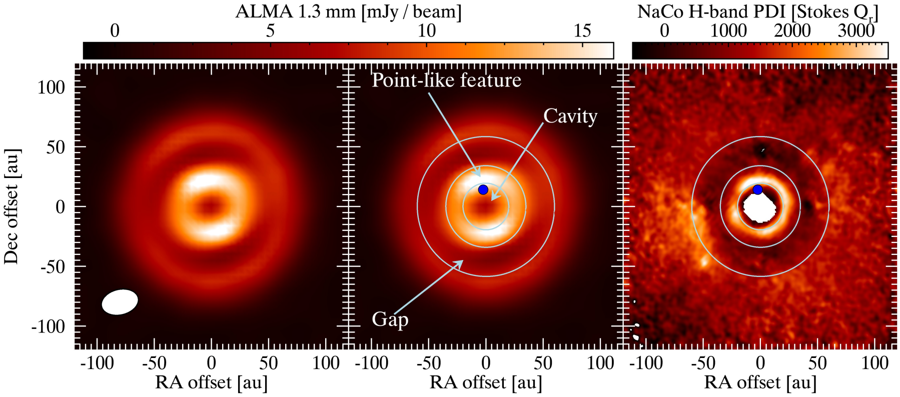

Figure 3.1: (Left) ALMA 1.3 mm continuum map with Briggs weighting, robust = 0.5. (Center) Overlaid with the position and size of the inner dust cavity and gap, and the position of the L'−band point-like feature. (Right) NaCo H−band polarimetric differential image (Quanz et al. 2013).

interval was set to 300 sec, the second phase and amplitude solutions had the solution interval set equal to the binned integration time. Self-calibration solutions from the TDM spectral window were cross-applied to each FDM spectral window. Continuum subtraction of the line data was made in uv−space based on a single-order polynomial fit to all line-free channels in each spectral window. CLEAN imaging for the continuum was made using different weighting schemes: Briggs (Briggs 1995), uniform, and superuniform (Table 3.1). In the remaining paper we adopt the first (which provides the minimum r.m.s.). For the lines, CLEAN imaging was made with natural weighting. Data reduction was performed with the Common Astronomy Software Applications (CASA, McMullin et al. 2007).

3.4 Results

The 1.3 mm continuum and all the three CO isotopolog lines are readily detected. Figures 3.1, 3.2, and 3.3 show the dust continuum map, the line-integrated intensity maps, and the radial profiles, respectively. The channel maps of the three lines are presented in Figures 3.8, 3.9, and 3.10 in the Appendix.

3.4.1 Dust continuum emission

The 1.3 mm continuum map (Figure 3.1) and the radial profile (Figure 3.3) reveal a double-ring structure in the dust distribution with an inner cavity ~$0\farcs17$ in radius and a dust gap between ~$0\farcs28 - 0\farcs48$. The dust continuum emission drops steeply beyond $0\farcs64$. The different structures are highlighted in Figure 3.1 (center panel) along with the position of the point-like L'−band emission (Biller et al. 2014; Reggiani et al. 2014). The radial profile (Figure 3.3) is shown at two different position angles, P.A. = 5° (major axis) and P.A. = 95° (minor axis). Along the minor axis, the continuum is slightly asymmetric, with the west side brighter than the east side. The flux difference between the two sides is ~17 mJy (~2.5σ).

The ALMA continuum map shows some similarities with the H−band polarimetric differential imaging (PDI, Quanz et al. 2013; Momose et al. 2015). The NaCo H−band PDI image is shown in Figure 3.1, and Figure 3.4 shows the radial intensity profile. The position and size of the inner dust ring and gap are consistent between both wavelength ranges. In the outer disk, the ALMA continuum emission is clearly more compact than the H−band emission (Figure 3.4).

The dearth of dust continuum emission inside the inner dust cavity and the dust gap together with the similarities between the H−band PDI and the dust continuum emission suggest that the cavity and the gap are due to a substantial depletion of dust particles. An upper limit to the dust mass inside the gap can be estimated from the r.m.s. of the continuum flux density (Table 3.1). With the assumption of optically thin emission, the dust mass is (e.g., Roccatagliata et al. 2009)

$$M_{\rm dust\ gap} = \frac{S_{\nu\ \rm gap}\ d^2}{k_\nu\ B_\nu\ (T_{\rm dust\ gap})}, \tag{3.1}$$

where $S_{\nu\ \rm gap}$ (Jy) is the upper limit on the flux density, d (cm) the distance, $k_\nu = 2$ (cm^2 g^{-1}) the mass absorption coefficient at 230 GHz (Beckwith et al. 1990), $T_{\rm dust\ gap}$ (K) the dust temperature inside the gap and B_ν (Jy sr^{-1}) the Planck function. We assume $T_{\rm dust\ gap}$ = 50 K (see Figure 3.5). The flux density upper limit is computed by adopting a constant flux of 2.1×10^{-4} Jy beam^{-1} (i.e., 3 × r.m.s.) over the entire gap area. This corresponds to a dust mass 3σ upper limit of $\sim$0.3 $M_\oplus$. With the same assumptions, the dust mass upper limit inside the cavity (assuming $T_{\rm dust\ cavity}$ = 150 K, Figure 3.5) is $\sim 10^{-2}$ $M_\oplus$.

3.4.2 CO isotopolog emission

The integrated intensity maps (Figure 3.2) and the radial profile (Figure 3.3) of the three CO isotopologs show different intensity distributions: the ^{12}CO emission is centrally concentrated with most of the line intensity originating within a $\sim$0.″20 radius; the peak of the ^{13}CO emission corresponds to that of ^{12}CO, but with a secondary ring-like structure farther out in the disk; in the case of C^{18}O, the emission map shows an inner (weak) ring centered on $\sim$0.″1 − 0.″2 and a (strong) outer ring peaking at $\sim$0.″55 with a tail up to $\sim$1.″7. The gas emission is more extended than the dust continuum emission (Figure 3.3). Moreover, the H−band scattered-light emission in the outer disk follows the same intensity distribution as that of ^{12}CO.

The positions of the two C^{18}O peaks are spatially coincident with the location of the dust rings. Along the disk minor axis, the C^{18}O is slightly asymmetric, with the west side brighter than the east side (similar to the continuum asymmetry). The flux difference between the two peaks is $\sim$18 mJy ($\sim 3\sigma$). The line emission maps are consistent with a disk inclination of 13° and a position angle of the disk major axis of 5°.

The different radial distributions of the emission from the three isotopologs is readily explained by an optical depth effect because the $J = 2 - 1$ transition of the three species has different τ, with $\tau(^{12}\mathrm{CO}) > \tau(^{13}\mathrm{CO}) > \tau(\mathrm{C}^{18}\mathrm{O})$. The optically thick ^{12}CO emission is mostly sensitive to the gas temperature, and as a consequence, its line intensity peaks toward the central hotter region of the disk. As the optical depth decreases, the line emission is less sensitive to the gas temperature and more sensitive to the gas column density. This is clear from the distribution of ^{13}CO and

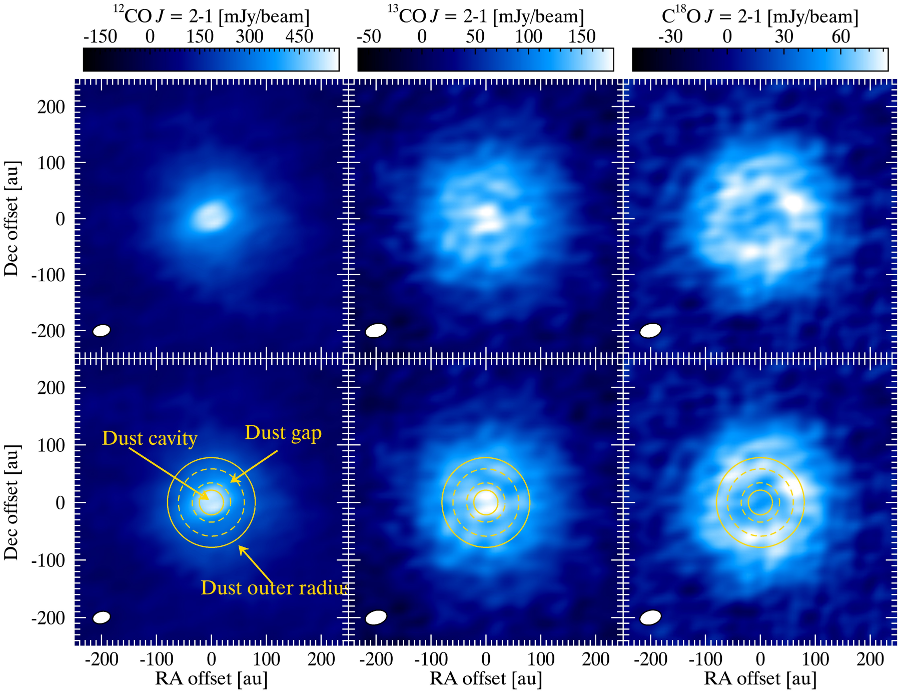

Figure 3.2: (Top) Integrated intensity maps (natural weighting) of ^{12}CO (left), ^{13}CO (center), and C^{18}O (right) $J = 2-1$. (Bottom) Overlaid with the dust rings structure.

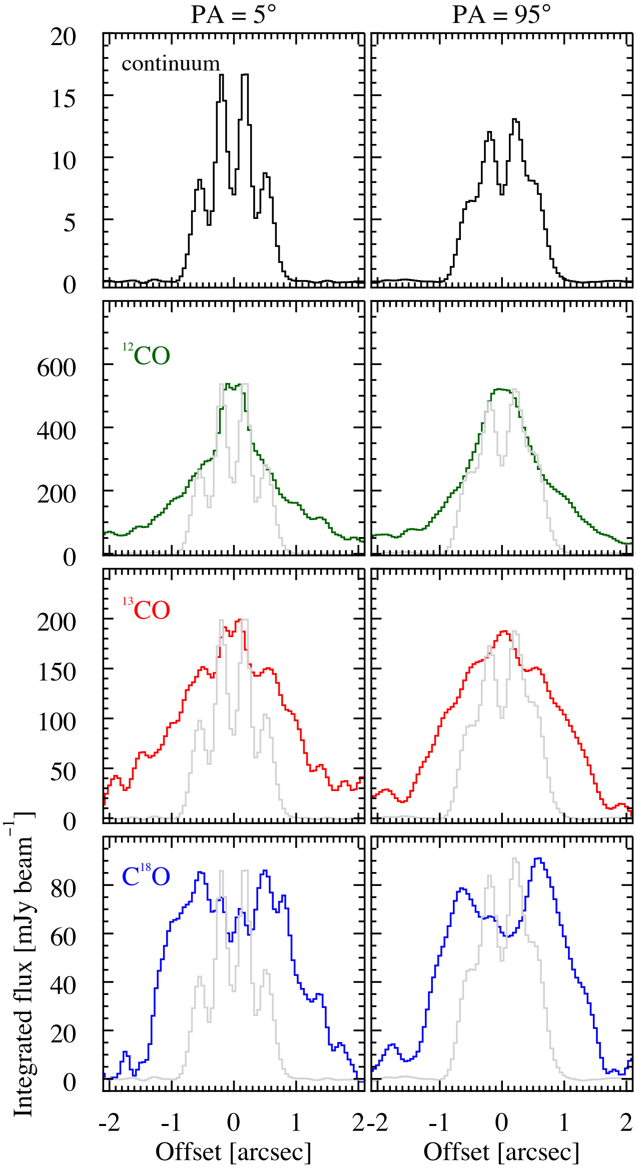

Figure 3.3: Intensity profiles of the dust continuum and CO isotopolog integrated emission maps along the major (P.A. = 5°, left) and minor (P.A. = 95°, right) disk axis. The normalized continuum profile is overlaid (gray) on the CO panels for comparison. Note that the large-scale ($> 2''$) emission of ^{12}CO and ^{13}CO is the result of the reduced image quality (see Section 3.3).

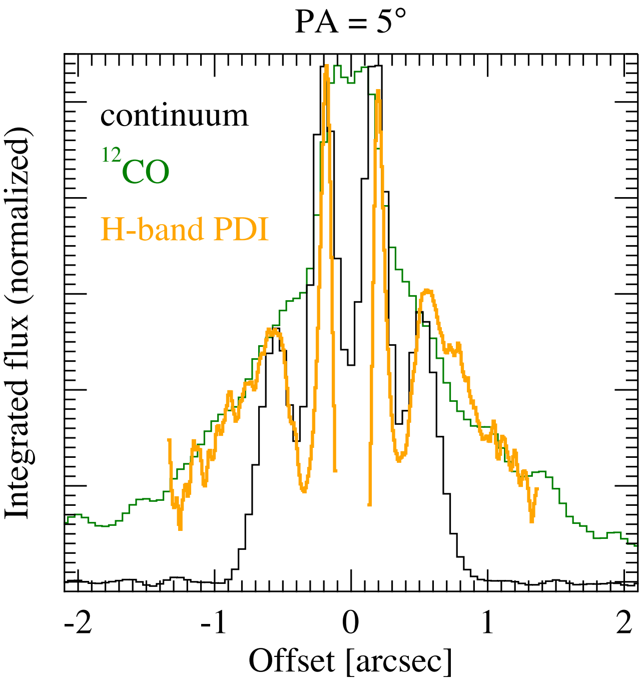

Figure 3.4: Intensity profile of the $H-$band scattered light emission (azimuthally averaged to increase the signal-to-noise ratio) overlaid on the 1.3 mm continuum and ^{12}CO profiles.

C^{18}O: in the first case, the emission is less peaked (than ^{12}CO) toward the central region, and it also shows a secondary peak (ring-shaped) in the outer colder disk. Finally, the optically thin C^{18}O emission mostly originates in the outer disk, which shows a clear ring-like structure. The ring-like shape seen in the ^{13}CO and C^{18}O emission map is spatially coincident with the outer dust ring.

3.4.3 Disk surface density

The spatial distribution of the emission of the three isotopologs provides direct insight into the gas content in the disk: the strong centrally peaked ^{12}CO emission indicates gas inside the dust gap and the dust cavity. On the other hand, the line intensity map of ^{13}CO and in particular C^{18}O implies a substantial drop in gas surface density by a factor δ_{gas} on the order of ~100 inside the dust gap and cavity (see Section 3.5). The similar intensity profiles of the scattered light and ^{12}CO emission in the outer disk is a strong indication that the small dust grains are dynamically and thermally coupled to the gas in the outermost layers of the disk. The intensity drop in the inner disk is also clearly visible in the individual channel maps shown in Figures 3.8, 3.9, and 3.10 in the Appendix.

The significance of the asymmetric emission along the minor axis (continuum and C^{18}O) is low ($\lesssim 3\sigma$), and more observations are needed to confirm this structure.

3.5 Analysis

In this section the ALMA observations of the 1.3 mm continuum and of the three CO isotopologs are compared with thermo-chemical disk model simulations. The goal is to quantify the decrease in dust and gas in the cavity and gap that we identified in the images.

3.5.1 Disk model description

The simulations presented here were generated using the thermo-chemical disk code DALI (Dust and Lines: Bruderer et al. 2012; Bruderer 2013). In this example, DALI takes as input a $T_{\rm eff}$ = 8400 K blackbody radiation field to simulate the stellar spectrum and a power-law surface density structure with an exponential tail

$$\Sigma_{\rm gas}(R) = \Sigma_{\rm c} \left(\frac{R}{R_{\rm c}}\right)^{-\gamma} \exp\left[-\left(\frac{R}{R_{\rm c}}\right)^{2-\gamma}\right], \tag{3.2}$$

with R the radial distance from the star, $R_{\rm c}$ the critical radius, and $\Sigma_{\rm c}$ the gas surface density at $R = R_{\rm c}$. The dust surface density is $\Sigma_{\rm gas}/\Delta_{\rm gd}$, where $\Delta_{\rm gd}$ is the gas-to-dust mass ratio. Along the vertical axis the gas density is parameterized by a Gaussian distribution with scale height h $(= H/R)$

$$h = h_{\rm c}\left(\frac{R}{R_{\rm c}}\right)^{\psi}, \tag{3.3}$$

with $h_{\rm c}$ the critical scale height and ψ the flaring angle. Following D'Alessio et al. (2006), the settling of the large dust particles is implemented by adopting two different power-law grain size populations, small (0.005 – 1 μm) and large (0.005 – 1000 μm), and a power-law exponent $p = 3.5$ (note that the size ranges are different from those adopted in D'Alessio et al. 2006). Dust mass absorption cross-sections are adopted from Andrews et al. (2011). The scale height of the two populations is h for the small grains and χh $(\chi < 1)$ for the large grains. The mass ratio between the two populations is controlled by the parameter $f_{\rm large}$: the dust surface density is $\Sigma_{\rm dust}$ $(1 - f_{\rm large})$ and $\Sigma_{\rm dust}$ $f_{\rm large}$ for the small and large grains, respectively.

DALI solves the 2D dust continuum radiative transfer and determines the dust temperature and radiation field strength at each disk position. In a second step, DALI iteratively solves the gas thermal balance and chemistry, and returns as output the continuum and line emission maps computed through ray tracing. Isotope-selective photodissociation is included in the chemistry, as described in Miotello et al. (2014).

3.5.2 Surface density

Starting from the ALMA observations, we define a surface density structure as shown in Figure 3.5 (left): the gas distribution extends from $R_{\rm gas\ in}$ to $R_{\rm gas\ out}$, while dust is only present between $R_{\rm dust\ in} - R_{\rm gap\ in}$ and between $R_{\rm gap\ out} - R_{\rm dust\ out}$. Along the radial axis, gas and dust densities are reduced by different decrease factors for the gas inside the dust cavity ($\delta_{\rm gas\ cavity}$) and inside the dust gap ($\delta_{\rm gas\ gap}$) and for the dust in the ring ($\delta_{\rm dust}$) as follows:

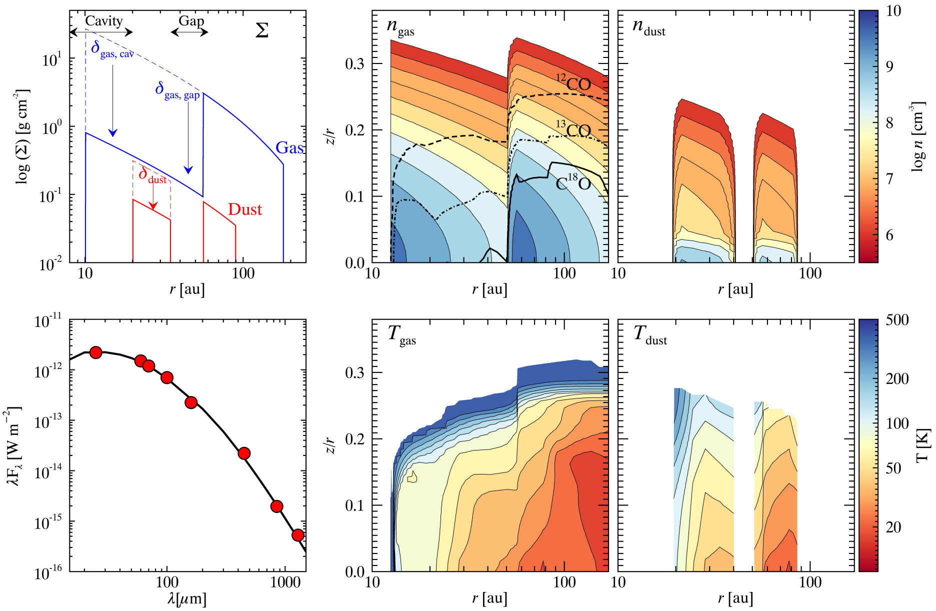

Figure 3.5: Fiducial model. (Top left) Surface density profile. (Top middle) Gas density structure: the $\tau = 1$ layer of the $J = 2-1$ transition is overlaid as the dashed (^{12}CO), dot-dashed (^{13}CO), and solid (C^{18}O) curves. (Top right) Dust density structure. (Bottom left) Spectral energy distribution with fiducial model (black solid curve): data (red dots) are from IRAS, *Herschel* (Pascual et al. 2016), SCUBA (Sandell et al. 2011), and ALMA (this work). (Bottom middle) Gas temperature structure. (Bottom right) Dust temperature structure.

$$n_{\rm gas} = \begin{cases} 0 & \text{for } R < R_{\rm gas\ in} \\ n_{\rm gas} \times \delta_{\rm gas\ cavity} & \text{for } R_{\rm gas\ in} < R < R_{\rm dust\ in} \\ n_{\rm gas} \times \delta_{\rm gas\ gap} & \text{for } R_{\rm dust\ in} < R < R_{\rm gap\ out} \\ n_{\rm gas} & \text{for } R_{\rm gap\ out} < R < R_{\rm gas\ out} \\ 0 & \text{for } R > R_{\rm gas\ out} \end{cases} \tag{3.4}$$

$$n_{\rm dust} = \begin{cases} 0 & \text{for } R < R_{\rm dust\ in} \\ n_{\rm dust} \times \delta_{\rm dust} & \text{for } R_{\rm dust\ in} < R < R_{\rm gap\ in} \\ 0 & \text{for } R_{\rm gap\ in} < R < R_{\rm gap\ out} \\ n_{\rm dust} & \text{for } R_{\rm gap\ out} < R < R_{\rm dust\ out} \\ 0 & \text{for } R > R_{\rm dust\ out}. \end{cases} \tag{3.5}$$

Figure 3.5 shows the modeled disk density structure. We note that our model does not include the small ring of hot dust inside 0.27 au (e.g., Wagner et al. 2015). This does not influence our results as the extinction produced by this small amount of dust is negligible and does not affect the propagation of the ultraviolet radiation farther out in the disk.

Table 3.2: Fiducial disk model parameters

Parameter	Value		Description
	fixed		
$M_\star$ [$M_\odot$]	$1.65^{\diamond}$		stellar mass
$T_{\rm eff}$ [K]	$8400^{\ddagger}$		stellar temperature
$L_\star$ [$L_\odot$]	$10^{\dagger}$		stellar luminosity
d [pc]	$117^{\dagger}$		stellar distance
i [°]	$13^{\star,\,\dagger}$		disk inclination
P.A. [°]	$5^{\star,\,\dagger}$		disk position angle
χ, $f_{\rm large}$	$0.2,\ 0.85^{\dagger}$		settling parameters
	range / step	best fit	
ψ	0.0 – 0.2 / 0.05	0.0	degree of flaring
γ	0 – 2 / 0.5	1.0	$\Sigma(r)$ power-law exponent
$h_{\rm c}$	0.05 – 0.09 / 0.01	0.07	scale height at $R = R_{\rm c}$
$R_{\rm c}$ [au]	50 – 200 / 50	100	critical radius
$\Delta_{\rm gd}$	50 – 100 / 10	80	gas-to-dust mass ratio
$\Sigma_{\rm c}$ [g cm^{-2}]	5 – 8 / 0.5	6.5	$\Sigma_{\rm gas}(R)$ at $R = R_{\rm c}$
$R_{\rm gas\ in}$ [au]	11 – 15 / 1	13	gas inner radius
$R_{\rm dust\ in}$ [au]	18 – 22 / 1	20	dust inner radius
$R_{\rm gap\ in}$ [au]	32 – 36 / 1	35	dust cavity inner radius
$R_{\rm gap\ out}$ [au]	52 – 60 / 2	56	dust outer radius
$R_{\rm gas\ out}$ [au]	170 – 210 / 10	180	gas outer radius
$R_{\rm dust\ out}$ [au]	81 – 91 / 2	83	dust outer radius
$\delta_{\rm dust}$	0.25 – 0.35 / 0.02	0.27	dust depletion for $R_{\rm dust\ in} < R < R_{\rm gap\ in}$
$\delta_{\rm gas\ cavity}$	0.01 – 0.05 / 0.005	0.025	gas depletion for $R_{\rm gas\ in} < R < R_{\rm dust\ in}$
$\delta_{\rm gas\ gap}$	0.01 – 0.05 / 0.005	0.025	gas depletion for $R_{\rm dust\ in} < R < R_{\rm gap\ in}$

Notes. References: ($\diamond$) Blondel & Djie (2006); ($\ddagger$) Dunkin et al. (1997); ($\star$) Raman et al. (2006); ($\dagger$) this work.

3.5.3 Model grid

We created a grid of disk models by varying the most relevant geometrical and physical parameters. These are:

- the gas and dust mass (regulated by the combination of $\Sigma_{\rm c}$, γ, $R_{\rm c}$ and $\Delta_{\rm gd}$), which control the overall continuum and line emission as well as the SED,
- the flaring angle (ψ), which mostly influences the radial intensity profile of the optically thick ^{12}CO emission (arising from the outermost layers),
- the scale height ($h_{\rm c}$), which has a great effect on the intensity of the gas and dust emission and on the SED,
- the gas and dust decrease factors ($\delta_{\rm gas\ cavity}$, $\delta_{\rm gas\ gap}$, $\delta_{\rm dust}$), which control the gas and dust emission inside the dust gap,
- the size and position of the cavity and of the gap ($R_{\rm gas\ in}$, $R_{\rm dust\ in}$, $R_{\rm gap\ in}$, $R_{\rm gap\ out}$), and
- the outer dust and gas radii ($R_{\rm dust\ out}$, $R_{\rm gas\ out}$).

Table 3.2 lists the definition, range, and step size of the different parameters. Using DALI, we created model images of the dust continuum emission and of the

$J = 2 - 1$ transition of the three CO isotopologs. In the case of the CO isotopolog lines, the model channel maps are computed with the same spectral resolution as the observations. From the DALI model images, we measured synthetic visibilities, synthetic observations, and residual (data − model) images reading the *uv* coordinates, integration time, source position, hour angle, and spectral window parameters directly from the observed ALMA measurement set. For this task, we used the CASA tools SIMOBSERVE and CLEAN.

The model grid is compared to the observations with the aim of constructing a fiducial model that quantitatively reproduces the ALMA observations. The observed radial intensity profiles (along the disk minor and major axes) and the SED are fitted against the model grid. The fiducial model is defined by the set of parameters that minimize the difference between observations and model grid within the explored parameter space.

3.5.4 Fiducial model and comparison with observations

The surface density distribution, the density and temperature structure, and the SED of the fiducial model are shown in Figure 3.5. Figures 3.6 and 3.7 show the comparison with the observations: Figure 3.6 shows (from left to right) the ALMA observations (continuum or line-integrated map), synthetic observations, and residual images (computed in the *uv*-plane); Figure 3.7 shows the radial intensity profiles along the disk major and minor axes. In order to asses the quality of the fit, Figure 3.11 in the Appendix shows the radial profile differences for a subset of the model grid.

Dust surface density: the fiducial model reproduces the dust continuum image well, with an inner dust cavity of $R \approx 20$ au, an inner ring between ∼20 − 35 au, a gap between ∼35 − 56 au, and an outer ring between ∼56 − 83 au. The cavity and the gap are empty of millimeter-sized dust particles down to the noise level; there is an upper limit to the dust mass of $\sim 10^{-2}\ M_{\oplus}$ and $0.3\ M_{\oplus}$ in the cavity and gap, respectively. The inner ring is decreased by a factor of ∼3.7 ($= 1/\delta_{\mathrm{dust}}$) (Figure 3.3). The total dust mass is $1 \times 10^{-4}\ M_{\odot}$. The cavity and the gap are also free of micron-sized dust particles, as suggested by the NACO polarimetric observations (Figure 3.4).

Gas in the inner disk: our analysis confirms the gas inside the dust gap (i.e., $35\ \mathrm{au} < R < 56\ \mathrm{au}$) and inside the dust cavity ($R < 20$ au) down to an inner radius of ∼13 au. The gas surface density inward of the dust gap is decreased by a factor of ∼30 − 40 ($= 1/\delta_{\mathrm{gas\ gap}}$). Interestingly, we find that $\delta_{\mathrm{gas\ cavity}} = \delta_{\mathrm{gas\ gap}}$.

Gas in the outer disk: the gas surface density extends well beyond the dust outer radius. The fiducial model closely follows the slope of the radial profile of the three CO isotopologs in the outer disk. The outer gas radius of 180 au is set by the steep drop of the $C^{18}O$ emission at large radii. Adopting a larger outer gas radius would overestimate the $C^{18}O$ emission in the outer disk, leaving the profiles of ^{12}CO and $C^{13}O$ almost unchanged. The total gas mass is $1.9 \times 10^{-2}\ M_{\odot}$ for the adopted standard carbon abundance of $[C]/[H] = 2.4 \times 10^{-4}$. While the fiducial model reproduces the intensity profiles reasonably well, the absolute flux of the ^{13}CO emission is slightly underestimated. The difference in absolute flux is on the order of ∼10%.

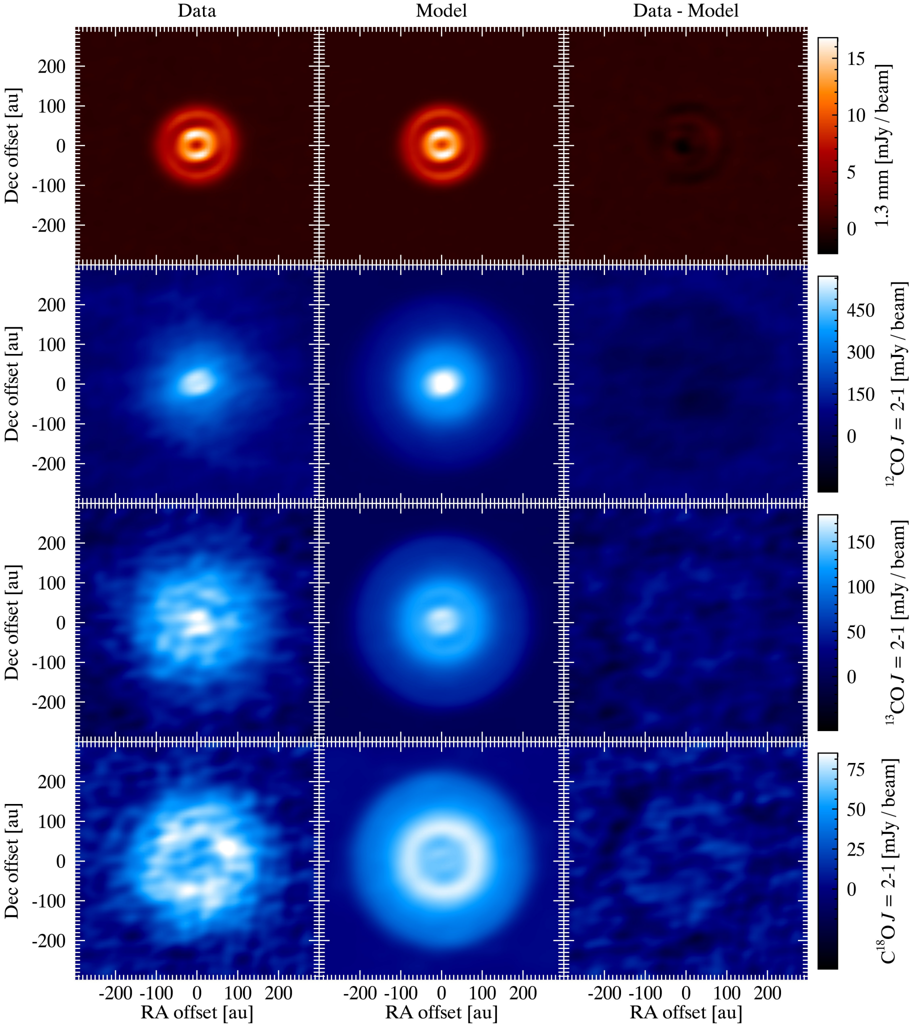

Figure 3.6: Results of the fiducial model: (from left to right) ALMA image, model image, residual image. Weighting scheme as in Figures 3.1 and 3.2.

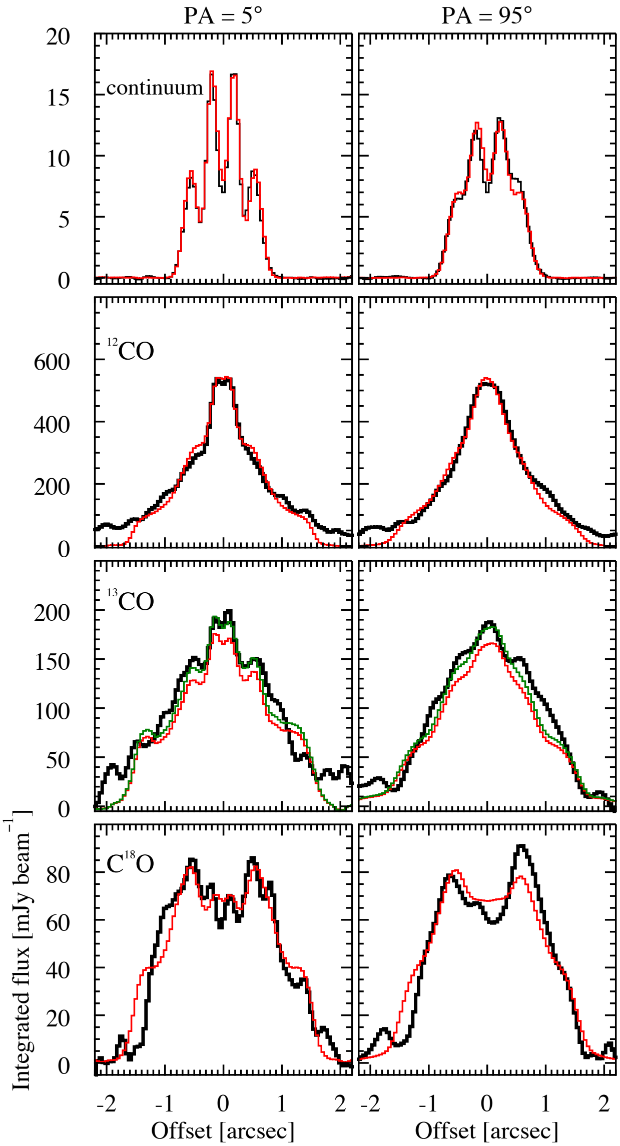

Figure 3.7: Results of the fiducial model: comparison of the observed (black curve) and modeled (red curve) radial intensity profiles. In the case of ^{13}CO, the green curve represents the fiducial model scaled up by 10% to match the absolute flux level.

3.6 Discussion

The radial distribution of the (optically thin) 1.3 mm emission showing two deep gaps is qualitatively consistent with two giant planets shaping the dust distribution. Pinilla et al. (2015) performed 2D hydrodynamical simulations coupled with a dust evolution model of a disk hosting two giant planets, which showed that planets can produce multiple dust traps. These simulations show that the formation of dust traps is due to a combination of three main parameters: planetary mass, disk viscosity, and dust fragmentation velocity. In particular, the trap is easily formed for a high planetary mass and/or a low disk viscosity. In the case of HD 169142, the lack of dust continuum emission inside the dust cavity ($R \lesssim 20$ au) and in the outer gap (35 au $\lesssim R \lesssim$ 56 au) suggests very efficient dust trapping by means of two giant planets.

Azimuthal asymmetries are sometimes observed in the dust continuum emission of Herbig Ae/Be systems, as in the case of HD 142527 (Casassus et al. 2012; Fukagawa et al. 2013) and IRS 48 (van der Marel et al. 2013). Such an asymmetry is thought to be due to dynamical interaction between the disk and a massive planet generating a vortex where dust particles are trapped (Rossby instability: de Val-Borro et al. 2007; Lyra et al. 2009). The lack of such an asymmetry in the two dust rings of HD 169142 implies an upper limit to the two masses of the two planets of $\lesssim 10\ M_{\rm Jupiter}$.

The density drop of gas inward of the dust gap requires a rather massive planet with $M_{\rm planet} \gtrsim 1\ M_{\rm Jupiter}$ for the outer planet. For a lower planetary mass, the cavity is "porous" and gas from the outer disk could flow inward and fill the gap (e.g., Lubow & D'Angelo 2006; Alexander & Armitage 2009). This is consistent with the prescriptions of Rosotti et al. (2016), which predict a mass of $\gtrsim 0.3\ M_{\rm Jupiter}$ (based on the size of the dust gap).

In the case of the inner dust cavity, the ALMA CO maps show no further drop of the gas density, suggesting inward gas flow. This poses a further limit to the planetary mass inside the inner dust cavity of $M_{\rm planet} < M_{\rm Jupiter}$.

Based on the lack of azimuthal asymmetric features and on the drop of the gas surface density, the ALMA data presented here are thus consistent with the presence of two giant planets of $M_{\rm planet} \approx 0.1 - 1\ M_{\rm Jupiter}$ and $M_{\rm planet} \approx 1 - 10\ M_{\rm Jupiter}$ for the inner and outer planet, respectively.

The ALMA 1.3 mm continuum image confirms a real dust gap (i.e., depletion of dust particles) between ~35 – 56 au. This gap was previously detected through near-infrared polarimetric imaging, but only thanks to ALMA it is possible to determine the density drop. The dust gap is most likely the outcome of dynamical interaction between the disk and a second unseen planet, as noted above. Moreover, while the dust continuum emission is confined within a radius of 83 au with a sharp decay, the gas emission extends up to ~180 au radius, as is shown in Figures 3.2 and 3.3. This dichotomy is also observed in other systems that are observed at high angular resolution, such as LkCa 15 (Isella et al. 2012), HD 163296 (de Gregorio-Monsalvo et al. 2013), HD 100546 (Walsh et al. 2014), and HD 97048 (Walsh et al. 2016; van der Plas et al. 2017). The smaller size of the dust disk compared to the gas is primarily due to an optical depth effect (e.g., Dutrey et al. 1996), but the sharp drop in dust emission hints at the radial drift of the dust particles (Weidenschilling 1977; Birnstiel & Andrews 2014), with the grains trapped at local pressure maxima induced by the planet-disk interaction. The similarity of the radial intensity profile of the $H-$band scattered light and of the ^{12}CO emission is indicative of dynamical and thermal coupling of the small dust grains with the gas in the outermost layers of the disk.

An alternative scenario that could also explain the surface density profile of HD 169142 is the case of magneto-rotational instability (MRI) creating dead-zones (e.g., Regály et al. 2012; Flock et al. 2015; Hasegawa & Takeuchi 2015). While a dead-zone itself results in a pressure bump with a gas density contrast of only a few, the combination with a mass-loss mechanism can cause this region to become largely devoid of gas by an amount similar to that observed in HD 169142. This process was investigated by Morishima (2012), for instance, in the case of MRI combined with photoevaporation, and by Pinilla et al. (2016) by including magnetohydrodynamics (MHD) wind (and dust evolution). However, we note that no signature of mass loss is visible in the CO isotopolog channel maps.

Other protoplanetary systems around Herbig Ae/Be stars show similar multiple-ring dust distribution structures, such as HD 100546 (Walsh et al. 2014), HD 97048 (Walsh et al. 2016), and HD 163296 (Isella et al. 2016). In these cases, the ALMA observations also suggest several planets that are responsible for the dynamical clearing of the disk. The emerging picture is that these Herbig Ae/Be protoplanetary disks are in a late evolutionary phase where planets have already formed at large distances from the star. Future ALMA observations will tell us whether this is true for the entire class of Herbig Ae/Be systems.

3.7 Conclusions

From the analysis of the ALMA observations presented in this paper we conclude that gas and dust in HD 169142 are physically decoupled, with the dust particles concentrated in two rings between ~20 – 35 au and ~56 – 83 au. Thanks to ALMA, we have for the first time strong constraints on the distribution and dynamics of the bulk of the dust and gas. We find a real dust depletion (i.e., absence of dust particles) inside the cavity ($R \lesssim 20$ au) and the gap ($35 \lesssim R \lesssim 56$ au). The dust cavity and gap are filled in with gas, as suggested by the emission maps of the three CO isotopologs, with the gas surface density reduced by a factor of ~30 – 40 for $R \lesssim 56$ au. The sharp edge of the continuum map at 83 au is indicative of a radial drift of dust grains (dust outer radius << gas outer radius).

Of the various theories proposed to explain the opening of gaps in disks (e.g., dynamical interaction with planets, MRI, dust sintering, and photoevaporation), the most likely scenario for HD 169142 is that several giant planets ($\gtrsim M_{\mathrm{Jupiter}}$) have carved out the disk and caused the cavity and the gap and trapped the dust particles beyond the planetary orbits. The combined effect of MRI (forming dead-zones) and MHD wind could also cause the ring and gap structure in both gas and dust, although with different characteristics, which may be tested by future data with higher signal-to-noise ratio and higher angular resolution.

We stress the importance of spatially resolved observations of multiple CO isotopolog transitions: thanks to the different optical depths, the spatially resolved channel maps of the three isotopologs allowed us to detect and quantify the very small amount ($\lesssim 0.1\ M_{\mathrm{Jupiter}}$) of gas inside the dust gap. This demonstrates the potential of CO isotopolog observations in probing the gas surface density and the evolutionary phase of protoplanetary systems.

Acknowledgements

This paper makes use of the following ALMA data: ADS/JAO.ALMA#2013.1.00592.S. ALMA is a partnership of ESO (representing its member states), NSF (USA) and NINS (Japan), together with NRC (Canada), NSC and ASIAA (Taiwan), and KASI (Republic of Korea), in cooperation with the Republic of Chile. The Joint ALMA Observatory is operated by ESO, AUI/NRAO and NAOJ. This work has made use of data from the European Space Agency (ESA) mission *Gaia* (`http://www.cosmos.esa.int/gaia`), processed by the *Gaia* Data Processing and Analysis Consortium (DPAC, `http://www.cosmos.esa.int/web/gaia/dpac/consortium`). Funding for the DPAC has been provided by national institutions, in particular the institutions participating in the *Gaia* Multilateral Agreement. DF acknowledges support from the Italian Ministry of Education, Universities and Research, project SIR (RBSI14ZRHR). MC and MRH are supported by a TOP grant from the Netherlands Organisation for Scientific Research (NWO, 614.001.352). CW acknowledges financial support from the Netherlands Organisation for Scientific Research (NWO, grant 639.041.335) and start-up funds from the University of Leeds, UK. The authors thank M. Tazzari, S. Facchini, G. Rosotti, L. Testi, and P. Pinilla for useful discussions and S. Quanz for providing the NaCo image.

Appendix A: Channel maps

The individual channel maps of ^{12}CO, ^{13}CO, and C^{18}O are shown in Figures 3.8, 3.9, and 3.10, respectively. The velocity scale is defined in the local standard of rest (LSR) system. In all cases, the maps are created using natural weighting, and the velocity resolution is resampled to 0.160 km s^{-1}(^{12}CO) and 0.168 km s^{-1}(^{13}CO and C^{18}O) with Hanning smoothing. The disk emission is detected from $v_{\rm LSR}$ = 4.9 km s^{-1} to $v_{\rm LSR}$ = 8.6 km s^{-1}, and the systemic velocity is $v_{\rm LSR}$ = 6.9 km s^{-1}.

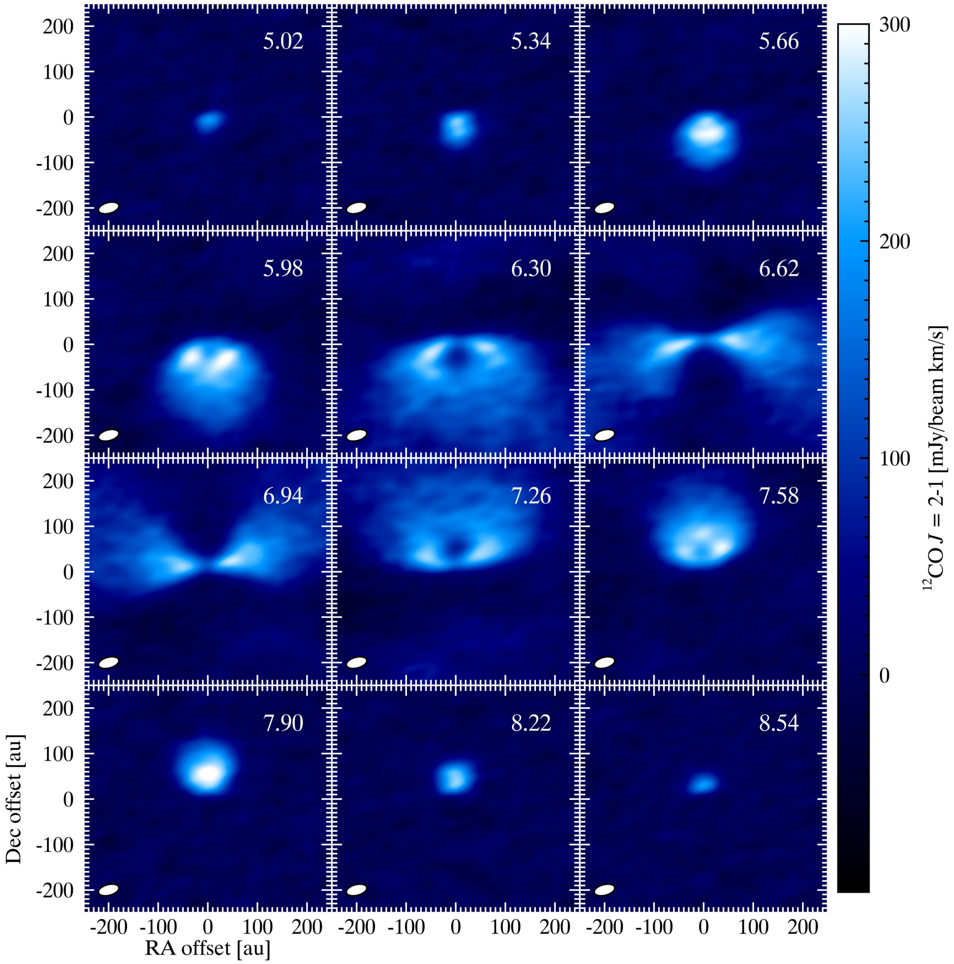

Figure 3.8: ALMA channel maps of ^{12}CO $J = 2 - 1$.

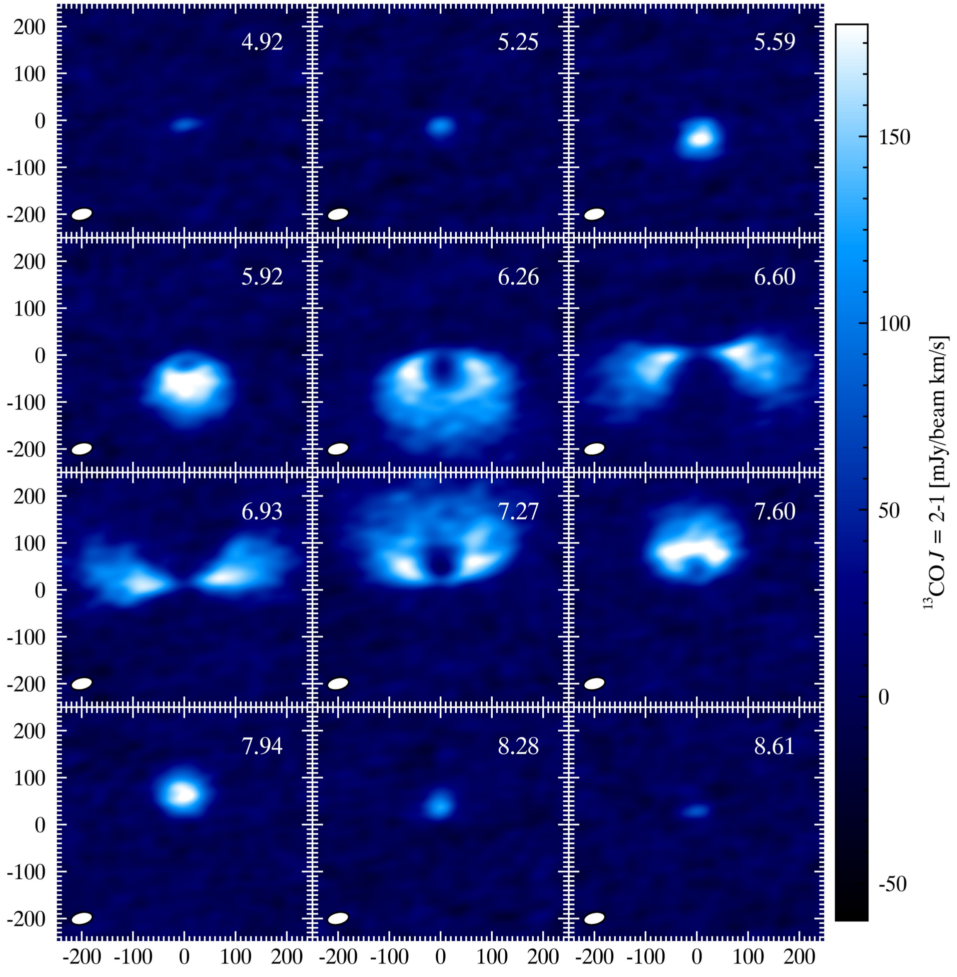

Figure 3.9: ALMA channel maps of ^{13}CO $J = 2 - 1$.

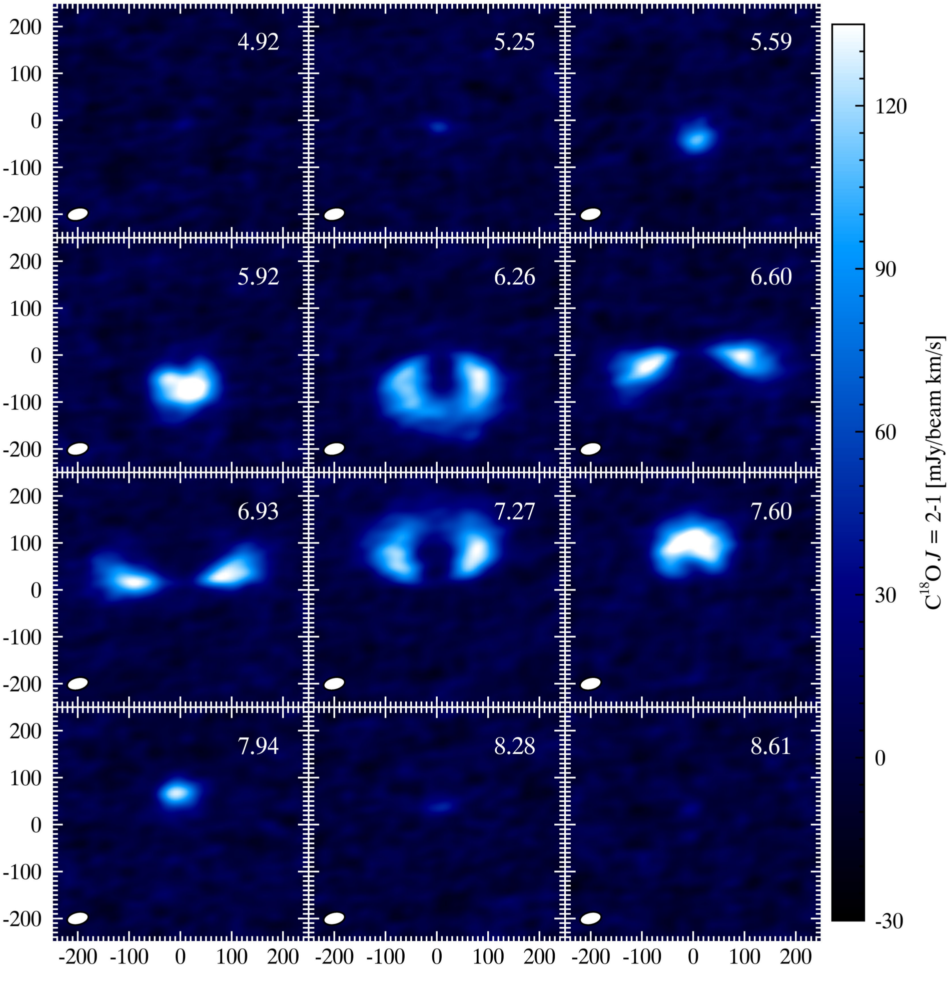

Figure 3.10: ALMA channel maps of C^{18}O $J = 2 - 1$.

Appendix B: Model grid

Figure 3.11 shows the results of the model grid (Section 3.5.3) where we vary one parameter at a time. Only a subset of the model grid is shown here. We note in particular that the ^{12}CO radial profile is very sensitive to $R_{\rm gas\ in}$ (the inner gas radius), while the inner dust radius ($R_{\rm dust\ in}$) affects not only the continuum radial profile, but also the strength of the ^{13}CO and C^{18}O emission in the inner disk.

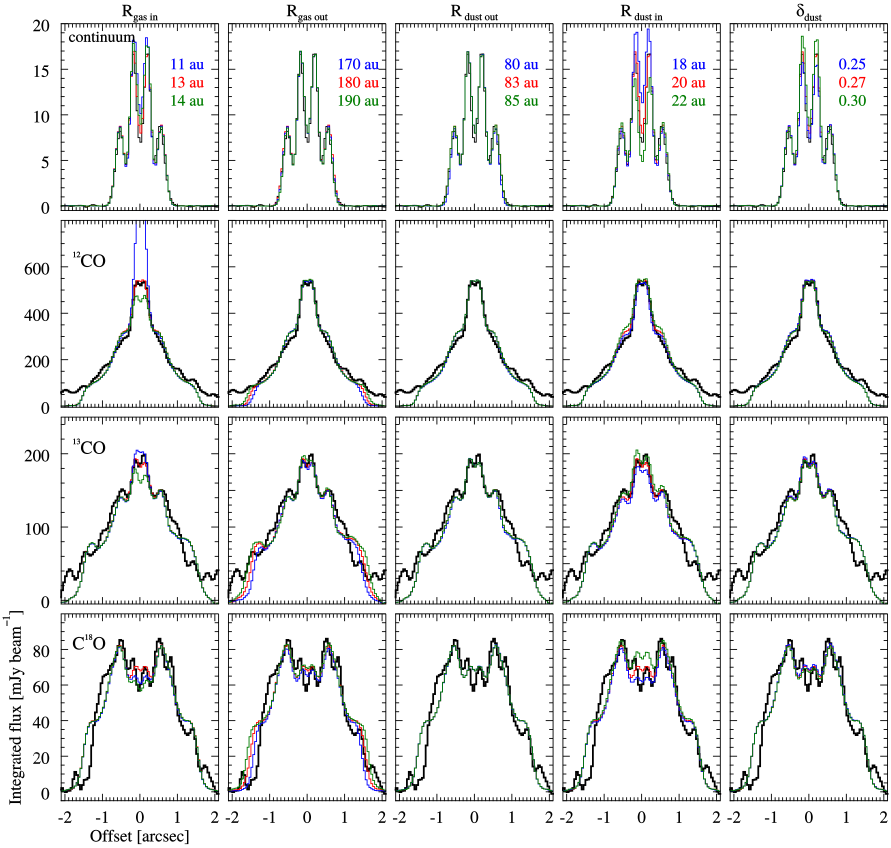

Figure 3.11: Radial intensity profile differences (P.A. = 5°) for a subset of the model grid. The ^{13}CO models are scaled up by 10% to match the absolute flux level of the observations.

References

Alexander, R. D. & Armitage, P. J. 2009, ApJ, 704, 989
ALMA Partnership, Brogan, C. L., Pérez, L. M., et al. 2015, ApJ, 808, L3
Andrews, S. M., Wilner, D. J., Espaillat, C., et al. 2011, ApJ, 732, 42
Andrews, S. M., Wilner, D. J., Zhu, Z., et al. 2016, ApJ, 820, L40
Beckwith, S. V. W., Sargent, A. I., Chini, R. S., & Guesten, R. 1990, AJ, 99, 924
Biller, B. A., Males, J., Rodigas, T., et al. 2014, ApJ, 792, L22
Birnstiel, T. & Andrews, S. M. 2014, ApJ, 780, 153
Blondel, P. F. C. & Djie, H. R. E. T. A. 2006, A&A, 456, 1045
Briggs, D.S.. 1995, Ph.D. thesis, The New Mexico Institute of Mining and Technology, Socorro, New Mexico, USA
Bruderer, S. 2013, A&A, 559, A46
Bruderer, S., van Dishoeck, E. F., Doty, S. D., & Herczeg, G. J. 2012, A&A, 541, A91
Casassus, S., Perez M., S., Jordán, A., et al. 2012, ApJ, 754, L31
D'Alessio, P., Calvet, N., Hartmann, L., Franco-Hernández, R., & Servín, H. 2006, ApJ, 638, 314
de Gregorio-Monsalvo, I., Ménard, F., Dent, W., et al. 2013, A&A, 557, A133
de Val-Borro, M., Artymowicz, P., D'Angelo, G., & Peplinski, A. 2007, A&A, 471, 1043
de Zeeuw, P. T., Hoogerwerf, R., de Bruijne, J. H. J., Brown, A. G. A., & Blaauw, A. 1999, AJ, 117, 354
Dunkin, S. K., Barlow, M. J., & Ryan, S. G. 1997, MNRAS, 286, 604
Dutrey, A., Guilloteau, S., Duvert, G., et al. 1996, A&A, 309, 493
Ercolano, B., Rosotti, G. P., Picogna, G., & Testi, L. 2017, MNRAS, 464, L95
Fedele, D., Bruderer, S., van Dishoeck, E. F., et al. 2013, A&A, 559, A77
Flock, M., Ruge, J. P., Dzyurkevich, N., et al. 2015, A&A, 574, A68
Fukagawa, M., Tamura, M., Itoh, Y., et al. 2010, PASJ, 62, 347
Fukagawa, M., Tsukagoshi, T., Momose, M., et al. 2013, PASJ, 65, L14
Gaia Collaboration, Brown, A. G. A., Vallenari, A., et al. 2016, A&A, 595, A2
Grady, C. A., Schneider, G., Hamaguchi, K., et al. 2007, ApJ, 665, 1391
Hasegawa, Y. & Takeuchi, T. 2015, ApJ, 815, 99
Honda, M., Maaskant, K., Okamoto, Y. K., et al. 2012, ApJ, 752, 143
Isella, A., Guidi, G., Testi, L., et al. 2016, Physical Review Letters, 117, 251101
Isella, A., Pérez, L. M., & Carpenter, J. M. 2012, ApJ, 747, 136
Lubow, S. H. & D'Angelo, G. 2006, ApJ, 641, 526
Lyra, W., Johansen, A., Klahr, H., & Piskunov, N. 2009, A&A, 493, 1125
Malfait, K., Bogaert, E., & Waelkens, C. 1998, A&A, 331, 211
McMullin, J. P., Waters, B., Schiebel, D., Young, W., & Golap, K. 2007, in Astronomical Society of the Pacific Conference Series, Vol. 376, Astronomical Data Analysis Software and Systems XVI, ed. R. A. Shaw, F. Hill, & D. J. Bell, 127
Meeus, G., Pinte, C., Woitke, P., et al. 2010, A&A, 518, L124
Miotello, A., Bruderer, S., & van Dishoeck, E. F. 2014, A&A, 572, A96
Momose, M., Morita, A., Fukagawa, M., et al. 2015, PASJ, 67, 83
Morishima, R. 2012, MNRAS, 420, 2851
Okuzumi, S., Momose, M., Sirono, S.-i., Kobayashi, H., & Tanaka, H. 2016, ApJ, 821, 82
Osorio, M., Anglada, G., Carrasco-González, C., et al. 2014, ApJ, 791, L36

Panić, O., Hogerheijde, M. R., Wilner, D., & Qi, C. 2008, A&A, 491, 219

Papaloizou, J. & Lin, D. N. C. 1984, ApJ, 285, 818

Pascual, N., Montesinos, B., Meeus, G., et al. 2016, A&A, 586, A6

Pinilla, P., de Juan Ovelar, M., Ataiee, S., et al. 2015, A&A, 573, A9

Pinilla, P., Flock, M., Ovelar, M. d. J., & Birnstiel, T. 2016, A&A, 596, A81

Pinte, C., Woitke, P., Ménard, F., et al. 2010, A&A, 518, L126

Quanz, S. P., Avenhaus, H., Buenzli, E., et al. 2013, ApJ, 766, L2

Raman, A., Lisanti, M., Wilner, D. J., Qi, C., & Hogerheijde, M. 2006, AJ, 131, 2290

Regály, Z., Juhász, A., Sándor, Z., & Dullemond, C. P. 2012, MNRAS, 419, 1701

Reggiani, M., Quanz, S. P., Meyer, M. R., et al. 2014, ApJ, 792, L23

Roccatagliata, V., Henning, T., Wolf, S., et al. 2009, A&A, 497, 409

Rosotti, G. P., Juhasz, A., Booth, R. A., & Clarke, C. J. 2016, MNRAS, 459, 2790

Sandell, G., Weintraub, D. A., & Hamidouche, M. 2011, ApJ, 727, 26

The, P. S., de Winter, D., & Perez, M. R. 1994, A&AS, 104, 315

van der Marel, N., van Dishoeck, E. F., Bruderer, S., et al. 2016, A&A, 585, A58

van der Marel, N., van Dishoeck, E. F., Bruderer, S., et al. 2013, Science, 340, 1199

van der Plas, G., Wright, C. M., Ménard, F., et al. 2017, A&A, 597, A32

Wagner, K. R., Sitko, M. L., Grady, C. A., et al. 2015, ApJ, 798, 94

Walsh, C., Juhász, A., Meeus, G., et al. 2016, ApJ, 831, 200

Walsh, C., Juhász, A., Pinilla, P., et al. 2014, ApJ, 791, L6

Weidenschilling, S. J. 1977, MNRAS, 180, 57

Zhang, K., Blake, G. A., & Bergin, E. A. 2015, ApJ, 806, L7

CHAPTER 4

PROBING MIDPLANE CO ABUNDANCE AND GAS TEMPERATURE WITH DCO$^+$ IN THE PROTOPLANETARY DISK AROUND HD 169142

M. T. CARNEY, D. FEDELE, M. R. HOGERHEIJDE, C. FAVRE, C. WALSH,
S. BRUDERER, A. MIOTELLO, N. M. MURILLO, P. D. KLAASSEN,
TH. HENNING, AND E. F. VAN DISHOECK.

ASTRONOMY & ASTROPHYSICS
VOLUME 614, ARTICLE A106, 15 PP. (2018)

Abstract

Context. Physical and chemical processes in protoplanetary disks affect the disk structure and the midplane environment within which planets form. The simple deuterated molecular cation DCO^+ has been proposed to act as a tracer of the disk midplane conditions.
Aims. This work aims to understand which midplane conditions are probed by the DCO^+ emission in the disk around the Herbig Ae star HD 169142. We explore the sensitivity of the DCO^+ formation pathways to gas temperature and CO abundance.
Methods. The DCO^+ $J = 3-2$ transition was observed with Atacama Large Millimeter/submillimeter Array at a spatial resolution of ~0.3″ (35 AU at 117 pc). We modeled the DCO^+ emission in HD 169142 with a physical disk structure adapted from the literature, and employed a simple deuterium chemical network to investigate the formation of DCO^+ through the cold deuterium fractionation pathway via H_2D^+. Parameterized models are used to modify the gas temperature and CO abundance structure of the disk midplane to test their effect on DCO^+ production. Contributions from the warm deuterium fractionation pathway via CH_2D^+ are approximated using a constant abundance in the intermediate disk layers.
Results. The DCO^+ line is detected in the HD 169142 disk with a total integrated line flux of 730 ± 73 mJy km s^{-1}. The radial intensity profile reveals a warm, inner component of the DCO^+ emission at radii $\lesssim$ 30 AU and a broad, ring-like structure from ~$50-230$ AU with a peak at 100 AU just beyond the edge of the millimeter grain distribution. Parameterized models show that alterations to the midplane gas temperature and CO abundance are both needed to recover the observed DCO^+ radial intensity profile. The alterations are relative to the fiducial physical structure of the literature model constrained by dust and CO observations. The best-fit model contains a shadowed, cold midplane in the region $z/r < 0.1$ with an 8 K decrease in $T_{\rm gas}$ and a factor of five CO depletion just beyond the millimeter grains ($r = 83$ AU), and a 2 K decrease in $T_{\rm gas}$ for $r > 120$ AU. The warm deuterium fractionation pathway is implemented as a constant DCO^+ abundance of 2.0×10^{-12} between $30-70$ K and contributes > 85% to the DCO^+ emission at $r < 83$ AU in the best-fit model.
Conclusions. The DCO^+ emission probes a reservoir of cold material in the HD 169142 outer disk that is not probed by the millimeter continuum, the spectral energy distribution, nor the emission from the ^{12}CO, ^{13}CO, or $C^{18}O$ $J = 2-1$ lines. The DCO^+ emission is a sensitive probe of gas temperature and CO abundance near the disk midplane and provides information about the outer disk beyond the millimeter continuum distribution that is largely absent in abundant gaseous tracers such as CO isotopologs.

4.1 Introduction

Protoplanetary disks have complex structures due to the many physical and chemical processes that shape their environment. This includes but is not limited to radiative heating from the central pre-main sequence (PMS) star, viscous heating, molecular line cooling, photodissociation and ionization, dust grain growth and radial drift, and the freeze-out of molecular species in cold disk regions (for a review of disk structure and evolution, see Williams & Cieza 2011). These processes culminate in the formation of terrestrial and giant planets, often before the gas disk is dispersed. The study of protoplanetary disk structure while the disks still retain their large gas reservoirs is important to understand the environments in which planets will form.

Several gas-rich protoplanetary disks have been imaged at high spatial resolution with the Atacama Large Millimeter/submillimeter Array (ALMA), revealing physical structures that may indicate the presence of low-mass companions or planets in the disk, for example, IRS 48, HD 142527, HD 100546, HL Tau, TW Hya, HD 97048, HD 163296, HD 169142, and AS 209 (van der Marel et al. 2013; Casassus et al. 2013; Walsh et al. 2014a; ALMA Partnership et al. 2015; Andrews et al. 2016; Walsh et al. 2016; Isella et al. 2016; Fedele et al. 2017a,b). Disks have a stratified vertical structure with an atomic upper layer, a chemically active warm intermediate layer, and a dense, cold midplane. The environment most conducive to planet formation is at the disk midplane, where various molecular species such as H_2O, CO_2, CO, and N_2 freeze out onto dust grains, creating an icy mantle that enhances grain sticking efficiency (Bergin & Tafalla 2007; Blum & Wurm 2008). Molecular ices can then be more easily incorporated into the bulk of planetary bodies than their gas-phase counterparts. The location at which ~50% of a given molecule has condensed into ice is called a snow line or ice line.

Probing the conditions of the midplane of the disk is difficult. Dust and molecular line opacities can obscure lower layers of the disk, particularly at radii close to the central star. Molecular snow lines can reside too near to the star to be directly observed, as is the case for H_2O (Zhang et al. 2013; Piso et al. 2015; Banzatti et al. 2015). They can also be obscured by opacity effects in the outer disk, as is the case for the farther out CO snow line, where ^{12}CO, ^{13}CO, and even C^{18}O can remain optically thick at large radii (Qi et al. 2015; Fedele et al. 2017a). Direct determination of the CO snow line can be done using emission from the rarest CO isotopologs (e.g., Yu et al. 2016; Zhang et al. 2017), but only for the closest objects. To characterize the disk midplane environment, less abundant species must be observed which trace chemical processes occurring deep in the disk, such as molecular freeze-out. The DCO$^+$ molecule has been suggested as an optically thin molecular tracer of the midplane regions around the CO snow line and as a simultaneous tracer of ionization occurring in the intermediate layers of the disk due to its formation via cold ($\lesssim$ 30 K) and warm ($\lesssim$ 100 K) deuterium fractionation pathways available in protoplanetary disks (Mathews et al. 2013; Favre et al. 2015; Huang et al. 2017).

The disk around HD 169142 makes an excellent testbed in which to explore the chemistry of DCO$^+$ in protoplanetary disks and its usefulness as a tracer of disk midplane conditions. HD 169142 hosts one of a handful of disks found to have millimeter dust rings, and which also exhibits CO emission that extends beyond the edge of the millimeter grains (ALMA Partnership et al. 2015; Andrews et al. 2016; Isella et al. 2016; Walsh et al. 2016; Fedele et al. 2017a). HD 169142 is an isolated system with a Herbig Ae spectral type A8Ve star and stellar mass $M_* = 1.65\ M_\odot$ (Grady et al. 2007; Blondel & Djie 2006). Recent distance measurements by Gaia put the system at a distance of $d = 117 \pm 4$ pc (Gaia Collaboration et al. 2016). The new distance results in a revised luminosity that is lower by a factor of ~0.65, which places the age of the system closer to ~10 Myr (Pohl et al. 2017). The new age estimate is older than previous estimates of 6^{+6}_{-3} Myr (Grady et al. 2007), but within the errors. With disk inclination $i = 13°$ and position angle P.A. = 5° (Raman et al.

2006; Panić et al. 2008), the system is viewed close to face-on, allowing for accurate characterization of the radial distribution of the continuum and molecular line emission. With an estimated total gas mass of 1.9×10^{-2} $M_\odot$ and ^{12}CO extending out to ~200 AU (Fedele et al. 2017a), the HD 169142 disk has a high concentration of gas. There is already known substructure in the dust around HD 169142. A hot inner ring of dust at ~0.2 AU was detected (Wagner et al. 2015) within a central dust cavity, and two dust rings at ~25 AU and ~60 AU are clearly visible in the 1.3 millimeter continuum with ALMA (Fedele et al. 2017a) and in scattered light with the Gemini Planet Imager and the Spectro-Polarimetric High-contrast Exoplanet REsearch instrument on the Very Large Telescope (VLT/SPHERE) (Monnier et al. 2017; Pohl et al. 2017). The gap carved out between the rings may be indicative of ongoing planet formation. An outer gap at ~85 AU just beyond the edge of the 1.3 millimeter continuum emission was also detected in scattered light (Pohl et al. 2017) and in 7 and 9 millimeter emission with the Very Large Array (Macías et al. 2017). While the millimeter grains terminate at ~85 AU, the micron-sized grains are present throughout radial extent of the gaseous disk. Determining the midplane conditions of this disk would provide insight into the cold disk environment during the planet-building epoch.

This paper presents ALMA observations of the $J = 3-2$ transition of DCO$^+$ toward HD 169142 and characterizes its distribution throughout the disk. Section 4.2 describes the observations and data reduction. The detection and distribution of DCO$^+$ throughout the disk is detailed in Section 4.3. Modeling of the disk structure and DCO$^+$ emission is explained in Section 4.4. Section 4.5 discusses the relationship between DCO$^+$ and the disk environment, followed by the conclusions in Section 4.6.

4.2 Observations and reduction

The star HD 169142 (J2000: R.A. = $18^h24^m29.776^s$, DEC = $-29°46'50.000''$) was observed with ALMA in band 6 (211 – 275 GHz) with 35 antennas on 2015 August 30 at a spatial resolution of ~0.3″. The project code is ADS/JAO.ALMA# 2013.1.00592.S. The data used in this work were reduced in the same manner as Fedele et al. (2017a). Their paper provides further details on calibration, self-calibration, and continuum subtraction. Data reduction was performed with version 4.3.1 of the Common Astronomy Software Applications (CASA; McMullin et al. 2007). Images were created using the CASA task CLEAN, with natural weighting for the lines to enhance sensitivity.

The full data set contained observations of the 1.3 mm continuum and the molecular lines ^{12}CO $J = 2-1$, ^{13}CO $J = 2-1$, C^{18}O $J = 2-1$, and DCO$^+$ $J = 3-2$. The DCO$^+$ $J = 3-2$ line at 216.1128 GHz was observed in the lower sideband and had a frequency (velocity) resolution of 61.0 kHz (0.084 km s^{-1}). This work focuses on the analysis of the DCO$^+$ $J = 3-2$ data and makes use of the 1.3 millimeter continuum and C^{18}O $J = 2-1$ images. A previous analysis of the continuum and the three CO isotopolog lines was reported in Fedele et al. (2017a). Macías et al. (2017) presented a brief analysis of the C^{18}O $J = 2-1$ and DCO$^+$ $J = 3-2$ data. In their comparison of the molecular radial intensity profiles, the authors use a *uv* taper to increase the signal-to-noise ratio, resulting in a lower resolution DCO$^+$ image. We instead use a Keplerian mask to improve the signal-to-noise ratio of the DCO$^+$ integrated intensity image, thus retaining the

Table 4.1: HD 169142 observational parameters

Project 2013.1.00592.S	
Date observed	2015 August 30
Baselines	13 – 1445 m | 10 – 1120 kλ
	DCO$^+$ $J = 3-2$
Rest frequency [GHz]	216.11258
Synthesized beam [FWHM]	$0.37'' \times 0.23''$
Position angle	$-74.8°$
Channel width [km s^{-1}]	0.085
rms noise [mJy beam^{-1}]	6
v_{LSR} [km s^{-1}]	6.9
FWHM [km s^{-1}]	1.76
Integrated flux^a [mJy km s^{-1}]	730 ± 73
Weighting	natural

Notes. Flux calibration accuracy is taken to be 10%. $^{(a)}$ Line flux obtained after applying a Keplerian mask to the image cube (Section 4.3).

high spatial resolution. We also present extensive modeling of the DCO$^+$ emission to explore the sensitivity of the emission to the disk physical conditions. Table 4.1 summarizes the observational parameters for the DCO$^+$ $J = 3-2$ emission in this work.

4.3 Results

The DCO$^+$ $J = 3-2$ line in the disk around HD 169142 was readily detected and imaged at $0.37'' \times 0.23''$ (43×27 AU at 117 pc) spatial resolution, with beam P.A. = $-74.8°$. The systemic velocity is 6.9 km s^{-1} (Fedele et al. 2017a). The spectrum shown in Figure 4.1 was extracted from the original self-calibrated, continuum-subtracted CLEAN image. The right ascension and declination axes of the image cube are collapsed over a circular region with radius $1.75''$ centered on the source position.

To enhance the signal-to-noise ratio of the DCO$^+$ emission maps and radial profile, a mask in right ascension, declination, and velocity was applied to the original image cube data, following Carney et al. (2017) and Salinas et al. (2017). The mask is based on the velocity profile of a rotating disk, which is assumed to be Keplerian around a central stellar mass of $M = 1.65\ M_\odot$ (Blondel & Djie 2006). A subset of pixels are identified in each velocity channel where the pixel Keplerian velocity matches the Doppler-shifted line velocity. Pixels with velocities that do not match the Keplerian rotational profile criteria are masked. The Appendix shows the DCO$^+$ $J = 3-2$ channel maps with the Keplerian mask outline visible as the blue contours. To obtain the integrated line flux for DCO$^+$ $J = 3-2$ reported in Table 4.1, the spectrum was extracted from the image cube after applying the Keplerian mask and integrated over the velocity range 5.4 – 8.8 km s^{-1}.

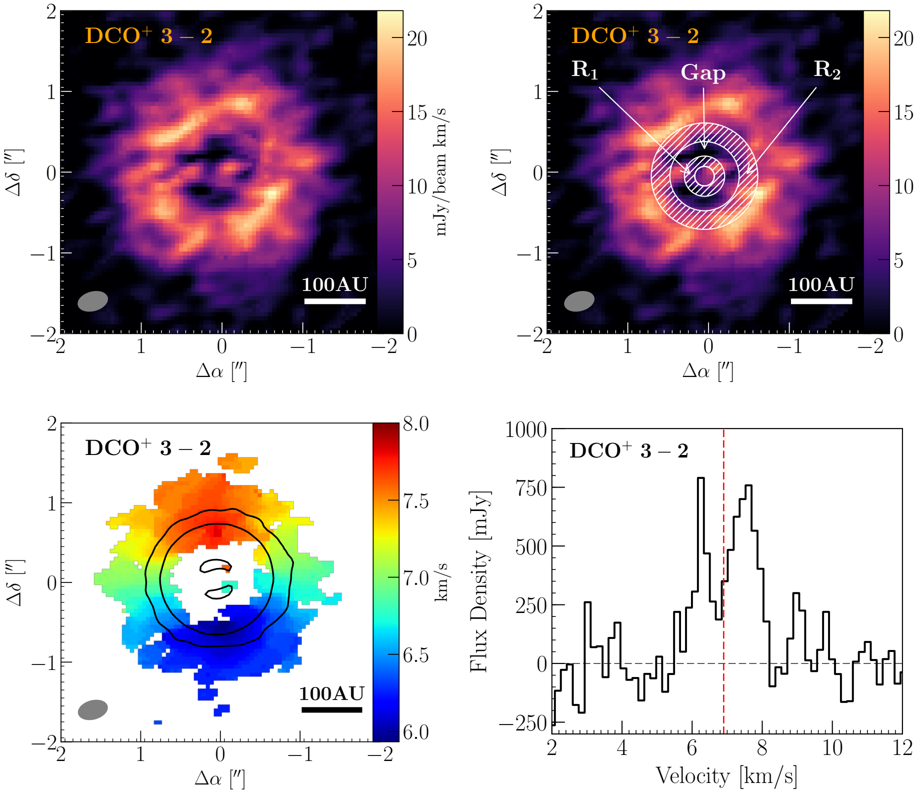

Figure 4.1: (Top left) Integrated intensity map of the DCO$^+$ $J = 3-2$ line from $5.4-8.8$ km s^{-1} after applying a Keplerian mask to the image cube. The synthesized beam and AU scale are shown in the lower corners. (Top right) DCO$^+$ $J = 3-2$ integrated intensity map overlaid with white marking the model inner dust cavity, the inner dust ring (R$_1$, hatched), the dust gap, and the outer dust ring (R$_2$, hatched). The synthesized beam and AU scale are shown in the lower corners. (Bottom left) Velocity-weighted coordinate map of the DCO$^+$ $J = 3-2$ line, clipped at 3.5σ. Solid black contours show the 233 GHz/1.3 mm emission at 7.0×10^{-5} Jy beam^{-1} (1σ) × [5, 50, 200]. The synthesized beam and AU scale are shown in the lower corners. (Bottom right) Disk-integrated spectrum of the DCO$^+$ $J = 3-2$ line before Keplerian masking, Hanning smoothed to 0.17 km s^{-1} channels. The horizontal dashed black line indicates the continuum-subtracted spectral baseline. The vertical red line shows the systemic velocity at 6.9 km s^{-1}.

4.3.1 Radial distribution of DCO$^+$

The DCO$^+$ emission has a ring-like morphology in this disk, with the majority of emission originating in a region between 0.4″ – 1.4″ (47 – 164 AU at 117 pc), based on the velocity-weighted coordinate (first-order moment) map in Figure 4.1 obtained from applying a 3.5σ clip to the emission in the Keplerian-masked DCO$^+$ image cube. The ring extends significantly beyond the outer edge of the 1.3 millimeter continuum, similar to the ^{12}CO, ^{13}CO, and C^{18}O molecular lines (Fedele et al. 2017a). Figure 4.1 also shows the integrated intensity (zero-order moment) map from velocity channels 5.4 – 8.8 km s^{-1}. Applying the Keplerian mask improved the signal-to-noise ratio of the integrated intensity image by a factor of three, from 5 to 15. The radial profile for DCO$^+$ in Figure 4.2 is obtained by taking the mean intensity in azimuthally averaged elliptical annuli projected to an inclination $i = 13°$ and position angle P.A. = 5°. The radial bin size was set to 0.1″ (11.7 AU at 117 pc). Errors are calculated as the standard deviation of the pixel intensity contained within each annulus divided by the square root of the number of beams.

With the increased signal-to-noise ratio of the averaged annuli, it is clear from the radial intensity profile that DCO$^+$ extends out to ~230 AU and peaks at a radius of ~100 AU. Within 100 AU, there is a gap between ~30 – 60 AU where the intensity drops, with some DCO$^+$ emission returning at radii $\lesssim$ 30 AU. Given the errors on the curve, the actual drop in emission in the 30 – 60 AU region may be small (see Figure 4.2). At ~150 AU there is a knee in the radial profile, and at ~200 AU there is a distinct bump.

The intensity at $r \lesssim 30$ AU already suggests that there is a warm component to the DCO$^+$ emission, as temperatures in this region of the disk are too high to allow the cold deuterium fractionation pathway to be active. As seen in Figure 4.2, the dip in DCO$^+$ intensity from $r = 30 - 60$ AU corresponds well to the gap between the two dust rings, indicated by the filled regions. With less dust and gas in the gap, the overall surface density profile falls dramatically, causing a corresponding dip in the DCO$^+$ radial profile, more prominently than seen in C^{18}O.

The DCO$^+$ intensity increases significantly within the outer dust ring, which is to be expected if DCO$^+$ is forming near the midplane where the dust temperature is sufficiently low for some degree of CO freeze-out. Interestingly, the peak in the radial profile at ~100 AU is beyond the outer edge of the second dust ring, and emission is present throughout the outer disk. This suggests that beyond the 1.3 mm continuum the disk remains cold due to the presence of micron-sized dust grains, as observed by Quanz et al. (2013), Monnier et al. (2017), and Pohl et al. (2017).

In addition, Figure 4.2 compares the radial profiles of DCO$^+$, C^{18}O, the 1.3 millimeter continuum, and the $J-$band (~1.2 μm) polarized intensity. The polarized intensity data is from VLT/SPHERE, with the radial profile obtained after azimuthally averaging the deprojection of the r^2-scaled $J-$band Q_ϕ image and normalizing to the maximum brightness of the inner ring (Pohl et al. 2017). The dust rings R$_1$ and R$_2$ are clearly visible in both the millimeter emission from ALMA and the micron emission from VLT/SPHERE. The $J-$band profile shows small grains existing throughout the extent of the gaseous disk out to ~200 AU. The radial profiles show that the DCO$^+$ emission is highly sensitive to changes in the disk structure, whereas C^{18}O is less affected. The feature at ~200 AU reveals that there is some mechanism in the disk causing more DCO$^+$ emission than would be

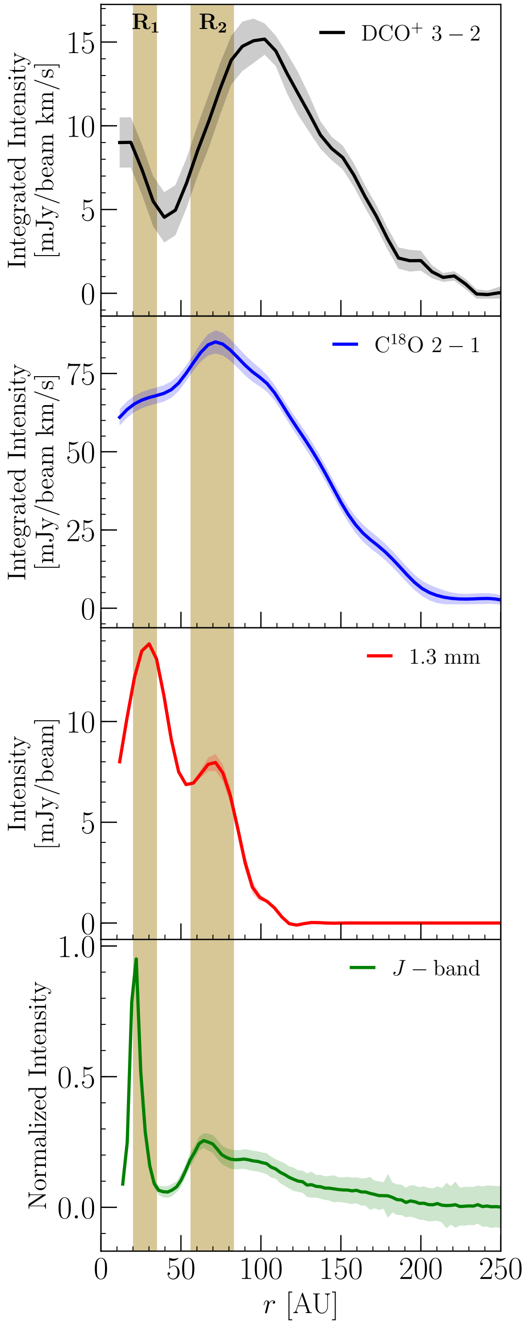

Figure 4.2: Azimuthally averaged radial intensity profiles of DCO$^+$ (top), C^{18}O (top middle), the 1.3 millimeter continuum (bottom middle), and the J–band (~1.2 μm) polarized light (bottom). Shaded regions represent 1σ errors on the intensity. Vertical brown shaded regions represent the dust rings.

expected for a smoothly decreasing abundance. There may be an accompanying slope change of the $C^{18}O$ at ~190 AU, but it is difficult to discern in Figure 4.2. A feature at large radii in the $C^{18}O$ is more apparent in the radial slice along the major axis of the disk shown in Figure 3 of Fedele et al. (2017a), where a small bump can be seen at ~1.7″ (200 AU at 117 pc), hinting at outer disk structure in $C^{18}O$. At these radii the DCO^+ is tracing midplane substructure in the disk that is not as apparent in the more abundant, optically thick CO isotopologs.

4.3.2 Column density and disk-averaged abundance in LTE

We estimate the disk-averaged abundance of the observed DCO^+ based on the total integrated line flux, an assumed excitation temperature, and the total disk mass. Following the formula used by Remijan et al. (2003) and Miao et al. (1995) for optically thin emission in local thermodynamic equilibrium (LTE), we can estimate the column density as

$$N = 2.04 \frac{\int I_\nu dv}{\theta_a \theta_b} \frac{Q_{\rm rot}\ \exp(E_u/T_{\rm ex})}{\nu^3 \langle S_{\rm ij} \mu^2 \rangle} \times 10^{20}\ {\rm cm}^{-2}, \tag{4.1}$$

where $\int I_\nu dv$ is the integrated line flux in Jy beam^{-1} km s^{-1}, θ_a and θ_b correspond to the semi-major and semi-minor axes of the synthesized beam in arcseconds, $T_{\rm ex}$ is the excitation temperature in K, and ν is the rest frequency of the transition in GHz. The partition function ($Q_{\rm rot}$), upper energy level (E_u, in K), and the temperature-independent transition strength and dipole moment ($S_{\rm ij}\mu^2$, in debye^2) for the DCO^+ molecule are taken from the Cologne Database for Molecular Spectroscopy (CDMS; Müller et al. 2005).

DCO^+ is expected to form primarily in the midplane close to the CO freeze-out temperature, where gas densities are typically higher (~10^9 cm^{-3}; Walsh et al. 2014b) than the critical density of the $J = 3 - 2$ transition at 20 – 30 K (~2×10^6 cm^{-3}; Flower 1999). Under these conditions, LTE is a reasonable assumption. Furthermore, the density of the H_2 gas taken from the Fedele et al. (2017a) model (see Figure 4.4) is greater than the critical density of DCO^+ for $z/r < 0.3$. Therefore, only if DCO^+ is present solely in the diffuse upper disk layers where the gas and dust temperature have decoupled would LTE be an unreasonable assumption. Currently, formation routes for DCO^+ place the molecule in significant abundance only in the intermediate disk layers ($\lesssim$ 100 K) and near the midplane, further justifying the use of LTE.

We explore excitation temperatures of 25, 50, and 75 K, which cover the range of expected DCO^+ emitting regions (Mathews et al. 2013; Favre et al. 2015). The total integrated line flux and excitation temperature are used to calculate a disk-averaged DCO^+ column density. Assuming optically thin emission, the disk-averaged column density was then used to estimate the total number of DCO^+ molecules in the disk $N({\rm DCO}^+) = N_{\rm avg} \times (a \times b)$, where $(a \times b)$ is the total emitting area of DCO^+. Assuming the total disk mass is primarily molecular hydrogen, we can estimate the total number of H_2 molecules $N({\rm H}_2) = M_{\rm disk}/m_{{\rm H}_2}$, where $m_{{\rm H}_2}$ is the molecular hydrogen mass. The emitting area is set to $a = b = 3''$ based on the diameter of emission in the integrated intensity map, and the total disk mass is $1.9 \times 10^{-2}\ M_\odot$. Table 4.2 shows the disk-averaged column density and abundance for $T_{\rm ex}$ = 25, 50, and 75 K, which are consistent to within a factor of two over the temperature range. DCO^+ column densities of order $10^{11} - 10^{12}$ cm^{-2} are similar

Table 4.2: DCO$^+$ disk-averaged column density and abundance.

$T_{\rm ex}$ [K]	$N_{\rm avg}$ [cm^{-2}]	$M_{\rm disk}$ [$M_\odot$]	$N({\rm DCO}^+)/N({\rm H}_2)$
25	3.7×10^{11}	1.9×10^{-2}	9.0×10^{-13}
50	4.8×10^{11}	1.9×10^{-2}	1.2×10^{-12}
75	6.3×10^{11}	1.9×10^{-2}	1.5×10^{-12}

to the values reported for HD 163296 (Mathews et al. 2013; Salinas et al. 2017), TW Hya (Qi et al. 2008), and DM Tau (Teague et al. 2015).

4.4 Modeling DCO$^+$ emission

The aim of modeling the DCO$^+$ emission in this disk was to determine the midplane conditions which create sufficient production of DCO$^+$ in the outer disk, and to estimate the contribution of cold and warm formation routes to the overall DCO$^+$ abundance. The initial physical structure of the HD 169142 disk is adopted from Fedele et al. (2017a), who constrained the density and temperature structure by simultaneously fitting the radial distribution of the 1.3 mm continuum and three CO isotopologs: ^{12}CO $J = 2-1$, ^{13}CO $J = 2-1$, and C^{18}O $J = 2-1$. The disk structure is then optimized to include a small grain dust population throughout the disk that was absent in the original model. With the optimized disk structure, we then reproduce the DCO$^+$ radial intensity profile in a parameterized way with a simple deuterium chemical network.

4.4.1 Fiducial physical structure

We use the thermo-chemical code Dust and Lines (DALI: Bruderer et al. 2012; Bruderer 2013) to obtain the physical disk structure. Input for DALI consists of a blackbody radiation field with $T_{\rm eff} = 8400$ K to estimate the stellar photosphere and a power-law gas surface density with an exponential drop-off

$$\Sigma_{\rm gas} = \Sigma_{\rm c} \left(\frac{R}{R_{\rm c}}\right)^{-\gamma} \left[\exp - \left(\frac{R}{R_{\rm c}}\right)^{2-\gamma}\right], \tag{4.2}$$

where $R_{\rm c}$ (100 AU) is the critical radius, $\Sigma_{\rm c}$ (6.5 g cm^{-2}) is the value of the gas surface density at the critical radius and γ (1.0) is the power-law exponent. The initial dust surface density is extrapolated from the gas surface density by assuming a gas-to-dust ratio ($\Delta_{\rm gd} = 80$) such that $\Sigma_{\rm dust} = \Sigma_{\rm gas}/\Delta_{\rm gd}$. The vertical gas density is described by a Gaussian distribution with a scale height $h = h_{\rm c}(R/R_{\rm c})^{\psi}$ that depends on the disk radius and the flaring exponent ψ (0.0) with a critical scale height, $h_{\rm c}$ (0.07), defined at the critical radius.

Dust settling is approximated in DALI by considering two different populations of dust grains following the power-law description from D'Alessio et al. (2006), with a power-law exponent $p = 3.5$. The small grains (0.005 – 1 μm) have a scale height h while large grains (0.005 – 1000 μm) have a scale height $h\chi$, where the settling parameter χ (0.2) is in the range $0-1$. The fractional distribution between the two populations of dust grains is set by the parameter $f_{\rm large}$ (0.85), which results in dust surface densities of $\Sigma_{\rm dust} f_{\rm large}$ for large grains and $\Sigma_{\rm dust}(1 - f_{\rm large})$ for the small grains.

The DALI code solves for dust temperatures and radiation field strength in each grid cell using two-dimensional radiative transfer, then determines the heating-cooling balance of the gas, molecular excitation, and chemical abundances based on an input chemical network. The DALI model described in this work uses the ISO chemical network, which includes CO freeze-out and CO isotope-selective photodissociation (Miotello et al. 2014, 2016).

Fedele et al. (2017a) modified the surface density profile from our Equation 4.2 to include gas depletion in the inner disk and two millimeter dust rings: R_1 from 20 – 35 AU and R_2 from 56 – 83 AU. These modifications result in a radially variable gas-to-dust ratio throughout the disk, with $\Delta_{\rm gd} = 80$ valid only for the R_2 outer dust ring from 56 – 83 AU. A full description and table of values including the parameter ranges and best-fit parameters of their fiducial DALI model can be found in Section 5.2, Figure 5, and Table 2 of their paper. Their fiducial model only included a small grain dust population within the millimeter rings since they fit only the millimeter emission. We expanded on their fiducial model by including small grains in other regions of the disk and optimized the model parameters to keep the fit to the spectral energy distribution, 1.3 mm emission, and CO isotopologs. See the Appendix for details.

4.4.2 Vertically averaged radial abundance profile in LTE

A radial abundance profile for the observed DCO$^+$ emission can be calculated using the method outlined in Section 4.3.2. Rather than estimate a global excitation temperature for DCO$^+$, with the model physical structure outlined in the previous section we can now obtain a radial description of the excitation temperature. To estimate $T_{\rm ex}$, which will be equivalent to the kinetic gas temperature assuming LTE, the midplane gas temperature in each radial bin was taken from the optimized DALI model. The line intensity was extracted from the integrated intensity map in radial bins as in Section 4.3.1, with a bin size of $0.1''$ (11.7 AU). Equation 4.1 was then used to determine the radial column density of DCO$^+$. Assuming the gas is composed primarily of H_2, the H_2 mass can be used to convert the gas surface density profile of the DALI model into a gas column density profile. Dividing the DCO$^+$ radial column density by the gas radial column density gives a radial abundance profile for DCO$^+$.

Figure 4.3 shows the DCO$^+$ radial abundance. The profile has an inner radius of 13 AU and an outer radius at 180 AU, corresponding to the inner and outer radii of the model gas surface density. Beyond $r \approx 50$ AU, the abundance increases with radius by a factor of about 5 with values ranging from $1 - 5 \times 10^{-12}$, which are comparable values to the DCO$^+$ radial abundance estimates for HD 163296 (Salinas et al. 2017). Similar trends of DCO$^+$ abundance increasing with radius have been observed in TW Hya and DM Tau (Qi et al. 2008; Teague et al. 2015). The sharp increase in abundance at $r \approx 50$ AU is due to the $\delta_{\rm gas\ gap} = 0.025$ depletion factor in the surface density of the gas for $r < R_{\rm gap\ out}$ (56 AU). Within the errors, the abundance profile remains relatively flat at radii less than $R_{\rm gap\ out}$. Due to the proximity to the central star, DCO$^+$ in this region is likely formed via the warm deuterium fractionation pathway.

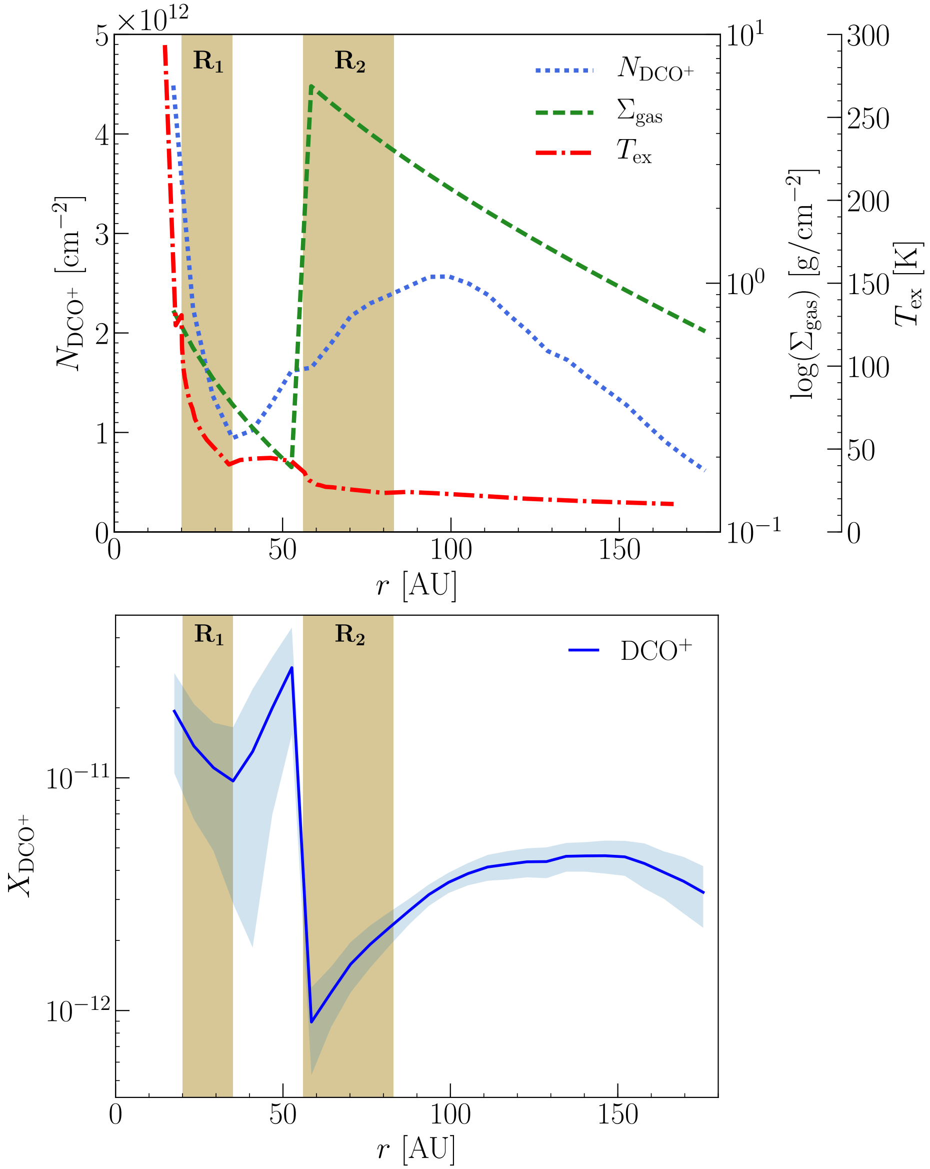

Figure 4.3: One-dimensional, radial structure in the HD 169142 disk. Vertical brown shaded regions represent the dust rings. (Top) The DCO$^+$ radial column density (dotted blue) calculated from Equation 4.1 using the DCO$^+$ the radial intensity profile (see Figure 4.2) and the midplane gas temperature of the optimized DALI model (dot-dash red) as the T_{ex} profile. The gas surface density profile (dashed green) was used to derive the DCO$^+$ radial abundance. (Bottom) Radial abundance structure of DCO$^+$ with respect to H$_2$. The blue shaded region represents 1σ errors on the abundance.

4.4.3 Parameterized models

We move from the one-dimensional derivation of the DCO$^+$ radial profiles to a two-dimensional DCO$^+$ structure to explore variations in abundance for different radii and heights in the disk. For this we parameterize the HD 169142 physical disk structure obtained from the optimized DALI model, shown in Figure 4.4. The DALI code calculates the dust temperature, the local radiation field, heating and cooling rates, molecular abundances, and gas temperature self-consistently, making it difficult to isolate and explore individual parameters that may affect DCO$^+$ emission. We examine the effect of alterations to the disk gas temperature and CO abundance on DCO$^+$ production by employing a simple, parameterized modeling technique using the steady-state, analytic chemical code (hereafter DCO+ CHEMNET) from Murillo et al. (2015). This time-independent chemical model is preferred because the chemical timescales for gas-phase reactions are sufficiently fast that a steady state is achieved at times much shorter than the expected lifetime of the HD 169142 disk (~10 Myr). Murillo et al. (2015) have already shown that the DCO+ CHEMNET code reproduces the trends of full, time-dependent chemical models for protostellar envelopes. We extend this treatment to the protoplanetary disk environment. Section 4.1, Table 1, and subsection 4.2.3 in their paper give a full description of the chemical network, the simplified set of DCO$^+$ formation and destruction reactions via the cold deuterium fractionation pathway, and a comparison to a full chemical network.

The DCO+ CHEMNET code takes as input the gas density, gas temperature, and CO abundance structure. The input profiles are taken from the output of the optimized DALI model described in the Appendix. Because DCO+ CHEMNET is a single-point code, each grid cell in (r, z) of the DALI disk grid was run separately to capture the full two-dimensional model structure. The gas density of the parameterized models is assumed to be equal to the molecular hydrogen density n_{H_2}, and the HD abundance is constant at $X_{\mathrm{HD}} = n_{\mathrm{HD}}/n_{\mathrm{H}} = 10^{-5}$ throughout the disk. The cosmic ray ionization rate of H$_2$ is set to $\zeta_{\mathrm{cr}} = 1.26 \times 10^{-17}$ s^{-1}.

The parameterized models are used to probe the conditions near the midplane of the outer disk, a region to which previously observed CO isotopolog tracers are not sensitive. The CO observations do not probe all the way down to the midplane in the outer disk and only a small amount of CO is absent from the total column density, while DCO$^+$ production is highly sensitive to the midplane conditions (Mathews et al. 2013; Qi et al. 2015; Favre et al. 2015; Huang et al. 2017). The CO lines become optically thick beyond $R_{\mathrm{dust\ out}}$ (83 AU) near the midplane of the optimized DALI model ($z/r < 0.2$ and < 0.1 for ^{12}CO and C^{18}O, respectively) so the physical structure is not constrained in this region. Therefore, in all parameterized models, only the region $r > 83$ AU and $z/r < 0.1$ was altered since this is the $\tau_{\mathrm{mm}} = 1$ surface of C^{18}O $J = 2-1$ from the DALI model. The region $z/r < 0.1$ quickly becomes highly optically thick for C^{18}O $J = 2-1$ with optical depths of $\tau_{\mathrm{mm}} = 10$ near the midplane. For $z/r > 0.1$, the C^{18}O abundance of the model would have been sensitive to changes in the gas temperature. Thus, where $z/r < 0.1$, we can alter the disk structure without affecting the intensity profiles of the CO isotopologs.

Five parameterized model scenarios are tested: a disk with high midplane CO abundance, a disk with low midplane CO abundance, a cold disk, a shadowed cold disk, and a shadowed cold disk including CO depletion. The aim is to initially test the CO abundance and the gas temperature separately to investigate

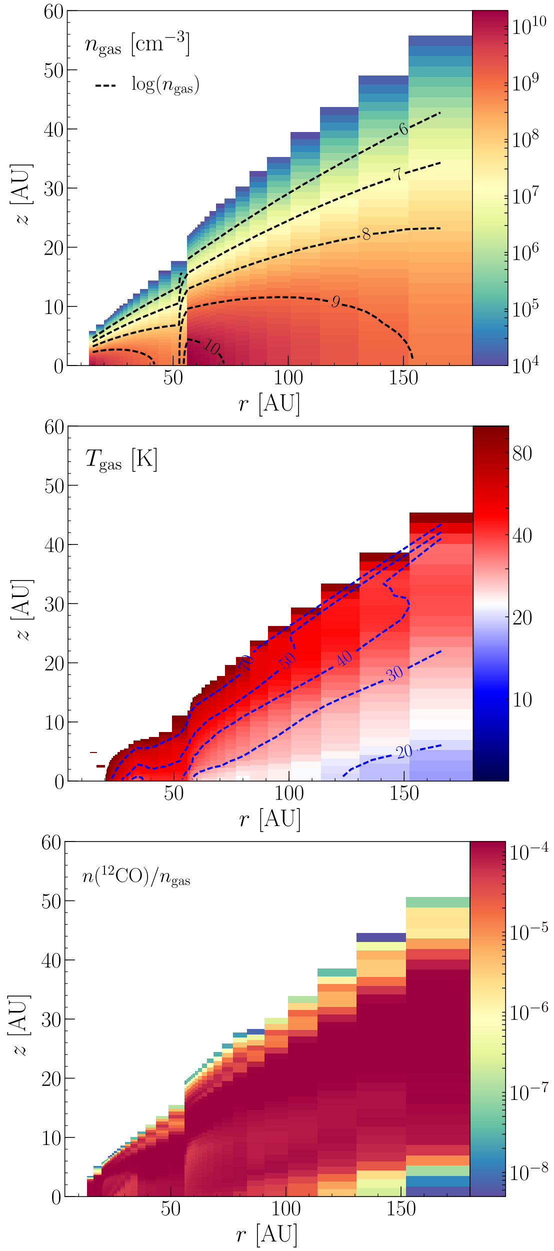

Figure 4.4: Two-dimensional physical structure of the HD 169142 disk from the optimized DALI model (see Appendix). (Top) Gas density structure. The gas density contours (dashed black) are shown as log of the molecular hydrogen number density $n_{\rm gas}$. (Middle) Gas temperature structure below 100 K. Temperature contours are shown in dashed blue. (Bottom) CO abundance structure with respect to H_2.

which parameter has a stronger influence on the production of DCO$^+$. These two parameters are intrinsically interlinked (i.e., more CO freeze-out will occur in lower temperature environments), and the parameterized models allow us to explore these effects in isolation. In the parameterized models we also include an additional DCO$^+$ constant abundance region to act as a proxy for warm DCO$^+$ formation.

Fits to the radial intensity profile of the data are used to evaluate the model parameters. To obtain model intensity profiles, synthetic DCO$^+$ image cubes are created using the two-dimensional gas density, gas temperature, and DCO$^+$ abundance structure from DCO+ CHEMNET as input to the Line Modeling Engine (LIME; Brinch & Hogerheijde 2010) radiative transfer code. The LIME code was run in LTE with 30000 grid points to create synthetic images of the DCO$^+$ $J = 3 - 2$ transition. The images are continuum-subtracted and sampled in the *uv* plane using the PYTHON `vis_sample`[1] routine, which reads the *uv* coordinates directly from our observed ALMA measurement set and creates synthetic visibilities of the model. The model visibilities are imaged in CASA using CLEAN with natural weighting, and an integrated intensity map is created over the same velocity range as the data ($5.4 - 8.8$ km s^{-1}). Azimuthally averaged elliptical annuli projected to the disk inclination and position angle are used to extract the integrated intensity of the model with the same radial bins as the data.

DCO$^+$ from deuterium fractionation

Formation of DCO$^+$ occurs as a result of deuterium fractionation, which is an enhancement in the D/H ratio observed in certain deuterium-bearing molecules. Typically, deuterium fractionation occurs in colder environments such as pre-stellar cores and below the surface layers of protoplanetary disks because of the lower zero-point energies of the deuterated molecular ions (Brown & Rice 1986; Millar et al. 1989). Deuterium fractionation in the low-temperature regime occurs via the reaction (Wootten 1987)

$$\mathrm{HD} + \mathrm{H_3^+} \longleftrightarrow \mathrm{H_2} + \mathrm{H_2D^+} + \Delta E, \tag{4.3}$$

where $\Delta E = 220$ K (Roberts & Millar 2000; Gerlich et al. 2002; Albertsson et al. 2013). This deuterium fractionation pathway is typically efficient at temperatures below ~30 K due to the energy ΔE needed for the back-reaction. The DCO$^+$ molecule is then formed by the following reaction

$$\mathrm{H_2D^+} + \mathrm{CO} \longrightarrow \mathrm{H_2} + \mathrm{DCO^+}. \tag{4.4}$$

Gas-phase CO is needed to produce DCO$^+$, but CO will also rapidly combine with H_3^+, quenching the production of H_2D^+. Thus there is a balance where CO must be sufficiently depleted for H_2D^+ to remain abundant yet enough gas-phase CO must be present so that DCO$^+$ may form. The simple chemical network from Murillo et al. (2015) is used in this work to model DCO$^+$ produced via the cold deuterium fractionation pathway. The model shown in Figure 4.4 suggests that DCO$^+$ is expected throughout much of the disk midplane, as temperatures are cold enough for CO freeze-out and the production of H_2D^+.

---

[1] `vis_sample` is publicly available at `https://github.com/AstroChem/vis_sample` or in the Anaconda Cloud at `https://anaconda.org/rloomis/vis_sample`

Table 4.3: Parameterized models of HD 169142.

Model	Disk Region		Temperature Profile	Abundance Modifications	
	r [AU]	z/r	T^a [K]	CO factor^b [$\times$CO]	$X(\mathrm{DCO}^+_{\mathrm{warm}})^c$
High CO	≥ 83	< 0.1	T_{gas}	10	2.0×10^{-12}
Low CO	≥ 83	< 0.1	T_{gas}	0.1	2.0×10^{-12}
Cold disk	≥ 83	< 0.1	$T_{\mathrm{gas}} - 2$	–	2.0×10^{-12}
Cold disk – shadowed	83 – 120	< 0.1	$T_{\mathrm{gas}} - 8$	–	2.0×10^{-12}
	> 120	< 0.1	$T_{\mathrm{gas}} - 2$	–	2.0×10^{-12}
Cold disk – shadowed	83 – 120	< 0.1	$T_{\mathrm{gas}} - 8$	0.2	2.0×10^{-12}
and depleted	> 120	< 0.1	$T_{\mathrm{gas}} - 2$	–	2.0×10^{-12}

Notes. $^{(a)}$ T_{gas} is the two-dimensional gas temperature structure taken from the optimized DALI model (Figure 4.4). $^{(b)}$ The CO factor is multiplied by the CO abundance structure taken from the optimized DALI model (Figure 4.4). $^{(c)}$ The $X(\mathrm{DCO}^+_{\mathrm{warm}})$ component is included from 30 – 70 K.

Deuterium fractionation in disks can also occur when HD and CH_3^+ combine to create H_2 and $\mathrm{CH}_2\mathrm{D}^+$ (Millar et al. 1989). The molecule DCO^+ is then formed via $\mathrm{CH}_2\mathrm{D}^+$ reactions directly or via one of its products, $\mathrm{CH}_4\mathrm{D}^+$. The energy required for the back-reaction of this deuterium fractionation pathway was recently revised (ΔE = 654 K; Roueff et al. 2013) and suggests that $\mathrm{CH}_2\mathrm{D}^+$, and therefore DCO^+, could be formed efficiently at higher temperatures. In recent models of the TW Hya disk with a full deuterium chemical network, Favre et al. (2015) find that $T \geq 71$ K is sufficient to switch off the production of DCO^+ formed via $\mathrm{CH}_2\mathrm{D}^+$. The warmer $\mathrm{CH}_2\mathrm{D}^+$ fractionation route dominates over the cold $\mathrm{H}_2\mathrm{D}^+$ fractionation route for temperatures greater than ~30 K because of the higher value for ΔE and the fact that H_2 will readily destroy $\mathrm{H}_2\mathrm{D}^+$ above ~30 K.

CO abundance versus gas temperature

Table 4.3 shows the parameters used for each model scenario. The high CO and low CO models respectively increase and decrease the CO abundance in the region of interest ($r > 83$ AU and $z/r < 0.1$) in order to determine how changes in the availability of gas-phase CO influence the DCO^+ emission. The cold disk model tests the influence of the gas temperature on the DCO^+ emission by moderately decreasing the temperature profile in the region of interest. The shadowed cold disk model expands on the cold disk model by creating a secondary colder region just outside of the edge of the millimeter grains.

In this work we do not include a chemical network describing the formation of DCO^+ via the warm deuterium fractionation pathway. The complexity of hydrocarbon cation chemistry on which the warm deuterium fractionation pathway depends introduces large uncertainties in the results of even basic chemical networks. As a first-order approximation, we instead adopt a region of constant DCO^+ abundance for 30 K $\leq T \leq$ 70 K, with the lower temperature limit based on the energy required for the back-reaction in Equation 4.3 and the upper temperature limit based on the results of Favre et al. (2015), where they find that formation of DCO^+ via the warm deuterium fractionation pathway is effectively switched off at 71 K. In this way we introduce a proxy in the model that is representative of DCO^+ production in the high-temperature regime, with the reasonable expectation that the warmer pathway will contribute little to the emission of the outer disk (Öberg et al. 2015), which is the focus of this work. Further investigation on the detailed contribution of the warm deuterium fractionation pathway to the overall DCO^+ production, with particular attention to the inner regions of the disk at radii $\lesssim 50$ AU, will be the focus of future work.

The constant abundance component from $30-70$ K is tuned so that the model radial profile matches the intensity of the observed DCO^+ emission from $40-70$ AU, where warm DCO^+ is the primary contributor before peaking and turning over at $70-80$ AU. This gives $X(\mathrm{DCO}^+_{\mathrm{warm}}) = 2.0 \times 10^{-12}$, which is consistent with the DCO^+ abundance found by Willacy & Woods (2009) in models of a protoplanetary inner disk at radii less than 30 AU, and consistent with the abundance between $30-70$ K in more recent work by Öberg et al. (2015) in their model of IM Lup. It is roughly one to two orders of magnitude lower than the abundance found by Favre et al. (2015), but their warm DCO^+ was confined to a thin layer spanning only $1-2$ AU at radii less than 60 AU. In HD 169142 the $30-70$ K layer spans roughly $5-15$ AU, depending on the radius, and results in a DCO^+ column density on the order of 10^{12} cm^{-2}, which is consistent with Favre et al. (2015). With this treatment, the warm deuterium fractionation pathway contributes $< 20\%$ to the DCO^+ radial intensity profile for $r > 83$ AU in all models considered. For $r < 83$ AU, the warm component is the primary contributor to the overall DCO^+, producing $> 80-95\%$ of the emission, depending on the model. For $r \lesssim 30$ AU, no warm component of DCO^+ exists in the model because the midplane gas temperature reaches 70 K at ~30 AU. Because the warm component is set to the same abundance value for all parameterized models, we consider the outer disk at $r > 83$ AU for comparison between the data and the model.

Figure 4.5 shows the gas temperature map and CO abundance map used as input, the DCO^+ abundance map calculated by DCO+ CHEMNET with the additional constant abundance warm component included, and the DCO^+ radial intensity profiles derived from the LIME synthetic images with only the cold deuterium fractionation pathway active (C only) and with the constant abundance warm component included (C + W). The no modifications model in the first row of Figure 4.5 uses the input from our optimized DALI model with no alterations to the midplane disk structure. It is already clear that the DCO^+ emission is underproduced by the DCO+ CHEMNET code for the disk structure outlined in the Appendix.

In the low CO abundance case, an order of magnitude decrease in midplane gas-phase CO abundance results in a factor of two to three decrease in DCO^+ emission because there is no longer enough gas-phase CO available to efficiently form DCO^+. The high CO abundance model with an order of magnitude increase in gas-phase CO abundance results in only a factor of two increase in DCO^+ emission, highlighting the non-linear nature of the chemistry. CO abundances in this model become much higher than the canonical value of ~10^{-4} with respect to H_2 in the midplane of disk where CO depletion is expected; hence, this model is physically unrealistic. Order of magnitude variations to the CO abundance do not have a significant influence on the formation of DCO^+ near the outer disk midplane for the physical structure given by the optimized DALI model.

The second and third rows of Figure 4.5 illustrate increasingly colder midplane scenarios. In the cold disk model case, a decrease of 2 K in the gas temperature provides an improved fit to the DCO^+ radial profile but still fails to fully recover much of the DCO^+ between $80-140$ AU. It matches the observed intensity profile well beyond 150 AU. The shadowed cold disk model expands on the cold disk model to invoke a secondary cold region from $r = 83 - 120$ AU with $T = T_{\rm gas} - 8$ K. For the secondary cold region, the outer boundary and temperature drop parameters are explored from $100 - 140$ AU in steps of 10 AU and from $T_{\rm gas} - 3$ K to $T_{\rm gas} - 10$ K in steps of 1 K, respectively. The outer boundary at 120 AU and the temperature drop of $T_{\rm gas} - 8$ K was found to provide the best improvement on the fit to the DCO$^+$ profile. More DCO$^+$ is produced in the shadowed cold disk model between $80 - 150$ AU than in the cold disk model case, but it is still not enough to capture the 100 AU peak. The final model invokes additional CO depletion in the secondary cold region of the shadowed cold disk model, which would be expected for significantly colder disk regions. The CO abundance is further reduced by a factor of five between $r = 83 - 120$ AU. CO depletion factors of two, five, and ten are tested, with a factor of five resulting in the right amount of DCO$^+$ emission. In this scenario, the DCO$^+$ radial intensity profile, including the 100 AU peak, is reproduced well.

The efficiency of the cold deuterium fractionation pathway, and thus the production of DCO$^+$, is also affected by cosmic ray ionization $\zeta_{\rm cr}$, and the ortho-to-para (o/p) ratio of H$_2$. Ionization of H$_2$ in the disk by cosmic rays will affect the number of H_3^+ ions and the number of free electrons. The DCO+ CHEMNET code was rerun for the model with no modifications to test changes to the cosmic ray ionization rate, initially set to $\zeta_{\rm cr} = 1.26 \times 10^{-17}$ s^{-1}. There is evidence that the local ISM in the HD 169142 region may reach values of $\zeta_{\rm cr} = 1 - 5 \times 10^{-16}$ s^{-1} (Indriolo et al. 2007; Neufeld & Wolfire 2017). An increase in $\zeta_{\rm cr}$ of one order of magnitude results in DCO$^+$ emission comparable to the cold disk model, meaning that the amount of DCO$^+$ observed at $r > 120$ AU may be a consequence of a higher local cosmic ray ionization rate or may be due to a moderate decrease in the gas temperature of the outer disk. Ionization of the outer disk by UV radiation may influence the cold deuterium fractionation pathway and free electron population differently, but the effect is not modeled here. Such ionization would influence primarily the disk upper layers, as UV photons will not reach the disk midplane with a sufficient flux to outpace ionization due to cosmic rays.

The ortho-to-para (o/p) ratio of H$_2$ influences the survival of H_2D^+ in cold regions of the disk because the back-reaction in Equation 4.3 requires less energy for o-H$_2$ ($\Delta E = 61$ K) than for p-H$_2$ ($\Delta E = 232$ K; Walmsley et al. 2004). We apply a thermal treatment of the o/p ratio of H$_2$ in LTE following Murillo et al. (2015) with $\mathrm{o/p} = 9 \times \exp(-170/T)$, where T is the gas temperature, and again rerun DCO+ CHEMNET code for the no modification model including the H$_2$ o/p ratio, which was not considered in the original models. In this case, too much DCO$^+$ emission is produced in the outer disk for $r > 150$ AU, but DCO$^+$ is underproduced for $r < 150$ AU. However, this treatment requires an efficient equilibration of the H$_2$ spin temperature with the gas temperature, rather than the 3:1 o/p ratio obtained from grain surface formation of H$_2$. The degree of cosmic ray ionization and the precise distribution of the o/p ratio of H$_2$ will affect the exact values for the temperature drop and CO depletion necessary to obtain a fit to the DCO$^+$ radial intensity profile, but our overall conclusions remain unchanged.

Based on the best-fit shadowed and depleted cold disk model, a significantly colder outer disk midplane with increased CO freeze-out is the most likely scenario for DCO$^+$ production beyond the millimeter grains. The DCO$^+$ emission at $r > 120$ AU could be reproduced with a small drop in the gas temperature or an increase in the cosmic ray ionization rate. The modeling efforts presented here show that DCO$^+$ emission can reveal structure in low-temperature regions in the midplane of disks that are not apparent in the CO isotopologs.

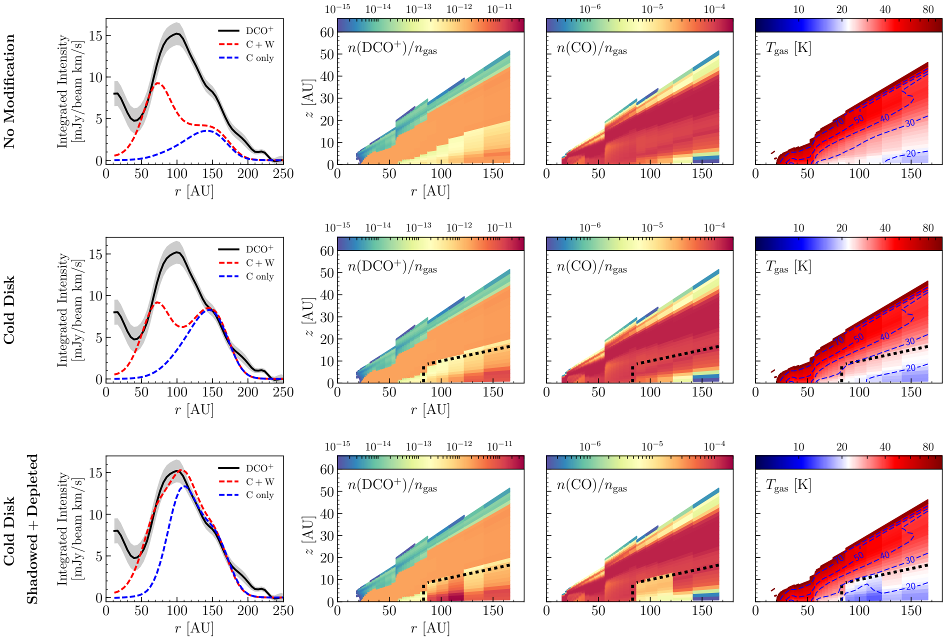

Figure 4.5: Parameterized modifications to the optimized DALI model described in the Appendix. The right and right middle plots show the gas temperature and CO abundance, respectively. The black dashed box shows the modified region. The left middle plot shows the DCO$^+$ abundance map calculated with DCO+ CHEMNET with the $30 - 70$ K constant abundance warm component included. The left plot shows the DCO$^+$ radial intensity profiles of the data (solid black with shaded gray 1σ errors) and of the model with the cold component only (C only; dashed blue) and with warm component included (C + W; dashed red). (Top) The optimized DALI model with no modifications made to the gas temperature or CO profile. (Middle) Cold disk model. The gas temperature is decreased by 2 K in the black dashed region. (Bottom) Shadowed and depleted cold disk model. This is an extension of the cold disk model to simulate a secondary colder region beyond the millimeter dust edge. The gas temperature is decreased by 8 K with CO depleted by a factor of five from $r = 83 - 120$ AU. The gas temperature is decreased by 2 K for $r > 120$ AU.

4.5 Discussion

The interpretation of DCO$^+$ emission regarding its chemical origins and location within the disk is complicated by the multiple deuterium fractionation pathways available. The two main pathways (cold, via H_2D^+ fractionation and warm, via CH_2D^+ fractionation) are efficient over different temperature ranges, therefore it is useful to consider DCO$^+$ emission from distinct regions of the disk where the conditions are expected to be more favorable for one fractionation pathway over the other. The inner disk provides warmer temperatures that can switch off the H_2D^+ pathway, while the outer disk hosts a cold midplane that allows the H_2D^+ pathway to operate efficiently.

4.5.1 Inner disk DCO$^+$

In models of TW Hya including a full deuterium chemical network, Favre et al. (2015) found that DCO$^+$ observed in the inner tens of AU is not primarily formed by the cold deuterium fractionation pathway via H_2D^+ because of the warm temperatures of the inner disk. The physical structure in Figure 4.4 shows that the disk around HD 169142 is far too warm in the inner 50 AU for the H_2D^+ fractionation pathway to be the main contributor. Instead, DCO$^+$ in this region is likely formed by the warmer CH_2D^+ fractionation pathway. The disk temperature at the midplane is greater than 70 K for $r < 30$ AU, therefore even the warm component is switched off. In this disk, DCO$^+$ formed via the CH_2D^+ fractionation pathway may continue to be active at temperatures greater than 70 K. Alternatively, we may be missing a cool inner component, such as inner disk dust rings that could keep temperatures low enough for the warm deuteration fractionation pathway to remain active. Andrews et al. (2016) observed optically thick millimeter dust rings on the order of a few AU in the disk around TW Hya. Recent work by Ligi et al. (2018) presented a tentative detection of another dust ring in the HD 169142 disk located at ~0.1″ (12 AU at 117 pc) using VLT/SPHERE radial differential imaging with the Infrared Dual-band Imager and Spectrograph and the Integral Field Spectrograph instruments.

The molecule DCN provides another avenue to probe the warm component of DCO$^+$ emission as it is also formed via warm deuterium fractionation in disks (Millar et al. 1989). Co-spatial peaks in DCO$^+$ and DCN would indicate that the warm deuterium fractionation pathway is a strong contributor to the production of DCO$^+$. Recent observations of DCN and DCO$^+$ in several T Tauri and Herbig Ae/Be sources show them peaking in different regions of the disk, but with some DCO$^+$ present where the DCN peaks, indicating that the warm deuterium fractionation pathway contributed partially to the DCO$^+$ emission (Qi et al. 2008; Öberg et al. 2012; Huang et al. 2017; Salinas et al. 2017).

4.5.2 Outer disk DCO$^+$

In order to recover the observed DCO$^+$ radial intensity profile, it was necessary to modify the structure of the optimized DALI model from Figure 4.4 to include a much colder, CO-depleted region beyond the edge of the millimeter grains. The cause of the decrease in temperature could be due to the number and location of micron-sized grains in the outer disk, which have been observed out to at least 200 AU in scattered light imaging (Quanz et al. 2013; Momose et al. 2015; Monnier et al. 2017; Pohl et al. 2017). The exact local distribution of the micron-sized grains in the HD 169142 disk might be different than the distribution approximated in the optimized DALI model, leading to lower gas temperatures in the outer disk.

The fact that the peak in the DCO^+ radial intensity profile occurs at 100 AU is already evidence that the colder H_2D^+ deuterium fractionation pathway is responsible for the majority of DCO^+ production in this disk. As mentioned in Section 4.5.1, the warm component is not significant beyond the edge of the millimeter grains (r = 83 AU), with DCO^+ formed via the cold network in DCO+ CHEMNET contributing > 80% to the radial intensity profile. In this context, it is probable that the 100 AU peak observed in the DCO^+ profile is tracing the CO snow line as CO begins to freeze out onto dust grains, but is still sufficiently abundant in the gas-phase to allow for the formation of DCO^+. Macías et al. (2017) previously compared the $C^{18}O$ and DCO^+ radial intensity profiles and similarly concluded that a co-incident slope change in the $C^{18}O$ and peak in the DCO^+ is evidence that DCO^+ is tracing the CO snow line, which they locate at ~100 AU. The modeling done in this work shows that invoking a cold, CO-depleted region in the outer disk midplane from ~80 – 120 AU is necessary to recover the DCO^+ radial intensity profile in the parameterized models, indicating that the bulk of the DCO^+ does indeed trace regions of CO freeze-out in the HD 169142 disk.

There is tentative evidence for an outer DCO^+ ring, seen as a bump in the DCO^+ radial profile at the edge of the gaseous disk around 200 AU. Similar DCO^+ structure has been seen in other disks, e.g., IM Lup, LkCa 15, and HD 163296 (Öberg et al. 2015; Huang et al. 2017; Salinas et al. 2017; Flaherty et al. 2017). An outer ring could indicate that some CO ice is returned to the gas phase in the outer disk via thermal desorption caused by a temperature inversion or via photodesorption by UV radiation (Huang et al. 2016; Cleeves 2016; Cleeves et al. 2016; Facchini et al. 2017). The observed bump is weaker than the outer DCO^+ ring in other disks, suggesting that the HD 169142 disk remains cold out to large radii or that the degree of CO freeze-out in this disk may not be as extreme as in other sources.

Follow-up observations of N_2H^+ in this disk could provide further insight into the relationship between DCO^+ and CO freeze-out. Formation of N_2H^+ requires low temperatures and significant CO depletion, and therefore is expected to be abundant only in the cold midplane where there is a high degree of CO frozen out onto the surface of dust grains (Walsh et al. 2012; Qi et al. 2015; van't Hoff et al. 2017). Co-spatial emission of N_2H^+ and DCO^+ in the outer disk would place strong constraints on the extent to which DCO^+ is directly tracing CO freeze-out.

4.6 Conclusions

In this paper we present ~0.3″ resolution ALMA observations of DCO^+ $J = 3-2$ in the protoplanetary disk around HD 169142. We update the fiducial DALI model from Fedele et al. (2017a) to include small dust grains throughout the disk and employ a simple deuterium chemical network to investigate the production of DCO^+ formed by the cold deuterium fractionation pathway (via H_2D^+). The CO abundance and gas temperature structure of the DALI disk model is adapted in a parameterized way using the DCO+ CHEMNET code to recover the observed DCO^+ radial intensity profile. The warm deuterium fractionation pathway (via CH_2D^+) is approximated with a constant abundance between 30 – 70 K in the parameterized models. The conclusions of this work are the following:

- DCO^+ has a broad, ring-like morphology over radii ~50 – 230 AU in the disk around HD 169142, with most of the emission located outside of the millimeter continuum edge. There is an inner component to the DCO^+ radial profile with emission returning in the central ~30 AU. The DCO^+ radial intensity profile peaks at ~100 AU, with a tentative secondary bump at ~200 AU.

- Parameterized modeling of the HD 169142 disk shows that lowering the gas temperature in optically thick regions near the midplane of the outer disk by several Kelvin has a significant effect on the DCO^+ profile. Order of magnitude changes to the CO abundance in the same region cause the DCO^+ radial profile to increase or decrease only by a factor of 2−3, still underproducing the amount of observed DCO^+. It was necessary to invoke both effects to successfully reproduce the full radial intensity profile.

- The best-fit parameterized model has a shadowed, cold region with CO depletion near the disk midplane just beyond the edge of the millimeter grains. For $z/r < 0.1$ and $r > 83$ AU, the model recovers the radial intensity profile of DCO^+ with a $T = T_{\rm gas} - 8$ K region with a factor of five CO depletion from $r = 83 - 120$ AU, and a $T = T_{\rm gas} - 2$ K region for $r > 120$ AU. The exact values for the drop in $T_{\rm gas}$ and CO abundance will also depend on the ionization degree and the ortho-to-para ratio of H_2. The fact that the added shadowed region is needed to recover the 100 AU radial intensity peak highlights the sensitivity of DCO^+ to small changes in the gas temperature and CO abundance structure.

- The best-fit model suggests that the contribution to the overall DCO^+ emission from the cold deuterium fractionation pathway via H_2D^+ is > 85% at $r > 83$ AU, while the contribution from the warm deuterium fractionation pathway via CH_2D^+ is > 80% at radii less than $r < 83$ AU using a constant abundance of $X(DCO^+_{\rm warm}) = 2.0\times10^{-12}$ from 30−70 K. The warm component does not recover the return of DCO^+ emission within ~30 AU for the current disk structure.

- DCO^+ is an optically thin molecular tracer that acts as a filter to detect disk substructure that is not observable in more abundant, and therefore more easily detectable, molecular tracers such as ^{12}CO, ^{13}CO, and $C^{18}O$. In this work, DCO^+ observations reveal the low-temperature ($\lesssim 25$ K) midplane structure in the disk around HD 169142.

This work shows that DCO^+ can be used as a valuable tracer of protoplanetary disk midplane conditions with simple models and chemical networks. To fully characterize the complex chemical origins of DCO^+ in the disk around HD 169142, full dust evolution models (e.g., Facchini et al. 2017) and an expanded deuterium chemical network such as the one used by Favre et al. (2015) would be required. Further constraints could be placed on the origins of DCO^+ with future ALMA observations of additional chemical tracers, such as DCN and N_2D^+, that would correlate with DCO^+ formed via the warm and cold deuterium fractionation pathways, respectively.

Acknowledgements

The authors thank the anonymous referee for useful comments that helped to improve the paper. M.T.C. thanks A. Pohl for providing the VLT/SPHERE $J-$band polarized intensity data. M.T.C. and M.R.H. acknowledge support from the Netherlands Organisation for Scientific Research (NWO) grant 614.001.352. C.W. acknowledges the NWO (grant 639.041.335) and the University of Leeds for financial support. D.F. and C.F. acknowledge support from the Italian Ministry of Education, Universities and Research, project SIR (RBSI14ZRH). A.M. acknowledges an ESO Fellowship. This paper makes use of the following ALMA data: ADS/JAO.ALMA# 2013.1.00592.S. ALMA is a partnership of ESO (representing its member states), NSF (USA) and NINS (Japan), together with NRC (Canada), NSC and ASIAA (Taiwan), and KASI (Republic of Korea), in cooperation with the Republic of Chile. The Joint ALMA Observatory is operated by ESO, AUI/NRAO and NAOJ.

Appendix A: Model details

Modifications to the fiducial DALI model from Fedele et al. (2017a) were necessary to more accurately incorporate the (sub)micron-sized grain population into the HD 169142 disk model and to obtain a better description of the dust and gas temperature of the outer disk beyond the millimeter continuum edge. Here the modifications are discussed in more detail.

The Fedele et al. (2017a) model fit the 1.3 mm dust emission, and dust in their models exists only within dust rings from $r = 20-35$ AU and from $r = 56-83$ AU. There is no dust of any kind in their models outside of these radii. Observations by Quanz et al. (2013), Monnier et al. (2017), and Pohl et al. (2017) have revealed the presence of a micron-sized dust population in the millimeter ring gap and in the outer disk beyond the millimeter-sized dust population. Monnier et al. (2017) discussed an outer disk in the context of micron-sized grains observed in the *J* band with the Gemini Planet Imager. The authors detected a dip in polarized light at ~55 AU which they model as a $40-70$ AU gap, and they observed a flared outer ring that peaks at ~75 AU. The authors adopted a distance of 145 pc for HD 169142. Their radii scaled to the new Gaia distance of 117 pc gives a $32-56$ AU gap and a 60 AU outer ring peak in the *J* band, consistent with the values for the millimeter gap and outer ring observed by Fedele et al. (2017a).

The original dust structure of the Fedele et al. (2017a) model was

Table 4.4: HD 169142 DALI model parameters.

Parameter	Value	Ref.
M_*	1.65 $M_\odot$	1
$T_{\rm eff}$	8400 K	2
L_*	10 $L_\odot$	3
d	117 pc	3
i	13°	3,4
P.A.	5°	3,4
χ	0.2	3
$f_{\rm large}$	0.85	3
ψ	0	3
γ	1	3
$h_{\rm c}$	0.07	3
$R_{\rm c}$	100 AU	3
$\Delta_{\rm gd}$	80	3
$\Sigma_{\rm c}$	6.5 g cm^{-2}	3
$R_{\rm gas\ in}$	13 AU	3
$R_{\rm dust\ in}$	20 AU	3
$R_{\rm gap\ in}$	35 AU	3
$R_{\rm gap\ out}$	56 AU	3
$R_{\rm dust\ out}$	83 AU	3
$R_{\rm gas\ out}$	180 AU	3
$\delta_{\rm dust}$	0.27	3
$\delta_{\rm gas\ cavity}$	0.025	3
$\delta_{\rm gas\ gap}$	0.025	3

Notes. References. 1: Blondel & Djie (2006); 2: Dunkin et al. (1997); 3: Fedele et al. (2017a); 4: Raman et al. (2006).

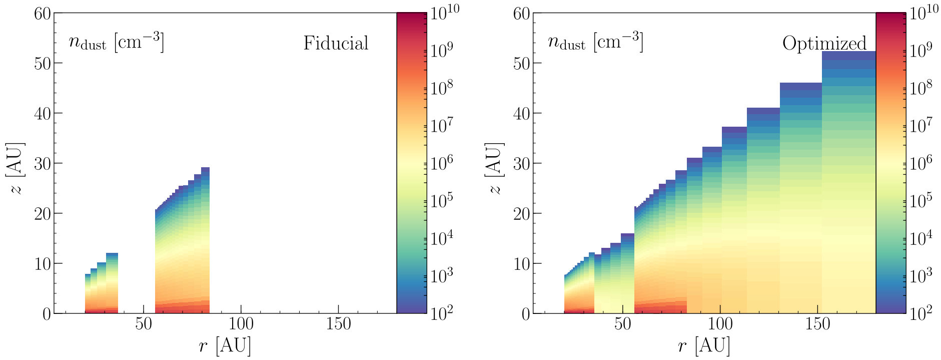

Figure 4.6: (Left) Dust structure of the fiducial DALI model from Fedele et al. (2017a) with small (0.005 – 1 μm) and large (0.005 – 1000 μm) grains present only in the millimeter rings. (Right) Dust structure of the optimized DALI model with small grains in the millimeter gap and in the outer disk. The hot inner dust ring is not visible due to the extremely small scale height at $r = 0.2$ AU.

$$n_{\rm dust} = \begin{cases} 0 & \text{for } r < R_{\rm dust\ in} \\ \delta_{\rm dust} \times n_{\rm dust} & \text{for } R_{\rm dust\ in} < r < R_{\rm gap\ in} \\ 0 & \text{for } R_{\rm gap\ in} < r < R_{\rm gap\ out} \\ n_{\rm dust} & \text{for } R_{\rm gap\ out} < r < R_{\rm dust\ out} \\ 0 & \text{for } r > R_{\rm dust\ out}. \end{cases} \tag{4.5}$$

However, the gap is not empty and the micron-sized grains are detected throughout the outer disk, thus their fiducial DALI model was neglecting the presence of micron-sized grains that would insulate the outer disk midplane and thus lower dust and gas temperatures.

We modified the dust structure of the Fedele et al. (2017a) fiducial model to expand the small grain ($n_{\rm dust\ small}$; 0.005 – 1 μm) dust population to be present within the gap between the dust rings ($r = 35 - 56$ AU) and at radii beyond the dust rings ($r > 83$ AU). In order to fit the spectral energy distribution (SED), we included a thin inner region of hot dust at $r = 0.2$ AU, as observed by Wagner et al. (2015). The optimized dust structure of the model is

$$n_{\rm dust} = \begin{cases} 10^{-5} \times n_{\rm dust\ small} & \text{for } 0.2 < r < 0.4 \text{ AU} \\ 0 \text{ otherwise} & \text{for } r < R_{\rm dust\ in} \\ \delta_{\rm dust} \times n_{\rm dust} & \text{for } R_{\rm dust\ in} < r < R_{\rm gap\ in} \\ 10^{-2} \times n_{\rm dust\ small} & \text{for } R_{\rm gap\ in} < r < R_{\rm gap\ out} \\ n_{\rm dust} & \text{for } R_{\rm gap\ out} < r < R_{\rm dust\ out} \\ n_{\rm dust\ small} & \text{for } r > R_{\rm dust\ out}. \end{cases} \tag{4.6}$$

Figure 4.6 shows the change in the dust structure between the fiducial model and our optimized model. The gas density structure of the optimized model remains unchanged as

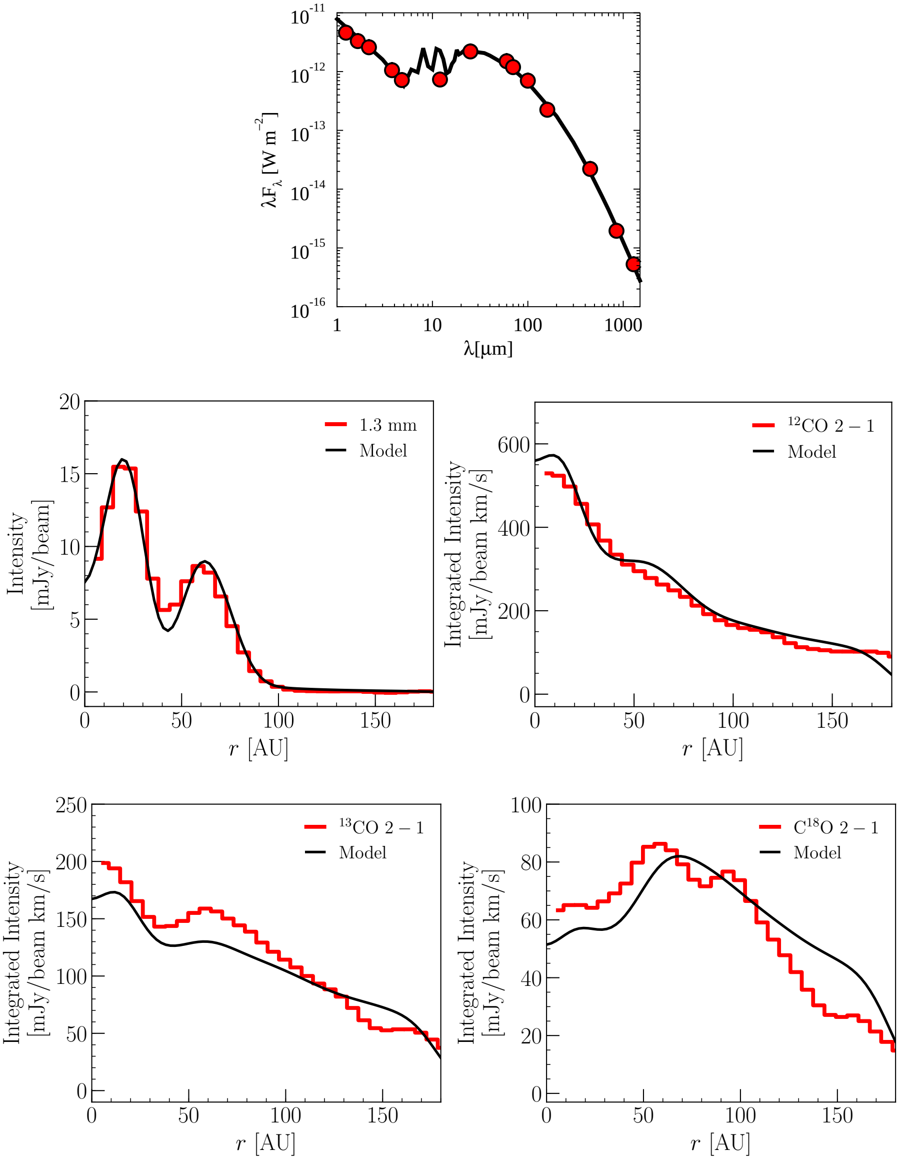

Figure 4.7: Fits to observables for the optimized DALI model. Unlike the azimuthally averaged radial profiles in Figure 4.2, the radial profiles shown here are cuts along the disk semi-major axis (P.A. = 5°). (Top) Near-infrared to submillimeter spectral energy distribution: the model is shown by the black solid curve and the data (red dots) are from Malfait et al. (1998), IRAS (Helou & Walker 1988), *Herschel* (Pascual et al. 2016), SCUBA (Sandell et al. 2011), and ALMA (Fedele et al. 2017a). (Middle left) Radial intensity profile of the 1.3 millimeter continuum. (Middle right) Radial intensity profile of ^{12}CO $J = 2-1$. (Bottom left) Radial intensity profile of ^{13}CO $J = 2-1$. (Bottom right) Radial intensity profile of C^{18}O $J = 2-1$.

$$n_{\mathrm{gas}} = \begin{cases} 0 & \text{for } r < R_{\mathrm{gas\ in}} \\ \delta_{\mathrm{gas}} \times n_{\mathrm{gas\ cavity}} & \text{for } R_{\mathrm{gas\ in}} < r < R_{\mathrm{dust\ in}} \\ \delta_{\mathrm{gas}} \times n_{\mathrm{gas\ gap}} & \text{for } R_{\mathrm{dust\ in}} < r < R_{\mathrm{gap\ out}} \\ n_{\mathrm{gas}} & \text{for } R_{\mathrm{gap\ out}} < r < R_{\mathrm{gas\ out}} \\ 0 & \text{for } r > R_{\mathrm{gas\ out}}. \end{cases} \tag{4.7}$$

Adjustments to the dust distribution will affect the SED, and the accompanying opacity and temperature variations will affect the molecular abundances and thus the radial profiles of ^{12}CO, ^{13}CO, and C^{18}O. The new parameters for the small grain ($0.005 - 1$ μm) dust population were chosen such that the fit to the SED was maintained and the fits to the CO isotopologs were consistent to within a factor of about 10%.

The PAH structure was also modified. Originally, the fiducial model dust temperature was set by PAH thermal emission in regions with no dust grains, with a global PAH abundance set equal to the interstellar medium (ISM) abundance. PAH abundances have been observed to be low in disks with respect to the ISM (Li & Lunine 2003; Geers et al. 2006; Thi et al. 2014). However, to achieve the required opacity for a reasonable fit to the ^{12}CO radial profile for $r < 25$ AU, it was necessary to keep a high PAH abundance in the inner regions. The PAH abundance in our optimized model was therefore set equal to the ISM abundance for $r \leq 83$ AU and set to 1% with respect to the ISM abundance for $r > 83$ AU, which is comparable to current estimates for the HD 169142 disk (Seok & Li 2016).

Figure 4.7 shows the fit to the SED and radial profile of the CO isotopologs from the optimized DALI model structure. Each point in the SED is well-fit by the DALI model with the small grain population modifications. The PAH feature is slightly overproduced because of the high abundance in the model at $r \leq 83$ AU. Fits to the ^{12}CO, ^{13}CO, and C^{18}O radial intensity profiles remain consistent with the previous fits from Fedele et al. (2017a) to within 10%.

Appendix B: Channel maps

Figures 4.8 – 4.10 show channel maps of the DCO$^+$ $J = 3 - 2$ line observed with ALMA and from the modeling presented in this paper. Channel maps in Figure 4.8 are from the ALMA observations imaged with CLEAN in CASA. Channel maps in Figure 4.9 are from the model synthetic image cube created with LIME, sampled in the *uv* plane with the PYTHON `vis_sample` routine, and imaged with CLEAN in CASA. Channel maps in Figure 4.10 show the residuals of the model subtracted from the data in each velocity channel.

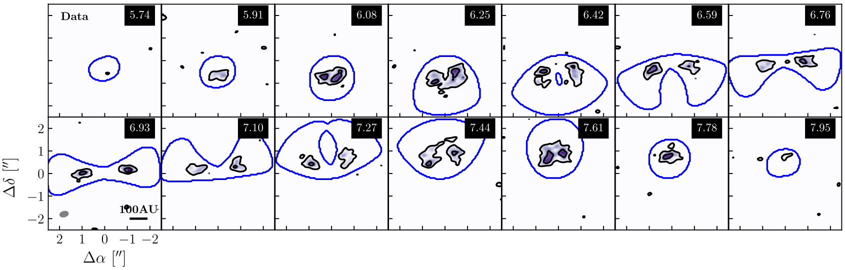

Figure 4.8: DCO$^+$ $J = 3-2$ channel maps from 5.74 – 7.95 km s^{-1}, Hanning smoothed to 0.17 km s^{-1} channels. Black contours show 5.5 mJy beam^{-1} (1σ) × [3, 6, 9]. The blue contours show the outline of the Keplerian mask. Channel velocity is shown in the upper-right corner. The synthesized beam and AU scale are shown in the lower-left panel.

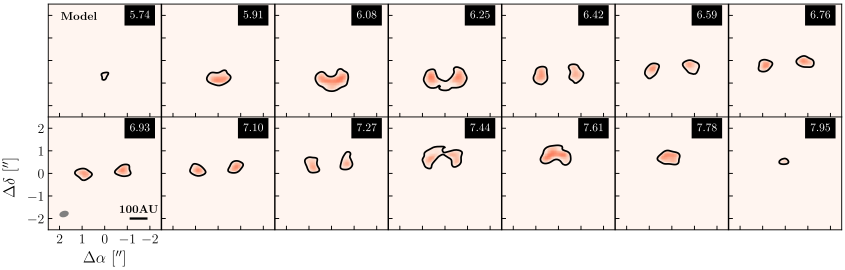

Figure 4.9: DCO$^+$ $J = 3-2$ best-fit model channel maps. Black contours show 5.5 mJy beam^{-1} (1σ) × [3]. Channel velocity is shown in the upper-right corner. The synthesized beam and AU scale are shown in the lower-left panel.

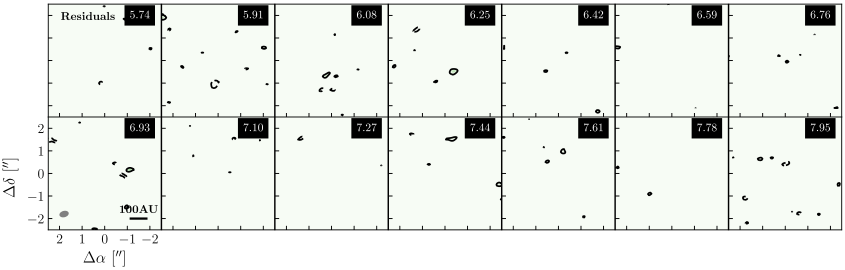

Figure 4.10: DCO$^+$ $J = 3-2$ residual (data – model) channel maps. Black contours show 5.5 mJy beam^{-1} (1σ) × [3]. Dashed contours are negative at the same intervals. Channel velocity is shown in the upper-right corner. The synthesized beam and AU scale are shown in the lower-left panel.

References

Albertsson, T., Semenov, D. A., Vasyunin, A. I., Henning, T., & Herbst, E. 2013, ApJS, 207, 27
ALMA Partnership, Brogan, C. L., Pérez, L. M., et al. 2015, ApJ, 808, L3
Andrews, S. M., Wilner, D. J., Zhu, Z., et al. 2016, ApJ, 820, L40
Banzatti, A., Pinilla, P., Ricci, L., et al. 2015, ApJ, 815, L15
Bergin, E. A. & Tafalla, M. 2007, ARA&A, 45, 339
Blondel, P. F. C. & Djie, H. R. E. T. A. 2006, A&A, 456, 1045
Blum, J. & Wurm, G. 2008, ARA&A, 46, 21
Brinch, C. & Hogerheijde, M. R. 2010, A&A, 523, A25
Brown, R. D. & Rice, E. H. N. 1986, MNRAS, 223, 429
Bruderer, S. 2013, A&A, 559, A46
Bruderer, S., van Dishoeck, E. F., Doty, S. D., & Herczeg, G. J. 2012, A&A, 541, A91
Carney, M. T., Hogerheijde, M. R., Loomis, R. A., et al. 2017, A&A, 605, A21
Casassus, S., van der Plas, G., M, S. P., et al. 2013, Nature, 493, 191
Cleeves, L. I. 2016, ApJ, 816, L21
Cleeves, L. I., Öberg, K. I., Wilner, D. J., et al. 2016, ApJ, 832, 110
D'Alessio, P., Calvet, N., Hartmann, L., Franco-Hernández, R., & Servín, H. 2006, ApJ, 638, 314
Dunkin, S. K., Barlow, M. J., & Ryan, S. G. 1997, MNRAS, 286, 604
Facchini, S., Birnstiel, T., Bruderer, S., & van Dishoeck, E. F. 2017, A&A, 605, A16
Favre, C., Bergin, E. A., Cleeves, L. I., et al. 2015, ApJ, 802, L23
Fedele, D., Carney, M., Hogerheijde, M. R., et al. 2017a, A&A, 600, A72
Fedele, D., Tazzari, M., Booth, R., et al. 2017b, ArXiv e-prints
Flaherty, K. M., Hughes, A. M., Rose, S. C., et al. 2017, ApJ, 843, 150
Flower, D. R. 1999, MNRAS, 305, 651
Gaia Collaboration, Brown, A. G. A., Vallenari, A., et al. 2016, A&A, 595, A2
Geers, V. C., Augereau, J.-C., Pontoppidan, K. M., et al. 2006, A&A, 459, 545
Gerlich, D., Herbst, E., & Roueff, E. 2002, Planet. Space Sci., 50, 1275
Grady, C. A., Schneider, G., Hamaguchi, K., et al. 2007, ApJ, 665, 1391
Helou, G. & Walker, D. W., eds. 1988, Infrared astronomical satellite (IRAS) catalogs and atlases. Volume 7: The small scale structure catalog, Vol. 7, 1–265
Huang, J., Öberg, K. I., & Andrews, S. M. 2016, ApJ, 823, L18
Huang, J., Öberg, K. I., Qi, C., et al. 2017, ApJ, 835, 231
Indriolo, N., Geballe, T. R., Oka, T., & McCall, B. J. 2007, ApJ, 671, 1736
Isella, A., Guidi, G., Testi, L., et al. 2016, Phys. Rev. Lett., 117, 251101
Li, A. & Lunine, J. I. 2003, ApJ, 594, 987
Ligi, R., Vigan, A., Gratton, R., et al. 2018, MNRAS, 473, 1774
Macías, E., Anglada, G., Osorio, M., et al. 2017, ApJ, 838, 97
Malfait, K., Bogaert, E., & Waelkens, C. 1998, A&A, 331, 211
Mathews, G. S., Klaassen, P. D., Juhász, A., et al. 2013, A&A, 557, A132
McMullin, J. P., Waters, B., Schiebel, D., Young, W., & Golap, K. 2007, in Astronomical Society of the Pacific Conference Series, Vol. 376, Astronomical Data Analysis Software and Systems XVI, ed. R. A. Shaw, F. Hill, & D. J. Bell, 127
Miao, Y., Mehringer, D. M., Kuan, Y.-J., & Snyder, L. E. 1995, ApJ, 445, L59
Millar, T. J., Bennett, A., & Herbst, E. 1989, ApJ, 340, 906

Miotello, A., Bruderer, S., & van Dishoeck, E. F. 2014, A&A, 572, A96

Miotello, A., van Dishoeck, E. F., Kama, M., & Bruderer, S. 2016, A&A, 594, A85

Momose, M., Morita, A., Fukagawa, M., et al. 2015, PASJ, 67, 83

Monnier, J. D., Harries, T. J., Aarnio, A., et al. 2017, ApJ, 838, 20

Müller, H. S. P., Schlöder, F., Stutzki, J., & Winnewisser, G. 2005, Journal of Molecular Structure, 742, 215

Murillo, N. M., Bruderer, S., van Dishoeck, E. F., et al. 2015, A&A, 579, A114

Neufeld, D. A. & Wolfire, M. G. 2017, ApJ, 845, 163

Öberg, K. I., Furuya, K., Loomis, R., et al. 2015, ApJ, 810, 112

Öberg, K. I., Qi, C., Wilner, D. J., & Hogerheijde, M. R. 2012, ApJ, 749, 162

Panić, O., Hogerheijde, M. R., Wilner, D., & Qi, C. 2008, A&A, 491, 219

Pascual, N., Montesinos, B., Meeus, G., et al. 2016, A&A, 586, A6

Piso, A.-M. A., Öberg, K. I., Birnstiel, T., & Murray-Clay, R. A. 2015, ApJ, 815, 109

Pohl, A., Benisty, M., Pinilla, P., et al. 2017, ApJ, 850, 52

Qi, C., Öberg, K. I., Andrews, S. M., et al. 2015, ApJ, 813, 128

Qi, C., Wilner, D. J., Aikawa, Y., Blake, G. A., & Hogerheijde, M. R. 2008, ApJ, 681, 1396

Quanz, S. P., Avenhaus, H., Buenzli, E., et al. 2013, ApJ, 766, L2

Raman, A., Lisanti, M., Wilner, D. J., Qi, C., & Hogerheijde, M. 2006, AJ, 131, 2290

Remijan, A., Snyder, L. E., Friedel, D. N., Liu, S.-Y., & Shah, R. Y. 2003, ApJ, 590, 314

Roberts, H. & Millar, T. J. 2000, A&A, 361, 388

Roueff, E., Gerin, M., Lis, D. C., et al. 2013, Journal of Physical Chemistry A, 117, 9959

Salinas, V. N., Hogerheijde, M. R., Mathews, G. S., et al. 2017, A&A, 606, A125

Sandell, G., Weintraub, D. A., & Hamidouche, M. 2011, ApJ, 727, 26

Seok, J. Y. & Li, A. 2016, ApJ, 818, 2

Teague, R., Semenov, D., Guilloteau, S., et al. 2015, A&A, 574, A137

Thi, W.-F., Pinte, C., Pantin, E., et al. 2014, A&A, 561, A50

van der Marel, N., van Dishoeck, E. F., Bruderer, S., et al. 2013, Science, 340, 1199

van't Hoff, M. L. R., Walsh, C., Kama, M., Facchini, S., & van Dishoeck, E. F. 2017, A&A, 599, A101

Wagner, K. R., Sitko, M. L., Grady, C. A., et al. 2015, ApJ, 798, 94

Walmsley, C. M., Flower, D. R., & Pineau des Forêts, G. 2004, A&A, 418, 1035

Walsh, C., Juhász, A., Meeus, G., et al. 2016, ApJ, 831, 200

Walsh, C., Juhász, A., Pinilla, P., et al. 2014a, ApJ, 791, L6

Walsh, C., Millar, T. J., Nomura, H., et al. 2014b, A&A, 563, A33

Walsh, C., Nomura, H., Millar, T. J., & Aikawa, Y. 2012, ApJ, 747, 114

Willacy, K. & Woods, P. M. 2009, ApJ, 703, 479

Williams, J. P. & Cieza, L. A. 2011, ARA&A, 49, 67

Wootten, A. 1987, in IAU Symposium, Vol. 120, Astrochemistry, ed. M. S. Vardya & S. P. Tarafdar, 311–318

Yu, M., Willacy, K., Dodson-Robinson, S. E., Turner, N. J., & Evans, II, N. J. 2016, ApJ, 822, 53

Zhang, K., Bergin, E. A., Blake, G. A., Cleeves, L. I., & Schwarz, K. R. 2017, Nature Astronomy, 1, 0130

Zhang, K., Pontoppidan, K. M., Salyk, C., & Blake, G. A. 2013, ApJ, 766, 82

CHAPTER 5

UPPER LIMITS ON CH_3OH IN THE HD 163296 PROTOPLANETARY DISK: EVIDENCE FOR A LOW GAS-PHASE CH_3OH/H_2CO RATIO

M. T. Carney, M. R. Hogerheijde, V. V. Guzmán, C. Walsh, K. I. Öberg,
E. C. Fayolle, L. I. Cleeves, J. M. Carpenter, C. Qi.

Submitted to Astronomy & Astrophysics

Abstract

Context. Methanol (CH_3OH) is at the root of organic ice chemistry in protoplanetary disks. Its connection to prebiotic chemistry and its role in the chemical environment of the disk midplane makes it an important target for disk chemistry studies. However, its weak emission has made detections difficult. To date, gas-phase CH_3OH has been detected in only one Class II disk, TW Hya.
Aims. We aim to constrain the methanol content of the HD 163296 protoplanetary disk.
Methods. We use the Atacama Large Millimeter/submillimeter Array (ALMA) to search for a total of four CH_3OH emission lines in bands 6 and 7 toward the disk around the young Herbig Ae star HD 163296. The disk-averaged column density of methanol and its related species formaldehyde (H_2CO) are estimated assuming optically thin emission in local thermodynamic equilibrium. We compare these results to the gas-phase column densities of the TW Hya disk.
Results. No targeted methanol lines were detected with Keplerian masking in the image plane nor with matched filter analysis in the *uv* plane individually or after line stacking. The 3σ disk-integrated intensity upper limits are < 51 mJy km s^{-1} for the band 6 lines and < 26 mJy km s^{-1} for the band 7 lines. The band 7 lines provide the strictest 3σ upper limit on disk-averaged column density with $N_{\rm avg} < 5.0 \times 10^{11}$ cm^{-2}. The methanol-to-formaldehyde ratio is CH_3OH/H_2CO < 0.24 in the HD 163296 disk compared to a ratio of 1.27 in the TW Hya disk.
Conclusions. The HD 163296 protoplanetary disk is less abundant in methanol with respect to formaldehyde compared to the disk around TW Hya. Differences in the stellar irradiation in this Herbig Ae disk as compared to that of a disk around a T Tauri star likely influence the gaseous methanol and formaldehyde content. Possible reasons for the lower HD 163296 methanol-to-formaldehyde ratio include: a higher than expected gas-phase formation of H_2CO in the HD 163296 disk, uncertainties in the grain-surface formation efficiency of CH_3OH and H_2CO, and differences in the disk structure and/or CH_3OH and H_2CO desorption processes that drive the release of the molecules from ice mantles back into the gas-phase. These results provide observational evidence that the gas-phase chemical complexity found in disks is strongly influenced by the spectral type of the host star.

5.1 Introduction

Methanol is an astrobiologically relevant molecule because it acts as a precursor to more complex organic molecules (COMs) that may develop into amino acids and other building blocks of life (Öberg et al. 2009; Herbst & van Dishoeck 2009). Maintaining an understanding of methanol chemistry through the numerous stages of star and planet formation is essential to make predictions on the molecular complexity available for incorporation into extrasolar planetary bodies (e.g., Drozdovskaya et al. 2014). The CH_3OH molecule is regularly detected in the earlier, embedded stages of star formation both in the solid phase through ice absorption (Grim et al. 1991; Skinner et al. 1992; Dartois et al. 1999; Pontoppidan et al. 2004; Bottinelli et al. 2010; Kristensen et al. 2010; Shimonishi et al. 2010; Boogert et al. 2015) and in the gas-phase (Friberg et al. 1988; van Dishoeck et al. 1995; Graninger et al. 2016; Lee et al. 2017). These observations provide evidence for the presence of CH_3OH ices in cold molecular clouds and protostellar envelopes.

To date, methanol has been detected in two protoplanetary disks: the Class II TW Hydrae (Walsh et al. 2016) and the younger Class I V883 Orionis, an outbursting FU Orionis object (van 't Hoff et al. 2018). There are currently few informative upper limits on gas-phase methanol in disks. The reason for the apparent absence of gas-phase methanol in protoplanetary disks is not immediately obvious because CH_3OH is expected to form via the hydrogenation of CO ices (Watanabe et al. 2003; Cuppen et al. 2009) on the surface of dust grains. Also, the colder, outer regions of protoplanetary disks are expected to inherit a reservoir of methanol ice formed earlier during the protostellar or interstellar phase. Methanol is produced by the same grain-surface formation pathway as formaldehyde, which is readily detected in disks (Aikawa et al. 2003; Öberg et al. 2010; Qi et al. 2013; van der Marel et al. 2014; Loomis et al. 2015; Öberg et al. 2017; Carney et al. 2017). However, because of its much higher binding energy to ice mantles, methanol is expected to be frozen out over a much larger region of the disk than formaldehyde.

Variation in the formaldehyde and methanol content across protoplanetary disks may point to differences in their formation processes. Formaldehyde can be formed in the gas-phase and on grain surfaces, therefore a lower than expected methanol-to-formaldehyde ratio could be due to a more efficient gas-phase pathway to form H_2CO (Fockenberg & Preses 2002; Atkinson et al. 2006), less efficient conversion of H_2CO into CH_3OH on grain surfaces than expected, or lower than expected CH_3OH photodesorption rates and/or immediate UV photodissociation of gas-phase CH_3OH (Bertin et al. 2016; Cruz-Diaz et al. 2016).

The HD 163296 (MWC 275) system is an ideal testbed for exploring chemical processing in protoplanetary disks, in particular for organics. It is an isolated Herbig Ae pre-main sequence (PMS) star with spectral type A2Ve at an age of ~5 Myr (Alecian et al. 2013). The star is surrounded by a large, bright gas-rich protoplanetary disk that extends out to ~550 AU in the gas based on CO measurements (de Gregorio-Monsalvo et al. 2013). The disk has an inclination of 44°, a position angle of 133°, and a total mass $M_{\rm disk} \approx 0.09\ M_\odot$ based on physical models (Qi et al. 2011; Rosenfeld et al. 2013). At such an inclination, the vertical structure as well as the radial structure can be inferred directly from the molecular line emission maps (Rosenfeld et al. 2013; Flaherty et al. 2015).

Recent measurements of the stellar parallax by Gaia put the HD 163296 system at a distance $d = 101 \pm 1$ pc (Gaia Collaboration et al. 2018), significantly closer than previous distance estimates of 122 pc (van den Ancker et al. 1998).[1] While the new distance will affect the stellar parameters, this work adopts the previously reported values for stellar mass (2.3 $M_\odot$; Qi et al. 2011) and distance ($d = 122$ pc). The analysis presented here focuses on the disk-averaged molecular column density ratios of methanol and formaldehyde within the same disk. The column density is derived from the disk-integrated line flux, therefore the updated Gaia distance measurements will affect the line flux similarly for molecular species within the same disk, and the effect of the new distance is canceled out.

The proximity and size of the disk combined with the strong UV field of the Herbig Ae PMS star provides a unique opportunity to fully resolve the location of the CO snow line, i.e., the midplane radius beyond which gas-phase CO will freeze out into ice (Qi et al. 2011; Mathews et al. 2013; Qi et al. 2015). Current estimates by Qi et al. (2015) place the CO snow line at a midplane radius of 90 AU, corresponding to a gas and dust temperature of ~24 K in this disk. Recent work has revealed that the disk consists of several rings and gaps in the millimeter dust and in the gas (Isella et al. 2016), while the CO gas shows asymmetries at specific velocities (Pinte et al. 2018; Teague et al. 2018), both of which may be indicative of planet-disk interaction from embedded forming planets. Given its large radial extent of ~550 AU and resolved, relatively close-in CO snow line position, HD 163296 is one of the best candidates to probe the formation of organics that require the freeze-out of abundant volatiles such as CO.

---

[1] The updated distance $d = 101 \pm 1$ pc results in a stellar luminosity of ~23 $L_\odot$, which is 30% lower than the previous estimate (Alecian et al. 2013). Applying the adjusted luminosity value to the H-R diagram used by Alecian et al. (2013) to determine the age of the system and stellar mass results in an updated age of ~9 Myr and an adjusted stellar mass closer to 2.1 $M_\odot$.

This paper presents observations from the Atacama Large Millimeter/submillimeter Array (ALMA) of the CH_3OH molecule toward HD 163296. Section 5.2 describes the observations and data reduction. Results including the upper limits on the methanol content of the HD 163296 disk and a comparison to the TW Hya disk are described in Section 5.3. In Section 5.4 we discuss the implications of the upper limits on the detectability of methanol in disks similar to HD 163296. Section 5.5 presents the conclusions of this work.

5.2 Observations and reduction

HD 163296 (J2000: R.A. = $17^h56^m21.280^s$, DEC = $-21°57'22.441''$) was observed with ALMA in band 6 and band 7 during Cycle 4 under project 2016.1.00884.S. Band 6 and band 7 are receivers operating in the 211 – 275 GHz and 275 – 373 GHz range, respectively. Band 6 observations were done with the ALMA 12-meter array on 2016 November 11, 2016 December 01, and 2017 March 15 with 42 antennas. Band 7 observations were carried out with the Atacama Compact Array (ACA) on 2016 October 05, 08, 13, 26 using 10 of the 7-meter ACA antennas, and with the ALMA 12-meter array on 2017 April 13 using 45 antennas. In total, four transitions of CH_3OH were targeted across the two bands with the frequency domain mode (FDM) correlator setting: two CH_3OH $5_{05}-4_{04}$ (A/E) lines in band 6 at 241.791 GHz and 241.700 GHz with a frequency (velocity) resolution of 244 kHz (0.303 km s^{-1}); and in band 7, CH_3OH $2_{11}-2_{02}$ (A) at 304.208 GHz and CH_3OH $1_{10}-1_{01}$ (A) at 303.367 GHz with a frequency (velocity) resolution of 141 kHz (0.139 km s^{-1}). All CH_3OH lines were in the upper side band (USB) of their execution blocks along with observations of the continuum. The lower side band (LSB) contained observations of the continuum, $C^{17}O$ $J = 2-1$, CN $J = 2-1$, and CH_3CN $J = 13-12$ in band 6, and the continuum, DCN $J = 4-3$, and four H_2CO lines in band 7 which have been presented in Guzmán et al. (2018). Table 5.1 summarizes the observational parameters for each CH_3OH line and the continuum.

Band 6 observations were obtained over three execution blocks with 6.05 sec integration steps and 68 minutes total time on-source. System temperatures varied from 60 – 140 K and the average precipitable water vapor varied from 1.5 – 2.3 mm. J1924-2914 was the bandpass calibrator and Titan was the flux calibrator for all execution blocks. The average flux values for Titan were: 1.15 Jy in the USB and 1.01 Jy in the LSB for 2016 November 11 and December 01; 0.963 Jy in the USB and 0.846 Jy in the LSB for 2017 March 15. The gain calibrator was different for each execution block: J1745-2900 on 2016 November 11, J1742-

Table 5.1: HD 163296 observational parameters

	Band 6	
Dates observed	2016 November 11, December 01; 2017 March 15	
Baselines	15 – 1000 m | 12 – 776 kλ	
	CH$_3$OH $5_{05} - 4_{04}$ (E)	CH$_3$OH $5_{05} - 4_{04}$ (A)
Rest frequency [GHz]	241.700	241.791
Synthesized beam [FWHM]	$1.46'' \times 1.13''$	$1.46'' \times 1.13''$
Position angle	−76.6°	−76.6°
Channel width [km s^{-1}]	0.303	0.303
rms noise^a [mJy beam^{-1}]	3.0	3.0
Weighting	natural	natural
Continuum frequency [GHz]	233.0	
Synthesized beam [FWHM]	$0.55'' \times 0.37''$	
Position angle	76.8°	
rms noise [mJy beam^{-1}]	0.17	
Integrated flux [mJy]	754 ± 75	
Weighting	Briggs, robust = 0.5	
	Band 7	
Dates observed	ACA	2016 October 05, 08, 13, 26
	12-meter array	2017 April 13
Baselines	ACA	9 – 49 m | 9 – 48 kλ
	12-meter array	15 – 460 m | 15 – 454 kλ
	CH$_3$OH $1_{10} - 1_{01}$ (A)	CH$_3$OH $2_{11} - 2_{02}$ (A)
Rest frequency [GHz]	303.367	304.208
Synthesized beam [FWHM]	$1.37'' \times 1.14''$	$1.36'' \times 1.15''$
Position angle	91.1°	90.6°
Channel width [km s^{-1}]	0.139	0.139
rms noise^a [mJy beam^{-1}]	2.5	2.5
Weighting	natural	natural
Continuum frequency [GHz]	296.0	
Synthesized beam [FWHM]	$0.63'' \times 0.48''$	
Position angle	87.8°	
rms noise [mJy beam^{-1}]	0.09	
Integrated flux [mJy]	1288 ± 128	
Weighting	Briggs, robust = 0.5	

Notes. Flux calibration accuracy is taken to be 10%. For specifics on the line transition data, see Table 5.2. [a] Noise levels are per image channel.

1517 on 2016 December 01, and J1733-1304 on 2017 March 15. The derived flux values for J1745-2900, J1742-1517, and J1733-1304 were 3.29 Jy, 0.212 Jy, and 1.47 Jy, respectively. All measurement sets were subsequently concatenated and time binned to 30 sec integration time per visibility for imaging and analysis.

Band 7 observations were obtained with the 12-meter array over three execution blocks with 6.05 sec integration steps and 105 minutes total time on-source. Data was also obtained with the ACA over four execution blocks with 10.1 sec integration steps and 184 minutes total time on-source. System temperatures varied from 80 – 150 K and the average precipitable water vapor varied from 0.5 – 1.1 mm. J1924-2914 was the bandpass calibrator for all execution blocks. Titan, Neptune, J1733-1304, and J1751+0939 were used as flux calibrators. The average flux values were: Titan – 1.96 Jy in the USB and 1.82 Jy in the LSB for 2017 April 13; Neptune

– 22.5 Jy in the USB and 21.2 Jy in the LSB for 2016 October 08, 26; J1733-1304 – 1.32 Jy (2017 April 13), 1.14 Jy (2016 October 13) in the USB and 1.36 Jy (2017 April 13), 1.18 Jy (2016 October 13) in the LSB; J1751+0939 – 1.58 Jy in the USB and 1.60 Jy in the LSB for 2016 October 05. The gain calibrators were J1733-1304 for the 12-meter array data and J1745-2900 for the ACA data. The derived flux value for J1733-1304 was 1.36 Jy (2017 April 13) and the values for J1745-2900 were 3.2 Jy (2016 October 05, 08, 13), and 4.6 Jy (2016 October 26). All measurement sets were subsequently concatenated and time binned to 30 sec integration time per visibility for imaging and analysis.

Self-calibration for HD 163296 in band 6 was done with five spectral windows dedicated to continuum observations: two in the LSB at 223.5 GHz and 224 GHz, and three in the USB at 234 GHz, 241 GHz, and 242 GHz with a total combined bandwidth of 469 MHz. The band 6 reference antenna was DA41. Band 7 self-calibration was done with three spectral windows dedicated to continuum observations: one in the LSB at 289 GHz and two in the USB at 302 GHz and 303.5 GHz with a total combined bandwidth of 469 MHz. The band 7 reference antenna was DA59 for the 12-meter array and CM03 for the ACA. A minimum of four baselines per antenna and a minimum signal-to-noise ratio (SNR) of two were required for self-calibration. Calibration solutions were calculated twice for phase and once for amplitude. The first phase solution interval (solint) was 200 sec, the second phase and amplitude solutions had solint equal to the binned integration time (30 sec). Self-calibration solutions for the continuum spectral windows were mapped to the line spectral windows nearest in frequency. Continuum subtraction for the line data was done in the *uv* plane using a single-order polynomial fit to the line-free channels. CLEAN imaging was performed with natural weighting for each continuum-subtracted CH_3OH line with a *uv* taper to achieve a $1''$ beam in order to increase the sensitivity.

This paper also makes use of Submillimeter Array (SMA) H_2CO data for the HD 163296 disk (Qi et al. 2013), ALMA H_2CO data for the HD 163296 disk (Carney et al. 2017), ALMA H_2CO data for the TW Hya disk (Öberg et al. 2017), and ALMA CH_3OH data for the TW Hya disk (Walsh et al. 2016). The following software and coding languages are used for data analysis: the CASA package version 4.7.2 (McMullin et al. 2007) and PYTHON.

5.3 Results

No methanol lines listed in Table 5.1 are detected in the disk around HD 163296 neither individually nor after line stacking. In this section, we first describe the stacking and masking methods used to maximize the SNR to attempt to extract the disk-integrated intensity of the CH_3OH lines. The method used to estimate the column density and abundance of methanol in the HD 163296 disk is then described. A comparison is presented between the CH_3OH and H_2CO content in the disks around HD 163296 and TW Hya based on data taken from the literature. Finally, model spectra of the band 7 CH_3OH lines are created for HD 163296 and compared to the sensitivity of the observations.

5.3.1 Line extraction

We attempt to extract the targeted CH_3OH lines from the CLEAN image cubes using a circular aperture with an 8″ diameter centered on the source, which yields no detections (see Figure 5.1). To increase the SNR we repeat this analysis after stacking the CH_3OH lines using different line stacking schemes. We further attempt to increase the SNR of the CH_3OH data by applying masking techniques: Keplerian masking in the image plane, and matched filter analysis in the *uv* plane to search for any signal in the raw visibilities.

Line stacking

Stacking is done for band 6 and band 7 lines separately, and then again for both bands together. The band 7 lines are more easily excited due to their lower upper energy (E_u < 22 K) values compared to the band 6 lines (E_u > 34 K; see Table 5.2), thus band 7 observations should be sensitive to lower CH_3OH column densities and should be easier to detect.

First, we stack the lines in the image plane by adding together the integrated intensity maps ($v = 2.4-9.2$ km s^{-1}) created from the CH_3OH continuum-subtracted and *uv*-tapered CLEAN image cubes. Second, we stack in the *uv* plane by concatenating ALMA measurement sets prior to imaging. Stacking in the *uv* plane is done using the CASA task CVEL, which is used to regrid the velocity axis of line data and has the option to combine visibility data for multiple lines. For *uv* stacking across all bands, the band 7 lines are regridded to 0.303 km s^{-1} channels to match the channel width of the band 6 lines. Methanol remains undetected after implementing the stacking methods described above.

Keplerian masking in the image plane

For maximum SNR in the image plane, we apply a Keplerian mask to the CLEAN image cube for each CH_3OH line (Carney et al. 2017; Salinas et al. 2017) to exclude noisy pixels that are not associated with the emission expected from a disk in Keplerian rotation. The mask is based on the velocity profile of a rotating disk, which is assumed to be Keplerian around a central stellar mass of $M = 2.3\ M_\odot$ (Alecian et al. 2013). A subset of pixels (x, y, v) are identified in the CH_3OH image cubes where the Doppler-shifted line velocity projected along the line of sight matches the pixel Keplerian velocity (x, y, v_K) projected along the line of sight. Pixels with velocities that do not match the Keplerian rotational profile criteria are masked. Integrated intensity maps and disk-integrated spectra are again created from the Keplerian-masked cubes of the CH_3OH lines individually and after line stacking; however, in all cases, CH_3OH remains undetected. Figure 5.1 shows the aperture-masked spectra and the Keplerian-masked spectra of the four methanol lines targeted in HD 163296.

Upper limits on the integrated intensity for each CH_3OH line are calculated using the projected Keplerian mask (x, y, v_K) derived for the HD 163296 disk. To obtain the strictest upper limits on the integrated line intensity, we include only the positions and velocities associated with the disk. Therefore, the mask cube contains pixels set equal to unity for (x, y, v_K) positions only, and all other pixels are set to zero. The upper limit is set at 3σ where $\sigma = \delta v \sqrt{N} \sigma_\mathrm{rms}$, δv is the velocity channel width in km s^{-1}, N is the number of independent measurements contained within the projected Keplerian mask, and σ_rms is the rms noise per channel in mJy

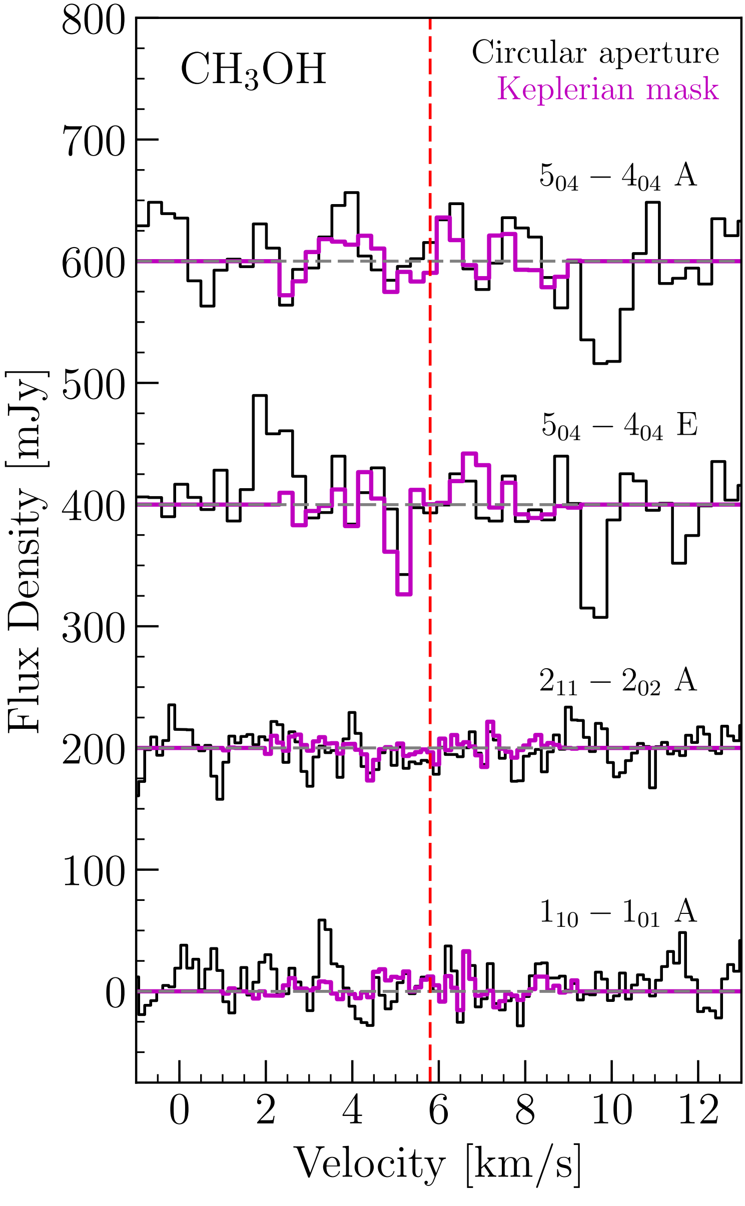

Figure 5.1: Spectra at the expected velocity of CH_3OH line emission in the HD 163296 disk showing non-detections from aperture-masked image cubes using an 8″ diameter circular aperture (black) and Keplerian-masked image cubes (magenta). The two bottom spectra are observed in band 7 in 0.139 km s^{-1} channels while the two top spectra are in band 6 in 0.303 km s^{-1} channels. The horizontal gray dashed line represents the spectrum baseline, which is offset by 200 mJy for each line. The vertical red dashed line shows the systemic velocity at 5.8 km s^{-1} (Qi et al. 2011).

beam^{-1} (see Table 5.1). To account for correlated noise within the size of the beam, we sum over all (x, y, v_K) pixel positions and divide by the number of pixels per beam $n_{\rm ppb}$, to get $N = \Sigma(x, y, v_K)/n_{\rm ppb}$, the number of independent measurements over the integrated Keplerian mask. The disk-integrated upper limits for each CH_3OH line are listed in Table 5.2.

Matched filter analysis in the *uv* plane

To maximize the SNR in the *uv* plane, we apply a matched filter to the CH_3OH line visibility data (Loomis et al. 2018). In this technique, a template image cube is sampled in *uv* space to obtain a set of template visibilities that act as the filter. The filter is then cross-correlated with a set of low SNR visibilities (in this case, the CH_3OH data) in an attempt to detect any signal that is co-spatial with the template emission. Loomis et al. (2018) and Carney et al. (2017) have published positive detections using the matched filter technique for CH_3OH and H_2CO, which can provide an improvement in SNR of $> 50 - 500\%$ over the traditional aperture masking, depending on the spectral resolution of the observed visibilities.

We use the H_2CO $3_{03} - 2_{02}$ detection towards the HD 163296 disk reported in Carney et al. (2017) as the template emission profile under the assumption that CH_3OH and H_2CO reside in similar regions. The emission morphologies will be dominated primarily by Keplerian rotation, therefore a high degree of co-spatiality is expected. The H_2CO line is re-imaged with CLEAN to achieve a spatial and spectral resolution equal to the observed CH_3OH lines. Channels with H_2CO emission ($v = 1.6 - 10$ km s^{-1}) are sampled in *uv* space using the PYTHON `vis_sample`[2] routine. The matched filter is run for the CH_3OH line visibility data individually and after line stacking.

Figure 5.2 shows the spectrum that is produced by the matched filter analysis for the band 7 CH_3OH data. The filter response in units of σ is the measure of the SNR of the cross-correlation between the CH_3OH line visibility data and the filter derived from the template H_2CO emission. A correlation between the CH_3OH data and the filter would result in a peak at the source velocity. No such feature is seen in the filter response spectrum of any CH_3OH lines in the HD 163296 disk, suggesting that the detection threshold for methanol is well below the sensitivity achieved in our ALMA observations. The matched filter analyses confirm the non-detection of CH_3OH found during analysis in the image plane. The same analysis for the band 6 lines also results in no detection, which is expected given that the band 7 lines should be brighter.

5.3.2 CH_3OH column density and abundance upper limits

We estimate the disk-averaged column density of CH_3OH based on the integrated line intensity upper limit, an assumed excitation temperature, and the total disk mass. Following the formula used by Remijan et al. (2003) and Miao et al. (1995) for optically thin emission in local thermodynamic equilibrium (LTE), we can estimate the column density

$$N = 2.04 \frac{\int I_\nu dv}{\theta_a \theta_b} \frac{Q_{\rm rot}\ \exp(E_u/T_{\rm ex})}{\nu^3 \langle S_{ij} \mu^2 \rangle} \times 10^{20}\ {\rm cm}^{-2}, \tag{5.1}$$

---

[2] `vis_sample` is publicly available at `https://github.com/AstroChem/vis_sample` or in the Anaconda Cloud at `https://anaconda.org/rloomis/vis_sample`

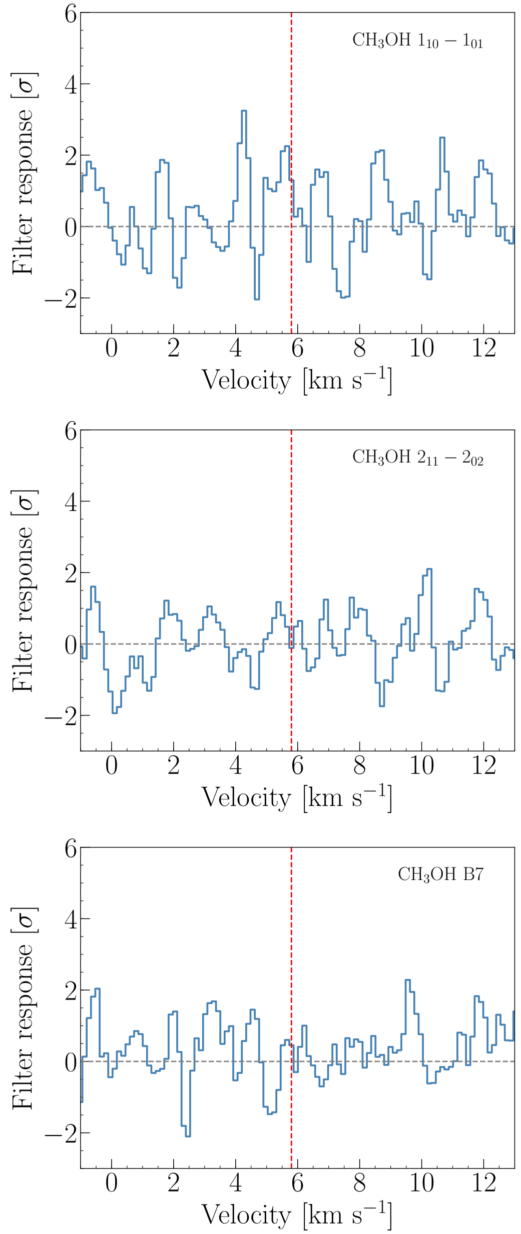

Figure 5.2: Matched filter results for the band 7 CH_3OH lines in the HD 163296 disk using the H_2CO emission as a template. A peak $> 3\sigma$ at the source velocity ($v = 5.8$ km s^{-1}; red dashed line) would signify a positive detection of methanol. The band 7 lines should be the strongest in our sample, but there is no evidence of CH_3OH in the matched filter for the band 7 individual lines nor the band 7 stacked lines. (Top) CH_3OH $1_{10} - 1_{01}$ (A) line. (Middle) CH_3OH $2_{11} - 2_{02}$ (A) line. (Bottom) Stacked band 7 CH_3OH lines.

Table 5.2: Disk-averaged column density and abundance of CH_3OH in HD 163296 and TW Hya.

Object	Line	$\int I_\nu d\nu^\dagger$ [mJy km s^{-1}]	E_u [K]	$\log(A_{ij})$ [s^{-1}]	$n_{crit}{}^a$ [cm^{-3}]	N_{avg} [cm^{-2}]	CH_3OH/H_2
HD 163296	CH_3OH $5_{05} - 4_{04}$ (E)	< 51	47.9	−4.22	1.6(06)	< 6.9(12)	< 2.1(−11)
	CH_3OH $5_{05} - 4_{04}$ (A)	< 51	34.8	−4.22	4.3(05)	< 4.1(12)	< 1.3(−11)
	CH_3OH $1_{10} - 1_{01}$ (A)	< 26	16.9	−3.49	4.3(07)	< 7.0(11)	< 2.2(−12)
	CH_3OH $2_{11} - 2_{02}$ (A)	< 26	21.6	−3.49	5.0(06)	< 5.0(11)	< 1.6(−12)
TW Hya	CH_3OH stacked*	26.5 ± 2.7^b	28.6	−3.49	3.0(06)	4.7(12)	1.1(−12)

Notes. The disk-averaged column density is calculated using Equation 5.1 with $T_{ex} = 25$ K. The format $a(b)$ translates to $a \times 10^b$. Flux errors are dominated by systematic uncertainties, taken to be 10%.
$^{(\dagger)}$ Upper limits are derived at the 3σ level using the HD 163296 Keplerian mask (see Section 5.3.1).
$^{(*)}$ The stacked detection consists of three CH_3OH transitions: CH_3OH $2_{11} - 2_{02}$ (A) at 304.208 GHz, CH_3OH $3_{12} - 3_{03}$ (A) at 305.472 GHz, and CH_3OH $4_{13} - 4_{04}$ (A) at 307.166 GHz. Excitation parameters for the CH_3OH $3_{12} - 3_{03}$ (A) line are used to calculate column density.
References: $^{(a)}$ Rabli & Flower (2010); $^{(b)}$ Walsh et al. (2016).

where $\int I_\nu d\nu$ is the integrated line intensity in Jy beam^{-1} km s^{-1}, θ_a and θ_b correspond to the semi-major and semi-minor axes of the synthesized beam in arcseconds, T_{ex} is the excitation temperature in K, and ν is the rest frequency of the transition in GHz. The partition function (Q_{rot}), upper energy level (E_u, in K), and the temperature-independent transition strength and dipole moment ($S_{ij}\mu^2$, in debye^2) for CH_3OH are taken from the Cologne Database for Molecular Spectroscopy (CDMS; Müller et al. 2005).

Methanol is expected to form primarily in ice in cold regions of protoplanetary disks, where gas densities are higher ($\sim 10^9$ cm^{-3}; Walsh et al. 2014) than the critical density of the observed CH_3OH transitions ($10^6 - 10^7$ cm^{-3}; Rabli & Flower 2010). Recent physical models of the HD 163296 disk have gas densities > 10^6 cm^{-3} in the region $z/r < 0.4$ (Qi et al. 2011; de Gregorio-Monsalvo et al. 2013; Rosenfeld et al. 2013), where z and r are the disk height and radius, respectively. In recent models of the TW Hya disk, Walsh et al. (2016) varied the methanol emitting region over the range $z/r < 0.1$, $0.1 < z/r < 0.2$, and $0.2 < z/r < 0.3$, which all fit the data equally well. These models all had methanol present at $z/r < 0.3$, suggesting that emission is arising from dense regions within the disk. Under these conditions, LTE is a reasonable assumption, and thus T_{ex} is expected to equal the kinetic temperature of the gas.

Assuming optically thin emission, the disk-averaged column density can be used to estimate the total number of CH_3OH molecules in the disk $N(CH_3OH) = N_{avg}(a \times b)$, where $(a \times b)$ is the total emitting area of the disk. Assuming the total disk mass is primarily molecular hydrogen, we can estimate the total number of H_2 molecules $N(H_2) = M_{disk}/m_{H_2}$, where m_{H_2} is the molecular hydrogen mass. The CH_3OH emitting area is set to $a = b = 7''$ based on the H_2CO emission diameter in the HD 163296 disk (Carney et al. 2017), assuming a similar chemical origin and distribution. The total disk mass is ~0.09 $M_\odot$ based on models of CO observations (Qi et al. 2011; Rosenfeld et al. 2013). Table 5.2 shows the disk-averaged column density and abundance for the single temperature assumption $T_{\rm ex}$ = 25 K in LTE, which is approximately the same as the excitation temperature found for H_2CO in the HD 163296 disk (Qi et al. 2013; Carney et al. 2017). The CH_3OH $2_{11} - 2_{02}$ (A) line provides the strictest upper limit on the methanol column density and abundance in HD 163296, with $N_{\rm avg} \lesssim 5.0\times10^{11}$ cm^{-2} and $CH_3OH/H_2 \lesssim 1.6\times10^{-12}$, based on its disk-integrated line intensity upper limit and assuming an excitation temperature of $T_{\rm ex}$ = 25 K. Table 5.4 in the Appendix shows the disk-averaged column density and abundance for a range of LTE excitation conditions with $T_{\rm ex}$ = 25, 50, and 75 K. The abundances do not vary with $T_{\rm ex}$ by more than a factor of 2 – 3 in the most extreme cases.

5.3.3 H_2CO and CH_3OH in HD 163296 and TW Hya

We estimate the fraction of methanol relative to formaldehyde based on our upper limits for CH_3OH in HD 163296 and compare to the TW Hya disk, the only Class II protoplanetary disk for which there is a gas-phase methanol detection (Walsh et al. 2016). Integrated line intensities for H_2CO detections in HD 163296 and TW Hya are taken from the literature, and their disk-averaged column densities and abundances are derived in the same manner as described in Section 5.3.2 to ensure consistency when comparing the H_2CO and CH_3OH content. The TW Hya disk mass is ~0.05 $M_\odot$ based on observations of the HD molecule (Bergin et al. 2013). The emitting area for H_2CO in TW Hya is set to $a = b = 3''$ based on the diameter of emission observed by Öberg et al. (2017). The same 3″ emitting area is used for CH_3OH in TW Hya. Table 5.3 shows the calculated column densities and abundances for the H_2CO observations.

For HD 163296, the CH_3OH $2_{11} - 2_{02}$ (A) line is used to calculate the methanol-to-formaldehyde ratio as it gives the strictest upper limits on the methanol abundance. For TW Hya, we obtained the integrated line intensity of the stacked methanol detection by Walsh et al. (2016), assume that the majority of emission is due to the strongest individual line (CH_3OH $3_{12} - 3_{03}$ (A) at 305.473 GHz with $E_{\rm u}$ = 28.6 K: Walsh et al. 2014; Loomis et al. 2018), and use the excitation parameters of that line with Equation 5.1 to derive the TW Hya CH_3OH column density and abundance, and subsequently the CH_3OH/H_2CO ratio for the disk.

Results for the CH_3OH/H_2CO ratio in TW Hya and HD 163296 can be found in Table 5.3. Ratios calculated with the H_2CO $3_{12} - 2_{11}$ line should be representative of the true CH_3OH/H_2CO ratio since the H_2CO $3_{12} - 2_{11}$ upper energy level ($E_{\rm u}$), Einstein A coefficient ($A_{\rm ij}$), and critical density ($n_{\rm crit}$) are similar to that of the band 7 methanol lines observed in these disks. Thus, we obtain CH_3OH/H_2CO ratios of < 0.24 for HD 163296 and 1.27 for TW Hya, which suggests that the disk around HD 163296 is less abundant in methanol relative to formaldehyde compared to the TW Hya disk.

5.3.4 Model CH_3OH spectra for HD 163296

In addition to the extraction methods described in previous sections, we also attempt a forward modeling approach to interpret the CH_3OH non-detections toward HD 163296. We model the HD 163296 CH_3OH band 7 spectra using a parameterized disk structure and radiative transfer methods in order to compare the

Table 5.3: Disk-averaged column density and abundance of H_2CO in HD 163296 and TW Hya.

Object	Line	$\int I_\nu dv$ [mJy km s^{-1}]	E_u [K]	$\log(A_{ij})$ [s^{-1}]	n_{crit}^{a} [cm^{-3}]	N_{avg} [cm^{-2}]	H_2CO/H_2	CH_3OH/H_2CO†
HD 163296	$H_2CO\ 3_{12} - 2_{11}$	890 ± 89^{b}	33.4	−3.55	5.7(06)	2.1(12)	6.3(−12)	< 0.24
TW Hya	$H_2CO\ 3_{12} - 2_{11}$	291 ± 29^{c}	33.4	−3.55	5.7(06)	3.7(12)	8.9(−13)	1.27 ± 0.13

Notes. The disk-averaged column density is calculated using Equation 5.1 with $T_{ex} = 25$ K. The format $a(b)$ translates to $a \times 10^{b}$. Flux errors are dominated by systematic uncertainties, taken to be 10%.
($\dagger$) Ratios are determined using the CH_3OH disk-integrated column density from Table 5.2. HD 163296: based on the strictest upper limit from the $CH_3OH\ 2_{11} - 2_{02}$ (A) line. TW Hya: based on the stacked CH_3OH detection.
References: (a) Wiesenfeld & Faure (2013); (b) Qi et al. (2013); (c) Öberg et al. (2017).

modeled emission to the noise level in the Keplerian-masked image cubes. We adopt the physical structure and the abundance structure of the model used by Carney et al. (2017) to reproduce ALMA observations of H_2CO in the HD 163296 disk, then scale the CH_3OH abundance with respect to the H_2CO abundance. The Line Modeling Engine (LIME: Brinch & Hogerheijde 2010) 3D radiative transfer code is run in LTE with 10000 grid points at the source distance of the original Qi et al. (2011) physical model (d = 122 pc) to create synthetic images of the CH_3OH observations. The synthetic images are continuum-subtracted, sampled in uv space with the PYTHON `vis_sample` routine, and imaged with CLEAN at the same velocity resolution as the observations.

Figure 5.3 shows the disk-integrated model spectra for the CH_3OH band 7 lines for a range of methanol-to-formaldehyde ratios, as indicated by the legend. The spectra show that a line should have been detected in the disk around HD 163296 for a CH_3OH/H_2CO ratio of ~0.2 for the most sensitive case (stacked band 7 lines). This result is consistent with the upper limit on this ratio derived from the integrated intensity of the Keplerian mask cube as presented in Section 5.3.3.

5.4 Discussion

The results presented in Table 5.3 suggest that the HD 163296 disk has a lower overall gas-phase methanol content with respect to formaldehyde than the TW Hya disk. In this section we discuss possible reasons for a lower CH_3OH/H_2CO ratio in HD 163296, as well as a brief assessment of the observing time needed to detect the low predicted abundances of gas-phase methanol in this disk.

5.4.1 The CH_3OH/H_2CO ratio in HD 163296 and TW Hya

It should be noted that there are uncertainties on the order of a factor of a few when deriving the CH_3OH/H_2CO ratio as described in this work. Namely, the column density calculation for the methanol detection in TW Hya is a result of three stacked line transitions rather than a single common transition as for H_2CO observed in both disks. The $CH_3OH\ 3_{12} - 3_{03}$ (A) line at 305.473 GHz is the strongest methanol line observed in TW Hya, but it is not the sole contributor to

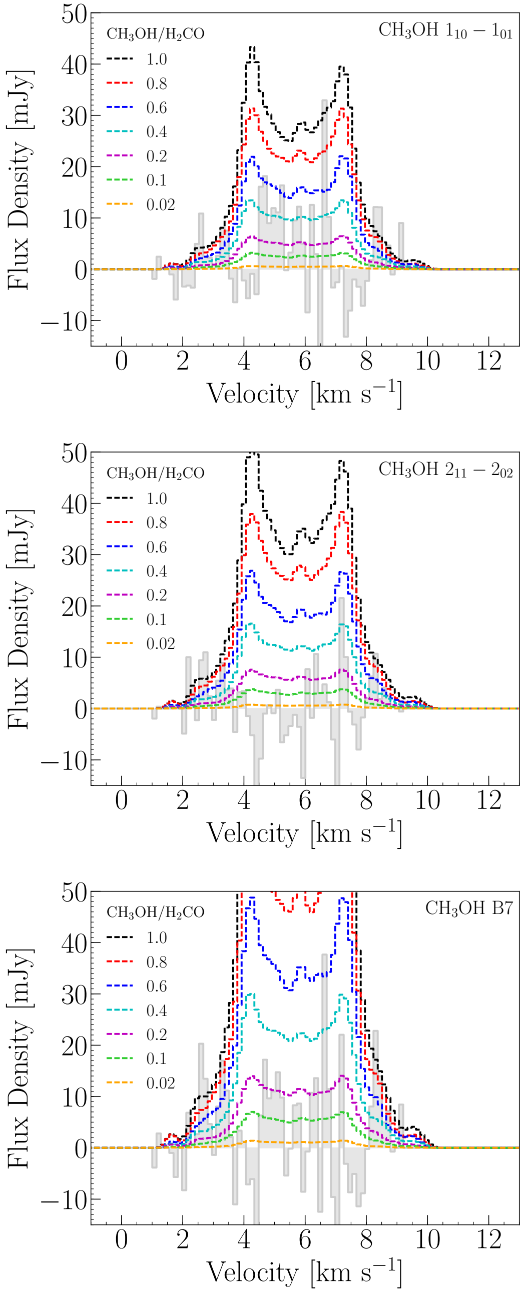

Figure 5.3: Model CH_3OH spectra at different CH_3OH/H_2CO abundance ratios (colored dashed lines) compared to the ALMA CH_3OH non-detections after Keplerian masking (gray) in the HD 163296 disk. Given the sensitivity levels achieved, the ALMA observations should be sensitive to the presence of methanol in the disk for $CH_3OH/H_2CO \gtrsim 0.2$ based on the stacked band 7 lines. (Top) CH_3OH $1_{10} - 1_{01}$ (A) line. (Middle) CH_3OH $2_{11} - 2_{02}$ (A) line. (Bottom) Stacked band 7 CH_3OH lines.

the detected line emission. However, even if all three lines are equally strong and the 305.473 GHz line contributes only 33% to the total stacked line intensity, then the inferred TW Hya CH_3OH/H_2CO ratio of 0.42 is still higher than our upper limit for HD 163296 of < 0.24. Matched filter analysis of the TW Hya CH_3OH detections (e.g., Figure 7 in Loomis et al. 2018) shows that the CH_3OH $3_{12} - 3_{03}$ (A) line is indeed stronger than the other two band 7 lines used by Walsh et al. (2016) for line stacking, suggesting that a contribution of ~50% to the stacked emission is a reasonable estimate.

Modeling by Willacy (2007) explored complex gas-grain chemical models of protoplanetary disks including H_2CO and CH_3OH with the following desorption processes: thermal desorption, desorption due to cosmic-ray heating of grains, and photodesorption. Their models, based on the UMIST Database for Astrochemistry network, show that outer disk abundances should give $CH_3OH/H_2CO \approx 0.04$, which underestimates the value found for both TW Hya and HD 163296. However, these models neglected radical-radical pathways to form larger complex organic molecules. Gas-grain chemical models by Semenov & Wiebe (2011) based on the Ohio State University (OSU) network predict low column densities of methanol ice due to the high diffusion barrier used in the grain-surface chemistry, which highlights the importance of the assumed chemical parameters in these models. Their models and work by Furuya & Aikawa (2014) show that production of CH_3OH is sensitive to turbulent mixing and that the abundance of gas-phase CH_3OH, and thus the CH_3OH/H_2CO ratio, will increase when turbulent mixing is strong. The HD 163296 disk has a low degree of turbulence $\lesssim 0.05c_s$ (Flaherty et al. 2015, 2017), while the TW Hya disk has similar low values of $\lesssim 0.05 - 0.10\ c_s$ (Flaherty et al. 2018), suggesting vertical mixing is not strong in these disks.

Other recent work by Walsh et al. (2014) based on the OSU network investigates the production of complex molecules in disks, including H_2CO and CH_3OH, using an extensive full chemical network with chemical ingredients similar to the previously mentioned works. The Walsh et al. (2014) models include gas-phase two-body reactions, photoreactions, cosmic-ray and X-ray reactions, gas-grain interactions, grain-surface two-body reactions, grain-surface photoreactions, and grain-surface cosmic-ray-induced and X-ray-induced photoreactions. The models in that work show that their outer disk ($R = 250$ AU) hosts a large methanol and formaldehyde ice reservoir with a sufficient number of these molecules released into the gas phase to give $CH_3OH/H_2CO \approx 0.33$, which is less than the value found for the TW Hya disk, but similar to what is estimated for the HD 163296 based on the upper limits presented here. Their model is based on a disk around a typical T Tauri star but does not reproduce the TW Hya CH_3OH/H_2CO ratio well, which perhaps points to important differences in how these two molecules are formed in T Tauri disks versus Herbig Ae/Be disks.

The underlying physical structure in the TW Hya disk and the HD 163296 disk might explain the observed discrepancy between their CH_3OH/H_2CO ratios. Recent observations of submillimeter and scattered light in these disks highlight important differences in their dust structure. The micron-sized dust observed in scattered light is highly coupled to the gas and traces the surface layers of the disk, while millimeter-sized dust has mostly decoupled from the gas and settled toward the disk midplane (Dullemond & Dominik 2004; D'Alessio et al. 2006; Williams & Cieza 2011). The TW Hya disk was observed with ALMA in the band 6 continuum at 850 μm and with VLT/SPHERE in $H-$band at 1.62 μm (Andrews et al. 2016; van Boekel et al. 2017), showing several rings and gaps in both millimeter- and micron-sized dust. The micron-sized dust rings tracing the surface layers extend beyond the millimeter-sized dust in this disk.

In contrast, recent scattered light observations by VLT/SPHERE in the *H* band, Keck/NIRC2 in the *J* band, and ALMA 1.3 millimeter observations of the HD 163296 disk show that no scattered light is observed beyond the innermost millimeter dust ring, suggesting that the surface layers of the outer disk are relatively flat and may be shadowed by the innermost dust ring (Muro-Arena et al. 2018; Guidi et al. 2018). Ultraviolet radiation from the central star can release molecular ices back into the gas phase via UV photodesorption (Öberg et al. 2009, 2015; Huang et al. 2016), which may be suppressed if the HD 163296 outer disk is shadowed.

Alternatively, both disks may have a similar degree of UV irradiation, but as a Herbig Ae star HD 163296 will have a harder UV spectrum than TW Hya, which is dominated by Lyman-α emission (e.g., Figure 1 in Walsh et al. 2015). The UV photodesorption rate of methanol ice is a strong function of photon energy and absorption cross-section (Cruz-Diaz et al. 2016), and therefore will depend on the shape of the radiation field as well as the strength (Bertin et al. 2016). A harder, stronger Herbig Ae radiation field will lead to more CH_3OH fragmentation upon photodesorption and thus methanol ice will be converted into other gas-phase species which could go on to seed H_2CO formation in the gas phase.

Another possibility is that the HD 163296 disk formed from a protostar that did not inherit a large degree of methanol ice. Perhaps during formation, temperatures remained too warm for CO freeze-out needed to produce the high CH_3OH/H_2O ice ratios seen in ISM ices. Chemical models with some methanol already formed at earlier stages (Walsh et al. 2014) host a more abundant methanol ice reservoir than models which start from atomic abundances, which have orders of magnitude lower methanol ice abundances (e.g., Molyarova et al. 2017).

While both formaldehyde and methanol are thought to be formed via hydrogenation of CO ices (Watanabe & Kouchi 2002), formaldehyde can also be formed in the gas-phase. Recent chemical models by Agúndez et al. (2018) that do not include grain-surface chemistry are able to reproduce observed column densities of H_2CO, but not CH_3OH, in the outer regions of T Tauri and Herbig Ae/Be disks. Reactions between CH_3 and atomic oxygen can occur in the disk surface layers where oxygen-bearing species are photodissociated (Fockenberg & Preses 2002; Atkinson et al. 2006). This reaction, however, has not been shown to contribute significantly to the H_2CO abundance in recent chemical models of disks around T Tauri stars (Walsh et al. 2014). The contribution may be larger in warmer, strongly irradiated disks around Herbig Ae/Be stars. Ion-molecule chemistry – which has a large influence on the gas-phase reservoir in the intermediate layers of protoplanetary disks – involving e.g., HCO^+, H_3O^+, and H_3^+ may also contribute to the overall gas-phase H_2CO abundance (Vasyunin et al. 2008). It may be that the HD 163296 disk is particularly rich in H_2CO formed in the gas-phase, thus reducing its overall CH_3OH/H_2CO ratio. Detailed chemical models of the HD 163296 protoplanetary disk beyond the scope of this work are required to test and quantify the importance of the production and destruction routes for H_2CO and CH_3OH discussed here.

5.4.2 Detectability of methanol

We can estimate the required ALMA observing time for a 3σ detection of CH_3OH in the HD 163296 disk given a range of CH_3OH/H_2CO ratios consistent with our upper limit of < 0.24. We consider methanol abundances relative to formaldehyde of 0.20, 0.10, 0.05, as these would be below our current 3σ upper limit of < 0.24 listed in Table 5.3. To observe the CH_3OH $2_{11} - 2_{02}$ (A) line of methanol with similar spatial and spectral resolution at these assumed CH_3OH/H_2CO ratios, we would need to increase our sensitivity by factors of about ~1.5, ~2.5, and ~5, respectively. Because the telescope sensitivity is inversely proportional to the square root of the observing time, $\sigma_S \propto 1/\sqrt{t}$, the time required to realize these increases in sensitivity would multiply by factors of 2.25, 6.25, and 25, respectively. Based on the band 7 observations presented here with 105 minutes of total on-source time, these factors translate to total on-source times of ~4 hrs, ~11 hrs, ~44 hrs for methanol at 20%, 10%, and 5% of the formaldehyde content in HD 163296, respectively. The detection of 10% methanol relative to formaldehyde is a clear practical limit for the HD 163296 disk based on these required integration times.

Disk size has a significant effect on methanol detectability. Using our HD 163296 model, we decrease the outer radius of the disk and scale the disk physical structure proportionally to test the effect of disk size on the band 7 methanol line strengths for Herbig disks similar to HD 163296. The LIME models are rerun for an outer disk radius from $R_{\mathrm{out}} = 100-600$ AU in steps of 50 AU for CH_3OH/H_2CO = 0.10. The disk-integrated line intensity for the band 7 CH_3OH lines decreases by one order of magnitude for disks with $R_{\mathrm{out}} = 250$ AU and by more than two orders of magnitude for disks with $R_{\mathrm{out}} = 100$ AU. It is highly unlikely that methanol will be detected within an observing time of < 20 hours in most disks smaller than ~300 AU, considering the difficulty in detecting methanol relative to formaldehyde at the $< 25\%$ level in the HD 163296 disk, which has a radius of ~550 AU and a proximity closer than most nearby star-forming regions. These results depend on the assumption that CH_3OH shares the same extended emitting area as H_2CO.

It may be that the methanol lines targeted in this work are not suitable candidates for disks around Herbig Ae/Be stars. The choice to target these four CH_3OH lines with ALMA in band 6 and band 7 was motivated by the chemical modeling of a disk around a T Tauri star (Walsh et al. 2014) and by the methanol detection in the disk around TW Hya, also a T Tauri star (Walsh et al. 2016). Disks around Herbig Ae/Be stars are warmer, with a larger thermally desorbed inner reservoir due to the stronger stellar radiation. There is a potential reservoir of hot methanol in the inner disk atmosphere, similar to the hot water reservoir already observed in disks around less luminous T Tauri stars (Carr & Najita 2008; Salyk et al. 2008). Such emission could be compact yet still accessible in Herbig Ae/Be disks.

In summary, the CH_3OH lines in ALMA band 7 presented here should be detectable in disks with a CH_3OH/H_2CO ratio down to ~10% within realistic observing times, but only in disks with similar mass, size, distance, and H_2CO abundance as those found in the HD 163296 disk.

5.5 Conclusions

This paper presents ALMA observations targeting two CH_3OH lines in band 6 and two CH_3OH lines in band 7 in the protoplanetary disk around HD 163296. We determine upper limits on the abundance of methanol likely to be present in the HD 163296 disk and compare to TW Hya, currently the only Class II disk with a positive detection of gas-phase methanol. The conclusions of this work are as follows:

- None of the four CH_3OH lines are detected in the disk around HD 163296 individually nor after line stacking. Upper limits on the integrated intensity at the 3σ level are < 51 mJy km s^{-1} for band 6 lines and < 26 mJy km s^{-1} for band 7 lines. Neither aperture masking in the image plane, Keplerian masking in the image plane, nor matched filter analysis in the *uv* plane recover any methanol emission, indicating that our calculated 3σ upper limits are highly robust.
- The CH_3OH $2_{11} - 2_{02}$ (A) line provides the strictest upper limit on the disk-averaged column density and abundance of methanol in the HD 163296 disk, with $N_{\rm avg} < 5.0 \times 10^{11}$ cm^{-2} and $CH_3OH/H_2 \lesssim 1.6 \times 10^{-12}$ at the 3σ level.
- The upper limit on the methanol-to-formaldehyde ratio in the HD 163296 disk is $CH_3OH/H_2CO < 0.24$ at the 3σ level. This ratio is lower than that of the TW Hya disk at $CH_3OH/H_2CO = 1.27 \pm 0.13$, indicating that the HD 163296 disk has a low amount methanol with respect to formaldehyde relative to the TW Hya disk.
- Possible explanations for the lower CH_3OH/H_2CO ratio in HD 163296 include: a low amount of gas-phase methanol is desorbed from icy grains at the disk midplane due to the flatter, shadowed disk geometry as seen in recent images taken by VLT/SPHERE; differences in the desorption processes in the HD 163296 disk compared to the TW Hya disk; and a higher-than-expected gas-phase formaldehyde abundance, as H_2CO may also be formed in the gas-phase in the disk upper layers.
- To detect methanol at the 3σ level in the HD 163296 disk, we estimate that it is necessary to increase the total on-source observing time with the full ALMA 12-meter array up to 4 hours to be sensitive to $CH_3OH/H_2CO \approx 20\%$ and up to 11 hours to be sensitive to $CH_3OH/H_2CO \approx 10\%$. These estimates apply to other Herbig Ae/Be disks with masses, sizes, and distances similar to that found for the HD 163296 disk.

Acknowledgements

The authors acknowledge support by Allegro, the European ALMA Regional Center node in The Netherlands, and expert advice from Luke Maud. M.T.C. and M.R.H. acknowledge support from the Netherlands Organisation for Scientific Research (NWO) grant 614.001.352. V.V.G. acknowledges support from the National Aeronautics and Space Administration under grant No. 15XRP15 20140 issued through the Exoplanets Research Program. C.W. acknowledges financial support from the University of Leeds. This paper makes use of the following ALMA data: ADS/JAO.ALMA# 2016.1.00884.S and #2013.1.01268.S. L.I.C. acknowledges the support of NASA through Hubble Fellowship grant HST-HF2-51356.001-A awarded by the Space Telescope Science Institute, which is operated by the Association of Universities for Research in Astronomy, Inc., for NASA, under contract NAS 5-26555. ALMA is a partnership of ESO (representing its member states), NSF (USA) and NINS (Japan), together with NRC (Canada), NSC and ASIAA (Taiwan), and KASI (Republic of Korea), in cooperation with the Republic of Chile. The Joint ALMA Observatory is operated by ESO, AUI/NRAO and NAOJ.

Appendix A: Molecular abundances for different T_{ex}

Here the disk-averaged column densities and abundances are calculated for CH_3OH and H_2CO in the disk around HD 163296 and the disk around TW Hya for different excitation temperatures T_{ex}. The method used is described in Section 5.3.2. Equation 5.1 assumes optically thin emission and LTE excitation conditions. The excitation temperature T_{ex} is set to 25, 50 and 75 K, indicating different regions of the disk from which the emission lines may originate. At most, differences of factors $2-3$ are seen in the disk-averaged column density and abundance for the values of T_{ex} explored here.

Table 5.4: Disk-averaged column density and abundance of CH_3OH and H_2CO in HD 163296 and TW Hya for varying T_{ex}.

Object	Line	$\int I_\nu dv$[†] [mJy km s^{-1}]	E_{u} [K]	$\log(A_{\mathrm{ij}})$ [s^{-1}]	T_{ex} [K]	n_{crit}[a b] [cm^{-3}]	N_{avg} [cm^{-2}]	CH_3OH/H_2	CH_3OH/H_2CO[††]
				CH_3OH					
HD 163296	CH_3OH $5_{05}-4_{04}$ (E)	< 51	47.9	−4.22	25	1.6(06)	< 6.9(12)	< 2.1(−11)	
					50	1.9(06)	< 8.6(12)	< 2.6(−11)	
					75	2.1(06)	< 1.1(13)	< 3.5(−11)	
	CH_3OH $5_{05}-4_{04}$ (A)	< 51	34.8	−4.22	25	4.3(05)	< 4.1(12)	< 1.3(−11)	
					50	5.0(05)	< 6.6(12)	< 2.0(−11)	
					75	5.0(05)	< 9.6(13)	< 3.0(−11)	
	CH_3OH $1_{10}-1_{01}$ (A)	< 26	16.9	−3.49	25	4.3(07)	< 7.0(11)	< 2.2(−12)	
					50	5.6(07)	< 1.6(12)	< 5.0(−12)	
					75	6.4(07)	< 2.7(12)	< 8.2(−12)	
	CH_3OH $2_{11}-2_{02}$ (A)	< 26	21.6	−3.49	25	5.0(06)	< 5.0(11)	< 1.6(−12)	
					50	5.4(06)	< 1.1(12)	< 3.3(−12)	
					75	5.5(06)	< 1.7(12)	< 5.2(−12)	
TW Hya	CH_3OH stacked[*]	26.5 ± 2.7[c]	28.6	−3.49	25	3.0(06)	4.7(12)	1.1(−12)	
					50	3.0(06)	8.6(12)	2.1(−12)	
					75	3.1(06)	1.3(13)	3.2(−12)	
				H_2CO					
HD 163296	H_2CO $3_{12}-2_{11}$	890 ± 89[d]	33.4	−3.55	25	5.7(06)	2.1(12)	6.3(−12)	< 0.24
					50	6.2(06)	3.0(12)	9.2(−12)	< 0.43
					75	6.4(06)	4.2(12)	1.3(−11)	< 0.50
TW Hya	H_2CO $3_{12}-2_{11}$	291 ± 29[e]	33.4	−3.55	25	5.7(06)	3.7(12)	8.9(−13)	1.27 ± 0.13
					50	6.2(06)	5.3(12)	1.6(−12)	1.62 ± 0.16
					75	6.4(06)	7.5(12)	1.8(−12)	1.73 ± 0.17

Notes. The format $a(b)$ translates to $a \times 10^b$. Flux errors are dominated by systematic uncertainties, taken to be 10%.

(†) Upper limits are derived at the 3σ level using the HD 163296 Keplerian mask (see Section 5.3.1).

(††) Ratios are determined using the CH_3OH disk-integrated column density from Table 5.2. HD 163296: based on the strictest upper limit from the CH_3OH $2_{11}-2_{02}$ (A) line. TW Hya: based on the stacked CH_3OH detection.

(*) The stacked detection consists of three CH_3OH transitions: CH_3OH $2_{11}-2_{02}$ (A) at 304.208 GHz, CH_3OH $3_{12}-3_{03}$ (A) at 305.472 GHz, and CH_3OH $4_{13}-4_{04}$ at 307.166 GHz. Excitation parameters for the CH_3OH $3_{12}-3_{03}$ (A) line are used to calculate column density.

References: (a) Rabli & Flower (2010); (b) Wiesenfeld & Faure (2013); (c) Walsh et al. (2016); (d) Qi et al. (2013); (e) Öberg et al. (2017).

References

Agúndez, M., Roueff, E., Le Petit, F., & Le Bourlot, J. 2018, A&A, 616, A19

Aikawa, Y., Momose, M., Thi, W.-F., et al. 2003, PASJ, 55, 11

Alecian, E., Wade, G. A., Catala, C., et al. 2013, MNRAS, 429, 1001

Andrews, S. M., Wilner, D. J., Zhu, Z., et al. 2016, ApJ, 820, L40

Atkinson, R., Baulch, D. L., Cox, R. A., et al. 2006, Atmospheric Chemistry & Physics, 6, 3625

Bergin, E. A., Cleeves, L. I., Gorti, U., et al. 2013, Nature, 493, 644

Bertin, M., Romanzin, C., Doronin, M., et al. 2016, ApJ, 817, L12

Boogert, A. C. A., Gerakines, P. A., & Whittet, D. C. B. 2015, ARA&A, 53, 541

Bottinelli, S., Boogert, A. C. A., Bouwman, J., et al. 2010, ApJ, 718, 1100

Brinch, C. & Hogerheijde, M. R. 2010, A&A, 523, A25

Carney, M. T., Hogerheijde, M. R., Loomis, R. A., et al. 2017, A&A, 605, A21

Carr, J. S. & Najita, J. R. 2008, Science, 319, 1504

Cruz-Diaz, G. A., Martín-Doménech, R., Muñoz Caro, G. M., & Chen, Y.-J. 2016, A&A, 592, A68

Cuppen, H. M., van Dishoeck, E. F., Herbst, E., & Tielens, A. G. G. M. 2009, A&A, 508, 275

D'Alessio, P., Calvet, N., Hartmann, L., Franco-Hernández, R., & Servín, H. 2006, ApJ, 638, 314

Dartois, E., Schutte, W., Geballe, T. R., et al. 1999, A&A, 342, L32

de Gregorio-Monsalvo, I., Ménard, F., Dent, W., et al. 2013, A&A, 557, A133

Drozdovskaya, M. N., Walsh, C., Visser, R., Harsono, D., & van Dishoeck, E. F. 2014, MNRAS, 445, 913

Dullemond, C. P. & Dominik, C. 2004, A&A, 421, 1075

Flaherty, K. M., Hughes, A. M., Rose, S. C., et al. 2017, ApJ, 843, 150

Flaherty, K. M., Hughes, A. M., Rosenfeld, K. A., et al. 2015, ApJ, 813, 99

Flaherty, K. M., Hughes, A. M., Teague, R., et al. 2018, ApJ, 856, 117

Fockenberg, C. & Preses, J. M. 2002, Journal of Physical Chemistry A, 106, 2924

Friberg, P., Madden, S. C., Hjalmarson, A., & Irvine, W. M. 1988, A&A, 195, 281

Furuya, K. & Aikawa, Y. 2014, ApJ, 790, 97

Gaia Collaboration, Brown, A. G. A., Vallenari, A., et al. 2018, ArXiv e-prints

Graninger, D. M., Wilkins, O. H., & Öberg, K. I. 2016, ApJ, 819, 140

Grim, R. J. A., Baas, F., Geballe, T. R., Greenberg, J. M., & Schutte, W. A. 1991, A&A, 243, 473

Guidi, G., Ruane, G., Williams, J. P., et al. 2018, ArXiv e-prints

Guzmán, V. V., Öberg, K. I., Carpenter, J., et al. 2018, ApJ, 864, 170

Herbst, E. & van Dishoeck, E. F. 2009, ARA&A, 47, 427

Huang, J., Öberg, K. I., & Andrews, S. M. 2016, ApJ, 823, L18

Isella, A., Guidi, G., Testi, L., et al. 2016, Phys. Rev. Lett., 117, 251101

Kristensen, L. E., van Dishoeck, E. F., van Kempen, T. A., et al. 2010, A&A, 516, A57

Lee, C.-F., Li, Z.-Y., Ho, P. T. P., et al. 2017, ApJ, 843, 27

Loomis, R. A., Cleeves, L. I., Öberg, K. I., Guzman, V. V., & Andrews, S. M. 2015, ApJ, 809, L25

Loomis, R. A., Öberg, K. I., Andrews, S. M., et al. 2018, AJ, 155, 182

Mathews, G. S., Klaassen, P. D., Juhász, A., et al. 2013, A&A, 557, A132

McMullin, J. P., Waters, B., Schiebel, D., Young, W., & Golap, K. 2007, in

Astronomical Society of the Pacific Conference Series, Vol. 376, Astronomical Data Analysis Software and Systems XVI, ed. R. A. Shaw, F. Hill, & D. J. Bell, 127
Miao, Y., Mehringer, D. M., Kuan, Y.-J., & Snyder, L. E. 1995, ApJ, 445, L59
Molyarova, T., Akimkin, V., Semenov, D., et al. 2017, ApJ, 849, 130
Müller, H. S. P., Schlöder, F., Stutzki, J., & Winnewisser, G. 2005, Journal of Molecular Structure, 742, 215
Muro-Arena, G. A., Dominik, C., Waters, L. B. F. M., et al. 2018, A&A, 614, A24
Öberg, K. I., Furuya, K., Loomis, R., et al. 2015, ApJ, 810, 112
Öberg, K. I., Garrod, R. T., van Dishoeck, E. F., & Linnartz, H. 2009, A&A, 504, 891
Öberg, K. I., Guzmán, V. V., Merchantz, C. J., et al. 2017, ApJ, 839, 43
Öberg, K. I., Qi, C., Fogel, J. K. J., et al. 2010, ApJ, 720, 480
Pinte, C., Price, D. J., Ménard, F., et al. 2018, ApJ, 860, L13
Pontoppidan, K. M., van Dishoeck, E. F., & Dartois, E. 2004, A&A, 426, 925
Qi, C., D'Alessio, P., Öberg, K. I., et al. 2011, ApJ, 740, 84
Qi, C., Öberg, K. I., Andrews, S. M., et al. 2015, ApJ, 813, 128
Qi, C., Öberg, K. I., & Wilner, D. J. 2013, ApJ, 765, 34
Rabli, D. & Flower, D. R. 2010, MNRAS, 406, 95
Remijan, A., Snyder, L. E., Friedel, D. N., Liu, S.-Y., & Shah, R. Y. 2003, ApJ, 590, 314
Rosenfeld, K. A., Andrews, S. M., Hughes, A. M., Wilner, D. J., & Qi, C. 2013, ApJ, 774, 16
Salinas, V. N., Hogerheijde, M. R., Mathews, G. S., et al. 2017, A&A, 606, A125
Salyk, C., Pontoppidan, K. M., Blake, G. A., et al. 2008, ApJ, 676, L49
Semenov, D. & Wiebe, D. 2011, ApJS, 196, 25
Shimonishi, T., Onaka, T., Kato, D., et al. 2010, A&A, 514, A12
Skinner, C. J., Tielens, A. G. G. M., Barlow, M. J., & Justtanont, K. 1992, ApJ, 399, L79
Teague, R., Bae, J., Bergin, E. A., Birnstiel, T., & Foreman-Mackey, D. 2018, ApJ, 860, L12
van Boekel, R., Henning, T., Menu, J., et al. 2017, ApJ, 837, 132
van den Ancker, M. E., de Winter, D., & Tjin A Djie, H. R. E. 1998, A&A, 330, 145
van der Marel, N., van Dishoeck, E. F., Bruderer, S., & van Kempen, T. A. 2014, A&A, 563, A113
van Dishoeck, E. F., Blake, G. A., Jansen, D. J., & Groesbeck, T. D. 1995, ApJ, 447, 760
van 't Hoff, M. L. R., Tobin, J. J., Trapman, L., et al. 2018, ArXiv e-prints
Vasyunin, A. I., Semenov, D., Henning, T., et al. 2008, ApJ, 672, 629
Walsh, C., Loomis, R. A., Öberg, K. I., et al. 2016, ApJ, 823, L10
Walsh, C., Millar, T. J., Nomura, H., et al. 2014, A&A, 563, A33
Walsh, C., Nomura, H., & van Dishoeck, E. 2015, A&A, 582, A88
Watanabe, N. & Kouchi, A. 2002, ApJ, 571, L173
Watanabe, N., Shiraki, T., & Kouchi, A. 2003, ApJ, 588, L121
Wiesenfeld, L. & Faure, A. 2013, MNRAS, 432, 2573
Willacy, K. 2007, ApJ, 660, 441
Williams, J. P. & Cieza, L. A. 2011, ARA&A, 49, 67

“Would you tell me, please, which way I ought to go from here?”
“That depends a good deal on where you want to get to,” said the Cat
“I don’t much care where–” said Alice.
“Then it doesn’t matter which way you go,” said the Cat.

– Lewis Carroll, *Alice’s Adventures in Wonderland*

ANATOMY OF A THESIS

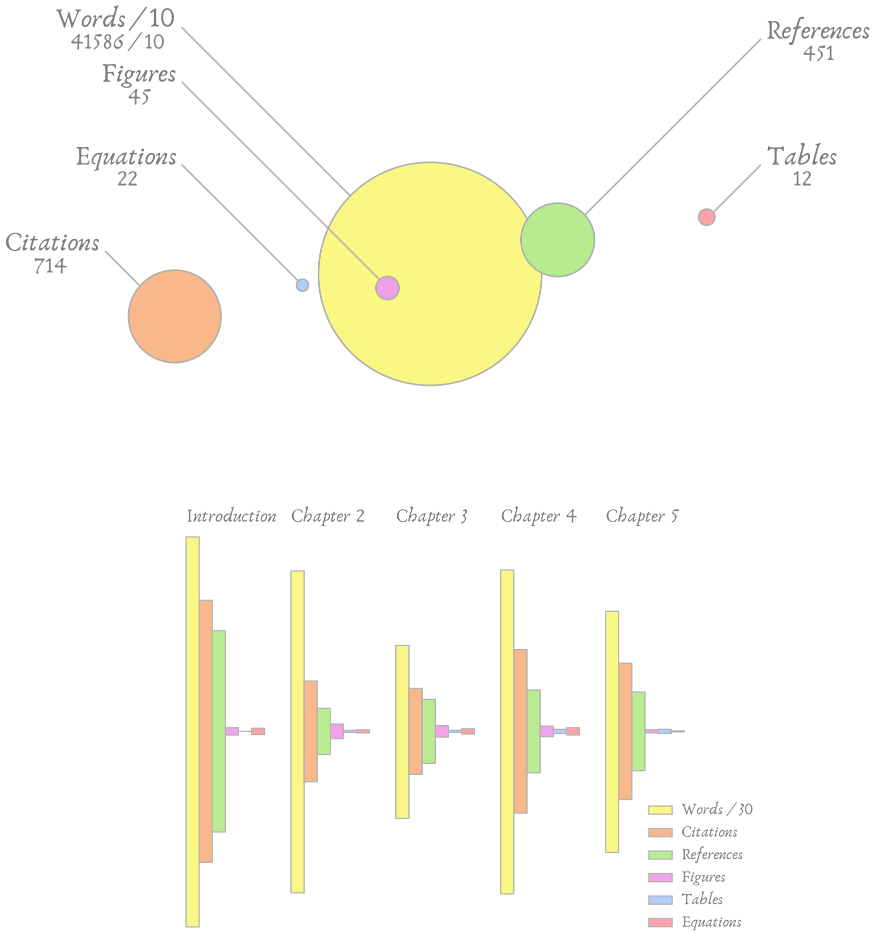

Figure: (Top) Total count of thesis content in the introduction and scientific chapters. (Bottom) Relative contributions of content broken down by chapter.

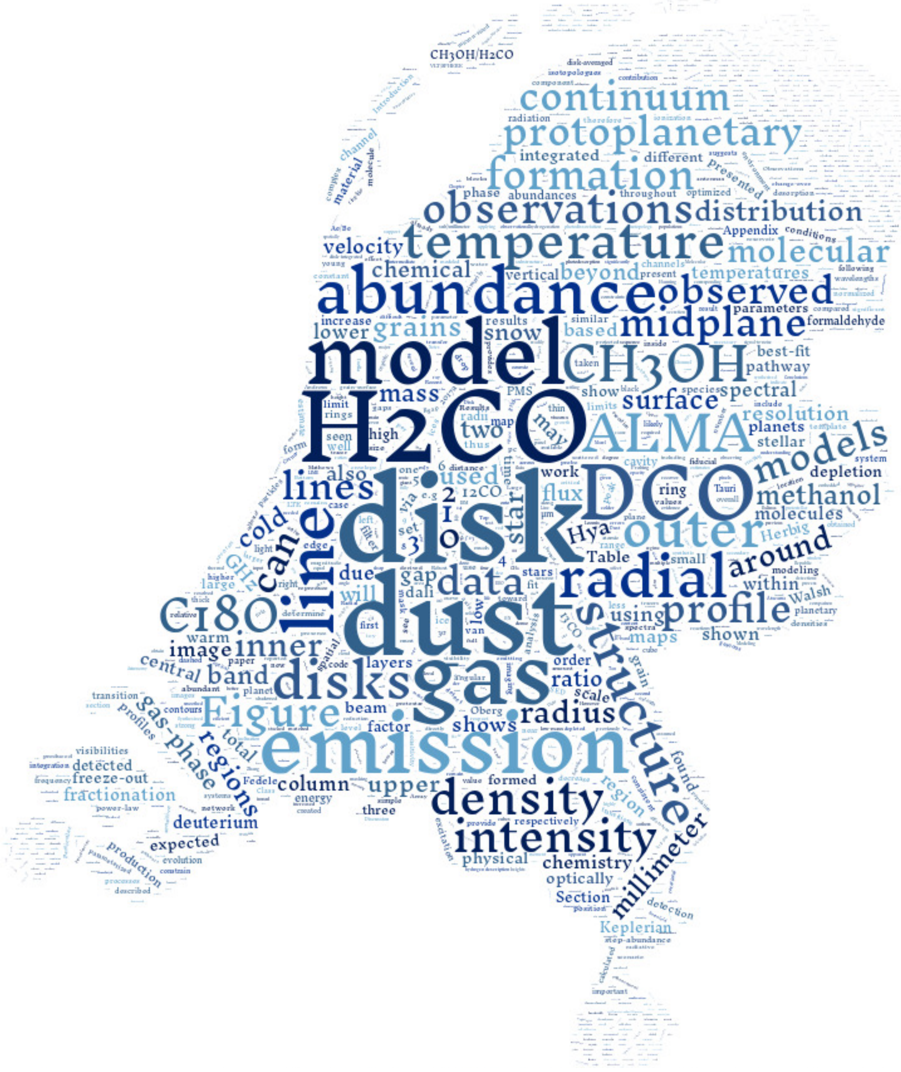
CH3OH/H2CO
continuum
protoplanetary
integrated
different
formation
observations
distribution
temperature
molecular
velocity
chemical
abundance
observed
midplane
model
CH3OH
H2CO
ALMA
models
disk
DCO
lines
methanol
outer
radial
around
line
dust
data
profile
C18O
structure
inner
disks
gas
Figure
radius
emission
density
intensity
millimeter
grains
snow
surface
spectral
mass
two
resolution
flux
cold
can
regions
gas-phase
band
ratio
freeze-out
fractionation
deuterium
column
upper
shows
Keplerian
chemistry
optically
Section
physical
expected
detected
image

Figure: Word cloud of the thesis text contained in the introduction and scientific chapters. Words that are used more frequently appear larger in the graphic above[1].

---

[1] Created at `https://www.wordclouds.com`

ENGLISH SUMMARY

We are curious about our place in the universe. We want to know how we came to exist and whether we are truly alone among an uncountable sea of stars. To study our origins we look to the Earth and the rest of the Solar System, searching for clues as to how the earliest forms of life may have originated on our planet. Perhaps life formed in the oceans of a pre-historic Earth, or the right combination of organics were delivered by comets from the outer Solar System. We still have no definitive answer. To study the question of whether or not life can exist elsewhere we turn our telescopes toward the sky to observe other stars. Nearly 25 years ago we discovered the first planet around a star other than our own Sun, which led to a surge in extrasolar planet (or exoplanet) research. By now we have discovered over $3,500$ exoplanets in more than $2,500$ different systems, hundreds of which have more than one planet. These planetary systems have a wide variety of configurations, orbits, planetary sizes, masses, and compositions which together reveals a great amount of diversity in the types of worlds which may be able to host life.

To understand the origins of such a rich catalog of planetary systems, we must examine the birthplaces of planets long before they emerge fully formed. Planets, asteroids, and comets are remnants of the disk of gas and dust that exists around young stars as they form. These circumstellar disks, or protoplanetary disks, are themselves a natural outcome of the star formation process. Inside giant clouds of molecular gas that float through the interstellar medium, some dense pockets of gas and dust collapse to form young protostars. As the collapse continues, a protoplanetary disk is formed around the young star in order to redistribute momentum due to the initial rotation of the molecular cloud. This prevents the forming star from spinning so quickly that it breaks up. Over millions of years, the star accretes material from the protoplanetary disk and the disk evolves to form planetesimals and planets before it is depleted. This is the environment in which planets are born, and it is crucial to understand the connection between the structure and chemistry of the protoplanetary disk and the planets that ultimately form.

The tools used for the study of protoplanetary disks are ground-based and spaced-based telescopes, most often in the micron (infrared) and millimeter (microwave) wavelength range of the electromagnetic spectrum. Peering into disks at these wavelengths allows astronomers to observe the small and large dust grains as well as many species of atomic and molecular gas. To properly understand the

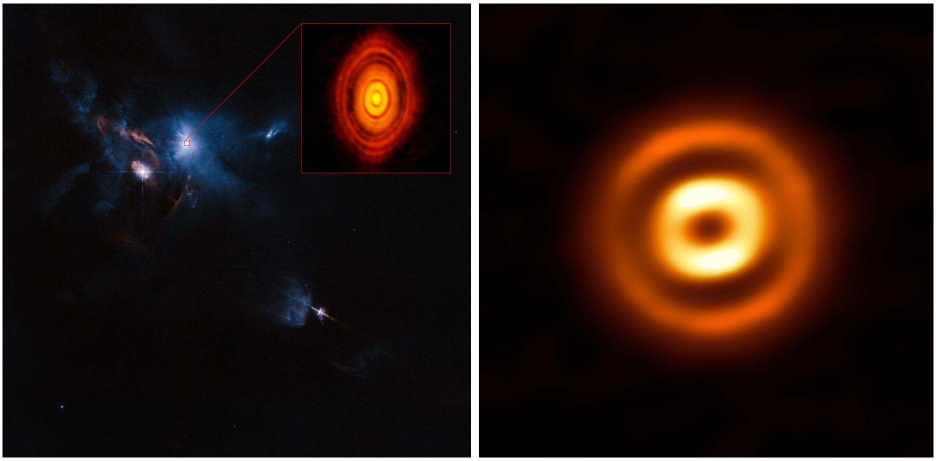

Figure: (Left) Composite image from the Hubble Space Telescope and ALMA showing the environment around the young star HL Tau in visible light (main image). The disk around HL Tau (inset) has been observed in great detail at millimeter wavelengths by ALMA, showing the incredible resolving power of the array. (Right) ALMA observations of the millimeter dust continuum in the disk around the young star HD 169142. The image clearly shows two distinct bright rings that may have been carved out by planets sweeping up material in the disk.
Credit: (Left) ALMA (ESO/NAOJ/NRAO), ESA/Hubble and NASA; (Right) ALMA (ESO/NAOJ/NRAO), Fedele et al. 2017

structure of a disk and the environments with active chemistry, both dust and gas must be observed. Modern day telescopes are now powerful enough to resolve many protoplanetary disks in the millimeter wavelength regime using interferometry. Interferometers combine the observing capabilities of several separate antennas or receivers into one large, discretely sampled telescope to increase the total observing diameter and thus improve the resolution. It is analogous to massively increasing the size of the mirror on an optical telescope, but with large holes in the mirror and sections missing. The technique greatly improves the resolving power of the whole telescope to give detailed views of the inner workings of disks. The largest millimeter wavelength interferometer currently operating is the Atacama Large Millimeter/submillimeter Array (ALMA), a vast combination of 50 full array antennas with a 12-meter diameter, 12 compact array antennas with a 7-meter diameter and 4 single-dish antennas with a 12-meter diameter. The array can be reconfigured to achieve a total telescope diameter of up to 16 kilometers. The facility has been operational since 2011 at an elevation of 5000 meters on Llano de Chajnantor, Chile. ALMA has produced nearly all observing data used in this thesis. The facility is already churning out groundbreaking images that are allowing astronomers to study in more detail the complexities in the structure and chemistry of protoplanetary disks.

Thesis overview

This thesis examines the anatomy of planet-forming regions within protoplanetary disks using ALMA observations of dust and simple molecules as probes. It is important to understand the structure and chemistry of these regions because they hold the ingredients for planets, some of which may have the conditions suitable for life. The chapters focus on the connection between the distribution of dust grains and the chemistry that determines the emission of simple molecules, in particular carbon monoxide (CO), formaldehyde (H_2CO), the deuterium-bearing ion DCO^+, and methanol (CH_3OH). Each of these molecules is thought to be affected by the freeze-out of gas into ice around the surface of dust grains deep in the cold disk midplane, which is an important process both for building planetesimals with sticky ice grains and for regulating gas-phase chemistry by removing certain molecules from the gas phase. There is also a solid-phase chemistry active on the icy grain surfaces that can lead to the formation of more complex molecules. Any constraints on the chemical origins of these molecules may provide insight into the physical and chemical complexity of planetary birthplaces.

In chapter two, the distribution of formaldehyde gas and its relation to carbon monoxide gas structure is investigated in the protoplanetary disk around the young Herbig Ae star HD 163296. Formaldehyde is expected to form primarily in the solid phase by the addition of hydrogen to CO ices in the cold disk midplane, but there is also an additional contribution from a warmer gas-phase formation pathway. When formed by solid-phase chemistry, formaldehyde can act as a precursor to more complex molecular species such as methanol and other alcohols. In this chapter, analysis of three H_2CO lines is presented which were observed with ALMA toward the HD 163296 disk. Existing models of the HD 163296 disk are used to reproduce the observed emission of H_2CO and $C^{18}O$, a rarer isotope form (isotopolog) of CO gas. To fit the observations, the H_2CO abundance must increase sharply by a factor of two while the CO abundance must decrease sharply by a factor of ten at the edge of the millimeter grains. The depletion of CO may be due to freeze-out in the disk midplane or photodissociation by stellar radiation in the disk surface layers, while the increase in H_2CO may be due to increased formation on icy grain surfaces or a more active gas-phase chemistry in the outer disk. The exact formation pathway of the additional formaldehyde beyond the millimeter grains remains unclear, but this chapter shows that H_2CO production is fundamentally connected to the dust structure in the HD 163296 disk.

In chapter three, recent ALMA observations are presented that reveal rings and gaps in the millimeter dust and the gas in the protoplanetary disk around the Herbig Ae star HD 169142. The millimeter continuum observations reveal two distinct dust rings that are resolved for the first time. ALMA observations of three CO isotopologs (^{12}CO, ^{13}CO and $C^{18}O$) show differences in the gas and dust structure, indicating that the dust has decoupled from the gas. Models of the disk structure and molecular excitation are used to reproduce the observed dust and gas emission. The substructure observed in the dust is well fit with an empty central cavity, a mildly depleted inner ring, a totally depleted dust gap, and an outer ring. The gas structure has a small inner cavity and is depleted by a factor of 30 – 40 out to the edge of the dust gap. The gas outer radius is about 100 astronomical units greater than the dust outer radius, which is indicative of radial drift due to dust grain growth. This chapter argues that structure seen in the dust and gas is consistent with multiple Jupiter-mass giant planets carving out gaps in the disk as they orbit the central star and sweep up disk material.

In chapter four, ALMA observations of the molecular ion DCO^+ in the protoplanetary disk around HD 169142 are analyzed in order to gauge the ability of DCO^+ to trace physical structure in the dust and gas near the midplane. The DCO^+ molecule is expected to be an excellent tracer of the disk midplane environment and an indicator of CO freeze-out in disks as its formation requires a balance of gas-phase CO and CO depletion. The physical disk structure obtained from Chapter 3 is used with a simple deuterium network chemical model to reproduce the observed DCO^+ emission. The models indicate that in order to recreate the DCO^+ emission, the HD 169142 disk structure must be adapted to include a region that is colder and more CO-depleted than in the original model just beyond the edge of the millimeter grain distribution. The results indicate that DCO^+ is an effective CO freeze-out tracer in the HD 169142 disk, and that the molecule can reveal disk midplane structure that is not apparent in CO isotopologs.

In chapter five, four lines of the CH_3OH molecule are searched for with ALMA toward the disk around the young Herbig Ae star HD 163296. Methanol acts as a starting point for complex prebiotic chemistry and is therefore a desirable molecule to detect and characterize in protoplanetary disks. Its formation is expected to be linked with that of formaldehyde because they can both form via solid-phase chemistry by hydrogen addition to CO ice. Currently, the only optically visible protoplanetary disk with a detection of gas-phase methanol is the disk around TW Hya. No methanol is detected in the HD 163296 disk, but upper limits place strong constraints on the methanol abundance suggesting a fraction of $\lesssim 10^{-12}$ relative to molecular hydrogen. Analysis of the methanol-to-formaldehyde ratio suggests that methanol is less abundant with respect to formaldehyde in the HD 163296 disk by almost a factor of ten when compared to the TW Hya disk. The difference may be due to variation in how CH_3OH and H_2CO are released from ices back into the gas between the disks, more efficient gas-phase formation of H_2CO in HD 163296, or perhaps differences in the efficiency of formaldehyde and methanol formation on grain surfaces.

In summary, this thesis shows that the observations of simple molecules such as CO isotopologs, DCO^+, and H_2CO at high spatial and spectral resolution examine the anatomy of protoplanetary disk regions connected to the birthplaces of planets. Any substructure in the disk is reflected in the abundance structure of these molecules, which can be used as powerful diagnostics of the physical disk environment. Other simple organic species remain elusive and difficult to detect in disks, as is the case for CH_3OH despite the expected link with H_2CO, which is readily detected in disks. The degree to which H_2CO and CH_3OH production is connected in protoplanetary disks remains to be seen. Future observations with ALMA and other facilities will continue to provide insights into the complicated physical and chemical processes that determine the structure, molecular ingredients, and conditions of the planet-forming environment in protoplanetary disks.

NEDERLANDSE SAMENVATTING

We willen weten wat onze plek is in het universum. We zijn benieuwd hoe we zijn ontstaan en of we wel echt de enige zijn in de zee van ontelbare sterren. Om onze oorsprong te bestuderen kijken we naar de aarde en de rest van het zonnestelsel, op zoek naar aanwijzingen. Wellicht is het leven begonnen in de oceanen van een pre-historische aarde, of is de juiste combinatie van organische moleculen door een komeet gebracht? Antwoorden op deze vragen hebben we niet. Om te achterhalen of leven elders kan bestaan richten we onze telescopen naar andere sterren. Bijna 25 jaar geleden hebben we de eerste planeet in een baan rond een andere ster ontdekt. Dat heeft geleid tot een enorme groei in het onderzoek naar exoplaneten. Ondertussen hebben we bijna 3.500 exoplaneten ontdekt in meer dan 2.500 verschillende planetenstelsels, waarvan honderden meer dan één planeet bevatten. Deze planetenstelsels verschillen van elkaar in grootte, samenstelling, massa en planeetbanen. Dit alles leidt ertoe dat er een grote verscheidenheid aan werelden kan zijn die leven kunnen bevatten.

Om de oorsprong van zo een rijke verzameling aan planetenstelsels te begrijpen moeten we de geboorteplaatsen van deze planeten onderzoeken nog voordat deze planeten volledig gevormd zijn. Planeten, asteroïden en kometen zijn restanten van de schijf van gas en stof die zich vormt om een jonge ster. Deze circumstellaire schijven zijn een bijproduct van het stervormingsproces. Binnen gigantische wolken van moleculair gas, die in het interstellaire medium zweven, storten dichte nevels van gas en stof ineen tot een jonge protoster. Gedurende de ineenstorting vormt zich een schijf rond de jonge ster die het hoekmoment, afkomstig van de oorspronkelijke rotatie van de moleculaire wolk, herverdeeld. Dit zorgt ervoor dat de jonge ster niet zo snel draait dat deze uiteen valt. Gedurende een periode van miljoenen jaren groeit de jonge ster door het materiaal in de circumstellaire schrijf op te nemen en de schijf ontwikkelt ook verder waardoor daar planten vormen. Onder deze omstandigheden worden planeten geboren en het is essentieel om de verbinding te begrijpen tussen de structuur en chemische samenstelling van een circumstellaire schijf en de uiteindelijke planten die gevormd worden.

Om de circumstellaire schijven te bestuderen worden zowel telescopen op aarde als in de ruimte gebruikt, die gevoelig zijn voor straling op infrarood of microgolf golflengtes. Door op deze golflengtes schijven te bestuderen kunnen astronomen zowel de kleine en grote stofkorrels onderscheiden als de verschillende soorten van atomair en moleculair gas. Om goed de structuur van een schijf te begrijpen moet

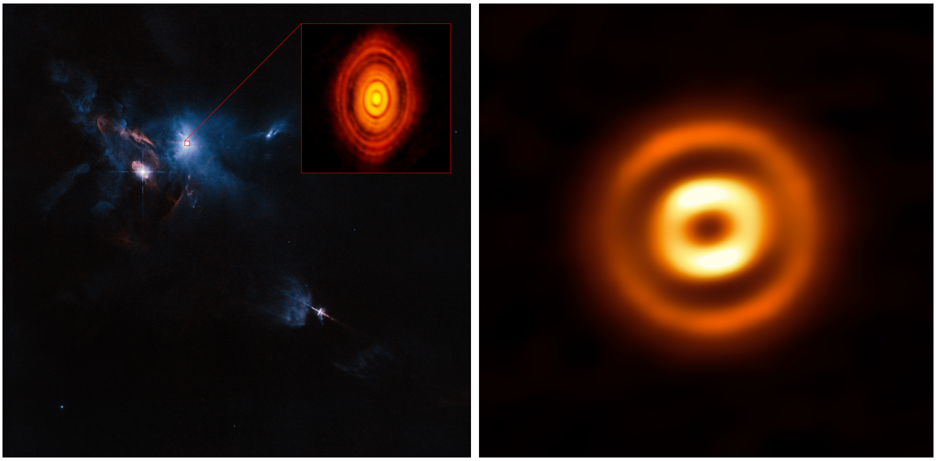

Figure: (Links) Samengestelde afbeelding van de Hubble Space Telescope en ALMA, die de omgeving van de jonge ster HL Tau in sichtbaar licht toont (hoodafbeelding). De schijf rond HL Tau (detail) is met grote scherpte afgebeeld door ALMA, wat het enorme oplossend vermogen van de interferometer laat zien. (Rechts) ALMA waarnemingen van het stof continuum in de schijf rond de jonge ster HD169142. De afbeelding laat duidelijk twee gescheiden heldere ringen zien, die mogelijk door planeten zijn gevormd die het stof opvegen.
Bron: (Links) ALMA (ESO/NAOJ/NRAO), ESA/Hubble and NASA; (Rechts) ALMA (ESO/NAOJ/NRAO), Fedele et al. 2017

er zowel stof als gas worden geobserveerd. Moderne telescopen zijn nu krachtig genoeg om circumstellaire schijven op microgolf golflengtes te ontleden door het gebruik van interferometrie. Interferometers combineren het observerend vermogen van verschillende antennes of ontvangers tot één grote telescoop om de totale diameter te vergroten en zo ook de resolutie te vergroten. De techniek vergroot het resolutievermogen van de gehele telescoop zodat deze een gedetailleerd beeld kan geven van de structuur van schijven. De grootste werkende interferometer op millimetergolflengte is de Atacama Large Millimeter/submillimeter Array (ALMA). ALMA heeft een vaste combinatie van 50 antennes met een diameter van 12 meter en is aangevuld met een compacte array van vier 12-meter en twaalf 7-meter antennes. De array kan geconfigureerd worden om een totale telescoop diameter te bereiken van 16 kilometer. ALMA is sinds 2011 operationeel en bevindt zich op een hoogte van 5000 meter op Llano de Chajnantor in Chili. ALMA heeft bijna alle observationele data geproduceerd die in dit proefschrift worden gebruikt. ALMA produceert revolutionaire beelden die astronomen in staat stellen om in meer detail de complexiteit van de structuur en de chemische samenstelling van circumstellaire schijven te bestuderen.

Dit proefschrift

Dit proefschrift onderzoekt de anatomie van de planeet-vormende gebieden in protoplanetaire schijven, waarbij gebruik wordt gemaakt van ALMA waarnemingen van stof en simpele moleculen. Het is belangrijk om de structuur en chemie van deze gebieden te begrijpen, want zij bevatten de bouwmaterialen voor planeten die misschien ook geschikt kunnen zijn voor leven. De hoofdstukken van dit proefschrift richten zich op de connectie tussen de verdeling van stofdeeltjes en de chemie die verantwoordelijk is voor de emissie van simpele moleculen, zoals koolstofmonoxide (CO), formaldehyde (H_2CO), het deuterium-dragende ion DCO^+ en methanol (CH_3OH). Van deze moleculen wordt verwacht dat zij vastvriezen op het oppervlak van stofdeeltjes diep in het midden van de protoplanetaire schijf. Dit is een belangrijk proces voor het vormen van planetesimalen, doordat ijzige stofdeeltjes beter plakken. Ook reguleert dit proces de gasfase chemie doordat moleculen uit de gasfase worden weggehaald. Op het ijzige oppervlak van de stofdeeltjes is ook een vaste fase chemie actief waaruit complexe moleculen kunnen ontstaan. Het doorgronden van de chemische oorsprong van deze complexe moleculen kan inzichten opleveren over de chemische en fysische samenstelling van planeet-vormende gebieden.

In hoofdstuk twee wordt de verdeling van formaldehyde gas onderzocht in de protoplanetaire schijf om de Herbig Ae ster HD 163296. Hierbij wordt ook gekeken de verdeling van CO gas in deze schijf en op welke manieren deze twee gassen aan elkaar gerelateerd zijn. De verwachting is dat formaldehyde voornamelijk gevormd wordt in de vaste fase door het toevoegen van waterstof aan CO ijs in de koude delen van de schijf. Er is echter ook een onbekende bijdrage van een warmer vormingsproces in de gasfase. Wanneer formaldehyde gevormd wordt in de vaste fase kan het fungeren als eerste stap op de weg naar vormen van meer complexere moleculen zoals methanol en andere alcoholen. In dit hoofdstuk wordt de analyse van formaldehyde emissie lijnen gepresenteerd die zijn waargenomen met ALMA in de schijf rond HD163296. Met behulp van bestaande modellen van HD 163296 wordt er geprobeerd de waargenomen emissie van H_2CO en $C^{18}O$, een zeldzamere isotopoloog van CO, te reproduceren. Om de waarnemingen te kunnen reproduceren moet de H_2CO abundantie abrupt toenemen met een factor twee aan de rand van het millimeter stof. Op dezelfde plek moet de CO abundantie abrupt afnemen met een factor tien. Deze afname van CO kan veroorzaakt worden doordat dit molecuul vastvriest op stofdeeltjes diep in de schijf. Een andere mogelijke oorzaak is dat CO in de bovenste delen van de schijf door straling van de ster gefotodissocieerd wordt. De toename in H_2CO kan komen door de formatie in de vaste fase efficiënter is of door een meer actieve gas fase chemie in het buitenste deel van de schijf. Het exacte vormingspad verantwoordelijk voor de extra formaldehyde voorbij de rand van het millimeter stof blijft onbekend, maar dit hoofdstuk toont aan dat de H_2CO productie op een fundamentele manier verbonden is aan de structuur van het stof in de schijf rond HD163296.

In hoofdstuk drie worden recente ALMA waarnemingen gepresenteerd van de schijf rond de Herbig Ae ster HD 169142. Deze waarnemingen onthullen ringen en spleten in de structuur van het stof. Deze structuren komen ook voor in de waargenomen CO emissie, die gerelateerd is aan de structuur van het gas. Waargenomen emissie van het continuum onthult twee duidelijke ringstructuren in het stof. Waarnemingen van ^{12}CO, ^{13}CO en $C^{18}O$ laten zien dat de structuur van het gas verschilt van de structuur van het stof. Dit duidt er op dat het stof zich heeft losgekoppeld van het gas. Gebruikmakende van modellen die de structuur van de schijf en de excitatie van de moleculen beschrijven kan de waargenomen stof en gas emissie worden gereproduceerd. De substructuur die de waarnemingen van het stof het beste nabootst is een centrale holte waar zich geen stof bevindt, daarbuiten een ring met kleine vermindering van stof, gevolgd door een spleet zonder stof en als laatste een buitenste ring van stof. De gas structuur heeft een kleine centrale holte en is tot aan de rand van de spleet in het stof vermindert met een factor 30 – 40. De buitenste rand van de gas schijf is ongeveer 100 astronomisch eenheden groter dan de buitenste rand van het stof. Dit is een teken dat de stofdeeltjes groter gegroeid zijn en zich inwaarts, richting de ster zijn gaan bewegen. Dit hoofdstuk beargumenteert dat de structuur gezien in het gas en het stof consistent is met meerdere Jupiter-achtige planeten die zich een weg banen door de schijf en daarbij stof en gas opvegen en de spleten in de schijf creëren.

In hoofdstuk vier worden waarnemingen geanalyseerd van het molecuul DCO^+ in de protoplanetaire schijf rond HD 169142. Het doel is vast stellen of DCO^+ geschikt is om de fysieke structuur van het stof en het gas diep in de schijf te onderzoeken. Van DCO^+ wordt verwacht dat het zeer geschikt is voor het beschrijven van dit gebied diep in de schijf. Verder zou DCO^+ ook gebruikt kunnen worden om de CO ijs lijn te traceren, omdat de vorming van DCO^+ afhangt van een balans tussen CO in de gas fase en CO in de vaste fase. De fysieke structuur van HD 169142 beschreven in hoofdstuk drie wordt hier gebruikt samen met een simpel deuterium chemie netwerk om de waargenomen DCO^+ emissie te reproduceren. De modellen geven aan dat er een kouder en CO armer gebied aan de schijfstructuur van HD 169142 moet worden toegevoegd net buiten de rand van het millimeter stof om het DCO^+ emissie profiel te reproduceren. Dit resultaat geeft aan dat DCO^+ goed te gebruiken is om de CO ijs lijn te traceren in de HD 169142 schijf. Ook kunnen met DCO^+ structuren diep in de schijf kunnen wordemoleculen onthult die niet gevonden kunnen met de isotopologen van CO.

In hoofdstuk vijf wordt ALMA gebruikt om te zoeken naar vier emissielijnen van CH_3OH in de schijf rond de jonge Herbig Ae ster HD 163296. Methanol is een beginpunt voor complexe prebiotische chemie en is daarmee een interessant molecuul om te vinden en beschrijven in protoplanetaire schijven. Van de vorming van dit molecuul wordt verwacht dat het samenhangt met de vorming van formaldehyde, omdat beide gevormd kunnen worden door het toevoegen van waterstof aan CO ijs. Op dit moment is methanol in de gas fase alleen gevonden in de protoplanetaire schijf rond TW Hya. Methanol wordt niet gevonden in de schrijf rond HD 163296 en de waarnemingen duiden op een fractie $\lesssim 10^{-12}$ ten opzichte van H_2. Analyse van de ratio tussen methanol en formaldehyde in de schijf rond HD163296 suggereert dat er een factor tien minder methanol ten opzichte van formaldehyde aanwezig is in HD 163296 dan in TW Hya. Dit verschil kan onstaan doordat de desorptie processen van DCO^+ verschillend zijn voor beide schijven. Ook zou de formatie van H_2CO in de gas fase efficiënter kunnen zijn in HD 163296 dan in TW Hya. Een derde mogelijkheid is een verschil in de efficiëntie waarmee methanol en formaldehyde gevormd worden op de stofdeeltjes.

Dit proefschrift laat zien dat de waarnemingen van simpele moleculen zoals de isotopologen van CO, DCO^+ en H_2CO, gedaan met hoge spectrale en ruimtelijke resolutie, gebruikt kunnen worden om de structuur van protoplanetaire schijven bloot te leggen, ook diep in de schijf. Alle substructuren in de schijf beïnvloeden waar in de schijf deze moleculen voorkomen. Waarnemingen van deze moleculen zijn dus een sterk stuk diagnostisch gereedschap om de fysische structuur van de schijf te onderzoeken. Andere simpele moleculen blijven moeilijk om te vinden in protoplanetaire schijven. Dit is ook het geval voor CH_3OH ondanks de verwachte correlatie tussen dit molecuul en H_2CO, een molecuul dat wel vaak is waargenomen in schijven. Het blijft dus een open vraag in hoeverre de productie CH_3OH en die van H_2CO aan elkaar gerelateerd zijn. Toekomstige waarnemingen met

ALMA en andere telescopen zullen doorgaan met het geven van inzichten over de complexe fysische en chemische processen die bepalend zijn voor de structuur, de moleculaire ingrediënten en de omstandigheden in de planeet-vormende gebieden van protoplanetaire schijven.

PUBLICATIONS

1. *Probing midplane CO abundance and gas temperature with DCO^+ in the protoplanetary disk around HD 169142.*
   M. T. Carney, D. Fedele, M. R. Hogerheijde, C. Favre, C. Walsh, S. Bruderer, A. Miotello, N. M. Murillo, P. D. Klaassen, T. Henning, and E. F. van Dishoeck.
   Astronomy & Astrophysics, 614:A106, June 2018.

2. *Increased H_2CO production in the outer disk around HD 163296.*
   M. T. Carney, M. R. Hogerheijde, R. A. Loomis, V. N. Salinas, K. I. Öberg, C. Qi, and D. J. Wilner.
   Astronomy & Astrophysics, 605:A21, September 2017.

3. *Classifying the embedded young stellar population in Perseus and Taurus and the LOMASS database.*
   M. T. Carney, U. A. Yıldız, J. C. Mottram, E. F. van Dishoeck, J. Ramchandani, and J. K. Jørgensen.
   Astronomy & Astrophysics, 586:A44, February 2016.

4. *ALMA unveils rings and gaps in the protoplanetary system HD 169142: signatures of two giant protoplanets.*
   D. Fedele, **M. Carney**, M. R. Hogerheijde, C. Walsh, A. Miotello, P. Klaassen, S. Bruderer, T. Henning, and E. F. van Dishoeck.
   Astronomy & Astrophysics, 600:A72, April 2017.

5. *Outflows, infall and evolution of a sample of embedded low-mass protostars. The William Herschel Line Legacy (WILL) survey.*
   J. C. Mottram, E. F. van Dishoeck, L. E. Kristensen, A. Karska, I. San José-García, S. Khanna, G. J. Herczeg, P. André, S. Bontemps, S. Cabrit, **M. T. Carney**, M. N. Drozdovskaya, M. M. Dunham, N. J. Evans, D. Fedele, J. D. Green, D. Harsono, D. Johnstone, J. K. Jørgensen, V. Könyves, B. Nisini, M. V. Persson, M. Tafalla, R. Visser, and U. A. Yıldız.
   Astronomy & Astrophysics, 600:A99, April 2017.

6. *Observations and modelling of CO and [C I] in protoplanetary disks. First detections of [C I] and constraints on the carbon abundance.*
   M. Kama, S. Bruderer, **M. Carney**, M. Hogerheijde, E. F. van Dishoeck, D. Fedele, A. Baryshev, W. Boland, R. Güsten, A. Aikutalp, Y. Choi, A. Endo, W. Frieswijk, A. Karska, P. Klaassen, E. Koumpia, L. Kristensen, S. Leurini, Z. Nagy, J.-P. Perez Beaupuits, C. Risacher, N. van der Marel, T. A. van Kempen, R. J. van Weeren, F. Wyrowski, and U. A. Yıldız.
   Astronomy & Astrophysics, 588:A108, April 2016.

Proceedings

1. *Modeling of a stepped Luneburg lens for all-sky surveys.*
   M. Carney and M. A. Kenworthy.
   Proceedings of the SPIE 10706, Advances in Optical and Mechanical Technologies for Telescopes and Instrumentation III, 107063H (10 July 2018).

CURRICULUM VITAE

I was born in the small town of Damariscotta, Maine in the USA on the 14th of May 1988. I grew up in the even smaller nearby town of Jefferson, Maine, where I completed my elementary and middle school education at Jefferson Village School. My first memorable encounters with astronomy involved perusing through the book *Our Universe* by Roy A. Gallant, which was kept around the house. It contained a dossier of each planet in the Solar System, showing breakdowns of planetary orbits, masses, sizes, and compositions – even the Latin god or goddess associated with the planet and their mythology. I thought it was the coolest thing in the world. I attended high school at Erskine Academy in South China, Maine, and graduated in 2006 with a mind to explore an astronomy education in the future.

I went to the University of Maine in Orono, Maine to study physics for my undergraduate degree. I enrolled in any astronomy course available, and during my time there I participated in three Research Experience for Undergraduate (REU) programs funded by the National Science Foundation. In the summer from June to August 2009 I participated in the Optics in the City of Light REU program, sponsored by the University of Michigan and ParisTech institutes, which sent six students to the École Polytechnique/Institut d'Optique in Paris, France to work in laser laboratory optics research for ten weeks. During the winter and spring from January to May 2010 I went to La Serena, Chile for an optical astronomy REU program hosted by the Cerro Tololo Inter-American Observatory (CTIO) and sponsored by the U.S. National Optical Astronomy Observatory (NOAO) and the Association of Universities for Research in Astronomy (AURA). There I worked on polarization light curves of the cataclysmic variable system HU Aquarii and conducted two nights of observations using the SMARTS 1.0-meter telescope located on Cerro Tololo. Throughout the summer and fall from June to December 2010 I was involved in a third REU program at the University of Maine Laboratory for Surface Science and Technology (LASST) where I tested the pressure response of a high-temperature surface acoustic wave sensor for use in harsh industrial and aeronautics environments. I graduated with summa cum laude honors from the University of Maine in December 2010 with a Bachelor of Science (B.Sc.) in Physics.

Following my bachelor's degree I took several months to travel to New Zealand, and shortly after returning I moved to The Netherlands in August 2011 to begin my graduate education at Leiden University. I received the NUFFIC Huygens Scholarship – since discontinued – for the two-year Research Astronomy master's program at Leiden Observatory. During the first year of the program I completed my minor research project with Dr. Matthew Kenworthy, which involved modeling a spherical Luneburg lens as a passive, all-sky optical survey instrument. In the second year I went on to do my major research project and master's thesis with Prof. dr. Michiel Hogerheijde on observations of warm carbon monoxide gas in protoplanetary disks. I graduated from Leiden Observatory in August 2013 with my Master of Science (M.Sc.) in Research Astronomy.

For one year from August 2013 to August 2014 I worked with Prof. dr. Ewine van Dishoeck and Dr. Joseph Mottram at Leiden Observatory. The project involved mapping dense gas in embedded young stellar objects located in several nearby star-forming regions in order to properly identify their evolutionary stage. In September 2014 I began my Ph.D. program investigating structure and chemistry near the midplane of protoplanetary disks under the supervision of Prof. dr. Michiel Hogerheijde, with Prof. dr. Ewine van Dishoeck as co-promoter. My thesis focuses on using spatially and spectrally resolved observations of simple molecules to place constraints on the ongoing chemical and physical processes related to gas and millimeter-sized dust in the planet-forming regions of disks. Throughout the course of my thesis I attended two international interferometry schools hosted at the European Southern Observatory (ESO) in Garching, Germany and at the Institut de Radioastronomie Millimétrique (IRAM) in Grenoble, France. I presented my research at local Dutch conferences and at international conferences in Cyprus and the USA – with funding provided by the Leids Kerkhoven-Bosscha Fonds – as well as Scotland. I collaborated with international teams of astronomers in Chile, the USA, and throughout Europe, and published results in one of the premier peer-reviewed astronomy journals, Astronomy & Astrophysics.

Upon completion of my thesis I will remain in The Netherlands for the next several years. I will move to the north of the country to live in the city of Groningen, where I will pursue career interests outside of astronomy.

ACKNOWLEDGEMENTS

There are many people in my life who have been sources of friendship and support in one form or another during my time in Leiden and the years before. In this section I name several, but there are countless others who contributed positively to my personal and professional growth in their own way. For that, I thank you.

I owe all of my parents far more than a few sentences can describe. You have always encouraged me to take advantage of opportunity, whether that be travel, an education in astronomy, or living abroad for more than seven years. You have my enduring gratitude for all that you have done. My sister Alison has been a life-long friend. I will always appreciate your kindness and sisterly goofiness. I am continually proud of the person you have become. To my older brothers, Jesse and Brett, I hold you both in high regard and have always looked up to with respect. To the whole family, I know I have not always been geographically close, but we have maintained connections across oceans and you continue to be an important part of my adult life.

My Ph.D. experience was made rich by the expertise and counsel of the Leiden Allegro director and newly appointed Professor of Instrumental Astronomy at the University of Amsterdam. I consider myself exceedingly fortunate to have worked with you over the years. To my officemates and co-supervisees, Nico and Eva, I will miss our time in the office and conference trips. It was a pleasure to spend many of those tedious research hours with two light-hearted, funny, and down-to-earth friends. We will forever be Michiel's Angels. To the new supervisees, Leon and Jeroen, I wish you the best of luck with your own doctorates. I know you are in good hands. To all other members of the van Dishoeck–Hogerheijde star and planet formation groups, I appreciate the scientific and friendly discussion over the years. Thank you in particular to Umut Yıldız and Joe Mottram for your help during my year of research prior to the Ph.D., and to Markus Schmalzl and Luke Maud at Allegro for teaching me the intricacies of interferometry and ALMA data. Cam, I enjoyed our mid-hallway life updates and your impeccable dad jokes. Jeroen, Marijke, and Henriette, I will always have fond memories of watching the sky go dark among whooping vikings on a Faroe Islands hilltop. To Sterrewachters unnamed, thank you for a great Leiden experience. You will be missed.

Outside of the observatory I was fortunate enough to forge many friendships. To Mark and Jori of House Flanorpad, nights around the Dutch house will always be memorable. Thanks for all the shared banter, laughs, meals, and retro gaming.

Graeme, I had the great joy of living with you at Pieter Huibertsgang. You were a model housemate, handyman, and brew partner. Guido, you became an unexpected roommate at Hoge Rijndijk, which made for a good transition toward solo living. We forged our own tradition of burly brunches and Band of Brothers. I owe a lot to you for dragging me to Belgium. That trip changed my life.

To the closest friends that I have made in Leiden, all of whom have made my life better in many ways. Mart Cornelis Johannes van de Wiel. My man! Sharing a home with you for three years was an adventure. We made glorious meals, shared tasty brews, and built up a library of inside jokes and pop culture references that should go down in the annals of history. Living with you at Koestraat will always be an important chapter in my life. Allison, over the years that we have shared in this city, you became one of my closest friends both inside and outside the observatory. Thanks for all of the Sterrewacht lunches and coffee breaks, Ph.D. venting sessions, countless board game nights, and your continued friendship in the years ahead. Alex West, a man that I respect and admire. It's been inspiring to watch you take the Dutch job market by storm. You are, of course, included in the thanks for countless board games. I will forever think of you when reading the New York Times. It was an honor to stand by your side at a significant new chapter of your own life with Allison. Gorana, I'm happy that I got to know you during the P. Huibertsgang era and beyond. You were the absolute champion in our battle over unjust bills! And you are an outstanding person. I have always appreciated that you have such strength and tenacity while being so kindhearted. Rene, you are the truest Dutchman I know, in all the right ways. Through Dutch dinners, Museumnachten, Eurovision contests, and poker nights, I have enjoyed getting to know you, your dance moves, and your sense of humor. Mark, you will be the first person to own a fully functional smart home. Thanks for all the good-natured conversation during brewery visits, beach days, and trips to the park. We absolutely nailed Allison's defense video. Olga, a seemingly infinite source of pep and energy! I love that you are always able to fire people up for some fun. It has been a joy to share escape rooms, New Year's Eve and Halloween parties, and a glass (or three) of fine wine with you. Alex South, our local Kiwi. I'm glad to have worked, brewed, and traveled with you over the years. It was a privilege to be there through your own observatory experience, and fantastic to have you as part of Dutch life again. Latecomers Erin and Layla, it was great getting to know you both as you bounced between the U.S. and Leiden. I hope you had as much fun making memories here as the rest of us. To those who have moved away: Marissa, you played such a large part in bringing people together and were always a good colleague, housemate, and friend throughout my years in Leiden. Tiff and Tom, I'm thankful that we have grown close and become friends. It was an honor to attend your wedding, and I wish you all the best in the future. I extend an affectionate thank you to every one of you for the game nights, boulderhal trips, brew days, movie nights, park afternoons, parties, gifts, boat trips, group dinners, weekend travels, and all the memories made and laughs shared along the way.

And finally, my partner Allie. When I met you near the beginning of my Ph.D. I could not have known that you would become a foundational part of my life for the next four years. I am thrilled to start a new chapter in Groningen! Life, with all of its routine and spontaneity, is now difficult to imagine without you. I consistently find your drive and focus inspiring and your intelligence and humor disarming. You are a source of happiness and support that I appreciate every single day. I am beyond excited to build our life together.